Modelling the Longer Term Effects of Spinal Burst Fracture Repair using Vertebroplasty

Corinne Angela Hanlon

Submitted in accordance with the requirements for the degree of

Doctorate of Philosophy

The University of Leeds

School of Mechanical Engineering

Institute of Medical and Biological Engineering

December, 2012

For Tony Óg

Acknowledgements

This research would not have been possible without the assistance of my two supervisors, Professor Ruth K. Wilcox and Professor David C. Barton, for whose guidance and support I am forever grateful. They believed in me when I didn’t believe in myself and for this, I thank them. I owe a special mention and thanks to Ruth for all the times that she managed to pick me up and dust me off!

Working as part of a collaboration with Sami Tarsuslugil at the University of Leeds and Rochelle O’Hara, Iwan Palmer, Nicholas Dunne, Fraser Buchanan, Susan Clarke and John Orr at Queen’s University Belfast was a great experience. I worked closely with Sami and I am grateful for all of his assistance. I would like to thank all of the team at Queen’s University Belfast for their valuable input and interesting discussions over the past four years, especially the “passage” conversation.

I would like to extend my thanks to all of my friends from the Spine Group, especially Al and Sarry, who helped me along on the path of research….and cake eating!

I wish all the best for everyone in the office, especially Kieran, Seb, Dan and Lee, who have helped to make my time at Leeds a better one from all the times we have spent laughing with, and at, each other!

I cannot express how valuable, and sometimes essential, my friendship with Beth has been throughout my time in Leeds. I count myself lucky to have been as fortunate as I have been to meet her. Beth has helped me overcome so many obstacles and I will always value the times we spent discussing all things PhD related, whether that was over a cup of tea or when munching on some fish and chips.

Finally, for my long suffering and ever supportive family: it’s over. I would like to thank each and every one of my family members for all of the ways that they have helped me throughout my long time in education. My Mum has been an amazing source of support and I would not have succeeded without her being there for me.

Abstract

Burst fractures account for 15% of all spinal fractures and generally occur in the younger, more active generations. Traditional treatments of burst fractures can be highly invasive and may involve spinal fixation. Favourable short term results have been obtained when vertebroplasty has been used to repair osteoporotic compression fractures. However, there have been limited studies into the use of vertebroplasty for burst fractures. The aim of this study was to develop *in vitro* and computational models that could be used to investigate the longer term effects of spinal burst fracture repair using vertebroplasty.

An experimental technique was established to create fractured porcine vertebrae, of a known severity grade, which were subjected to multiple-cycle loading in order to determine the post-fracture behaviour over time and to compare between augmentation materials. Finite element (FE) models were created using micro-computed tomography (µCT) images of the fractured porcine vertebrae and compared to the experimental results. Methods to represent the plastic deformation of the vertebrae were investigated. The models were used to investigate the effect of fracture dispersion and the level of cement augmentation on post-fracture behaviour.

The multiple-cycle loading regime captured the post-fracture behaviour for the majority of the specimens with some propagation of damage but without the complete failure of the specimens. The FE models were best able to predict post-fracture behaviour when there was a lower level of fracture and cement dispersion. The method used to simulate the plastic deformation of the vertebrae captured the displacement of the specimens but not their change in stiffness. The computational results showed that there was little difference between the ability of the polymethylmethacrylate and calcium phosphate cements to restore vertebral stiffness.

The results of the study indicate that with current cements, fractures with a severity grade greater than 10.5 should not be augmented without some other form of fixation such as posterior instrumentation. Further work is necessary to develop computational material models that provide better predictions of the fractured bone over multiple cycles.

List of Abbreviations

µCT	Micro-computed tomography
ALL	Anterior longitudinal ligament
BMD	Bone mineral density
BSE	Bovine spongiform encephalopathy
BVF	Bone volume fraction
CaP	Calcium phosphate
CJD	Creutzfeldt-Jakob Disease
CPU	Computational processing unit
DC1	Displacement Control, trial 1
DCML1	Displacement Control with maximum Load, trial 1
FE	Finite element
FSU	Functional spinal unit
LC1	Load Control, trial 1
NONE	Non-augmented specimens
PLL	Posterior longitudinal ligament
PMMA	Polymethylmethacrylate

Table of Contents

List of Tables

List of Figures

Chapter 1
Literature Review

1.1 Introduction

Burst fractures account for 15% of all spinal fractures (Amoretti *et al*. 2005) and result from the application of a high rate axial compressive load to the spine (Holdsworth 1963). Burst fractures generally occur in the younger, more active generations due to motor vehicle accidents or falls from height (Briem *et al*. 2007; Bensh *et al*. 2006). Traditional treatments of burst fractures can be highly invasive and may involve stabilisation of the fracture site and/or decompression of the spinal canal (Valentini *et al*. 2006; Verlaan, Oner and Dhert 2006; Chen and Lee 2004; Vaccaro *et al*. 2003; Dai 2001; Boerger, Limb and Dickson 2000; Shono, McAfee and Cunningham 1994).

Vertebroplasty is a minimally invasive percutaneous augmentation technique where bone cement is injected into the vertebral body and was initially used to treat metastatic lesions (Galibert *et al*. 1987). It is now used to treat osteoporotic vertebral compression fractures and aims to stabilise the fracture site, restore vertebral height and reduce associated pain. Vertebroplasty is usually carried out under local anaesthetic (Jensen *et al*. 1997) and results from short term clinical follow-ups have indicated that post-augmentation, patients reported a significant reduction in pain (Baroud and Bohner 2006; Levine *et al*. 2000; Jensen *et al*. 1997). However, longer term studies have shown that post-augmentation, there was a higher incidence of failure in the adjacent non-augmented, osteoporotic vertebrae (Rad *et al*. 2011; Chen *et al*. 2010; Trout and Kallmes 2006; Trout, Kallmes and Kaufmann 2006; Wilcox 2006; Baroud *et al*. 2003; Polikeit, Nolte and Ferguson 2003; Uppin *et al*. 2003; Berlemann *et al*. 2002; Grados *et al*. 2000). More recent studies have highlighted that vertebroplasty may not offer more pain relief than conservative treatments (Buchbinder *et al*. 2009; Kallmes *et al*. 2009) or a sham treatment (Klazen *et al*. 2010).

It may be possible to treat burst fractures using vertebroplasty but there have been limited studies on the matter (Doody *et al*. 2009; Amoretti *et al.* 2005; Huet *et al*. 2005; Chen and Lee 2004; Chen, Wu and Lee 2004). Because burst fractures generally occur in the younger and more active generations, the likelihood of osteoporosis and adjacent failure may be relatively low.

The potential treatment of burst fractures using vertebroplasty may be further aided by the use of a bioactive cement. A principal component of many bioresorbable cements is calcium phosphate (CaP) which encourages bone remodelling and bone in-growth. If a burst fracture were to be repaired using a bioactive cement, it is possible that in time, the augmented fracture site would be entirely composed of newly remodelled bone. However, the optimum material properties of a bioresorbable cement that would make it suitable for vertebroplasty of a burst fracture have yet to be established.

This PhD was part of a collaboration with Queen’s University Belfast which encompassed a total of four PhD projects. These have been structured to investigate and optimise the use of CaP bone cements in vertebroplasty to achieve effective primary fixation of spinal burst fractures. The overall aims of the programme were to identify the key mechanical properties that are required for the augmentation of spinal burst fractures using computational models, to manufacture and characterise CaP cements in order to meet the optimum properties, to measure the *in vivo* and *in vitro* behaviour of the optimised CaP cement and to predict the longer term effects of spinal burst fracture repair using vertebroplasty. It is aspects of these final two aims that are presented in this thesis.

1.2 Human Spinal Anatomy

The spinal column is divided into five distinct zones as shown in Figure 1.1. The cervical and thoracic regions are composed of the seven and twelve most superior vertebrae, respectively and the following five are classified as the lumbar region. The vertebrae in these three zones are separated by intervertebral discs that allow the vertebrae to articulate relative to each other. The sacral region is part of the pelvis and is made up of five fused vertebrae. The coccyx, also known as the tailbone, is composed of four fused vertebrae.

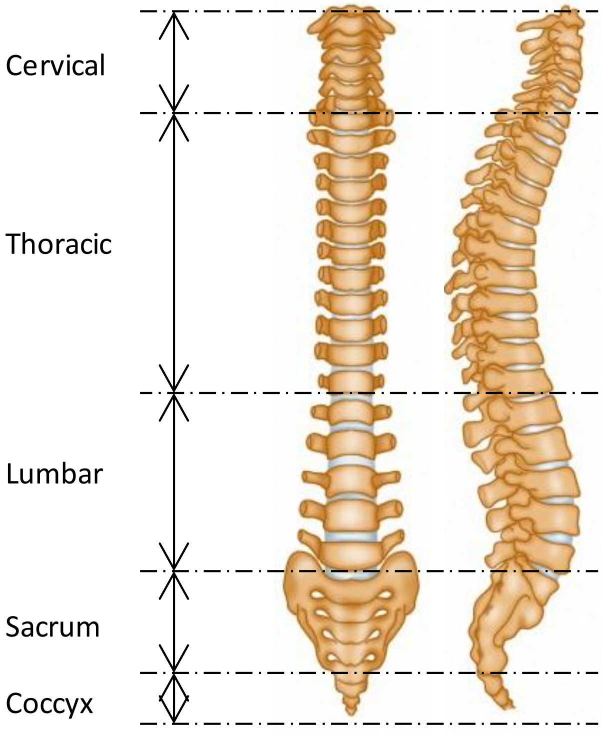

Figure 1.1 Coronal and sagittal views of the spine (adapted from Wellcome Images 2012).

Each vertebra within the spinal column may be divided into three regions; the anterior region or the vertebral body, the pedicles and the posterior elements, as shown in Figure 1.2.

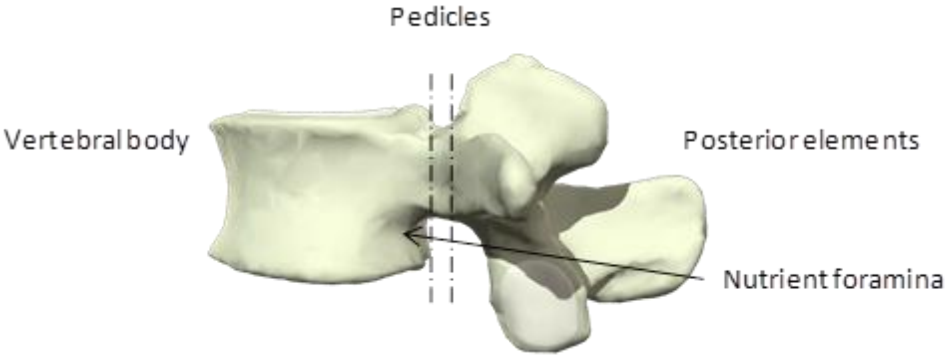

Figure 1.2 Sagittal view of a typical lumbar vertebra (adapted from Anatomy TV 2012).

As this project is concerned with the lumbar spine, the composition of a typical lumbar vertebra is explained in the following subsections with respect to these divisions. Also presented is a discussion of the ligaments of the lumbar spine which are most relevant to this study and a brief summary of the structure of the intervertebral disc.

1.2.1 The Lumbar Vertebra

The vertebral body forms the anterior region of the spine and is the primary weight bearing component. The vertebral body mainly supports axial loads although the vertebrae can also rotate and translate relative to each other, via the complex interactions of the disc and articular facet joints (Section 1.2.3). The superior and inferior surfaces of a typical lumbar vertebra are concave and the anterior of the vertebral body is also concave whilst the lateral edges are often concave. Located posteriorly on the vertebral body are one or more nutrient foramina. The nutrient foramina provide access for the nutrient arteries and basivertebral veins to the centre of the vertebrae. The major components of a typical lumbar vertebra are shown in Figure 1.3.

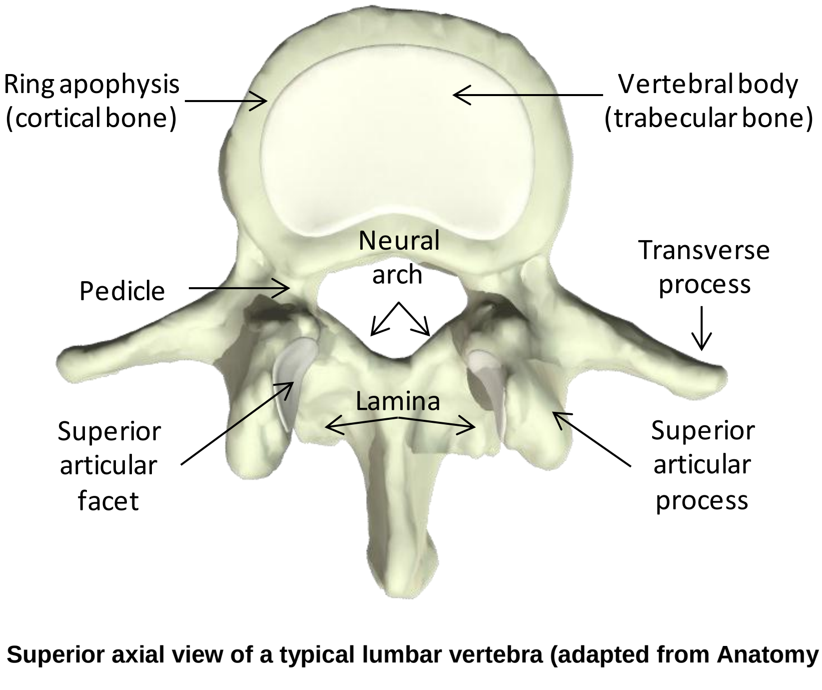

Figure 1.3 Superior axial view of a typical lumbar vertebra (adapted from Anatomy TV 2012).

Trabecular bone is found at the ends of long bones and within vertebrae. In the lumbar region, the trabecular bone supports up to 80% of the load applied to a vertebra (Silva, Keaveny and Hayes 1997). It is formed by individual bony struts called trabeculae which are usually 0.1 mm in diameter and with a spacing of approximately 1 mm between struts (Currey 2006). The trabeculae are surrounded by bone marrow, deposits of fat and a blood supply that is used for venous drainage. The apparent elastic modulus of trabecular bone has been seen to vary between 0.08 and 1 GPa (Linde, Hvid and Madsen1992).

The trabecular core is surrounded by a thin shell, the cortical shell, which can be up to 0.6 mm in thickness and is commonly described as being composed of cortical bone (Silva *et al*. 1994). However, the cortical bone in this region has been found to bear a closer resemblance to densely packed trabecular bone with a porosity of between 5% and 30% (Silva *et al*. 1994; Mosekilde 1993). There is a variation in the thickness of the cortical shell; the thickness of the posterior region of the cortical shell has been found to be less than half that of the anterior region (Silva *et al*. 1994). The ring apophysis is a narrow ring of raised bone on the superior and inferior edges of the cortical shell.

1.2.2 The Pedicles

Projecting superiorly from the posterior of the vertebral body are two stout cylindrical pillars called the pedicles. The pedicles connect the vertebral body to the posterior elements. All non-axial loads experienced by the spine are transmitted from the vertebral body to the posterior elements via the pedicles.

1.2.3 The Posterior Elements

Each set of posterior elements is composed of two superior and two inferior articular process, two superior and two inferior facet joints, two transverse processes and one spinous process as shown in Figure 1.4.

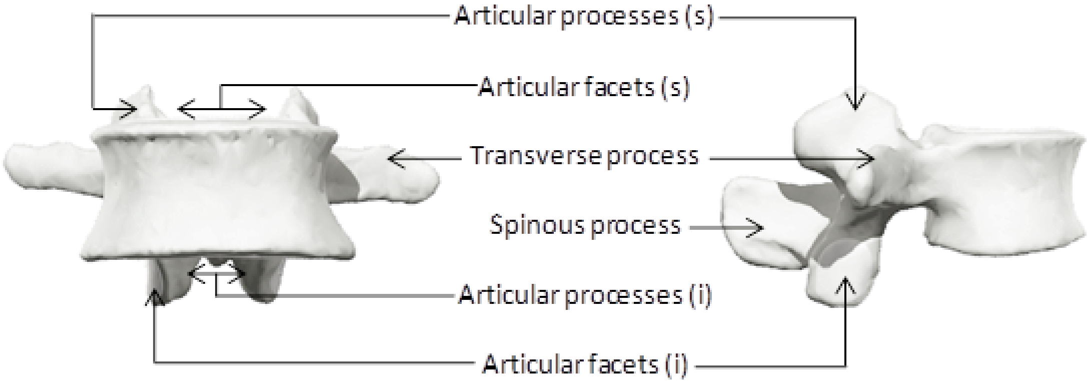

Figure 1.4 Coronal and sagittal views of a typical lumbar vertebra. The superior and inferior components are indicated by (s) and (i), respectively (adapted from Anatomy TV 2012).

The inferior processes are masses of bone which project inferiorly from the laminae, two thin broad surfaces that fuse to form the vertebral arch, and are connected to the superior processes of an adjacent vertebra through contact of the facet joints (also known as zygapophysial joints). The facets are smooth areas of articular cartilage on the medial side of each superior process and the lateral side of each inferior process. The facets come into contact to unite adjacent vertebrae. The facet joints allow for motion in the lumbar spine but resist excessive twisting and the forward sliding of the vertebrae. The transverse processes allow for the attachment of muscles and ligaments which assist in the rotation of the spine. Perpendicular to the transverse processes is the spinous process which also allows for the attachment of muscles and ligaments. The spinous process projects posteriorly from each vertebra at the junction of the two laminae and is the bone that can be felt below the surface of the skin.

1.2.4 Ligaments of the Lumbar Spine

The intersegmental system of spinal ligaments is usually held in tension and acts to hold the spine in compression along its length. The anterior longitudinal ligament (ALL) is a long band covering the anterior of the lumbar spine. The ALL is well developed in lumbar region, but it is not restricted to that region and consists of regions of collagen fibres spanning different levels. The posterior longitudinal ligament (PLL) is found throughout the entire spine. However, in the lumbar region, it forms a narrow band over the back of the vertebral body and expands laterally over the discs.

1.2.5 The Intervertebral Disc

The intervertebral disc forms a cartilaginous joint between adjacent vertebrae and resists compression but allows for rotational motion within the spine. Each disc is composed of three elements; the annulus fibrosus which acts to radially encase the nucleus pulposus and the vertebral endplates which superiorly and inferiorly encase the annulus fibrosus and nucleus pulposus. The endplates can be considered as part of the disc, rather than the vertebral body, because following trauma, where the disc is torn from the vertebral body, it has been observed that the endplate remains attached to the disc, not the vertebral body (Bogduk 2005). The thickness of the endplates ranges from about 0.2 to 0.5 mm and the main function is to prevent extrusion of the nucleus pulposus into the vertebral body, although this is not always possible, especially under high rate axial loading. The endplates also act as a nutritional pathway.

The annulus fibrosus is composed of highly ordered collagen fibres arranged in 15 to 20 layers called lamellae which are embedded in a gel. The lamellae are arranged in concentric rings which are thicker towards the centre of the disc. The laminae are finer and more tightly packed at the posterior of the disc which results in the annulus fibrosus being thinner there. The collagen fibres and lie parallel within each lamella and are structured at 65 to 70^o to the spinal axis and alternate by plus or minus 90^o from one lamellae to the next.

The nucleus pulposus is a gelatinous mass made up of a small amount of cells with a suspension of irregularly structured collagen fibres. However, in the adult human, solid properties have been observed (Guilak *et al.* 1999). The radial expansion of the nucleus pulposus is limited by the annulus fibrosus therefore, when an axial load is applied to the spine, the nucleus pulposus acts to exert a uniform load upon the adjacent endplate.

1.2.6 Biomechanics

The biomechanics of the lumbar vertebrae are presented in the following subsection with relation to the material properties, the typical loading experienced and the behaviour when subjected to reloading following overloading.

Material Properties

The ultimate load of intact human lumbar vertebrae vary considerably due to factors such as age and sex and have been reported to vary from 2 – 12 kN (Brinckmann, Biggemann and Hilweg 1989). A more recent study has observed a similar variation in results and reported an ultimate load of between 2 and 16 kN with stiffness values in the broad range of approximately 6 – 40 kN/mm (Kopperdahl, Pearlman and Keaveny 2000). The Young’s modulus of trabecular cores has also been found to vary considerably with a mean and standard deviation values of 396 ±181 MPa (Keaveny, Wachtel and Kopperdahl 1999). The variation observed in the material properties is due to the nature of cadaveric specimens where even if the sex and age of a selection of specimens is matched, the effects of health and lifestyle may lead to a broad range of values.

Reloading Behaviour

Cores of human trabecular bone have been reloaded following the application of a load greater than the ultimate load (Keaveny, Wachtel and Kopperdahl 1999). The reduction in Young’s modulus and strength were best related to the plastic strain and it was possible to quantify a reduction in modulus and strength as a percentage of plastic strain. The reduction in the modulus from the initial cycle to the reloading cycle ranged from approximately 5 – 91% whilst the average reduction in strength was between 4 – 64%.

In a similar study, intact human vertebrae were reloaded following overloading (Kopperdahl, Pearlman and Keaveny 2000). The reduction in the stiffness of the specimens ranged from approximately 0 – 84% and the reduction in the ultimate load ranged from 17 – 53%. As with the study of the trabecular cores, plastic strain was used to provide equations which quantified the reduction in stiffness and ultimate load. Equations that specify the reduction in the material properties of trabecular bone can be used in computational modelling to reduce the stiffness of a vertebral specimen from one cycle to another.

Typical Loading

A number of studies have used *in vivo* investigations to assess the loads experienced by the lumbar spine during a range of daily activities. *In vivo* measurement of spinal biomechanical responses is advantageous because all of the muscles and ligaments that are attached to the processes are included. The disadvantages include an increase in the errors associated with repeatability and the accuracy of the measurements obtained. However, computational biomechanical assessments of the spine have shown that *in vitro* studies, which cannot accurately include or replicate the actions of the muscles and ligaments, have a greater level of spinal instability and an increased likelihood of buckling (Gardner-Morse, Stokes and Laible 1995; Goel *et al*. 1993).

The values of compressive loads found in the literature have been presented either as an absolute value or as a multiple of the mean body weight of the subjects. In the instances where the mean body weight of the subjects was presented, the current author has assumed a weight of 70 kg, presented the findings in Newtons (N) and specified where 70 kg has been assumed.

The compressive load experienced by the lumbar spine during standing was found to range from 0.6 to 1.5 kN (Callaghan and McGill 2001) in a series of computational simulations. The respective results from one study on the compressive load experienced by the lumbar spine during sitting and two computational studies during walking indicate that a greater load was experienced when sitting (Callaghan and McGill 2001; Callaghan, Patla and McGill 1999; Cappozzo 1984). The range of compressive loads observed computationally when sitting was from 0.9 to 2.4 kN (Callaghan and McGill 2001) whilst the range of compressive loads when walking was found computationally to range from 0.7 to 2.1 kN (Callaghan, Patla and McGill 1999; Cappozzo 1984 (assumed body mass of 70 kg)). The peak loads from walking were observed at a frequency of 1.3 to 2.5 Hz (Cappozzo 1984). An additional study used a biomechanical model to investigate the variation of loads in the lumbar spine when an individual carried a backpack of up to 30% of their body mass (Goh, Thambyah and Bose, 1998). It was found that the compressive load on the L5-S1 region was approximately 1.5 times the body weight during a no-load scenario whilst this increased to approximately 2.4 times the body weight when a carrying a backpack of 30% the individual’s body mass (Goh, Thambyah and Bose, 1998).

1.3 Porcine Spinal Anatomy and Properties

Bovine, ovine and porcine spines have been frequently used in spinal research (Ahlgren *et al*. 1994; Gurwitz *et al*. 1993; Eggli *et al*. 1992; Allan *et al*. 1990) with bovine and porcine spines especially well-suited for thoracolumbar research due to the orientation of the facet joints (Cotterill *et al*. 1986). With the outbreak of Creutzfeldt-Jakob Disease (CJD) in humans, as a direct result from bovine spongiform encephalopathy (BSE), the use of porcine specimens for surgical research of the spine has been recommended (Busscher *et al*. 2010). Porcine spines are much more readily available than cadaveric specimens and offer a reduction in the variability of bone quality that is often associated with age and sex.

1.3.1 Vertebral Anatomy

The porcine thoracolumbar region may possess up to seven more vertebrae than the human thoracolumbar region (Menhusen 2002). A comparison of the number of vertebrae in the human and porcine cervical, thoracic and lumbar regions is shown in Table 1.1.

Table 1.1 Number of vertebrae in human and porcine spinal regions (Menhusen 2002).

	Human	**Porcine**
Cervical	7	7
Thoracic	12	14 – 15 (rarely 16 – 17)
Lumbar	5	6 – 7

The geometrical measurements of porcine and human vertebral specimens were compared in a study by Bass *et al*. (2008). In this study, the micro-computed tomography (µCT) images of 24 porcine spines and 16 cadavers were analysed. It was found that the porcine vertebral width and depth were smaller than the human vertebrae by 40% and 30%, respectively. The greatest correlation between human and porcine spines was observed in the lumbar region. However, a greater level of geometrical similarity was observed when the human thoracolumbar region was compared to the lower end of the porcine thoracic region (T6 – T16).

Additional studies have also compared the geometrical measurements of human and porcine spines and have recommended that porcine specimens are an adequate alternative to cadaveric specimens (Busscher *et al*. 2010; Dath *et al*. 2007).

1.3.2 Material Properties

The distribution of various mechanical properties across the vertebral width of trabecular porcine specimens from the lumbar region was investigated and the Young’s modulus was reported to be 521 MPa (Lin, Tsai and Chang 1997) which was similar to the value of 396 ±181 MPa obtained for trabecular cores from human lumbar vertebrae (Keaveny, Wachtel and Kopperdahl 1999).

The average ultimate strength of porcine trabecular bone was greater above the nucleus pulposus than above the annulus fibrosus by a factor of 1.2 (Lin, Tsai and Chang 1997). This was similar to findings from a comparable study using human cadaveric specimens where the relationship was found to vary by a factor of 1.3 (Keller *et al*. 1990).

Typical Loading

There is no data available on the typical loads experienced by pigs, however studies have investigated the manner in which porcine spines are loaded. The direction of the main trabecular struts in the porcine lumbar region, and in the human spine, is parallel to the spinal canal (Lin, Tsai and Chang 1997). As trabeculae formation is predominantly in the direction of load bearing, it can be concluded that the porcine lumbar region is loaded in a direction perpendicular to the endplates. Subsequent research has also shown that the quadruped spine is in fact loaded along its length (Smit 2002). Therefore, although porcine spines are not loaded whilst in an upright direction like human spines, loads are transmitted along the length of the spinal column, which is directly comparable to humans.

1.4 Spinal Burst Fractures

Spinal burst fractures result from the application of a high rate axial load to the spinal column and are characterised by the retropulsion of one or more bony fragments from the vertebral body into the spinal canal. Burst fractures generally occur in the thoracolumbar region (Bensch *et al*. 2006; Bohlman 1985). Early descriptions of the fracture mechanism state that the fracture is akin to an "explosion" of a vertebral body due to the inability of the endplate to prevent the penetration of the nucleus pulposus into the vertebral body (Holdsworth 1963). It has been suggested that this is due to an increase of the pressure within the intervertebral disc (Roaf 1960). However, more recent *in vitro* studies have suggested that the burst fracture mechanism is not due to an increase in the pressure of the intervertebral disc but instead due to the high loading rates at which burst fractures occur (Ochia and Ching 2002) and the high strains developed at the pedicles (Wilcox *et al*. 2004; Hongo *et al*. 1999).

1.4.1 Spinal Stability

Treatment of a burst fracture is administered on the basis of whether the vertebra is stable or not. Unfortunately, many definitions of spinal stability exist which can be both broad and vague due to the fact that research is conducted by both clinicians and engineers who may hold differing concepts of stability. The clinician may use the term "stable" to refer to an injury which does not pose a neurological threat whilst the engineer may associate spinal stability with a sound mechanical integrity. The definition of spinal instability which will be the foundation in this discussion is that by White and Panjabi (1990) where spinal instability is defined as "the inability of the spine under physiologic loads to maintain relationships between vertebrae so that there is neither initial nor subsequent neurological deficit, no major deformity, and no severe pain" (cited in Panjabi *et al*. 1995 p.1122). Using this definition, it follows that the mechanical integrity of the vertebrae is the key to stability as it is possible that a mechanically unsound vertebra may result in a subsequent neurological deficit.

1.4.2 Clinical Classification

In order to guide clinicians to the most appropriate treatment for burst fractures, methods to characterise the stability of the vertebrae have been investigated and several classification systems have been developed. Such classification can also be useful on an experimental level. If the severity of a set of fractured specimens was known, and found to be of a similar magnitude, it may be possible that the confidence associated with a trial would increase. Fractures of a similar severity would make it possible for the effect of various spinal fracture treatments to be determined in a less biased and more controlled biomechanical assessment.

Two Column Theory

The two column theory was introduced nearly half a century ago to help classify spinal injuries and to define stability (Holdsworth 1963). The posterior column was defined as being all elements posterior to the PLL as shown in Figure 1.5.

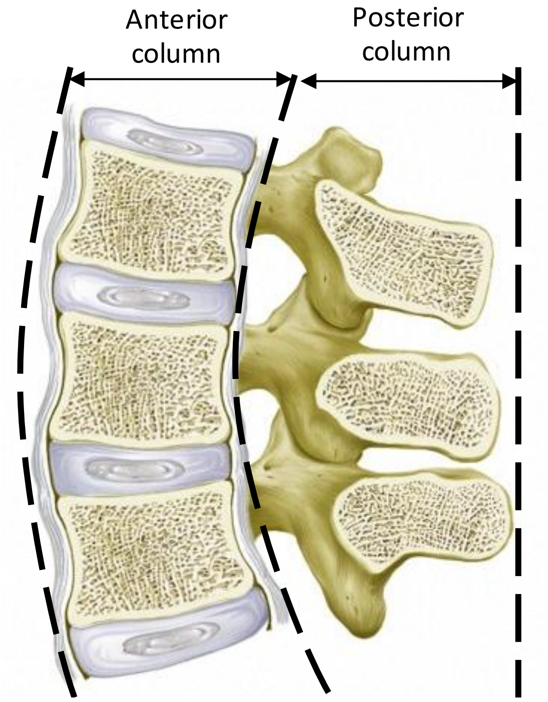

Figure 1.5 Sagittal view of the two column theory defined by Holdworth (1963) (adapted from Wellcome Images 2012).

Spinal instability was considered to pose a neurological threat and was indicated by a disruption to the posterior column. Using this theory, Holdsworth (1963) classified all burst fractures as stable injuries because they were observed to occur in the anterior column.

Three Column Theory

In an attempt to further classify burst fractures and define spinal stability, Denis (1983) divided the spine into three columns as shown in Figure 1.6. It was suggested that by determining which columns had failed, it would be possible to differentiate between fractures and to determine stability.

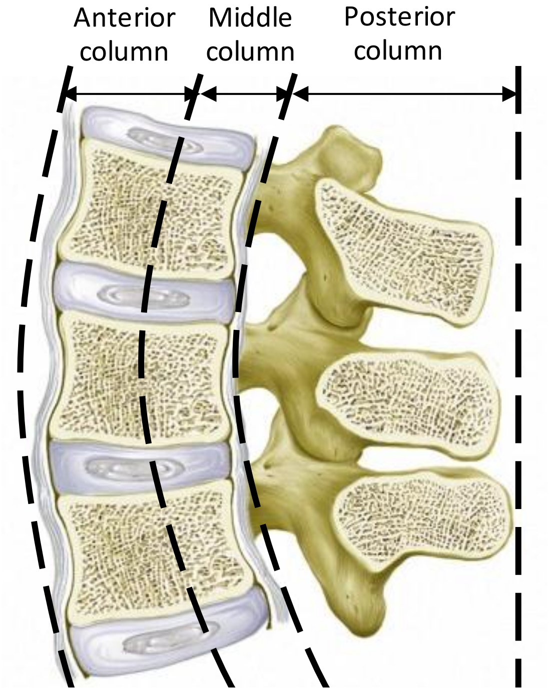

Figure 1.6 Sagittal view of the three column theory defined by Denis (1983) (adapted from Wellcome Images 2012).

Using the image presented in Figure 1.6, a burst fracture was defined as the compression of the anterior and middle columns whilst spinal instability was said to be not only the result of a disrupted posterior column, but also the disruption of the PLL and the posterior of the annulus fibrosus (Denis 1983).

Five groups were created which were reported to accurately describe the types of burst fractures that had been witnessed clinically during the trial. The defining characteristic of a burst fracture was given as the retropulsion of a body fragment into the spinal canal. However, the multiple divisions in the classification system were criticised as being clinically unnecessary because the proposed treatments were so similar (McAfee *et al*. 1983). Although the divisions may not have been practical in a clinical setting, the three column theory was used to provide some clear clinical guidance on the issue of stability; a stable burst fracture was defined as a fractured vertebra with intact posterior elements (McAfee *et al*. 1983).

The classification system of Denis (1983) is also significant on an experimental level due to the detailed descriptions of clinical burst fractures. The study plays an important role in allowing for *in vitro* burst fractures to be confidently identified and used in the experimental assessment of potential treatment methods for burst fracture.

Modified Three Column Theory

The physiological boundaries of the middle column proposed by Denis (1983) and employed by McAfee *et al*. (1983) were altered by Ferguson and Allen (1984) so that the volume of the middle column was reduced to encompass only the posterior third of the vertebral body, the corresponding region of annulus fibrosus and the PLL as shown in Figure 1.7.

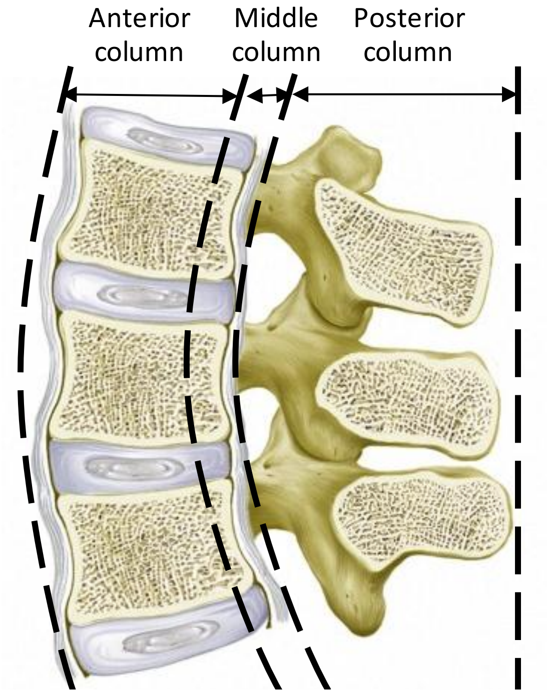

Figure 1.7 Sagittal view of the three column theory defined by Denis (1983) (adapted from Wellcome Images 2012).

The modified three column theory was used by Ferguson and Allen (1984) to classify the manner in which the bony fragments of burst fractures encroached upon the spinal cord. However, the findings are not of much relevance to this study although further studies based on Ferguson and Allen's (1984) definition of the middle column have made a significant contribution to the research undertaken.

Verification of Modified Three Column Theory

The modified middle column theory was noted to be more appropriate than previous definitions in determining the stability of a burst fracture (Panjabi *et al*. 1995). To provide a consistent protocol for assessing burst fracture stability, Panjabi *et al*. (1995) created a grading system that allowed for the mechanical integrity of the anterior, middle and posterior columns to be visually assessed and quantified.

In a clinical setting, patients with suspected burst fractures were imaged using a CT scanner. From the resulting images, each slice at every 3 mm interval was divided into 14 segments (Figure 1.8) and graded from zero to two; zero indicated an intact region, one a partial fracture and two a complete fracture.

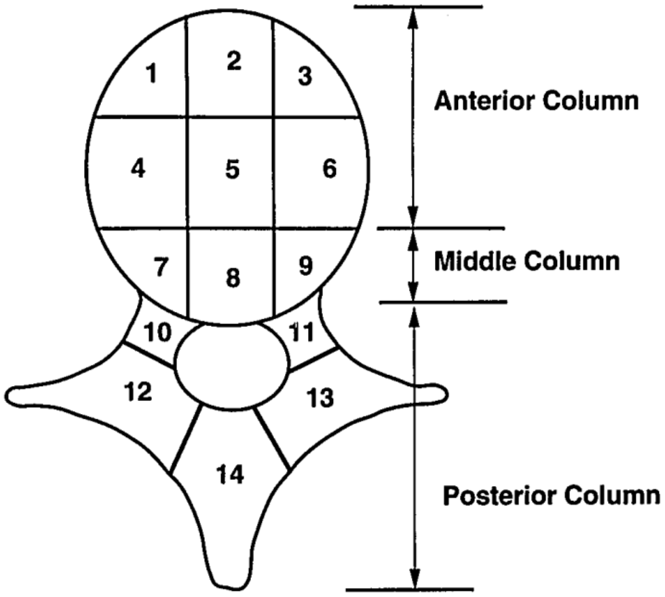

Figure 1.8 The grading system which correlated spinal instability with a high middle column score (Panjabi *et al*. 1995).

Following the grading, the mean grade from each of the columns was obtained and the trend between the columns analysed. It was found that instability correlated with a high middle column score. These findings supported the hypothesis by Denis (1983) that failure of the middle column is an indication of instability.

The 14 segment method for classifying burst fractures accounts for fracture and damage at every area of the vertebrae. In a demanding clinical setting, it may not be feasible to individually examine and grade each 3 mm slice. However, in an experimental setting, this method could be used to accurately quantify the severity of each fractured vertebra which could lead to improved subdivisions of specimens between different test groups.

1.4.3 Experimental Generation

A review of the current literature has identified several techniques that have been used to create burst fractures *in vitro*: corpectomy, loading in a materials testing machine at a low loading rate, repeated axial loading of an intact specimen and the use of a single high rate axial load on an intact specimen. All of the cases presented used either human, bovine or porcine functional spinal units (FSUs) of at least three vertebrae in length and all studies encased the most superior and inferior vertebrae to certain depth using a cement material to allow for a uniform loading surface.

Using a V-shaped drill bit, corpectomy has been employed to introduce either uniform deficits or pre-injuries to the vertebral bodies of specimens; corpectomy is the name given to the surgical procedure where part of the vertebral body is removed. To allow for a direct comparison of treatment methods, corpectomy has been used to produce consistent levels of damage in a selection of specimens which were treated immediately following the procedure (Chen *et al*. 2004; Gurwitz *et al*. 1993). Other authors have used corpectomy as a starting point for fracture initiation. Following the corpectomy procedure, specimens have been loaded in flexion at relatively low loading rates using a materials testing machine until a certain reduction in specimen height was observed that had been previously defined to correspond to failure (Wang *et al*. 2008; Lu *et al*. 2001).

Other authors have also used a low loading rate and a fracture detection method similar to the authors discussed previously however, the specimens that were used were intact and did not possess pre-injuries (Boisclair *et al*. 2011; Anathakishnan *et al*. 2004; Tran *et al*. 1995). Of the methods described to generate fractures using a low loading rate, occasionally the FSUs were held in flexion during loading (Boisclair *et al*. 2011; Anathakishnan *et al*. 2004) and the presence of a fracture was indicated by the reduction in vertebral height by either 25% or 50% or by a discontinuity in the load-displacement curve.

To obtain fractures that corresponded to a certain level of canal encroachment, one research group have reported that they repeatedly loaded each specimen, in flexion, using a mass that was free to fall from a constant height (Panjabi *et al*. 2000; Kifune *et al*. 1997; Kifune *et al*. 1995; Panjabi *et al*. 1995; Panjabi *et al*. 1995b). If the desired level of canal encroachment was not obtained following the initial impact, the mass was increased and the impact repeated. Although the method of repeated loading is not similar to the *in vivo* fracture mechanism, the group have argued that this technique eliminates waste in cadaveric specimens which are less readily available and less homogenous than animal specimens.

The technique which appears to be the most commonly used is similar to the freefalling mass technique discussed previously; however, the specimens were instead subjected to a singular impact load and were held in the neutral position (Tarsuslugil 2011; Wilcox 2004; Slosar *et al*. 1995; Tran *et al*. 1995; Fredrickson *et al*. 1992; Cotterill *et al*. 1987; Willen *et al*. 1984). This technique is more representative of the *in vivo* burst fracture mechanism and can be used to generate similar fracture patterns in the more homogenous animal spines. A summary of the advantages and disadvantages associated with each method used to experimentally generate fractures is presented in Table 1.2.

Table 1.2 Advantages and disadvantages associated with four methods used to generate experimental burst fractures.

	Advantages	Disadvantages
Pre-injury	Increased similarity between fractures No need for high velocity loading equipment	Pre-injury not clinically accurate Low loading rate not clinically accurate
Flexion and Compression	Fracture propagation was free Use of load-displacement graph gave clear indication of fracture Lordosis of the spine in a clinical setting considered	Pre-injury not clinically accurate Low loading rate not clinically accurate Different types of fracture due to different detection methods
Repeated Loading	High rate axial loading was clinically accurate Fracture free to initiate and propagate Specimen held in neutral position clinically accurate Conservation of cadaveric specimens	Increased fracture variability through repeated loading Canal encroachment used to indicate burst fracture
Single Impact	Fracture free to initiate and propagate Clinically accurate single, high rate axial load Held in the neutral position Fracture localised to each middle vertebra	Specimens can only be used once Higher variability in fractures

A comparison of the number of burst fractures obtained in porcine spines when various loading rates and angles of flexion were employed concluded that a high loading rate in conjunction with no flexion resulted in burst fractures with the greatest level of canal encroachment (Boisclair *et al*. 2011). Using this finding and the advantages and disadvantages highlighted above, the most clinically representative technique of burst fractures generation involved the application of a singular high rate axial load to three-vertebral segments when held in the neutral position. It has been found that the likelihood of obtaining a fracture in the middle vertebra was increased by securing the superior and inferior vertebrae in a cement material (Tarsuslugil 2011; Wilcox *et al*. 2003; Tsai, Chang and Lin 1997; Berkman *et al*. 1995; Willen *et al*. 1984).

1.4.4 Treatment

Previous recommendations on the way burst fractures should be treated were much less detailed than those available today. It was recommended by Sir Frank Holdsworth (1963) that following a burst fracture, the spine should be immobilised using a plaster cast and bed rest for approximately 12 weeks. With technological improvements in patient imaging devices, it is now easier for surgeons to determine a more appropriate course of action based on the specifics of the injury. It has been reported that clinicians generally agreed that unstable fractures, such as those with a complete neurological deficit, or a progressive neurological deterioration, always required an invasive surgical intervention which may include stabilisation and/or decompression (Valentini *et al*. 2006; Verlaan, Oner and Dhert 2006; Chen and Lee 2004; Vaccaro *et al*. 2003; Dai 2001; Boerger, Limb and Dickson 2000; Shono, McAfee and Cunningham 1994).

Decompression of the spinal canal is usually achieved through the direct anterior removal of the retropulsed bone or through the use of a technique called ligamentotaxis (Boerger, Limb and Dickson 2000). When ligamentotaxis of the spine is employed, the ligaments in close proximity to the retropulsed bone are held in tension in order to encourage the realignment of the bony fragments. Stabilisation of the spine is obtained through two main approaches, both of which require the insertion of instrumentation; the posterior or the anterior approach. The posterior approach acts to restore the natural lordosis of the spine through the use of distraction techniques such as the Harrington Rod Sleeve (Verlaan, Oner and Dhert 2006; Boerger, Limb and Dickson 2000; Shono, McAfee and Cunningham 1994). The anterior approach of stabilisation allows for the removal of the retropulsed bone and restores the height of the anterior and middle columns through the use of a bone graft and instrumentation (Shono, McAfee and Cunningham 1994).

However, for stable burst fractures, or injuries that have not resulted in a complete neurological deficit and are of mild to moderate deformity, there is no general consensus on what treatment should be delivered and a wide range of treatments have been employed (Valentini *et al*. 2006; Vaccaro *et al*. 2003). Although spinal instability has been adequately and clearly defined (White and Panjabi 1990, cited in Panjabi *et al*. 1995 p.1122), it has been reported that this definition has not translated into common clinical use and that spinal instability remains a poorly defined concept (Vaccaro *et al*. 2003). The study by Vaccaro *et al.* (2003) suggested that the inference of spinal stability is of crucial importance in the selection of appropriate burst fracture treatment and that treatment may not need to be invasive.

More recent developments have cast doubt on whether it is necessary to perform stabilisation and/or decompression in the treatment of stable burst fractures. An *in vitro* study of the burst fracture process suggested that the final resting position of the bony fragment was not an adequate indication of the maximum level of canal occlusion and should not determine whether highly invasive decompressive surgery is performed (Wilcox *et al*. 2004). Maximum canal occlusion was found to have occurred at the moment immediately following load application and subsequently reduced due to the high levels of tension in the PLL which acted to resist the retropulsion in a manner similar to ligamentotaxis. Therefore, the likelihood of neurological injury would have been greatest at the moment of impact, not post-impact as witnessed by surgeons on the radiographs. Decompressive surgery may not be necessary for patients with stable burst fractures and who display no decline in their neurological condition; this has been supported by a clinical review which stated that decompression of a stable burst fracture did not improve the neurological outcome of the injury (Boerger, Limb and Dickson 2000). Several authors have observed similar levels of recovery in burst fracture patients who had conservative treatment and individuals who had surgery (van der Roer *et al*. 2005; Wood *et al*. 2003; Dai 2001; Boerger, Limb and Dickson 2000), which suggests that invasive surgery may not be warranted for the treatment of mechanically and neurologically stable burst fractures which do not possess a high middle column score (Panjabi *et al*. 1995).

1.5 Vertebroplasty

Vertebroplasty is a percutaneous augmentation technique where bone cement is injected into a vertebral body. It was developed in France in 1984 to help treat metastatic lesions (Galibert *et al*. 1987) and has been widely used to treat osteoporotic vertebral compression fractures since the early 1990's (Sun and Liebschner 2004). The main aims of vertebroplasty are to stabilise the fracture, restore vertebral height and reduce the pain that is associated with the injury. Clinical trials for the augmentation of osteoporotic compression fractures have yielded promising short term results with a reduction in pain reported for 80 – 97% of cases (Baroud and Bohner 2006; Jensen *et al*. 1997) and an improvement in mobility reported for 70 – 80% of cases (Levine *et al*. 2000).

It has been hypothesised that post-augmentation pain reduction may be due to the thermal necrosis that occurs during polymerisation of the bone cement (Mjoberg *et al*. 1984) although it is now more widely accepted that immediate levels of pain reduction post-augmentation are due to the stabilisation of the fracture and reduction in mircomotion at the fracture surface (Siddall and Cousins 1997). However, the results of more recent randomised clinical trials have been inconclusive, with some suggesting that vertebroplasty provided pain relief over conservative treatment (Klazen *et al*. 2010) and others suggesting that vertebroplasty offered no improvement over a sham procedure (Buchbinder *et al*. 2009; Kallmes *et al*. 2009).

1.5.1 Methods

The vertebroplasty procedure is usually carried out under local anaesthetic using fluoroscopy for guidance and involves the injection of an acrylic-based cement, most commonly via an 11-gauge needle (Garfin, Yuan and Reiley 2001; Jensen *et al*. 1997). A radio-opaque agent may be added to the cement to aid visualisation. Access to the fracture site is either obtained through one pedicle, in a uni-pedicular manner, or through both pedicles, in a bi-pedicular manner (Figure 1.9).

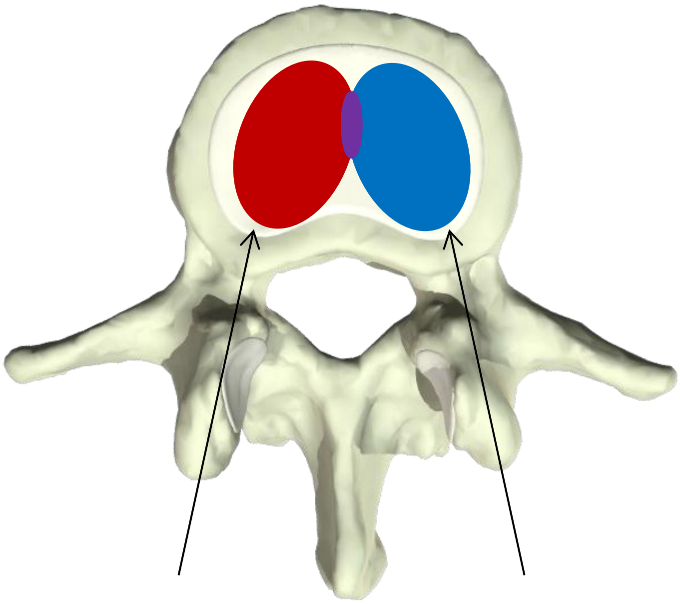

Figure 1.9 Superior axial view of uni-pedicular (red or blue) and bi-pedicular (red and blue) vertebroplasty (adapted from Anatomy TV 2012).

In a comparison of the effects of uni- and bi-pedicular augmentation, a study involving 10 osteoporotic cadaveric spines found that bi-pedicularly augmented vertebrae had a greater strength and stiffness than those treated uni-pedicularly (Tohmeh *et al*. 1999). However, the post-augmentation stiffness values did not reach those of pre-fractures levels whilst the strength did. This study has been criticised because although the effect of the cement on the strength and stiffness of the vertebrae was investigated, the effect on the load distribution was not (Liebschner, Rosenberg and Keaveny 2001). The specimens could have been subjected to lateral bending in order to investigate the load shift, or toggle motion, that may have been present post-augmentation.

1.5.2 Materials

The most extensively used cement is polymethylmethacrylate (PMMA) although there has been an increase in the level of research into bioactive materials such as calcium phosphate (CaP). An advantage of bioactive cements such as CaP over the biologically inert PMMA cement is the potential for new bone to grow into, and replace, the cement. In addition to this advantage, CaP cements may cause less damage to the surrounding bone because they cure at approximately 40°C which is 30°C lower than the polymerisation temperature of PMMA (Poitout 2004). Damaged bone tissue has been observed following exposure of more than one minute to a temperature of 50°C (Eriksson, Albrektsson and Magnusson 1984).

The compressive strength of CaP cements (20 – 60 MPa) is lower than that of PMMA cements (80 - 94 MPa) which may be disadvantageous (Poitout 2004). However, studies have suggested that although it lacks the mechanical integrity required, when used in conjunction with posterior instrumentation, CaP cements have the potential to repair fractures (Korovessis, Hadjipavlou and Repantis 2008; Oner *et al*. 2006; Verlaan *et al*. 2005; Lim *et al*. 2002). The major issue associated with the use of CaP cements for vertebroplasty is the brittle nature of the material. Therefore, it is possible that the fatigue performance of CaP cements may be less reliable than PMMA.

1.5.3 Disadvantages

The major advantage of treating painful compression fractures with vertebroplasty is the immediate reduction in pain due to the stabilisation of the fracture and reduction in mircomotion at the fracture surface (Siddall and Cousins 1997). However, there is the potential for complications to arise. These include bleeding at the puncture site, infection, damage to the nerve roots or spinal cord, leakage of the material into the surrounding epidural or paravertebral spaces and passage of the material into the venous system with embolization to the pulmonary vasculature or compression of neural tissue (Jensen *et al*. 1997). The prevalence of cement leakage into the spinal canal was found to be high at 12% during the augmentation of 66 cadaveric vertebral fractures (Heini, Walchli and Berlemann 2001), although the incidence of complications associated with vertebroplasty *in vivo* has since been reported to be low (Klazen *et al*. 2010).

The major issue associated with the augmentation of osteoporotic fractures is the risk of adjacent vertebra fracture. Longer term observations of augmented osteoporotic compression fractures have shown that there was an increase in the occurrence of fractures to the vertebrae adjacent to the augmented vertebra (Rad *et al*. 2011; Chen *et al*. 2010; Wilcox 2006; Trout and Kallmes 2006; Trout, Kallmes and Kaufmann 2006; Baroud *et al*. 2003; Polikeit, Nolte and Ferguson 2003; Uppin *et al*. 2003; Berlemann *et al*. 2002; Grados *et al*. 2000). This may be due to a change in the load distribution of the spine post-augmentation (Grados *et al*. 2000) or leakage of the augmentation material into the intervertebral disc (Chen *et al*. 2010). Others have suggested that the cement strengthens the osteoporotic vertebral body to such an extent that it acts as a “stress riser” and alters the stress distribution throughout the spine (Berlemann *et al*. 2002) and a similar opinion has been expressed elsewhere (Wilcox 2006; Baroud *et al*. 2003; Polikeit, Nolte and

Ferguson 2003; Uppin *et al*. 2003). However, there is no general consensus for the occurrence of adjacent vertebral failure in osteoporotic spines treated with vertebroplasty (Trout and Kallmes 2006) although a recent study suggests that adjacent fractures are not related to an increase in activity post-augmentation (Rad *et al*. 2011).

1.5.4 Optimum Configuration

There is debate as to the optimal vertebroplasty configuration required to treat osteoporotic fractures; some authors have suggested that vertebral strength and stiffness should be restored to pre-fracture levels (Belkoff *et al*. 2001) whilst other authors have suggested that vertebral strength should be restored to levels greater than those at pre-fracture (Tohmeh *et al*. 1999).

Restoration of the strength of a given vertebra to pre-fracture levels has been argued to allow for the prevention of further fractures when the spine was subjected to loads of a similar magnitude to the load that caused the original fractures (Belkoff *et al*. 2001). However, since the majority of osteoporotic patients are elderly, it is likely that a high percentage of osteoporotic fractures occurred with typical daily loading. It follows that if the fractured vertebra was to be restored to the same pre-fracture levels of strength, there may be a chance that an additional fracture could occur during typical daily loading.

Other authors believe that the strength of an augmented vertebra should be restored to normal, or pre-osteoporotic, levels (Tohmeh *et al*. 1999). Returning the strength of fractured vertebrae to normal levels would exceed the pre-fracture levels of osteoporotic patients and may lead to a greater level of “stress risers” due to more cement or a stronger, and possibly more stiff, cement being injected (Berlemann *et al*. 2002). Additionally, it would be difficult to ascertain what level of strength to administer because vertebral strength should be determined through gender, race and weight related observations in the population. However, other authors have concurred with the suggestion of restoring vertebral strength to pre-osteoporotic levels although the suggestion has been made that vertebroplasty should not be used as a fracture repair treatment, but as a prophylactic treatment in order to reinforce intact vertebrae that were deemed to be at risk of fracture (Sun and Liebschner 2004b).

1.5.5 Potential Use

With vertebroplasty associated with both a risk of adjacent vertebral failures in osteoporotic spines and with promising short term reductions in pain, it is possible that the procedure may be used in the repair of an alternative spinal injury. There have been limited studies into the use of vertebroplasty for burst fracture repair (Doody *et al*. 2009; Huet *et al*. 2005; Amoretti *et al.* 2005; Chen and Lee 2004; Chen, Wu and Lee 2004) and the post-operative follow up time ranged from three to 22 months (Chen, Wu and Lee 2004). Generally, the studies reported favourable short term results although this is inconclusive as only 27 patients were involved in total. In each of the studies, the decision to perform vertebroplasty was made following approximately 2.5 months of unsuccessful conservative treatment.

There are no longer term clinical studies on the effect of spinal burst fracture repair using vertebroplasty. Therefore, it is unknown whether the risk of adjacent vertebral failure that is associated with the augmentation of osteoporotic compression fractures is present for the repair of spinal burst fractures. Validated computational models may be able to predict the longer term effects of spinal burst fracture augmentation that is not currently available in the literature.

1.6 Computational Modelling

The Finite Element (FE) computational method is used in structural mechanics to predict the stress and strain fields within a specified geometry of an object under a load. To be able to do this, the material properties and the geometry must be defined in addition to the loading, boundary and interfacial conditions. Although the method has been in use since the 1950's, approximately 20 years passed before it was first applied to the field of orthopaedic biomechanics (Brekelmann, Poort and Slooff 1972). Since then, it has been widely used for biomechanical analysis mainly due to the ethical and cost considerations of running multiple *in vivo* and *in vitro* experiments.

The FE method is based on a number of numerical calculations that solve the boundary value problems at a number of points, called nodes. The nodes are the integration points that form elements which in turn form a mesh which is used to simulate the structure that is being modelled.

Computational modelling of vertebroplasty allows for specific parameters to be varied and investigated in order to predict the optimum configuration. A specific assessment of cement volume and cement distribution can be easily simulated. In addition, the use of FE models can help to eliminate the biological variability associated with cadaveric specimens.

1.6.1 Continuum Level

When a vertebral specimen is modelled on a continuum level, geometrical details such as individual trabeculae and the respective spacings are not individually captured but are reduced to a continuous representation. The material properties of the continuous representation are an average of the material properties of the trabeculae and the trabecular spacings. This method leads to lower computational expenses than trabecular level modelling. Continuum level models of the spine have ranged from less geometrically accurate representations of the hard tissue of the entire spine to more geometrically accurate specimen-specific models of individual vertebral segments and the accompanying soft tissue.

1.6.2 Intact Vertebrae

Many groups have constructed FE models of intact vertebrae and agreement between experimental stiffness and predicted stiffness values have generally been good. Studies have reported a correlation coefficient of 0.881 (Wilcox 2007) and a coefficient of determination of 0.71 (Crawford, Cann and Keaveny 2003) between the experimental and predicted stiffness values. The root mean square error for the stiffness of seven specimen-specific models was found to be 12.9% (Wijayathunga *et al*. 2008). A summary of the way in which material properties have been defined are presented in this subsection in addition to findings regarding the size of the elements in the model and the importance of load and boundary conditions.

Material Properties

The material properties of a vertebral specimen can be specified from the images of a CT scan through information on either the bone volume fraction (BVF) or the greyscale of the voxels which is measured in Houndsfield units. Material properties have been based on the bone mineral density (BMD) of the CT images which was calculated from the Houndsfield units using a linear relationship (Kopperdahl, Morgan and Keaveny 2002). However, more recent studies have found better strength predictions using a direct calculation of modulus from the greyscale values (Crawford, Rosenberg and Keaveny 2003). Other studies have used similar methods for the generation of specimen-specific models from either literature or greyscale data (Wijayathunga *et al*. 2008; Wilcox 2007; Crawford, Rosenberg and

Keaveny 2003; Polikeit, Nolte and Ferguson 2003; Kopperdahl, Morgan and Keaveny 2002; Liebschner, Rosenberg and Keaveny 2001; Bai *et al*. 1999). The advantage of directly assigning elemental greyscale based material properties for specimen-specific models is that a direct comparison of computational and experimental data is possible. This is generally not available when generically assigned material properties are applied to models with a generic geometry since this would allow only a comparison with the average experimental data.

A comparative study of generically assigned and element-specific material properties in a FE model of a whole vertebra showed that element-specific material properties yielded a greater level of computational accuracy (Wilcox 2007). A linear relationship between greyscale information and material properties has been found to provide more accurate strength predictions in comparison to BMD derived values (Kopperdahl, Morgan and Keaveny 2002) and more accurate stiffness predictions in comparison to square and cubic relationships between greyscale and material properties (Wijayathunga *et al*. 2008).

Element Size

For continuum level models of intact vertebrae, an element size ranging between 1.5 and 2 mm has been found to be sufficient (Wijayathunga *et al*. 2008; Jones and Wilcox 2007). An increase in the resolution of the models beyond these values did not correspond to an increase in computational accuracy. However, consistency within the size of the elements has been found to have a greater effect on model accuracy than the actual size of the elements (Crawford, Rosenberg and Keaveny 2003) and high resolution images downsized to a certain resolution provide a greater computational accuracy than images taken at that resolution (Yeni *et al*. 2005). Once an image has been downsized, geometrical details of the specimens are not accurately represented. Smoothing of the mesh has been shown to increase the anatomical likeness of the model, decrease the number of elements in the model and reduce the computational processing unit (CPU) time needed to solve the model (Wang *et al*. 2005).

Loads and Boundary Conditions

In order to accurately apply loads and boundary conditions, many groups have incorporated parallel loading plates on the experimental specimen which can be easily represented in specimen-specific models (Wijayathunga *et al*. 2008; Jones and Wilcox 2007; Crawford, Rosenberg and Keaveny 2003). The use of the parallel loading plates allows for the inferior plate, and hence the vertebra, to be constrained experimentally and computationally in all directions. The superior loading plate is used for the point of load application. It is important that the same point of load application is used experimentally and computationally because it has been found that a change in loading position by approximately 4.5 mm from the true loading position corresponded to an increase in the error of the predicted stiffness by 40% (Wijayathunga *et al*. 2008; Jones and Wilcox 2007).

1.6.3 Burst Fractures

FE analysis has been conducted in order to gain a greater understanding of the burst fracture process. It has been shown using FE analysis that when an axial load was applied to a cadaveric T12-L1 specimen, the endplates of the vertebrae bulged into the vertebral body (Qui *et al*. 2006). The greatest stresses in the model were seen at the area of the endplates in contact with the nucleus pulposus and in the cancellous bone situated near to the endplates. The stresses predicted at these areas appear to confirm the hypothesis by Holdsworth (1963) that the nucleus pulposus is forced into the vertebral body during a burst fracture. This study proposed that bony fragments were retropulsed into the spinal canal when the rate of nucleus pulposus entering the vertebral body was greater than that of the marrow and fat exiting (Qui *et al*. 2006). The burst fracture mechanism has been studied in further FE analyses where it was shown that a vertebra subjected to high rate axial compressive loading developed high tensile strains in the region attaching the pedicles to the vertebral body (Wilcox *et al*. 2004). It was hypothesised that the high tensile strains developed at this location were due to the over-closure of the facets.

Combining the findings from these two studies gives a greater insight into the burst fracture mechanism. The elements in the FE model of Wilcox *et al*. (2004) which developed the greatest tensile strain corresponded to the location of retropulsed bony fragments observed *in vitro*. This suggests that burst fractures initiate in the area of high tensile strains and propagates at these areas due to the disc being forced into the vertebral body and the increase in the interpedicular distance. It is not known which of these factors occurs first however, both contribute to the burst fracture mechanism. The characteristic wedge-shaped of the retropulsed bony fragments may be due a combination of the splaying of the pedicles and the reduced thickness of the cortical shell at the posterior of the vertebral body (Silva *et al*. 1994).

Rather than simulating a fracture, some studies have merely changed the material properties of the healthy trabecular and cortical bone to those of osteoporotic bone (Bai *et al*. 1999; Polikeit, Nolte and Ferguson 2003). This method may be acceptable when the FE model is concerned with osteoporotic compression fractures where the trabeculae are compressed upon one another, but it is not adequate to simulate spinal burst fractures where there are voids between the trabeculae which may be augmented with cement. As of yet, there have been few attempts to model the post-fracture behaviour of burst fractured specimens (Tarsuslugil 2011).

1.6.4 Vertebroplasty

There have been many studies that report on the use of FE models for the analysis of augmented vertebrae (Wijayathunga *et al*. 2008; Wilcox 2006; Baroud *et al*. 2003; Polikeit, Nolte and Ferguson 2003; Bai *et al*. 1999). There appears to be a lower computational accuracy associated with models of augmented specimens in comparison to non-augmented models that have been constructed in a similar manner. Using the same modelling technique that produced a root mean square error of 12.9% for the stiffness of intact vertebrae, the error for augmented vertebrae was much greater at 65% (Wijayathunga *et al*. 2008).

From a review of the literature, there appears to be two main techniques in use to simulate augmentation. The first technique of augmentation simulation merely altered the material properties of an area of trabecular bone to match those of the desired cement (Liebschner, Rosenberg and Keaveny 2001). This simulation did not accurately represent the clinical distribution of cement because the trabecular spacing, which corresponds to the augmented region *in vivo*, possessed the material properties of bone marrow which are much lower than those of cement.

The second technique that has been used to simulate augmentation involved the insertion of one or two cylindrically shaped solid parts into the vertebral body of the model to represent either uni- or bi-pedicular augmentation (Polikeit, Nolte and Ferguson 2003). Clinical cement distribution is more accurately simulated when solid cylindrical parts are introduced to the vertebral body, rather than altering the material properties of the trabecular bone and not the spacing. However, this augmentation simulation technique does not consider the properties of the existing trabecular bone, which may have had a significant effect on the resulting post-augmentation load distribution, or of the cement bone interface.

Alternatively, it is possible to make FE models of augmented vertebrae from the µCT data of an augmented specimen. Using commercially available software, it is possible to process the µCT images to segment the cement from the bone and to apply a homogenous material property to the cement and greyscale based material properties to the bone (Tarsuslugil 2011). This method of modelling augmented specimens allows for a direct comparison between the specimen-specific model predictions and the experimental result whilst the appropriate material properties are applied to the corresponding regions. This approach appears to be more ideal for use in the modelling of augmented burst fractures, where there are large fracture voids between the trabeculae, in comparison to osteoporotic compression augmentation where the trabeculae are compressed upon each other.

FE analysis has predicted that augmentation of one vertebra in a two vertebrae model resulted in a change to the stress distribution throughout the entire model (Polikeit, Nolte and Ferguson 2003). Post-augmentation, the compressive load distribution was seen to shift towards the anterior column possibly due to a reduction in the magnitude of stresses observed at the facet joints. The model predicted that the anterior load-shift increased the post-augmentation pressure in the nucleus pulposus and resulted in a greater endplate deflection towards the vertebral body of the non-augmented vertebra. Additional FE models have estimated that the pressure of the nucleus pulposus post-augmentation was almost 20% higher than pressure observed in non-augmented model (Bai *et al*. 1999). These findings on the post-augmentation load-shift within the spine help to explain the reason why an increase in the incidence of adjacent vertebrae failure has been witnessed *in vivo* following the augmentation of an adjacent vertebra (Trout and Kallmes 2006; Trout, Kallmes and Kaufmann 2006; Grados *et al*. 2000).

Cement Distribution

Cement distribution, such as whether the cement has been administered using either a uni- or bi-pedicular technique, has been found to result in a variation in the load distribution of the spine.

What was described as a greater “toggle motion” was observed in FE models of uni-pedicularly augmented vertebrae, in comparison to bi-pedicularly augmented models, when both were loaded in flexion (Liebschner, Rosenberg and Keaveny 2001). The toggle motion was said to be due to an induced instability because of a single sided load transfer. The uni-pedicularly augmented model displayed a rotation at the endplates during loading which was less pronounced for a model augmented using the bi-pedicular technique and that had a greater volume of fracture (Liebschner, Rosenberg and Keaveny 2001).

A load-shift towards the anterior column of the vertebral body was predicted to be more pronounced for bi-pedicularly augmented models than uni-pedicularly augmented specimens (Polikeit, Nolte and Ferguson 2003). The shift in load distribution was indicated by a decrease in the pressure at the facet joints following augmentation and an increase in the pressure of the nucleus pulposus.

Cement Volume

The predicted effects of augmentation have been observed to vary and are most dependant on the volume of cement administered (Wilcox 2004). It has been predicted that the stiffness of the augmented vertebral model is more dependent on the volume, rather than the distribution, of the administered cement (Liebschner, Rosenberg and Keaveny 2001). The same study predicted that as little as 2 ml of cement could restore vertebral stiffness to within 15% of pre-fractured levels although this claim has not been validated *in vitro*.

Modelling incremental increases in cement volume during augmentation simulation is a sensible approach when the effect of cement volume is to be investigated. However, there are models which have simulated vertebroplasty as the augmentation of the entire vertebra and thus changed all material properties from those of bone to cement (Bai *et al*. 1999). In defence of this simulation, it has been reported that during *in vivo* vertebroplasty, surgeons administer cement until leakage is observed; this however, does not constitute entire vertebral augmentation.

1.6.5 Plastic Deformation

Some studies have incorporated plastic behaviour into their models in order to simulate the post-yield behaviour of bone that would occur over a number of cycles (Wijayathunga *et al*. 2008; Keller, Kosmopoulos and Lieberman 2005; Liebschner, Rosenberg and Keaveny 2001). These groups used either a modulus-reduction technique or incorporated elastic-plastic behaviour into the models. The study performed by Liebschner, Rosenberg and Keaveny (2001) introduced elements of fracture into the model of a single pre-augmentation cadaveric specimen over two loading cycles. During the first cycle, elements which exceeded the yield strain were considered to have failed and the corresponding elastic modulus was reduced by up to 85% to form the fracture.

There is no known literature on the plastic deformation of burst fractures that have been repaired using vertebroplasty.

1.6.6 Model Verification and Validation

It is essential that a FE model is verified in order to check that there are enough nodes, or calculation points, to gain a sufficiently accurate solution for the required purpose (Anderson, Benjamin and Weiss 2007). Sensitivity studies should be used to evaluate the relative importance of the input parameters and the level of accuracy required. It is also essential that a FE model is validated through a direct comparison of the computational predictions and the experimental data in order to assess the accuracy of the model (Anderson, Benjamin and Weiss 2007).

There appears to be a limited level of model verification, validation and sensitivity studies performed in the studies that have presented FE predictions on the effect of vertebroplasty. Very little evidence is presented of a comparison between the simulated augmentation and the experimental augmentation. The study by Liebschner, Rosenberg and Keaveny (2001) attempted to validate the models by using the specimens that were used to define the material properties of the model. Model validity should not be based on the data that was used to create the model; additional specimens should be used for model validation wherever available (Jones 2009; Jones and Wilcox 2008).

Previous authors have used appropriate validation techniques on FE models of augmented vertebrae although there was a variation between the studies in the level of computational accuracy obtained from the development set and the validation set (Tarsuslugil 2011; Wijayathunga *et al*. 2008). The computational accuracies obtained by Tarsuslugil (2011) when modelling augmented burst fractures were similar between the sets whilst there was a reduction in the accuracy obtained by Wijayathunga *et al*. (2008) in the validation set when modelling an augmented osteoporotic compression fracture. The increased errors obtained by Wijayathunga *et al*. (2008) may be due to the nature of the compression fracture and the subsequent augmentation. When burst fractures are augmented, the cement region is more clearly defined than when a compression fracture is augmented because of the substantial void that is created between trabeculae in a burst fracture.

1.7 Summary of Literature Review

Spinal burst fractures are most prominently associated with younger patients and have been estimated to account for 15% of all spinal fractures (Amoretti *et al*. 2005). For fractures that pose a neurological threat, a highly invasive surgical procedure is usually required in order to stabilise the site (Valentini *et al*. 2006). There is a high level of understanding of the mechanism of burst fractures due to both experimental and computational efforts.

However, there is no general consensus on how to treat stable burst fractures; namely fractures that have not resulted in a complete neurological deficit and are of mild to moderate deformity (Valentini *et al*. 2006; Vaccaro *et al*. 2003). Some clinical, experimental and computational studies have suggested that it may not be necessary to perform highly invasive surgery for the treatment of stable burst fractures (van der Roer *et al*. 2005; Wilcox *et al*. 2004; Wood *et al*. 2003; Dai 2001; Boerger, Limb and Dickson 2000). Although spinal instability has been well defined (White and Panjabi (1990), cited in Panjabi *et al*. 1995 p.1122), this has not translated into clinical practice. The use of the burst fracture grading system by Panjabi *et al*. (1995) can be used to aid experimental practice to allow for a more precise record of the severity of burst fractures to be obtained; the rigid divisions and characteristics provide an accurate framework for individuals to independently and confidently classify fractures.

Vertebroplasty is a minimally invasive procedure and has been used for many years to repair osteoporotic compression fractures. However, it has been acknowledged that associated with the procedure is an increase in the incidence of fractures in the vertebrae adjacent to the augmented vertebra (Rad *et al*. 2011; Chen *et al*. 2010; Wilcox 2006; Trout and Kallmes 2006; Trout, Kallmes and Kaufmann 2006; Baroud *et al*. 2003; Polikeit, Nolte and Ferguson 2003; Uppin *et al*. 2003; Berlemann *et al*. 2002; Grados *et al*. 2000). The most commonly suggested reason why adjacent vertebra fractures occur was that brittle osteoporotic spines are unable to support a change in the load distribution (Wilcox 2006; Berlemann *et al*. 2002; Polikeit, Nolte and Ferguson 2003; Uppin *et al*. 2003; Grados *et al*. 2000). Short term results from the use of vertebroplasty to repair burst fractures in spines that were previously healthy have been encouraging (Doody *et al*. 2009; Amoretti *et al* 2005; Huet *et al*. 2005; Chen and Lee 2004; Chen, Wu and Lee 2004). However, there are no clinical or biomechanical results available for longer term effect of spinal burst fracture using vertebroplasty.

In order to investigate the biomechanical effect of spinal burst fracture repair using vertebroplasty, experimental and computational models are required. It is difficult to develop a method for generating reproducible burst fractures in human specimens as there is a high variation in properties such as stiffness due to age related issues and diseases. There is less variation in the properties of animal spines taken from a specific age range, which means the likelihood of generating repeatable fractures with an animal model is greater than with cadaveric specimens. In particular, porcine spines have been said to be especially well-suited for thoracolumbar research (Cotterill *et al*. 1986).

Computational modelling using FE methods has been widely used and is well established in the field of spinal research. Results from the models of intact vertebra are encouraging although there is a decrease in the computational accuracy of augmented models (Wijayathunga *et al*. 2008; Wilcox 2007; Crawford, Rosenberg and Keaveny 2003). Several studies have successfully employed either a modulus reduction technique or elastic plastic behaviour to simulate damaged trabeculae (Wijayathunga *et al*. 2008; Keller, Kosmopoulos and Lieberman 2005; Liebschner, Rosenberg and Keaveny 2001). However, these models did not investigate the fatigue behaviour of augmented specimens. The brittle nature of CaP cement indicates that it may not perform as well as PMMA during fatigue testing which is why it is important to characterise the behaviour of these cements over multiple cycles.

Although some work has been undertaken previously to examine burst fracture repair biomechanics, as yet the longer term performance over multiple loading cycles has not been investigated. It is possible that the longer term effects of spinal burst fracture repair using vertebroplasty may be investigated using validated computational models that incorporate some form of damage representation. However, such models would first need to be validated against experimental tests to prove their ability to simulate such behaviour.

1.8 Aims and Objectives

The aim of this project was to develop *in vitro* and computational models that could be used to investigate the longer term effects of spinal burst fracture repair using vertebroplasty. The models were then used to study the biomechanical performance of vertebroplasty with two types of cement, PMMA and a newly developed CaP (O’Hara 2010).

A combined experimental and computational approach enabled direct comparisons between the computational predictions and the corresponding experimental tests, as presented in Figure 1.10.

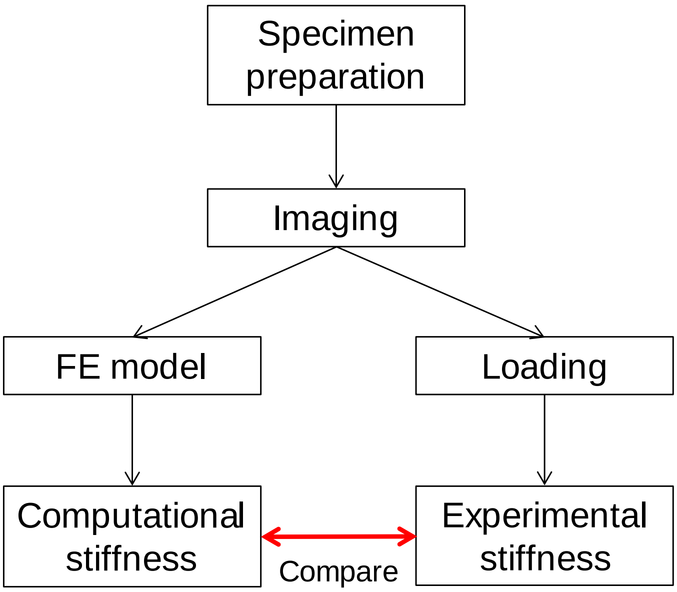

Figure 1.10 Validation of computational models against the experimental results.

Following this, the computational models could then be used to investigate additional augmentation scenarios and their potential impact upon the clinical environment.

The experimental objectives of this study were as follows:

- To develop a method to generate reproducible burst fractures in porcine vertebrae.
- To specify an experimental testing regime to subject fractured porcine vertebrae to a single cycle load in order to quantify the immediate post-fracture behaviour.
- To define a method for the experimental testing of fractured and augmented porcine vertebrae over multiple-cycles in order to quantify the post-fracture behaviour over time.
- To employ a reproducible fracture grading technique to define mechanical instability and assess fracture severity.

This work is presented in Chapter 2 and Chapter 3.

The remaining objectives of this study were computationally orientated and were as follows:

- To generate a set of FE models of fractured porcine vertebrae during single cycle loading and validate their predictions against *in vitro* behaviour.
- To investigate different ways of representing the plastic deformation and to compare this to the experimental data to determine the most appropriate technique.
- To generate a set of FE models of fractured and augmented porcine vertebrae during multi-cycle loading and validate this against *in vitro* behaviour.
- To investigate the effect of fracture dispersion and the level of cement augmentation on post-fracture behaviour.
- To assess whether vertebroplasty could restore the stiffness of fractured porcine vertebrae to pre-fracture levels and to compare two augmentation materials.

The work for the computational objectives is presented in Chapter 4 and Chapter 5.

Chapter 2

Experimental Methods and Preliminary Results

2.1 Introduction

This chapter is composed of four core sections. The initial section details the preliminary preparations that were performed in order to obtain a sufficient number of traumatically fractured, single vertebra specimens. The specimens were divided into three sets as indicated by Figure 2.1 and the three subsequent sections describe the individual procedures that were performed on each of these sets.

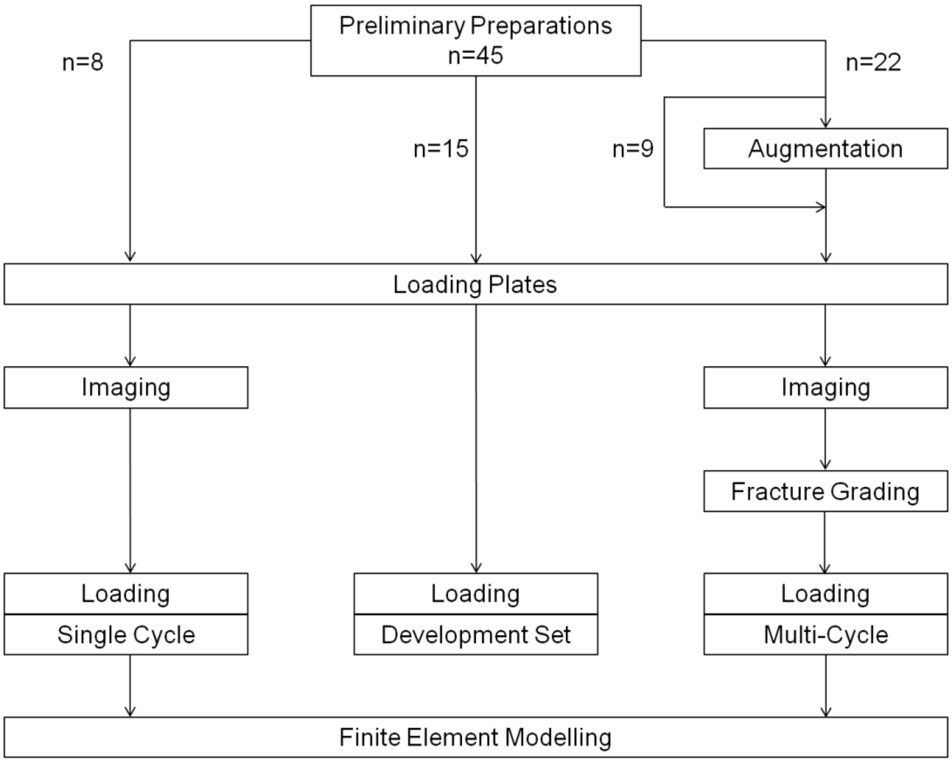

Figure 2.1 Schematic of the division of specimens.

The first set of specimens was subjected to single cycle loading. The second set was used to develop a method for multi-cycle loading and the preliminary results are presented here because they were used to specify the final method which the third set of specimens was subjected to. The specimens that were subjected to single cycle loading and multi-cycle loading were imaged in order to make specimen-specific FE models.

2.2 Fracture Generation

To obtain individual vertebra specimens with traumatic fractures, three-vertebra FSUs were dissected from intact spines, housed between parallel plates to allow for uniform loading and fractured by a freefalling mass. The following section describes this process in more detail.

2.2.1 Spinal Dissection

A total of 92 three-vertebra FSUs were harvested from the thoracolumbar region of 22 porcine spines aged between 6 and 8 months. The spines were obtained from the local abattoir (Penny and Sons, Rawdon, Leeds, UK) and came complete with sacrum and ribs. The nomenclature used for all specimens is the number of the spine (S), followed by the level of the vertebra. For example, a specimen extracted from the fifth lumbar vertebra of Spine 3 is given as S3L5.

It was assumed that each spine was composed of 14 thoracic vertebrae despite the variability in the total number of vertebrae present in different spines. The vertebrae were numbered such that T14 was the final vertebra with ribs attached. Initially, the spines were separated into five FSUs (T6-T8, T9-T11, T12-T14, L1-L3 and L4-L6). However, the most superior FSU was deemed inappropriate due to the location in which burst fractures are observed clinically (Denis 1983). The remaining 18 spines were separated into four FSUs (Figure 2.2).

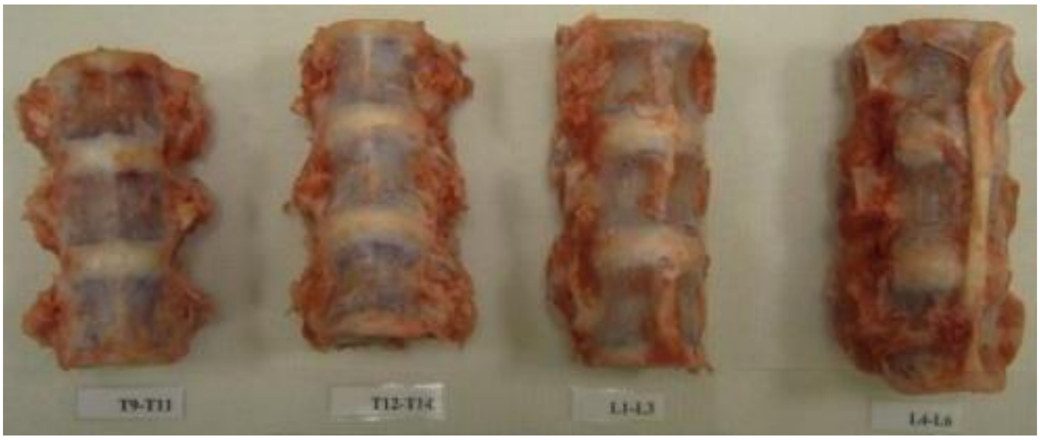

Figure 2.2 Four functional spinal units obtained from one spine.

Where applicable, the ribs were removed and the spinous and transverse processes trimmed to allow for ease of manipulation. Care was taken to ensure the posterior and anterior longitudinal ligaments were not severed during tissue removal. The masses of eight FSUs were obtained from two spines and were recorded for use in fracture generation (Section 2.2.4).

In the time that passed between procedures being undertaken on the FSUs, they were encased in tissue dampened with distilled water and stored at 5^{o}C to prevent disc dehydration. When it occurred that there were more than 48 hours between procedures, the FSUs were again wrapped in damp tissue but instead stored at a temperature of -20^{o}C.

2.2.2 Functional Spinal Unit Housing

The FSUs were housed between two parallel loading plates of PMMA using a custom built rig (Figure 2.3). Housing the specimens in this manner ensured that the FSUs were subjected to uniform loading during fracture generation, as is experienced during the clinical injury. During housing, a steel rod was held fast against the anterior of the spinal canal to ensure that the FSUs remained vertical and that the PMMA plates were parallel.

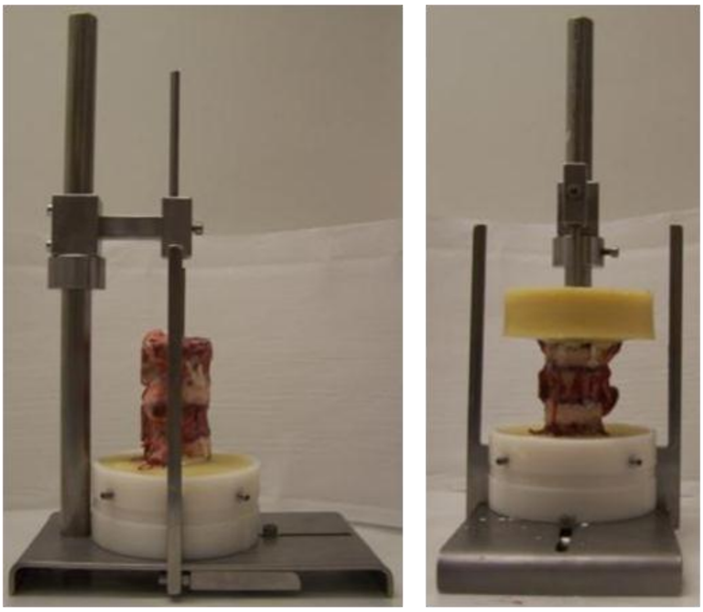

Figure 2.3 The two stages involved in housing a functional spinal unit between two parallel plates of PMMA.

The technique of housing FSUs between plates of PMMA in this manner was adapted from a previously developed method (Wilcox *et al*. 2003) and two variations of plate height were investigated. In the first instance (Housing 1, n=10), the PMMA which encased the superior and inferior vertebrae of each FSU was 20 mm in height and was equivalent to approximately half the vertebral body height.

A second technique was considered when fractures were seen to occur not only as desired in the middle vertebra of each FSU, but also in the adjacent vertebrae. It was hypothesised that if the location of the fracture were more localised, it may result in the middle vertebra of each FSU being exposed to a similar impact which could cause more uniform fracture patterns between FSUs. To investigate this, the adjacent vertebrae were fully encased in PMMA up to the height of the discs in order to inhibit radial expansion (Housing 2, n=10). It was envisioned that by preventing the radial expansion of the adjacent vertebrae, the nucleus pulposus of each FSU would be more inclined to enter, and hence fracture, the middle vertebrae.

2.2.3 Apparatus for Fracture Generation

Traumatic fractures were generated in the middle vertebra of each FSU using a custom built apparatus based on a drop-mass system (Figure 2.4).

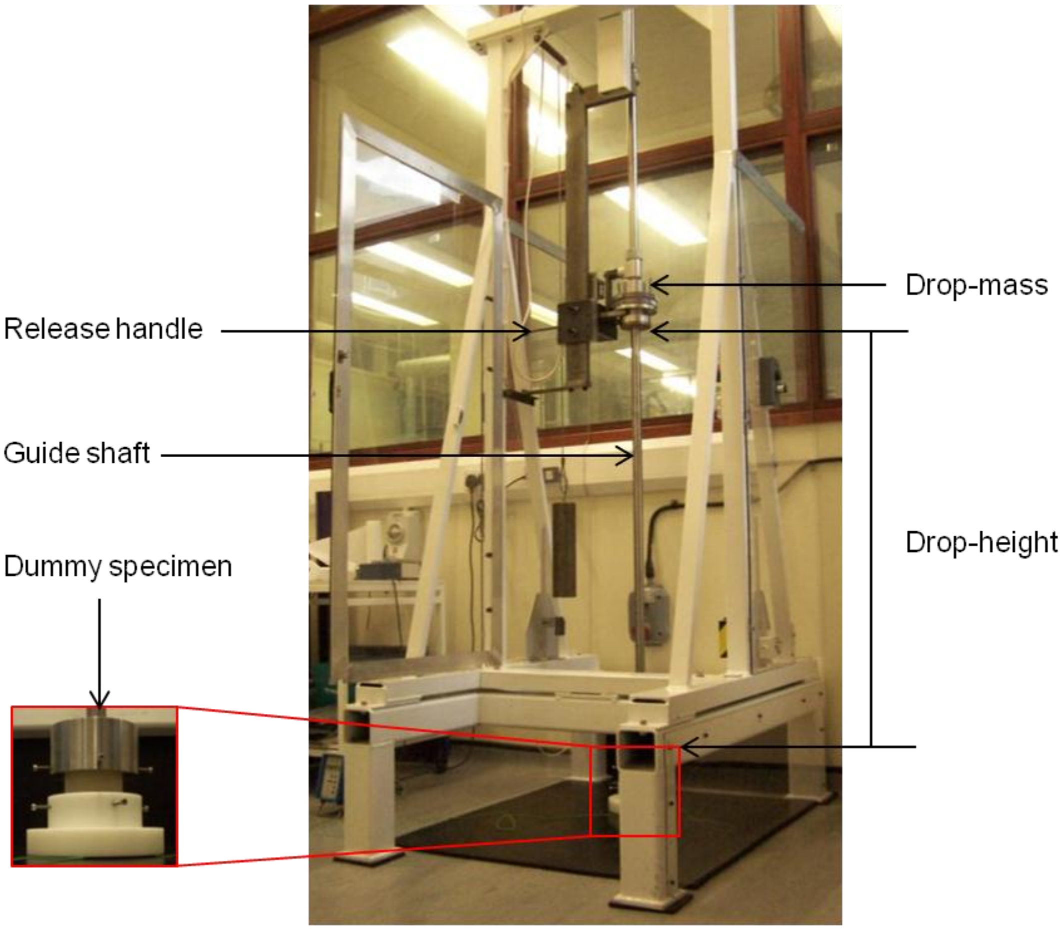

Figure 2.4 Drop-mass apparatus used to generate fractures in functional spinal units.

At the release of a handle, a variable drop-mass (2.5 – 12.8 kg) was allowed to freefall from an adjustable height (1.2 – 1.6 m) along a guide shaft onto a FSU. The superior loading plate was secured in the horizontal position whilst the inferior loading plate was secured via the mountings to allow only for axial motion. The FSU was held in a vertical position by means of the guide shaft.

A load cell was situated below the inferior mounting which could have been used to record the impact energies during fracture creation however; the appropriate software was not in place to reliably measure the output voltage and it was not possible to rectify this in the current study.

2.2.4 Fracture Generation

To obtain the greatest number of successfully fractured specimens from the 92 FSUs initially dissected and to minimise specimen wastage, the method for fracture generation was optimised using the average mass of each FSU level (Section 2.2.1) and the two variations of PMMA loading plate height (Section 2.2.2). The following subsections describe the optimisation process in more detail, present the preliminary results and give the recommended method for the generation of traumatically fractured vertebrae.

Method Development

To determine the optimum combination of mass and height required to obtain sufficiently traumatic fractures, four trials (Trial A, B, C and D) were performed using 44 of the 92 FSUs initially dissected. The settings of drop-height and drop-mass used during the trials are presented in Figure 2.5. The drop-height was measured as the distance from the base of the mass to the top of the superior mounting as illustrated in Figure 2.4.

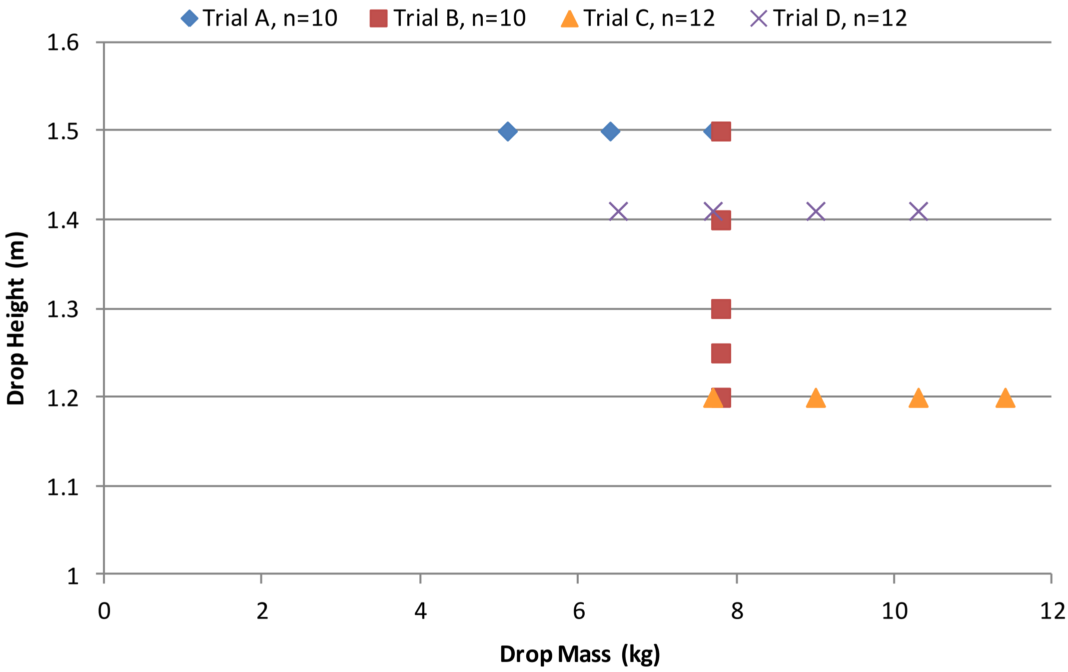

Figure 2.5 Drop-mass and height settings investigated to optimise fracture generation. For Trial A, three specimens were tested at each setting with four used on the 7.8 kg setting. For Trial B, two specimens were tested at each setting. For Trial C and D, three specimens were tested at each setting. Note the non-zero Y-axis starting position.

The FSUs of Trial A were the only specimens that were housed using the thinner loading plates of Housing 1 (Section 2.2.2). Trial B was the only investigation that employed a constant drop-mass with a variable height. The remaining trials (Trial C and D) varied the mass whilst the height was kept constant.

Following each trial, the middle vertebra of each FSU was excised and visually inspected to assess whether or not the fracture was satisfactory. Vertebrae that appeared to have either a compromised posterior column or a stable anterior column were disposed of. The 48 remaining FSUs, from the 92 initially dissected, were fractured using the settings of the trial with the most successful outcome. The mass of the eight FSUs as recorded from Section 2.2.1 were used to justify the selection of the final drop-masses.

Preliminary Results

A small amount of variation was observed between the masses of each FSU level as presented in Table 2.1.

Table 2.1 The mass of each functional spinal unit from two spines.

	Mass (kg)	
FSU Level	**Spine 1**	**Spine 2**
T9-T11	0.132	0.135
T12-T14	0.160	0.161
L1-L3	0.184	0.187
L4-L6	0.225	0.196

Only two spines were used in this investigation because to obtain an accurate measurement of mass, a considerable amount of effort was required to remove the excess soft tissue from each FSU and this was not beneficial in fracture generation. Following the observed similarity between the masses of the FSUs in Table 2.1, soft tissue was no longer removed during dissection which helped to reduce the amount of time, and therefore the level of dehydration, possible during preparation.

The greatest number of sufficiently fractured vertebrae was obtained using Housing 2. The failure rate of Housing 1 was 50% whilst that of Housing 2 was 70%. The remaining FSUs were housed in accordance with Housing 2, including those used in Trial C and Trial D.

Trials B and D were the most successful and produced the same number of fractures (Table 2.2). However, Trial D was employed as the final method for all subsequent fracture generations because the drop-height in Trial B was manually varied which resulted in a more labour intensive procedure than that of Trial D where the drop-height was constant.

Table 2.2 Number of sufficiently traumatic fractures obtained from the four trials.

	Specimens	Fractures
Trial A	10	0
Trial B	10	8
Trial C	12	7
Trial D	12	8

The mean mass of each FSU level showed a high level of correlation with the potential energy of each drop (Figure 2.6) because the increments the drop-masses increased by were selected based on the incremental increase of FSU mass. The high correlation indicated that the variation in drop-mass, in conjunction with an average constant drop-height of 1.4 m, were appropriate for the creation of sufficiently traumatically fractured specimens.

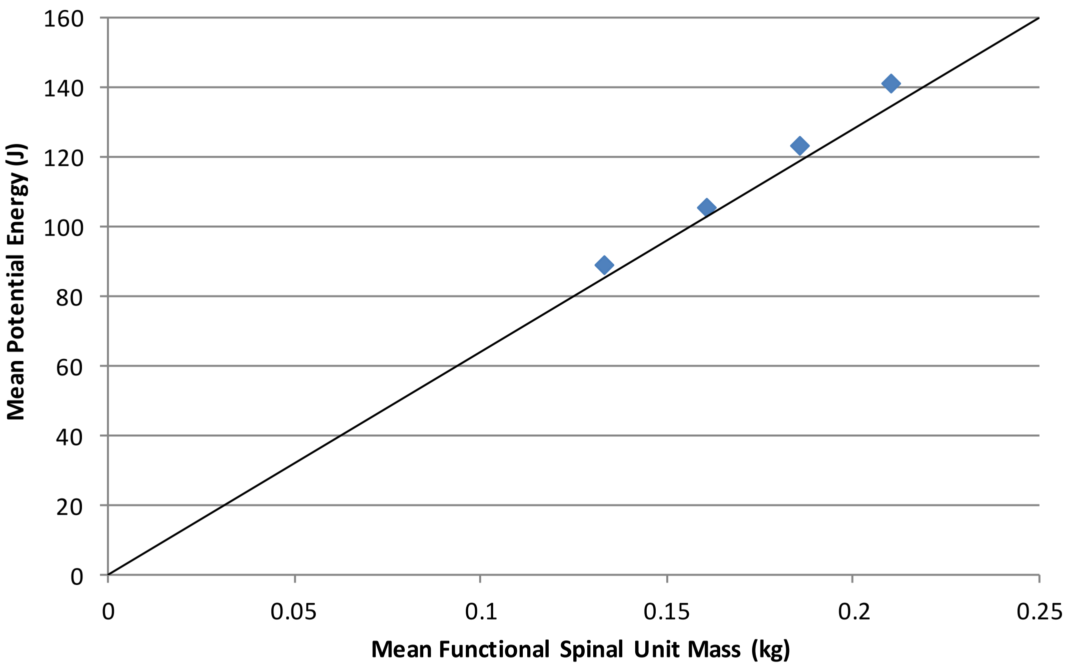

Figure 2.6 High correlation was witnessed between the average mass of each functional spinal unit level and the potential energy of each corresponding drop-mass from a constant drop-height of 1.4 m.

The constant drop-height of 1.4 m was an average of the drop-heights recorded using the FSUs from Trial B. There was a slight variation in the drop-heights, although the starting position of drop-mass remained constant, due to the height of the FSUs which fluctuated between FSU levels and between spines.

Recommended Method

The findings from the four trials were used to define the final method that was employed to generate fractures in the remaining 48 FSUs. The optimum settings for fracture generation are shown in Table 2.3.

Table 2.3 Optimum drop-mass values used to create fractures at 1.4 m.

FSU Level	Drop-Mass (kg)	Mean Potential Energy from Trial D (J)
T9-T11	6.5	89.3
T12-T14	7.7	105.8
L1-L3	9.0	123.6
L4-L6	10.3	141.5

From the 92 FSUs that were dissected, housed between loading plates and fractured, a total of 45 traumatically fractured, individual vertebral specimens were obtained. The specimens were divided into three sets as indicated in Figure 2.1. To summarise the divisions, eight specimens were subjected to a single cycle load (Section 2.3), 15 specimens were used in the development of a loading regime to subject specimens to multi-cycle loading (Section 2.4) and the remaining 22 specimens were subjected to multi-cycle loading (Section 2.5).

2.3 Single Cycle Loading Set

Eight individual, traumatically fractured specimens were housed between loading plates, imaged using a µCT system and subjected to the application of a point load through the centre of the vertebral body. The images from the µCT scanner were used to develop validated FE specimen-specific models as presented in Chapter 4.

2.3.1 Specimen Housing

Prior to being loaded, the specimens were housed between parallel plates of PMMA to ensure uniform loading surfaces were available. Similar to the housing of FSUs (Section 2.2.2), a steel rod was held fast against the anterior of the spinal canal throughout. As there was no specialised apparatus available for housing individual vertebrae, a spirit level was used to ensure the loading plates were parallel.

The specimens were dissected as discussed in Section 2.2.1.

With the rod in contact with the base plate, each specimen was held above the mould whilst PMMA was poured to a height of 12 – 15 mm and allowed to partially set. At this stage, each specimen was then lowered into the PMMA until the ring apophysis was fully submerged. Care was taken to ensure that the articular facet joints did not come into contact with the base plate as this would have introduced bias to the uniform loading surface. Once the cement had set, each specimen was moved to the other end of the steel rod and the procedure repeated (Figure 2.7). A spirit level was placed on the superior loading plate whilst the specimen was aligned with the lower mould.

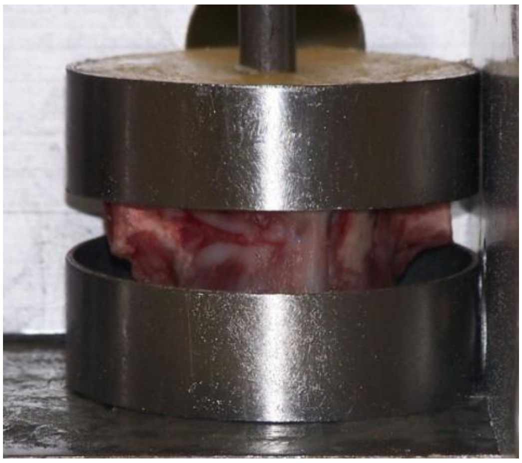

Figure 2.7 A fractured specimen being housed between parallel loading plates.

Housing each specimen in this manner resulted in guide holes being present in the PMMA plates at the anterior edge of the spinal canal. Using the guide holes as a reference, and with the depth and breathe of the vertebral body known from measurements taken prior to housing using a vernier calliper, it was possible to identify the midpoint of the vertebral body using the guide holes. The centre of a radio-opaque marker (Ø11 x 3 mm) was affixed to the midpoint of the vertebral body for use in loading the specimen both experimentally and computationally.

2.3.2 Imaging

Specimens were imaged using a µCT system (SCANCO µCT80, Scanco Medical, Bassersdorf, Switzerland) which contained an x-ray source that generated a conical shaped beam. The beam was directed at a specimen, within a container, and the intensity of the emerging beam was detected. The container was rotated around the vertical axis to allow for projections to be gathered from various angles. The information was reconstructed using the built-in software (IDL, Scanco Medical, Bassersdorf, Switzerland) and stacks of 2D dicom images with a resolution of 74 µm in all directions were obtained. The imaging was conducted at 70 kV and 114 µA with an integration time of 300 ms. Prior to the scanning of each specimen, it was important to ensure that the PMMA plates were parallel to the base of the container in order to reduce errors at the modelling stage.

2.3.3 Compressive Loading

A screw-driven materials testing machine (10 kN, Instron 3366, UK) was used to load the specimens at a rate of 1 mm/min, in accordance with previous studies (Tarsuslugil 2011; Wijayathunga *et al*. 2008), until a change in stiffness was visually detected which indicated that yield had occurred Specimens were secured in the machine using a custom built apparatus which fixed the lower PMMA plate in all directions (Figure 2.8). Using the radio-opaque marker as an indication of the midpoint of the vertebral body, a stainless steel loading disc (Ø140 x 7.5 mm) with a countersunk hole (Ø13 x 7.5 mm) was positioned over the upper PMMA plate to allow for an axial load to be applied to the midpoint of each specimen.

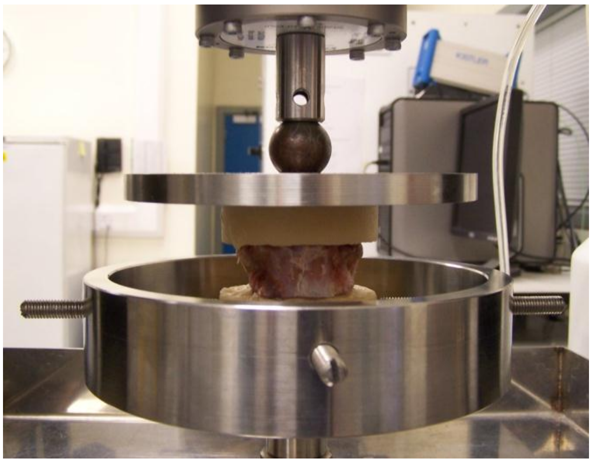

Figure 2.8 Axial loading of a specimen with the lower loading plate constrained in all directions.

The most linear region of the load-displacement curve for each specimen was used to obtain the stiffness. The stiffness was calculated over intervals of 0.5 mm within the linear region and the greatest stiffness value was used in the validation of the FE models. The results are presented in the following chapter whilst the modelling of these eight specimens is discussed in detail in Chapter 4.

2.4 Multi-Cycle Loading Development Set

To develop a method that would ultimately allow for the effects of multi-cycle loading upon augmented specimens to be observed, a development set of 15 specimens was used. The following section details the manner in which the specimens were housed between parallel loading plates, describes the two main methods employed and presents the preliminary results that were used in the selection of the final method. A successful specimen was defined as one that underwent a reduction in height without failure.

2.4.1 Specimen Housing

To ensure that the fractured vertebral body was the region subjected to multi-cycle loading, not the intact and more stiff posterior region, the posterior columns of the 15 specimens were removed at the pedicles prior to housing (Figure 2.9).

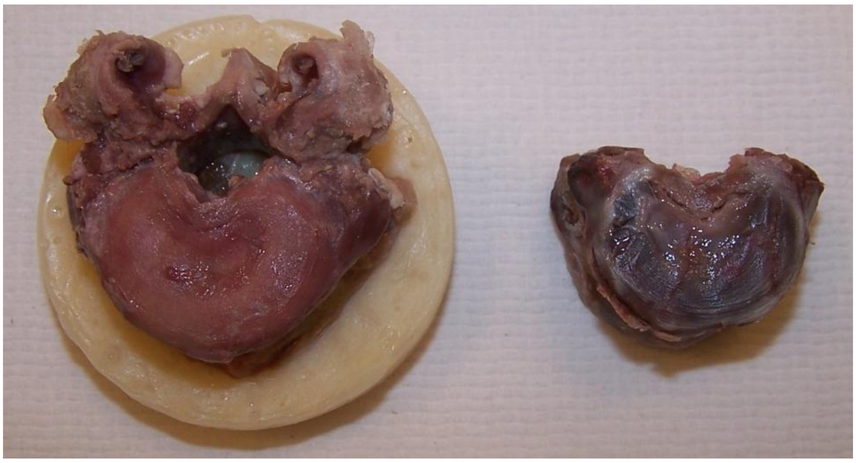

Figure 2.9 A comparison of an entire specimen and one truncated at the pedicles.

In a further attempt to obtain the true stiffness of the fractured anterior column, which may have been affected had the PMMA impregnated and hence secured the fractures during moulding, the loading plates were not allowed to bond to the specimens. By preventing this union, the stiffness of each specimen would not be altered through the interlock of the PMMA to the fracture. The endplates of each specimen were coated in petroleum jelly before being submerged to the most broad region of the ring apophysis in a very thin layer (4 – 6 mm) of partially set PMMA. As the housing was so thin, it was possible to visually identify the mid-point of the vertebral body. A radio-opaque marker was secured to that point after the loading plates were held parallel using insulating tape (Figure 2.10).

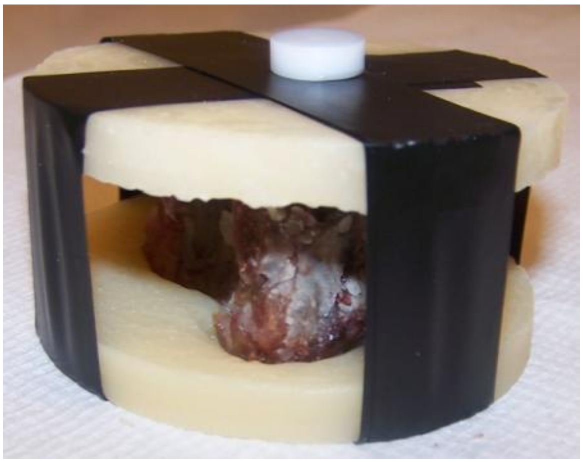

Figure 2.10 A specimen truncated at the pedicles housed between thin loading plates.

2.4.2 Biomechanical Fatigue Testing

In order to define a loading regime that would ultimately allow for augmented vertebrae to be modelled whilst they were subjected to multi-cycle loading, a spine fatigue simulator (Prosim, UK) was employed (Figure 2.11).

Figure 2.11 Six station spine fatigue simulator (Prosim, UK).

The aim was to fatigue traumatically fractured specimens in a biomechanical manner over a large number of cycles at relatively low loads. To replicate *in vivo* movement of the spine, the six station machine allowed for either force or displacement to be controlled in both axial and rotational directions. The machine was designed for testing the effects of biomechanical fatiguing on intervertebral orthopaedic devices and it was envisioned that following some preliminary studies, it may be possible to investigate the effect of fatigue upon augmented specimens. Therefore, a trial was conducted using three traumatically fractured, non-augmented specimens housed between loading plates of PMMA (Section2.4.1), but without the addition of the radio-opaque marker as it was not compatible with the rig of the spine fatigue simulator.

It was desirable for the FE modelling process, and for the potential clinical implications, that the loading of each specimen resulted in a reduction of height, but not the complete failure of each specimen. Therefore, the apparatus was configured to preload the specimens to 0.6 kN, load to 2 kN and unload to 0.6 kN at a rate of 1 kN/min for 100,000 cycles in a sinusoidal manner. It was known from the single cycle loading set that the specimens were unlikely to fail at 2 kN and these values also corresponded to those obtained from literature (Section 1.2.6).

The specimens were not subjected to a rotational displacement as this would have increased complexity at the computational modelling stage and potentially increased the associated error.

2.4.3 Multi-Cycle Compressive Loading

The screw-driven materials testing machine (10 kN, Instron 3366, UK) as described in Section 2.3.1, was used to investigate the effect of multi-cycle loading on specimens. Previously, the spine fatigue simulator coupled a lower load with a high number of cycles to simulate biomechanical fatigue. Due to the possibility of screw wear, it was not possible for the materials testing machine to load specimens over a high number of cycles. To capture the sudden change in height and stiffness that may correspond to a clinical trip or a fall, the materials testing machine subjected the specimens to a higher load for a lower number of cycles. It was anticipated that the materials testing machine would accelerate the rate at which specimen damage was observed in comparison to the spine fatigue simulator.

Three methods in which to specify the compression of each specimen were investigated: load control, displacement control to a given displacement and displacement control to a specified maximum load. Due to the limited number of specimens available to develop a method for cyclic loading, several specimens were used in more than one trial.

Load Control

Two trials were conducted (LC1 and LC2) to investigate the effects of loading rate (kN/min) and the maximum load on a traumatically fractured specimen. To induce a greater level of damage across a shorter number of cycles, but not the complete failure of the specimen, the magnitudes of the maximum load were chosen to be at least 1 kN larger than that of the spine fatigue simulator. A graphical representation of the settings investigated is presented in Figure 2.12.

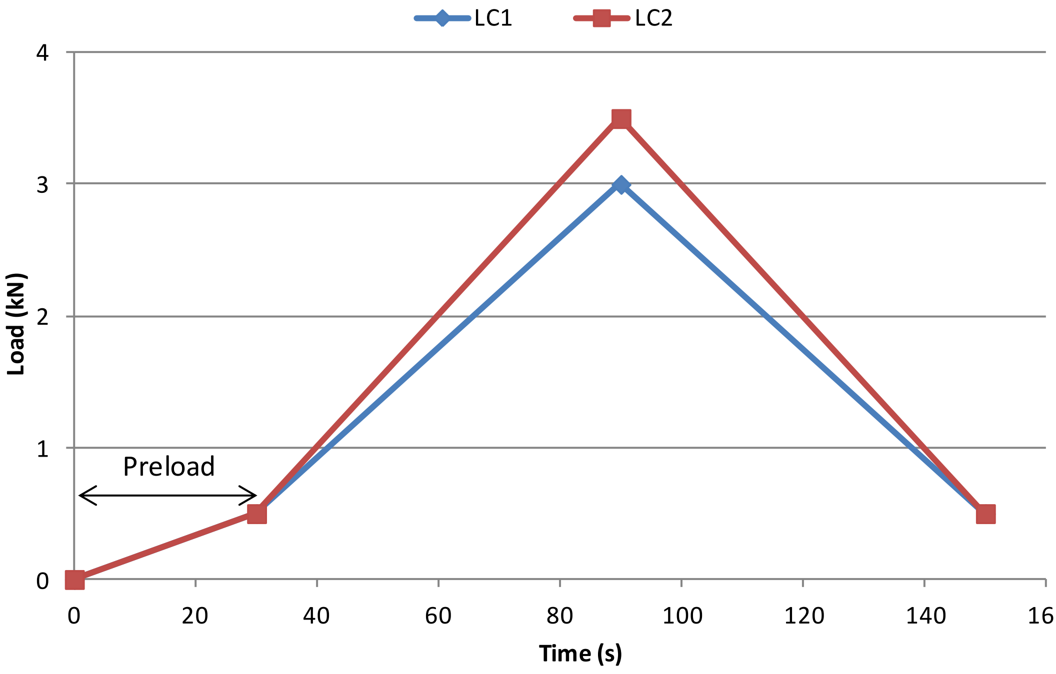

Figure 2.12 Load and loading rate specifications of the Load Control trials.

Displacement Control

To load specimens in a steady manner, displacement control (mm/min), rather than load control (kN/min), was used to define the speed of the cross head on the materials testing machine to a given displacement. Three trials were performed using Displacement Control settings (DC1, DC2 and DC3). Across all trials, the specimens were preloaded until a reduction in height of 0.5 mm was detected. A graphical representation showing the different loading rates and the maximum displacements investigated is shown in Figure 2.13.

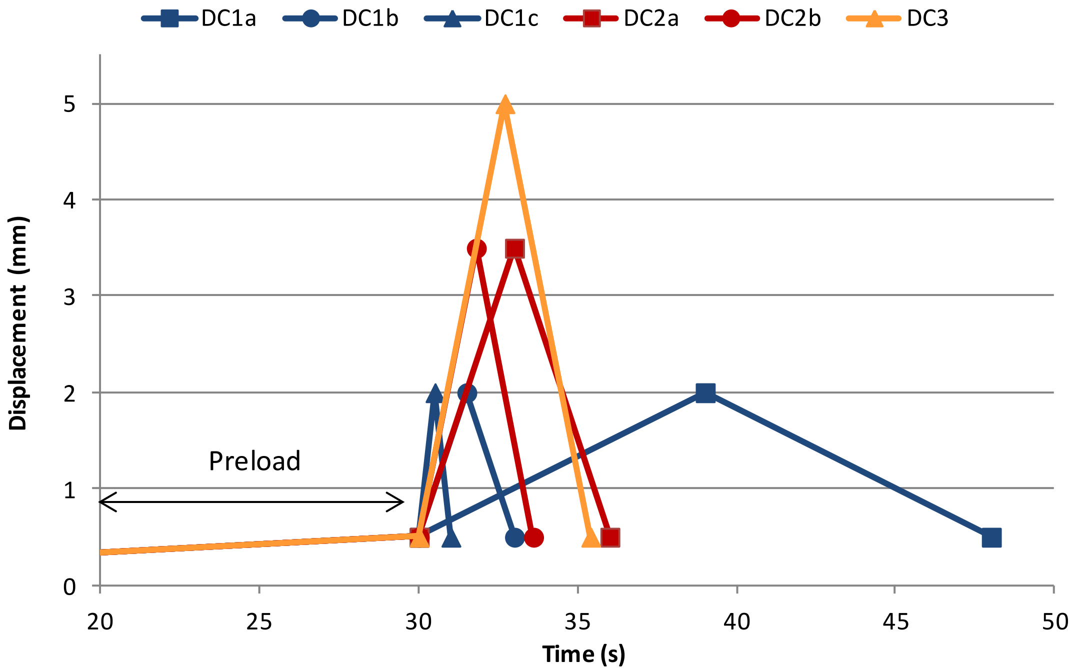

Figure 2.13 Displacement and loading rate specifications for the Displacement Control trials. Note the non-zero X-axis starting position.

In the first trial, DC1, the effect of loading rate was investigated (DC1a – DC1c) whilst the maximum and minimum displacements which the specimen was loaded and unloaded between was kept constant at 2 mm. In the second trial, DC2, the effect of loading rate was further investigated (DC2a and DC2b) whilst the maximum displacement was increased from that used in DC1. The final trial, DC3, investigated whether a specimen could be repeatedly displaced by 5 mm during multi-cycle loading.

Displacement Control with Maximum Load

Three trials of Displacement Control with Maximum Load (DCML1 – DCML3) were investigated where the loading rate was kept constant at 25 mm/min whilst the maximum load was varied as shown in Figure 2.14.

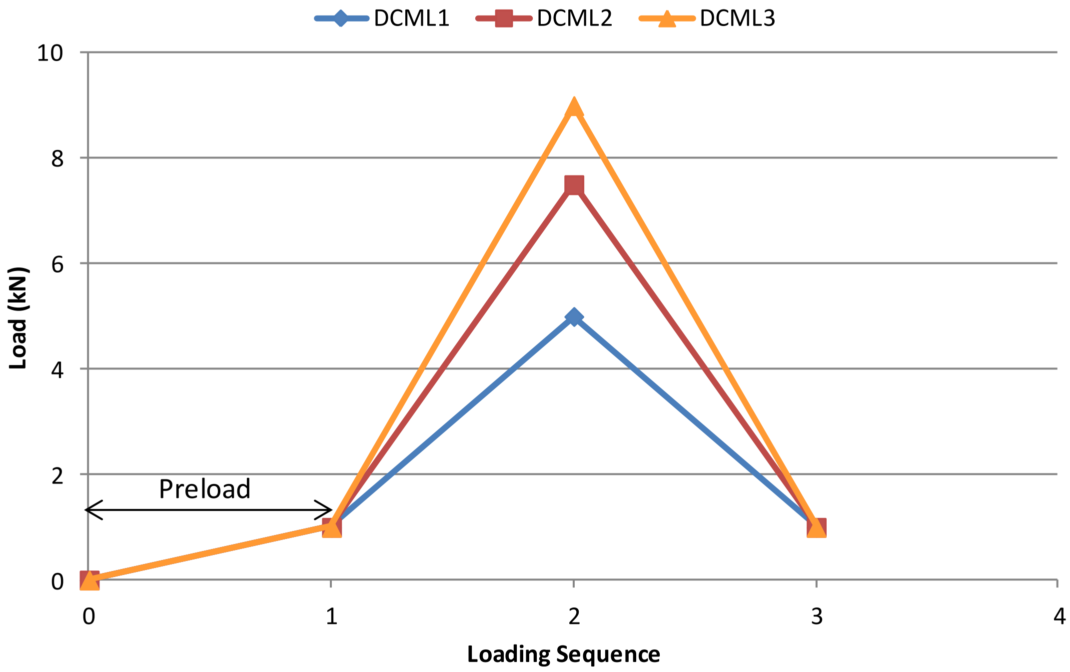

Figure 2.14 Maximum loads investigated in the Displacement Control with Maximum Load trials.

As the results from these trials were encouraging, a greater number of specimens were used in each trial to investigate the level of repeatability. For the first trial, DCML1, four specimens were each repeatedly loaded for the duration of 30 cycles. The maximum load was increased for the second trial, DCML2, where one specimen was subjected to three rounds of cyclic loading at 20 cycles each. Finally, five specimens were each loaded for 20 cycles as part of DCML3.

2.4.4 Results of Biomechanical Fatigue Testing

Due to operational difficulties, it was only possible to collect data from one station. The displacement-time graph corresponding to this specimen is shown in Figure 2.15 along with the stiffness-time graph. Due to the difficulties encountered, the machine was repeatedly restarted during the initial 4,000 cycles therefore this data has been excluded from the graph.

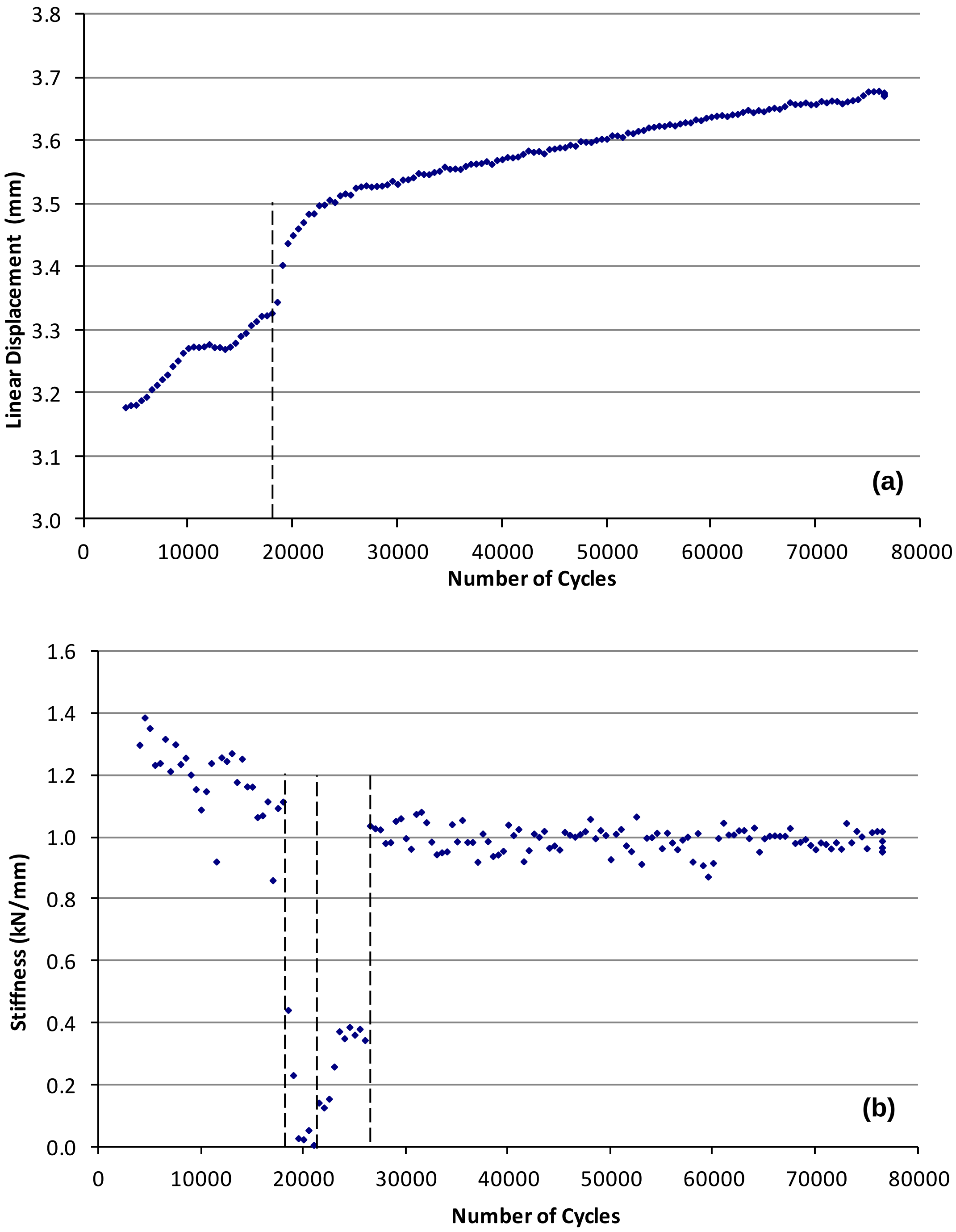

Figure 2.15 Plot of the displacement (a) and the stiffness (b) of a non-augmented, fractured specimen over a total of approximately 72,000 cycles. The initial 4,000 cycles were excluded due to the machine being restarted several times. The dashed lines at 18,000 cycles in (a) and (b) indicates where there was a sudden reduction in height and stiffness, respectively. The dashed line in (b) at 22,000 cycles indicates where the stiffness began to increase whilst the dashed line at 27,000 highlights where the stiffness began to gradually decrease. Note the non-zero Y-axis starting position in (a).

Initially the height and stiffness of the specimen decreased in a gradual manner. However, there was a sudden reduction in height and stiffness at approximately 18,000 cycles, perhaps indicating a further fracture, followed by a period of fracture reduction until approximately 27,000 cycles, at which point the stiffness continued to gradually decrease.

2.4.5 Results of Multi-Cycle Compressive Loading

The results from the trials used to investigate the most appropriate method to subject specimens to multi-cycle loading using the materials testing machine are presented in the following subsections.

Load Control

The first trial, LC1, was executed successfully however, the second trial, LC2, was only successful for the first two cycles. Following two cycles, the materials testing machine was no longer able to deliver a constant loading rate and an unusual load-displacement curve resulted (Figure 2.16).

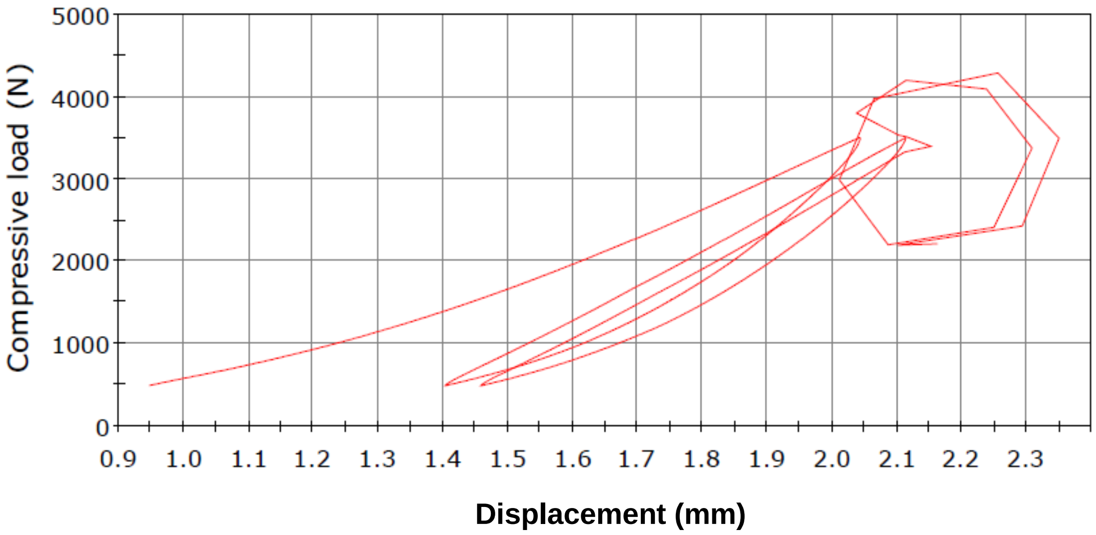

Figure 2.16 Load-displacement graph showing the inability of the materials testing machine to maintain a steady cross head speed during Load Control trial 2. Note the non-zero X-axis starting position.

The materials testing machine monitored the deformation of the specimen throughout loading and continuously recalculated the speed of the cross head to ensure a constant loading rate was being delivered. However, when the change in height was too abrupt for the machine to detect, the machine intermittently delivered over- and under-estimations of the required speed. There is a possibility of damage to the load cell when the machine recalibrates in this manner. For this reason, load control was not further investigated as a means to subject specimens to longer term changes in load.

Displacement Control

During the first set of trials, DC1a – DC1c, the greatest resulting load was observed when the highest loading rate was employed. The maximum load observed was 6 kN and the specimen was subjected to 15 cycles before failure occurred (Figure 2.17). The maximum loads observed when the lower loading rates were employed were 4.3 kN and 5.7 kN.

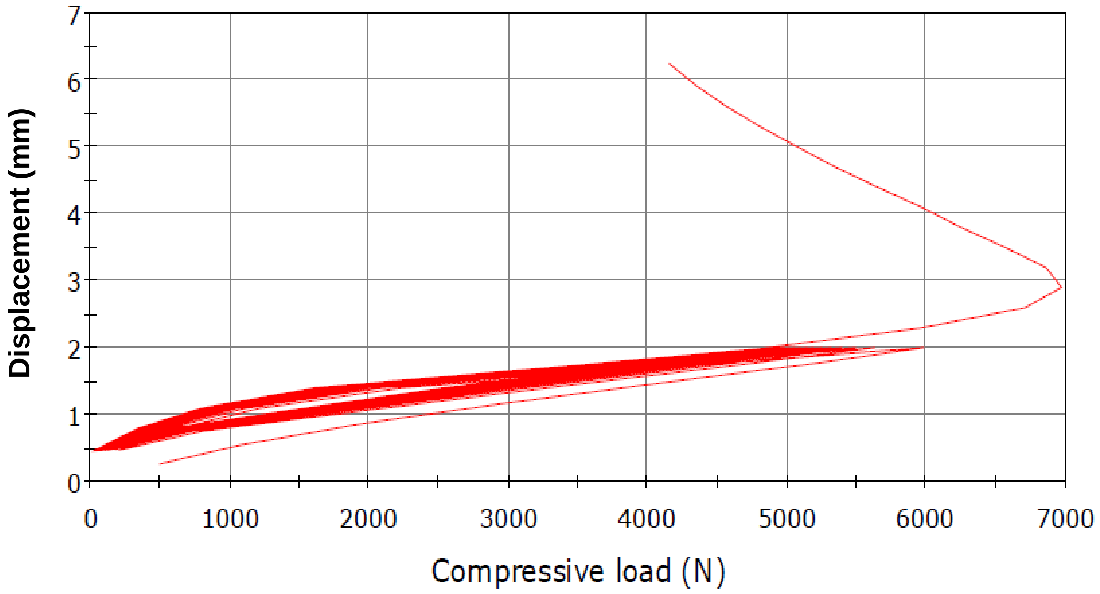

Figure 2.17 Failure of a specimen when loaded at the highest loading rate during Displacement Control trial 1.

Similarly, the greatest maximum load observed during the second trials, DC2a – DC2b, occurred when the higher loading rate was employed. The maximum load required to produce a uniform displacement increased from 4.2 – 4.8 kN (Figure 2.18). The increase in the maximum load observed suggested that cumulative compressive damage occurred within the specimen. The preferred loading rate to be taken forward to the final trial, DC3, was that of DC2b because the specimen survived the testing at this rate for 20 cycles and the maximum load observed was greater than that of the lower loading rate.

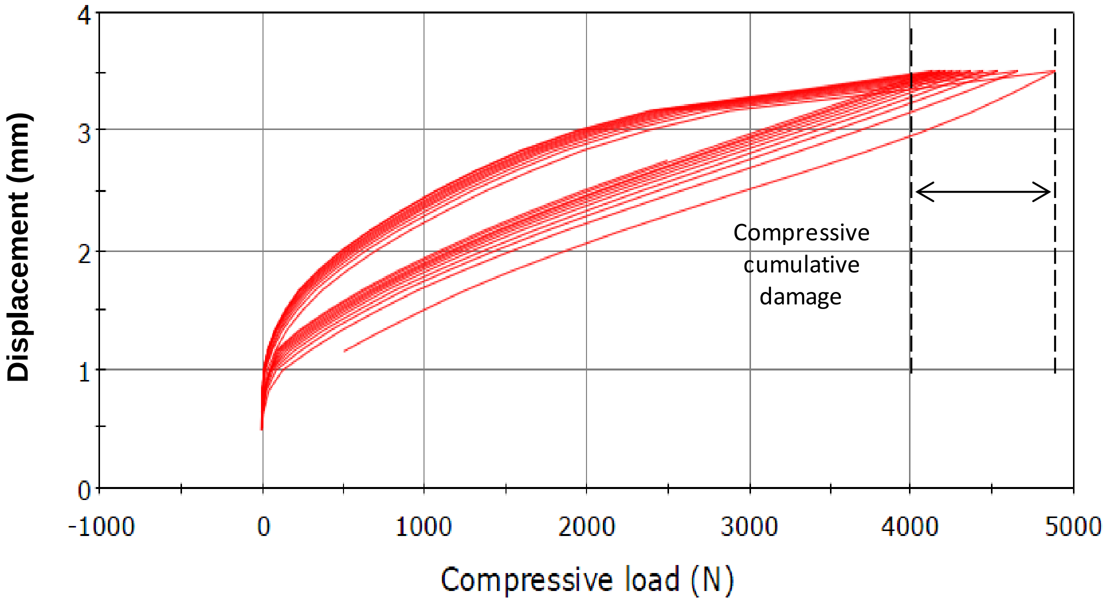

Figure 2.18 Evidence for cumulative compressive damage in the observed maximum load during Displacement Control trial 2.

The final trial, DC3, employed the optimum loading rate from the previous two trials with a greater maximum displacement. The specimen accumulated damage across four cycles after which point failure was observed when the maximum load experienced by the specimen was 4.8 kN.

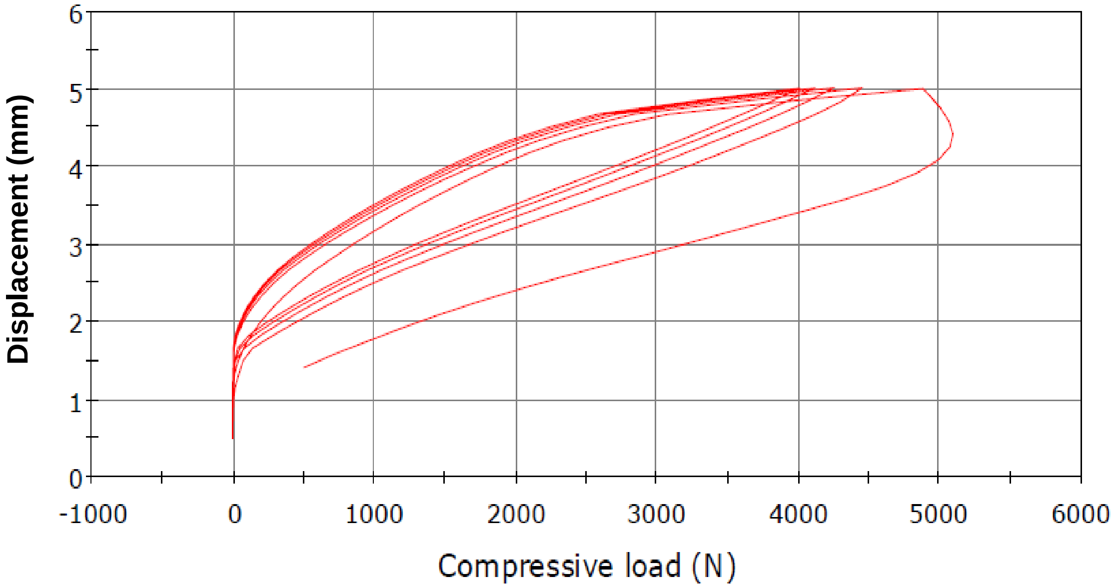

Figure 2.19 Failure of a specimen following four cycles during Displacement Control trial 3.

Displacement Control with Maximum Load

The three trials of the Displacement Control with Maximum Load, DCML1 – DCML3, investigated the maximum load specimens could be repeatedly subjected to.

Of the four specimens tested to 5 kN during DCML1, each one successfully underwent the 30 cycles of loading without failure although plastic deformation was observed in all cases. A selection of some of the load-displacement graphs can be seen in Figure 2.20. Marked on this figure are the criteria that define the initial and final displacements (S10T13 and S10T10, respectively) which will be discussed in subsequent sections and chapters.

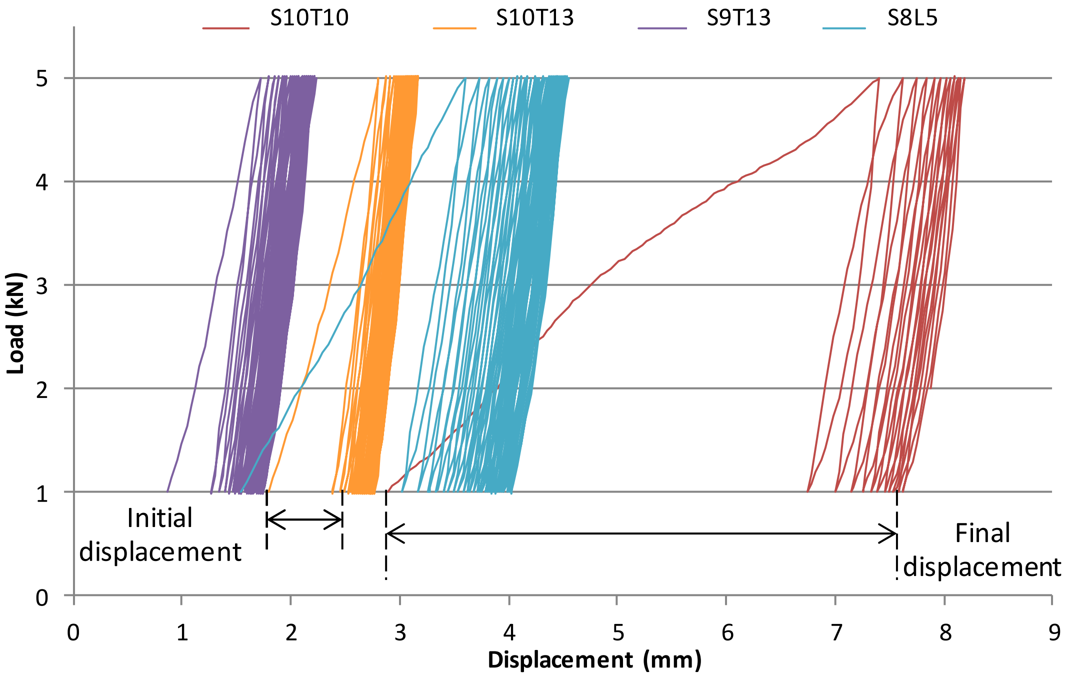

Figure 2.20 Load-displacement graphs of the specimens tested in the first trial of Displacement Control with Maximum Load.

The specimen that was tested to 7.5 kN in the second trial, DCML2, successfully underwent two multi-cycle loading regimes of 20 cycles each. However, upon the third test, the specimen failed at 15 cycles (Figure 2.21).

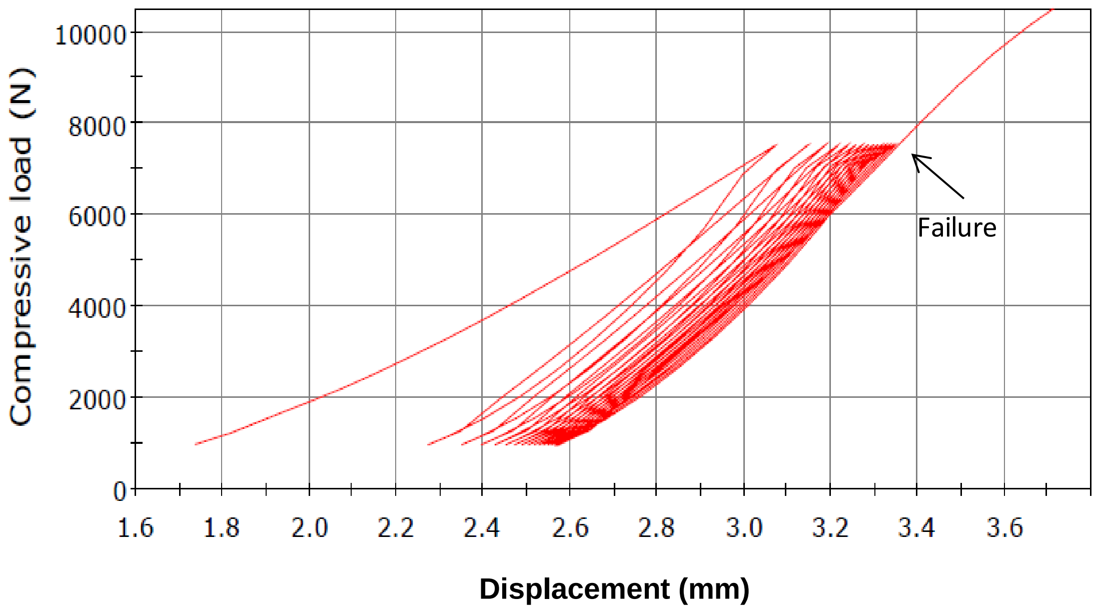

Figure 2.21 Failure of the specimen during Displacement Control with Maximum Load trial 2. Note the non-zero X-axis starting position.

Three of the five specimens tested during the third trial, DCML3, successfully underwent the 30 cycles where the maximum load was 9.5 kN. To investigate the number of cycles a specimen could be subjected to, the third specimen, S5T10, was subjected to three further rounds of multi-cycle testing. The specimen failed during the fourth round of multi-cycle testing following 15 cycles. The initial and final load-displacement graphs for the specimen subjected to four rounds of multi-cycle testing (S5T10_0 and S5T10_3) can be seen in Figure 2.22. Also shown are the load-displacement graphs of the fourth and fifth specimens (S9T10 and S10T10) which failed following the eighth cycle and during the initial cycle at 8.5 kN, respectively.

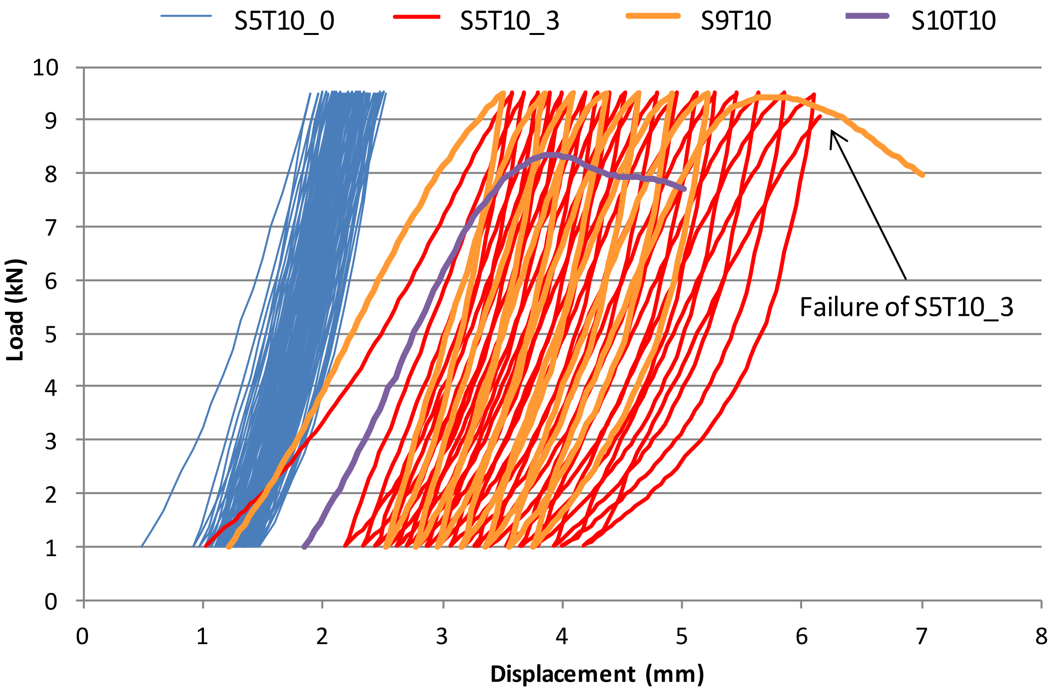

Figure 2.22 Load-displacement graphs of selected specimens from Displacement Control with Maximum Load trial 3.

2.4.6 Discussion and Recommended Method

A total of 15 specimens were used as the development set during the biomechanical fatigue trial (Section 2.4.2) and the multi-cycle compressive loading trials (Section 2.4.3). Several specimens were used in multiple tests which may have resulted in these specimens being more stiff than others due to the compression of trabecular bone. It was not clear which contributed greatest to the failure of specimens, the damage produced during several trials or the magnitude of the final load or loading rate.

Biomechanical Fatigue Testing Results

There were a number of faults with the stations of the spine fatigue simulator which made it incapable of efficiently subjecting specimens to multi-cycle loading. It was previously known that there was an existing technical fault with the three stations located at the rear of the machine so initially three specimens were prepared, rather than six. However, when initiating the trial, it was discovered that a further two stations were not functioning correctly. The input for rotational displacement was set as zero however, once the test began, the two stations were seen to immediately rotate into a locked position. The magnitude of this involuntary rotational displacement was not recorded in the output data. Due to the inaccuracy in the output data obtained from these stations in conjunction with the three previously faulty stations, only one station could be used.

Data was obtained from one specimen for approximately 76,000 cycles and the general reduction in stiffness, coupled with the abrupt reduction due to the sudden compression of fractures, illustrated that the spine fatigue simulator may have been beneficial to this study. However, due to the high number of errors associated with this machine, repair was not a viable option. As multi-cycle loading using the spine fatigue simulator of one specimen at a time was quite a time consuming process, it was decided not to investigate the effect of biomechanical fatiguing on specimens. It was therefore necessary to an use alternative apparatus in order to develop a regime that would ultimately allow for the effects of multi-cycle loading on augmented, traumatically fractured vertebrae to be measured.

Multi-Cycle Compressive Loading Results

The materials testing machine was employed in the multi-cycle loading of specimens in order to accelerate the rate at which damage occurred in comparison to the spine fatigue simulator. The findings from the initial two trials, Load Control and Displacement Control, were used to define the final trial which led to the recommended multi-cycle loading regime. The Load Control trials (LC1 and LC2) illustrated that it was not feasible to use the load control settings on the materials testing machine when testing fractured vertebrae. The Displacement Control trials (DC1, DC2 and DC3) highlighted that it was possible to witness the accumulation of compressive damage at higher loading rates. The greatest load observed during these trials was 6 kN.

The Displacement Control with Maximum Load trials (DCML1, DCML2 and DCML3) were devised to see whether a load similar in magnitude to the 6 kN witnessed during the Displacement Control trials could be sustained for a greater number of cycles when a lower loading rate was employed. Specimens were observed to be able to undergo repeated loading of 5 kN, 7.5 kN and 9 kN without failure. The findings from this trial were used to define the final multi-cycle loading regime.

Recommended Method

The final multi-cycle loading regime was specified to initiate with a pre-load of 1 kN at a loading rate of 10 mm/min. Following this, the specimens were loaded and unloaded at 25 mm/min between 6 kN and 1 kN for a total of 30 cycles.

2.5 Multi-Cycle Loading Set

Prior to fracture generation, it was anticipated that at least nine specimens would be obtained for a non-augmented control set and a further 12 would be obtained for augmentation with either PMMA or CaP. As each set was worked upon in the laboratory sequentially, it so happened that nine successfully fractured specimens were obtained for the control set; seven for the PMMA and six for the CaP augmentation. This section describes the augmentation procedure, the housing between loading plates, the imaging and the grading that was performed for each specimen.

2.5.1 Augmentation

Specimens were augmented in a bi-pedicular manner with either PMMA or CaP cement. A bone reaming device was used to create augmentation holes in the pedicles. As fluoroscopic guidance was not available, a visual inspection of the endplates was used to determine the direction and depth of the reaming. Disposable 10 cc laboratory grade syringes and 13-gauge needles were used (Figure 2.23)

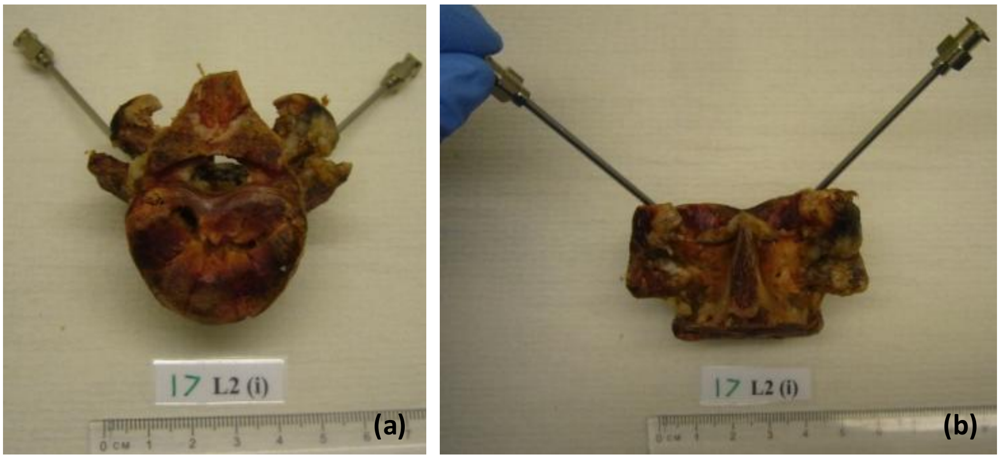

Figure 2.23 Preparation of a specimen for bi-pedicular augmentation in the (a) superior axial view and (b) posterior coronal view.

Polymethylmethacrylate Cement

For consistency with previous studies (Tarsuslugil 2011), lab grade PMMA cement (WHW Plastics, Hull, UK) was mixed in the ratio of 5:3 (ml:g). The liquid methylmethacrylate component was added to the acrylic powder in a fume hood and care was taken during mixing to reduce the introduction of air bubbles that could reduce the modulus of the cement. The ratio of 5:3 allowed for the cement to be easily drawn into the syringe and provided a window of approximately four minutes for injection. Damp tissue was held securely over the endplates to prevent premature leakage of cement. An eggshell technique was employed during augmentation whereby a small amount of cement was released followed by a pause of approximately 10 –15 seconds. The pause allowed for a partially solidified shell to form on the surface of the injected cement which helped to minimise leakage. Augmentation was performed until cement either escaped from fractures in the cortical shell or travelled back out of the augmentation holes. At this stage, the needles were slowly withdrawn whilst cement was continuously released in order to fill the augmentation holes. The final setting time of the cement was in the region of 45 minutes from when liquid component and powder first came into contact.

Calcium Phosphate Cement

The CaP cement employed was one of three developed as part of the collaboration as specified in Section 1.8 (O'Hara 2010) and recommended following the findings of a previous study (Tarsuslugil 2011). The cement was composed of 100% alpha-tricalcium phosphate powder (α-TCP (Queen's University Belfast)) and 4% weight aqueous solution of di-sodium hydrogen phosphate (Na_2HPO_4 (Fisher Scientific, UK)).

The aqueous solution was added to the powder in a liquid to weight ratio of 1:2 (ml:g) and mixed for one minute using a folding technique in order to expel any air bubbles. As instructed by the team at Queen's University Belfast, there was a time frame of one minute to transfer the cement to the syringe plus a three minute delay prior to augmentation. The delay was to allow for cohesion of the cement resulting in an increase in the viscosity which was understood to lead to a more desirable augmentation (Tarsuslugil 2011). The augmented specimens were immediately placed in an incubator (APT Line BD (E2), Binder, Germany) at 37^oC for 20 minutes before being fully immersed in Ringer's solution (Table 2.4) and left in the incubator for a further five days.

Table 2.4 Chemical composition of Ringer's solution used to simulate *in vivo* conditions for the setting of CaP cement

Mass/concentration	Compound	Supplier
8.6 g	Sodium chloride (NaCl)	Fisher Scientific, UK
0.33 g	Calcium chloride ($CaCl_2$)	Fisher Scientific, UK
0.3 g	Potassium chloride (KCl)	Fisher Scientific, UK
0.03%	Sodium azide (NaN_3)	Severn Biotech LTD, UK

The Ringer's solution contained 0.03% concentration of the biological preservative agent sodium azide (NaN_3) to help reduce spoilage of specimens during incubation. Over a five day time frame, a previous trial observed that the inclusion of NaN_3 in the Ringer's solution resulted in an increase in the Young's modulus of the cement by almost 12% (Tarsuslugil 2011). In the same trial, an increase in the stiffness of an intact porcine vertebra of 1.3% was seen to occur. The alternative method of preservation available during the trial was that of refrigeration. However, it was discovered that three days in Ringer's solution at 5^oC resulted in a 97% reduction in the Young's modulus of the cement. Therefore, although incorporating NaN_3 with the Ringer's Solution affected the modulus of the cement, it was the most favourable means of reducing spoiling during the incubation period.

2.5.2 Specimen Housing

The specimens were housed between loading plates of PMMA using a technique that was derived from those used previously (Section 2.3.1 and Section 2.4.1). Prior to housing, the 22 specimens were again trimmed to ensure that the fractured vertebral body was the primary load bearing region. However, they were not trimmed at the pedicles as was performed previously (Section 2.4.1). It was observed following the multi-cycle development set that truncating the more traumatically fractured specimens at the pedicles compromised the integrity of such specimens and rendered them unusable. To prevent the wastage of specimens that could otherwise be subjected to cyclic loading, the protruding facets joints were trimmed in a horizontal manner to a level slightly below the vertebral bodies (Figure 2.24).

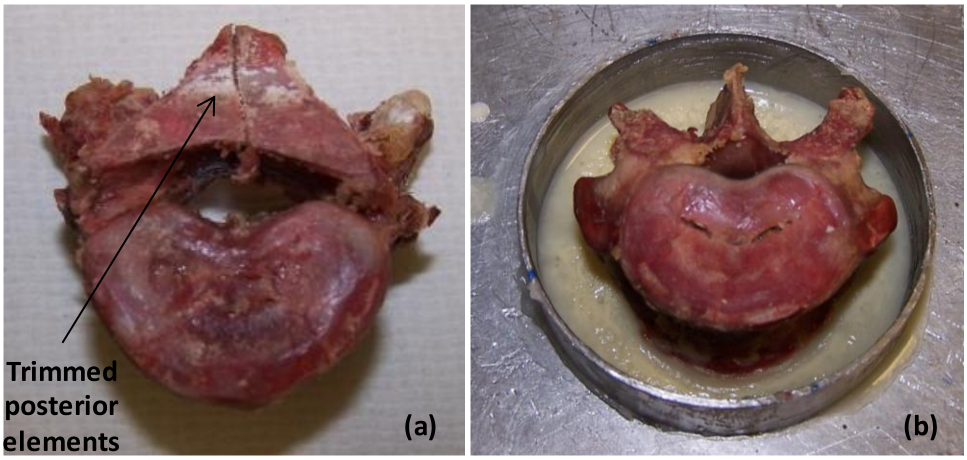

Figure 2.24 A vertebra trimmed at the posterior elements in (a) a horizontal manner and (b) shown encased in cement.

The specimens were housed to a depth corresponding to the most broad region of the ring apophysis and a spirit level was used to ensure the plates were parallel. A radio opaque marker was used to highlight the mid-point of the vertebral body.

Although housing the specimens prior to augmentation may have helped reduce cement leakage, it was decided to house the specimens post-augmentation to prevent the housing from increasing the stiffness of the fractured specimens and for ease of access to the pedicles during the augmentation process.

2.5.3 Imaging

The non-augmented specimens and those augmented with PMMA were scanned in accordance with the single cycle loading set as outlined previously in Section 2.3.2. However, due to the acquisition of a new µCT system (SCANCO µCT100, Scanco Medical, Bassersdorf, Switzerland), the specimens augmented with CaP were scanned with the same settings but at a resolution of either 88 or 103 µm.

Commercial image processing software (Simpleware, UK), described in full detail in Chapter 4, was used to obtain the volume of fracture and where applicable, the volume of augmented cement for each specimen as a percentage of the volume of bone.

2.5.4 Fracture Grading

To correlate the severity of a fractured specimen to the deformation due to loading, each specimen was graded using the images resulting from Section 2.5.3. A previous study (Panjabi *et al*. 1995) visually inspected and graded each slice at every 3 mm interval. Adhering to the three column theory proposed by Ferguson and Allen (1983), each slice was separated into a grid of 14 vertebral regions (Figure 1.8). Each region on the grid was assigned a score of either zero, one or two corresponding to whether it was intact, partially fractured or fractured.

The grid was created using the slice that contained the greatest proportion of vertebral body and was super-imposed on the remaining slices at the spinal canal. To reduce the variability in grading between slices, specimens and future users, the grid of each specimen was defined using the anterior edge of the spinal canal as a consistent reference point. The grid was further defined using a horizontal line at the most anteriorly protruding feature and the posterior edge of the spinal canal (Figure 2.25). The points at which the vertebral body was most broad were used to divide the vertebral body into nine regions. The anterior, middle and posterior column divisions according to Ferguson and Allen (1983) were defined as shown on the figure.

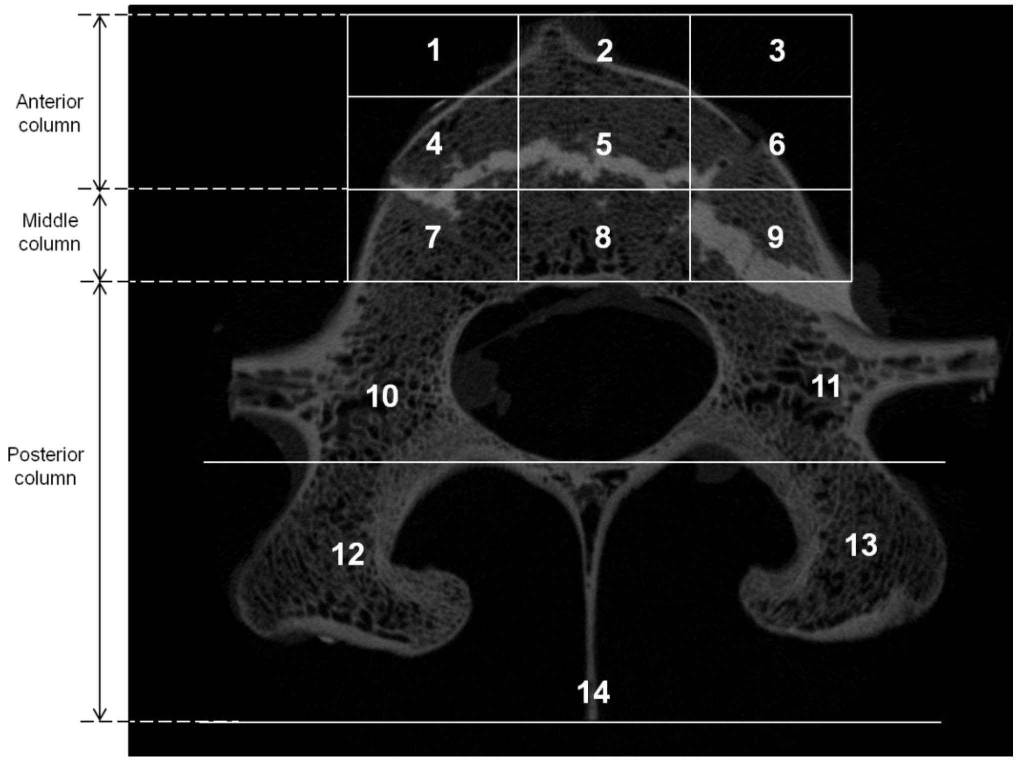

Figure 2.25 Adapted version of Panjabi *et al*. (1995) grading grid.

In conjunction with strictly defining the grading grid using consistent reference points, a further adaptation was taken whereby every slice at an interval of 2 mm was graded in order to increase the accuracy of each grade. All of the specimens were graded three times over a three day period and the normalised average taken as the final grade. The average of the anterior, middle and posterior column grades for each specimen was also taken. On each of the three days, the specimens from the non-augmented group were graded, followed by the PMMA and then CaP augmented specimens.

An ideal burst fracture, with the characteristic wedge shaped bony fragment retropulsed into the spinal canal, would have had a fracture severity grade of 8 due to the complete compromise of the sections numbered 5, 7, 8 and 9 (Figure 2.25). The mechanical stability of a vertebra with a burst fracture was considered by Panjabi *et al*. (1995) to be compromised when the fracture grade corresponding to Ferguson and Allen’s middle column (1984) was the highest of the three columns.

2.5.5 Injectability

Commercial image processing software (Simpleware, UK) which is described in full detail in Chapter 4, was used to obtain the volume of fracture as a percentage of the volume of bone for each specimen and where applicable, the volume of augmented cement as a percentage of the total volume of fracture. To obtain the volumes of bone, fracture and cement, the commercial image processing software captured the corresponding voxels using the greyscale values of the images from the µCT system.

2.5.6 Loading

The loading of the specimens was performed as described in Section 2.4.6. The stiffness of each loading cycle, per specimen, was taken as the gradient of the load-displacement curve within the range of 2 – 5 kN.

2.5.7 Further Imaging

Specimens that were observed to undergo larger deformations during loading were partially re-scanned. A lateral region in the middle of the vertebral body of approximately 10 mm in height was imaged. It was not possible to image a larger region of the vertebral body, or a higher number of specimens, due to the limited availability of the µCT scanner.

This chapter has described how 92 FSUs were manipulated in order to create 45 traumatically fractured, individual vertebral specimens. Of these 45 specimens, a total of 30 were used to create specimen-specific FE models as discussed in Chapter 4 whilst the remaining 15 were used as a method development set. Of the 30 specimens that were used to create specimen-specific FE models, eight non-augmented specimens were subjected to a single cycle load, nine non-augmented specimens were subjected to multi-cycle loading and 15 augmented specimens were subjected to the same multi-cycle loading regime. The results of the single cycle and multi-cycle specimens are presented in the following chapter.

Chapter 3

Experimental Results

3.1 Introduction

The results from the specimens subjected to single cycle and multi-cycle loading are presented in this chapter. The single cycle loading set are discussed in terms of the compressive loading and the stiffness values. The results of the non-augmented, PMMA and CaP augmented groups of the multi-cycle loading set are presented in terms of the fracture grading, injectability (where applicable), loading and stiffness values. In addition to this, some post-loading images of the multi-cycle loading set are also presented and discussed in order to determine whether vertebroplasty could be used to repair a traumatic fracture and to compare between cement types.

3.2 Single Cycle Loading Set

Eight specimens were traumatically fractured (Section 2.2.4) and tested under a single cycle load (Section 2.3.3). The results are presented in the following section and were subsequently used for FE model validation as described in Chapter 4.

3.2.1 Compressive Loading

The specimens originated from two spines, Spine 3 and Spine 4, and each middle vertebra from every FSU level was included in the set (T10, T13, L2 and L5). The load-displacement curves for each of the specimens from Spine 3 and Spine 4 are presented in Figure 3.1.

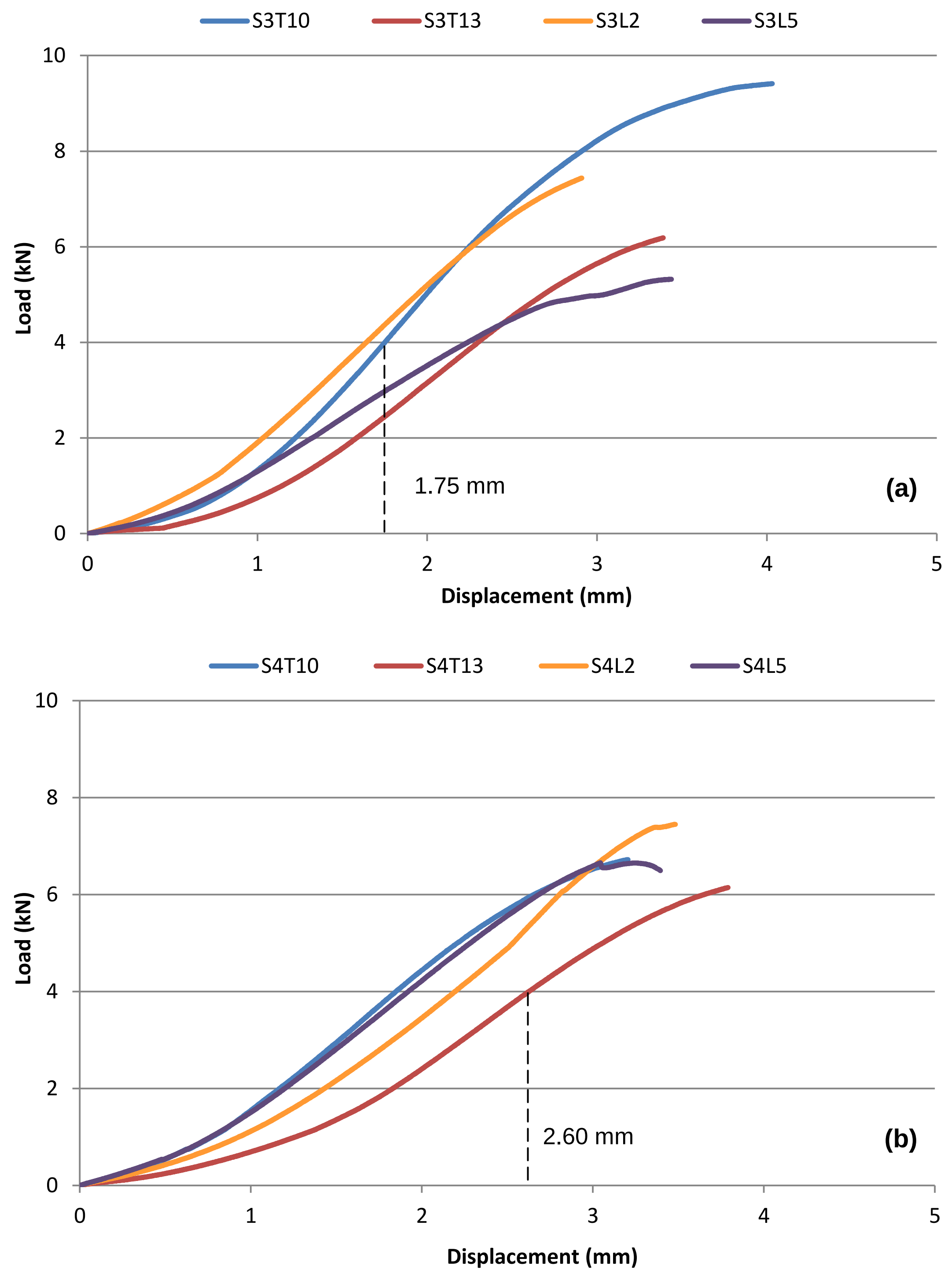

Figure 3.1 Load-displacement curves for Spine 3 (a) and Spine 4 (b) tested as part of single cycle loading. One specimen, S3L5, was seen to change in gradient before yield.

Although these loads are greater than what is experienced in the human spine *in vivo*, they cover the range of loads that have been observed (Section 1.2.6). In each case, the fractures of the specimen had come together, or stabilised, as much as possible as the load approached 2 kN and after this point, the gradient of each curve became constant. Once a specimen was seen to yield, as determined visually by a change in the gradient, the test was manually stopped in all instances except for one, S3L5, where there was a change in gradient before the yield which could have been due to the closure of a fractured region within the specimen (Figure 3.1a).

3.2.2 Stiffness Values

The most linear region in each of the load-displacement curves was 2 – 4 kN and the stiffness was calculated as explained in Section 2.3.3. The stiffness value corresponding to each specimen is shown in Figure 3.2.

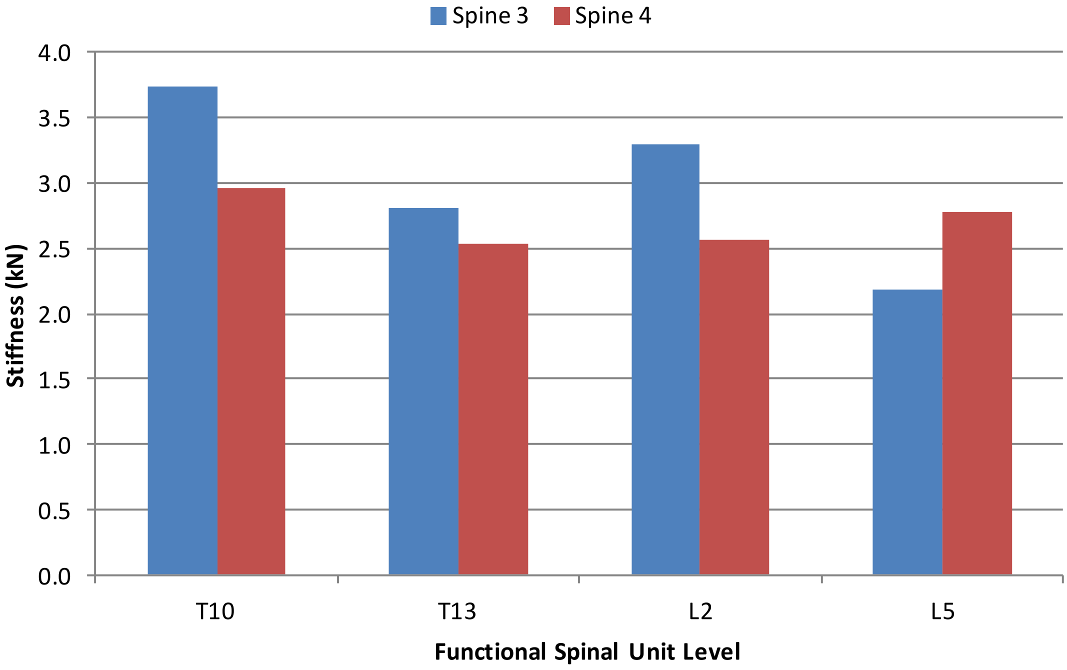

Figure 3.2 Stiffness values of the specimens subjected to single cycle loading.

3.2.3 Discussion

The specimen with the greatest stiffness value of the set was seen to be S3T10 and the corresponding load-displacement curve (Figure 3.1a) illustrated that this specimen also possessed the highest visually detected yield point of the set at approximately 7.5 kN. Similarly, the specimen with the second lowest stiffness value, S4T13, was seen to have the second lowest yield point at approximately 5 kN (Figure 3.1b). The displacements of these specimens at a specified load were as expected according to the ranking of the stiffness and yield values. At approximately 4.0 kN, the displacement of the most stiff specimen, S3T10, was 1.75 mm whilst the displacement of the second least stiff specimen, S4T13, was the highest of the set at 2.6 mm (Figure 3.1). This indicated that the toe region was similar for all specimens regardless of stiffness. It is likely that a specimen with a more severe fracture would undergo a greater displacement for a given load than a specimen with a less traumatic fracture. Images of the S4T13 and S3T10 endplates taken prior to loading are presented in Figure 3.3.

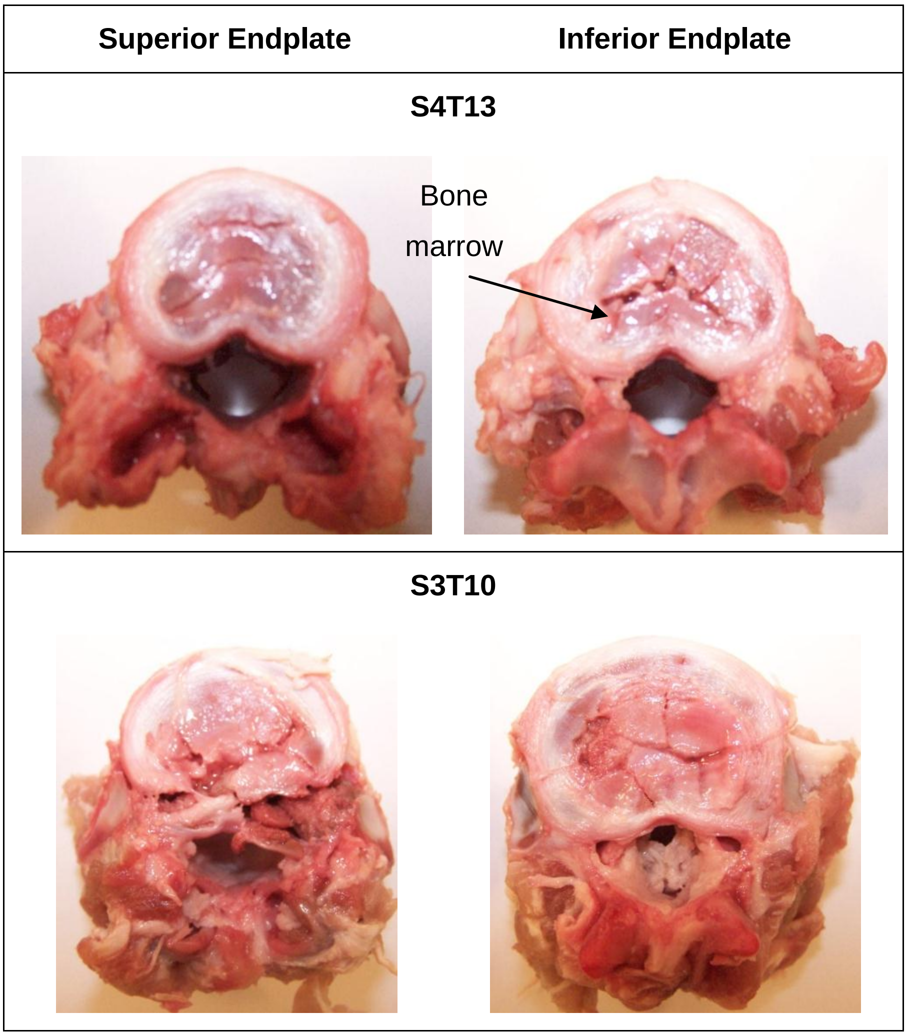

Figure 3.3 The endplates of S4T13 and S3T10 which possessed the greatest and least respective displacements of the single cycle set at 4 kN.

The superior endplate of S4T13 had merely sustained a hairline fracture whilst the inferior endplate displayed the characteristic wedge shaped bony fragment of a burst fracture (Denis 1983). The endplates of S3T10 appeared shattered in contrast to the endplates of S4T13. In addition to the variation in fracture pattern, expelled bone marrow could be seen on the inferior endplate of S4T13 which suggested that the fracture was of a greater depth, and hence severity, than that of S3T10. From these observations, it may be hypothesised that a larger displacement at 4 kN is a consequence of a more traumatic fracture. However, as the single cycle loading specimens were not graded, it was not possible to assess whether or not there was a trend between fracture severity, displacement and stiffness.

Whilst there were some limitations to this study, the fact that all specimens exhibited a linear load-displacement behaviour over a range of values enabled the post-fracture behaviour to be quantified and provided a method of comparison with the FE models presented in the next chapter.

3.3 Multi-Cycle Loading Set

Three groups of specimens were subjected to multi-cycle loading as described in Section 2.5.6; a control group consisting of nine non-augmented specimens, seven PMMA augmented specimens and six CaP augmented specimens. These groups will be referred to as NONE, PMMA and CaP in the following sections which give more information on the results obtained from each respective group.

3.3.1 Non-Augmented Group

The fracture grading results for the non-augmented group are presented in the following subsection, followed by the load-displacement curves of each specimen, the stiffness values and a selection of pre- and post-loading reconstructed µCT images.

Grading

All of the specimens were graded three times over a three day period (Section 2.5.4) and the mean taken as an indication of the severity of the fracture. An ideal burst fracture would have had a fracture grade of eight due to the nature of the retropulsed bony fragment (Section 2.5.4). The mean fracture grades, including standard deviations, for the non-augmented specimens are shown in Figure 3.4.

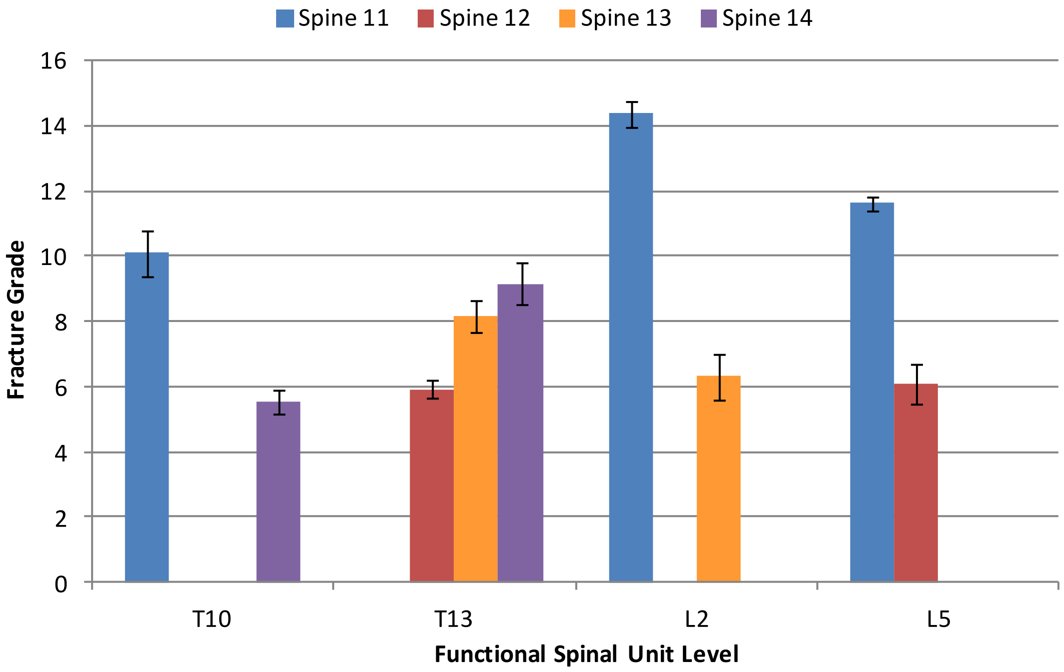

Figure 3.4 The mean fracture grade of the non-augmented multi-cycle specimens. The error bars represent the standard deviation of the three measurements.

The specimen with the greatest fracture severity grade was S11L2. Five of the nine specimens had a grade greater eight which indicated that those fractures may be more traumatic than a burst fracture.

The mean fracture grade of the anterior, middle and posterior columns was compared to the fracture grade for each specimen and the results are shown in Figure 3.5.

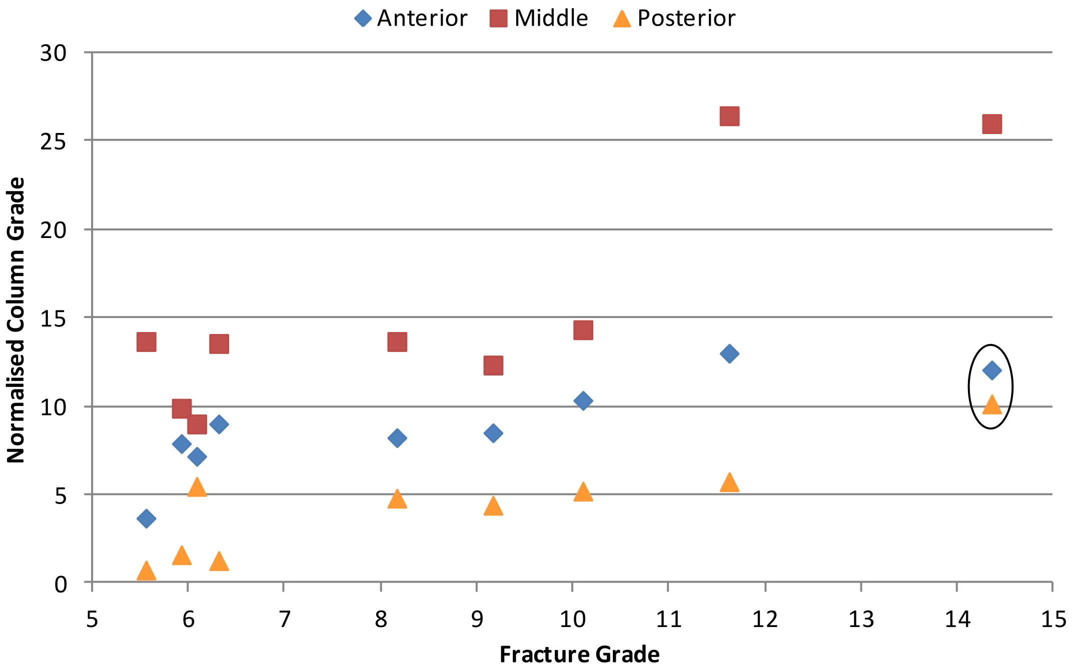

Figure 3.5 The mean fracture grade for each column of the non-augmented multi-cycle specimens. The circled specimen, S11L2, exhibited the lowest percentile increase from posterior to anterior column grade.

The figure illustrated that the grade of the middle column of each specimen was greater than the anterior or posterior column grades which is typical of a burst fracture (Panjabi *et al.* 1995). The outlier of the group was S11L2 because the anterior column grade was only 20% greater than the posterior which was the lowest percentage increase from posterior to anterior column grade across the set, although the posterior area of the specimen may not have been subjected to the same level of loading that was experienced by the anterior column. The difference between the middle column grade and the anterior grade was similar for S11L2 and S11L5 which has the second greatest fracture grade of the set at 11.6.

Loading

Of the nine specimens from the NONE group, eight underwent the full multi-cycle loading regime whilst one failed on the penultimate cycle. The specimen that failed, S11L2, displayed the greatest overall deformation. The load-displacement curves for the non-augmented specimens can be seen in Figure 3.6. The raw data from the pre-load was not collected therefore it was not possible to plot the 0 – 1 kN region of each load-displacement curve.

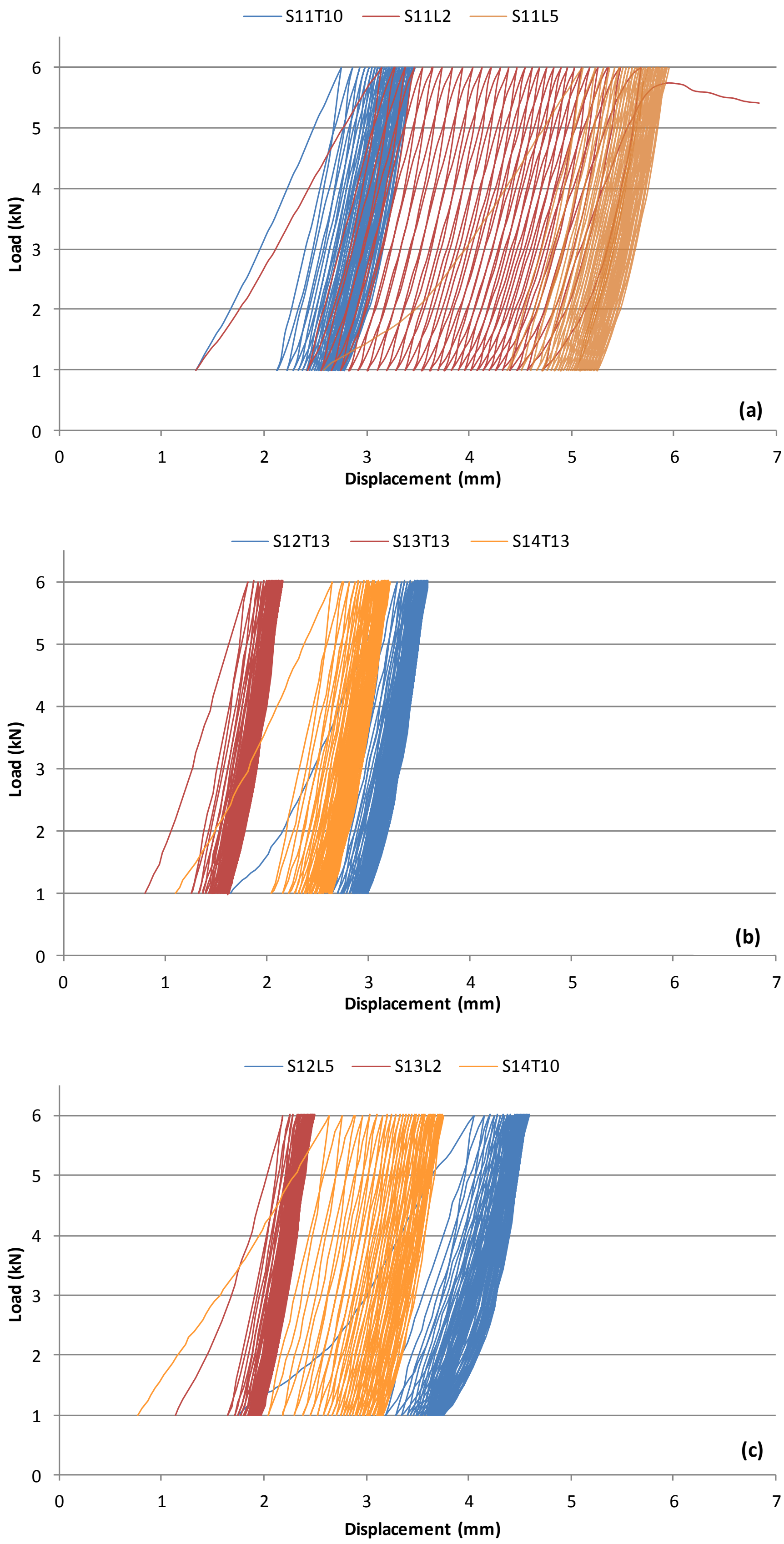

Figure 3.6 Load-displacement curves for the non-augmented multi-cycle specimens (a) S11T10, S11L2 and S11L5, (b) S12T13, S13T13 and S14T13 and (c) S12L5, S13L2 and S14T10.

In all instances, the fracture had stabilised as the load approached 2 kN except for S12L5 which did not exhibit linear behavior until approximately 2.5 kN (Figure 3.6c). There was a larger amount of plastic deformation in the initial load-displacement curve of each specimen. The additional plastic deformation was seen to gradually reduce for each subsequent loading cycle.

Stiffness Values

The stiffness of each specimen during the initial loading cycle was taken as the greatest gradient in the most linear region of each load-displacement curve; this was found to be within the 2 – 5 kN region. The stiffness value of each non-augmented specimen is presented in Figure 3.7.

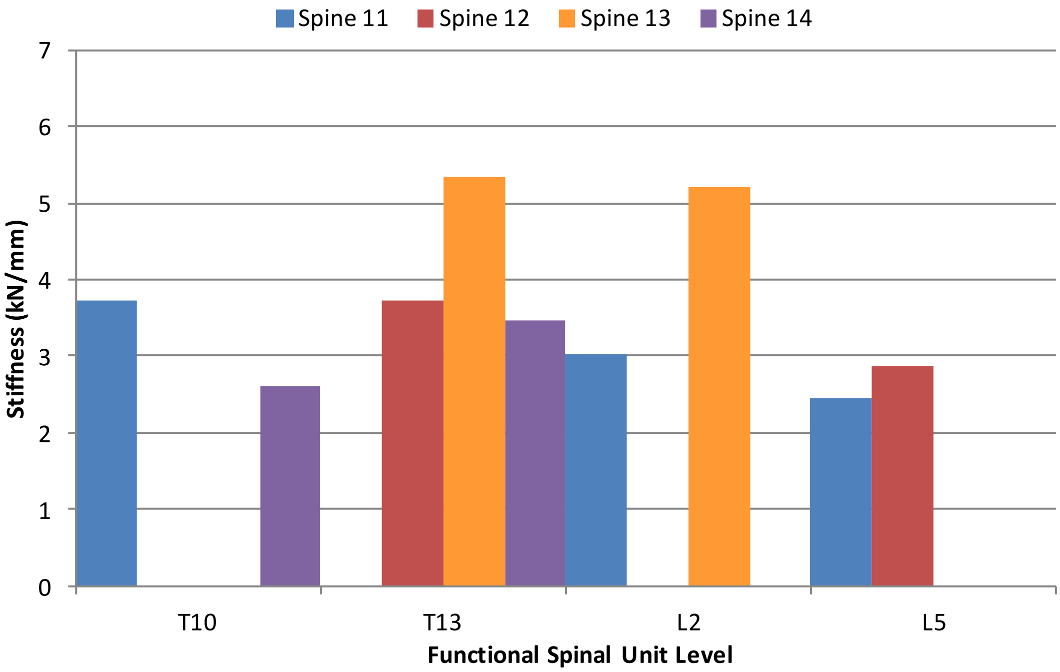

Figure 3.7 Stiffness values of the non-augmented multi-cycle specimens from the initial loading cycle.

There was a large variation in the stiffness values obtained with the greatest stiffness value (5.34 kN/mm) being twice that of the lowest stiffness value (2.46 kN/mm).

Post-Loading Imaging

Reconstructed µCT images of the S11L2 specimen prior to, and following, multi-cycle loading are shown in Figure 3.8. Of the non-augmented group, the S11L2 specimen had the highest fracture severity grade (Figure 3.4) and underwent the greatest overall displacement during loading (Figure 3.6)

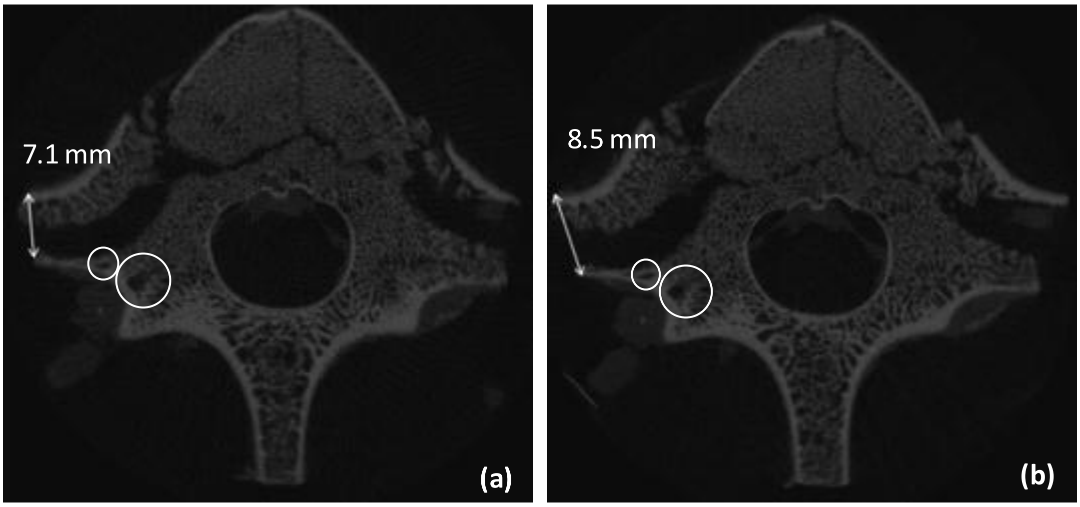

Figure 3.8 A non-augmented multi-cycle specimen, S11L2, (a) pre- and (b) post-loading. The circled regions represent distinguishable features.

The distinguishable features were used as reference points to ensure that the selected pre- and post-loading images corresponded to similar transverse levels. However, due to the differences in the alignment of the specimen in the container during each of the imaging sessions, it was not possible to locate consistent reference points across the entire width of the vertebral body.

The pre- and post-loading images show that a wedge of detached bone was further expelled from the vertebral body during loading (Figure 3.8). The distance from the most anterior truncated edge of this fragment to the corresponding truncated transverse process increased by approximately 1.4 mm during loading.

3.3.2 Polymethylmethacrylate Augmented Group

Similar to the non-augmented group, the results of the fracture gradings for the PMMA augmented group, in conjunction with the load-displacement curve of each specimen and the stiffness values are presented in the following subsections. In addition to these results, the injectability of each specimen is given as a percentage of the total fracture volume.

Grading

The specimens were graded three times (Section 2.5.4) and the mean taken as an indication of the severity of the fracture. The mean fracture grades, including standard deviations, for the PMMA-augmented group are presented in Figure 3.9.

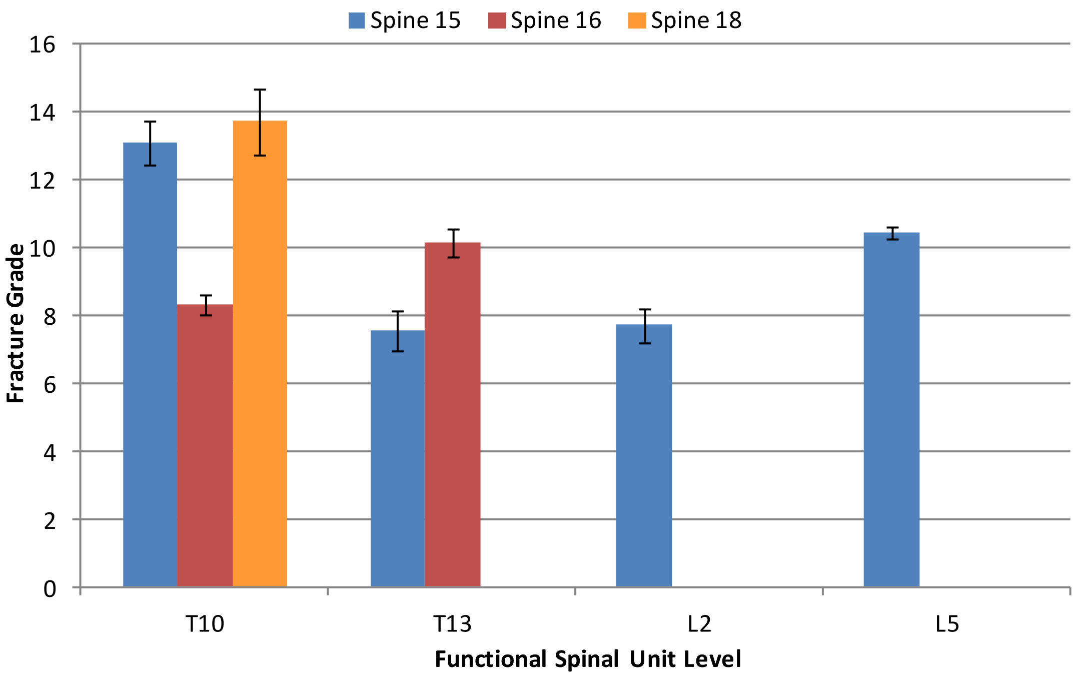

Figure 3.9 The mean fracture grade of PMMA augmented multi-cycle specimens. The error bars represent the standard deviation of the three measurements.

The specimen with the most severe fracture was S18T10. Five of the seven specimens had a fracture grade greater than eight which is that of an ideal burst fracture (Section 2.5.4).

The mean fracture grade of each of the anterior, middle and posterior columns is shown plotted against fracture grade for every specimen in Figure 3.10.

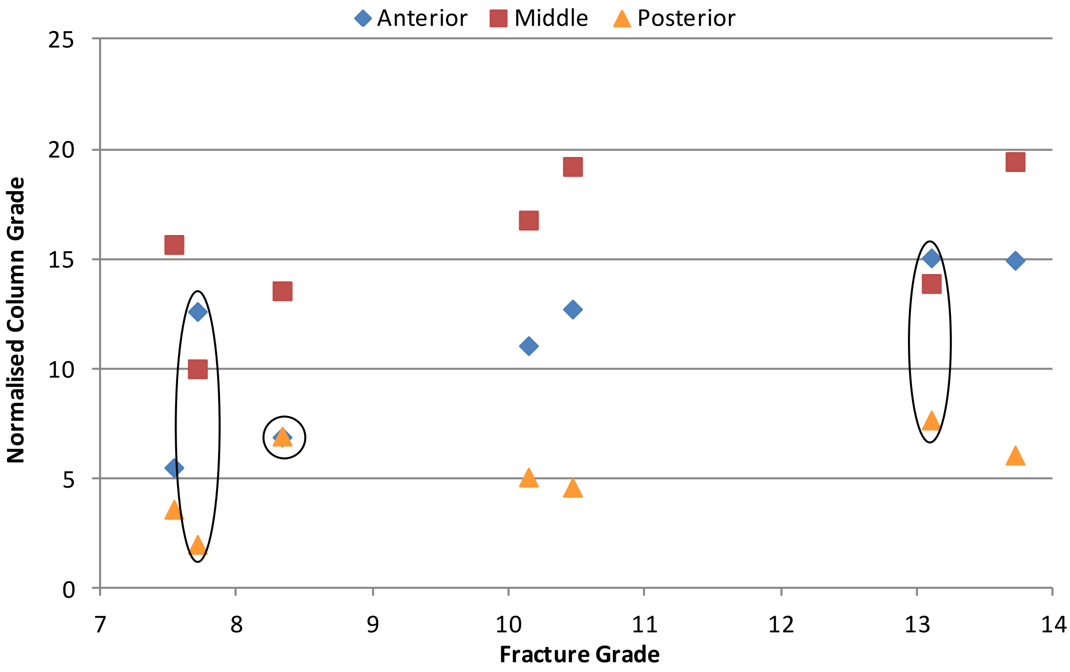

Figure 3.10 The mean fracture grade for each column of the PMMA augmented multi-cycle specimens. The circled specimens with a grade of 7.7 and 13.1 (S15T10 and S15L2), represent specimens where the anterior column grade was greater than the middle column grade. The circled specimen with a grade of 8.3 (S16T10), possessed the smallest percentile increase from posterior to anterior grade.

This figure illustrated that for five of the seven specimens, the mean middle column grade of each specimen was greater than that of the anterior or posterior columns. However, for two specimens, S15L2 and S15T10, the anterior column grade was greater than that of the middle column. In addition to these anomalies, the specimen S16T10 with a fracture grade of 8.3 was unusual because it had the smallest percentile increase in posterior to anterior column grade.

Injectability

The level of injectability of each of the augmented specimens was obtained as described in Section 2.5.5. The percentage of total fracture volume successfully augmented with PMMA for each specimen is shown in Figure 3.11.

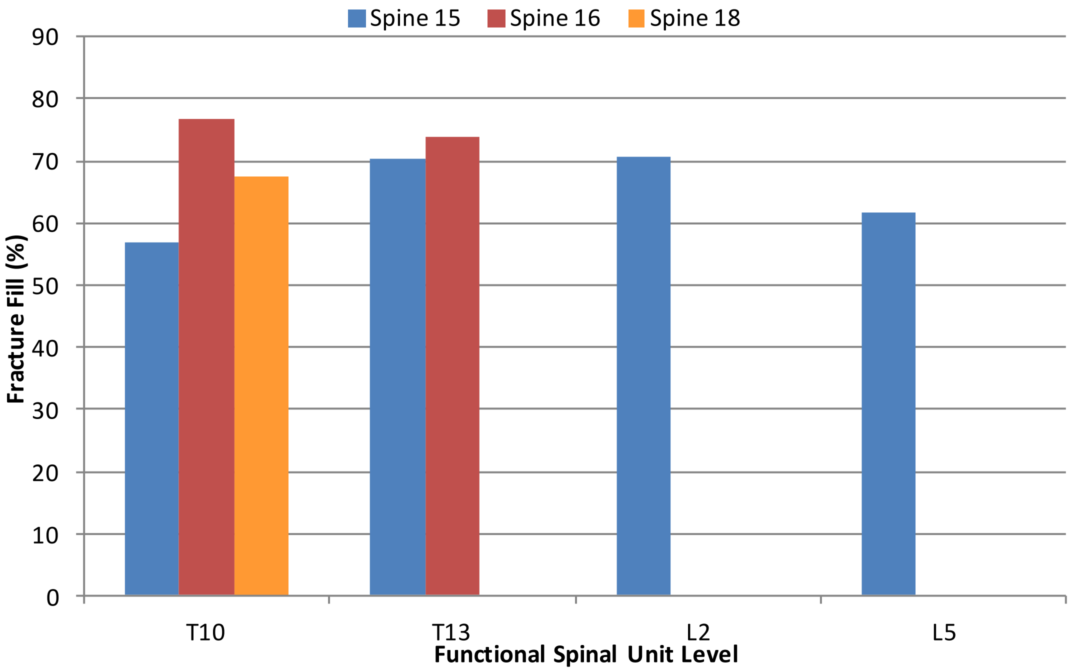

Figure 3.11 Percentage of total fracture volume successfully injected for the PMMA augmented multi-cycle specimens.

The minimum fracture volume that was augmented with PMMA was 57% (S15T10) whilst the most successful augmentation was that of S16T10 with 77% of the fracture volume augmented.

Loading

Three of the seven specimens in the PMMA group successfully underwent the multi-cycle loading. The remaining four were seen to yield within the 4 – 6 kN region. The load-displacement curves of the specimens are presented in Figure 3.12.

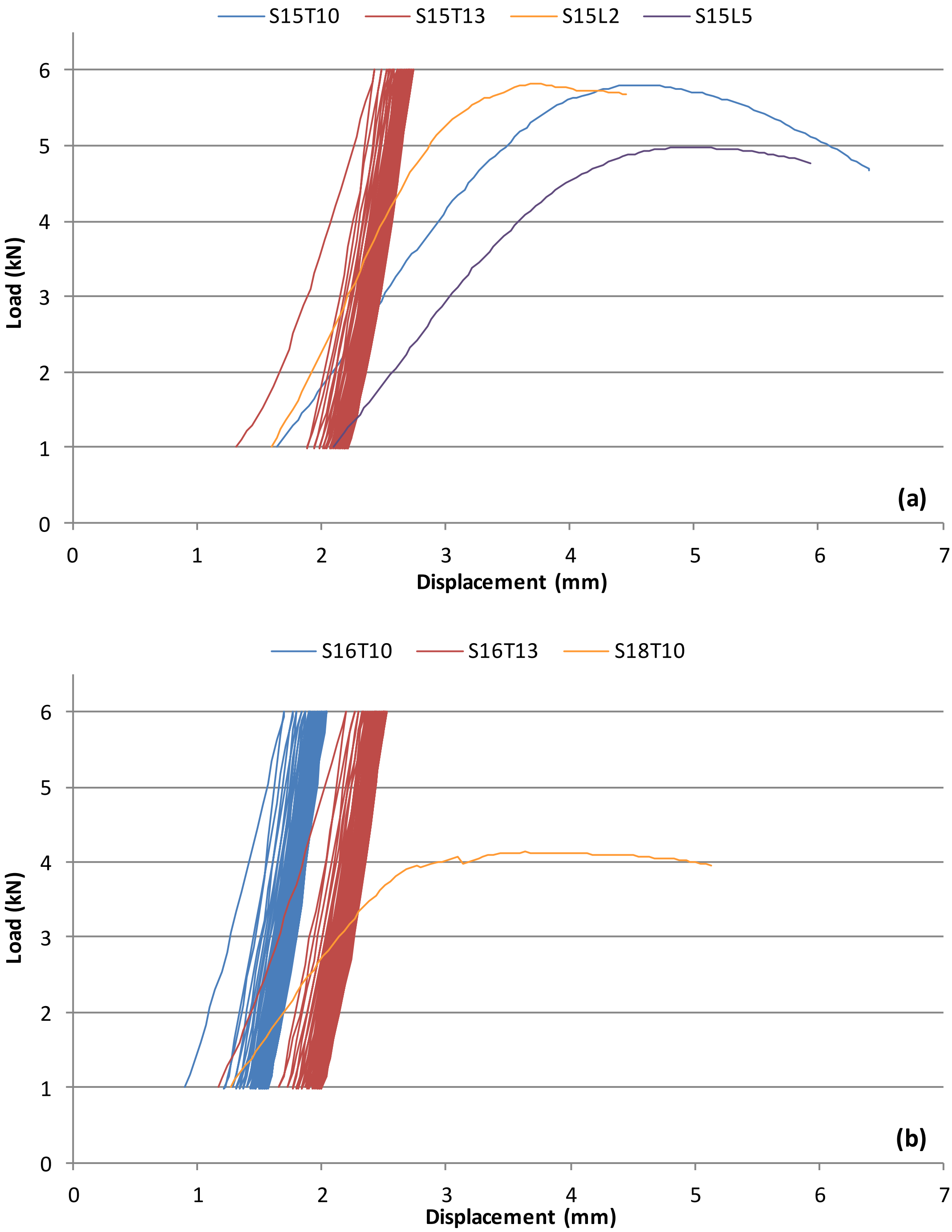

Figure 3.12 Load-displacement curves for the PMMA augmented multi-cycle specimens (a) S15T10, S15T13, S15L2 and S15L5 and (b) S16T10, S16T13 and S18T10.

The fracture of each specimen was stabilised as the load approached 2 kN. In the cases where the specimens successfully underwent the multi-cycle loading, the greatest plastic deformation was observed during the first loading cycle. Less additional plastic deformation occurred in the subsequent cycles. There was no correlation between FSU level and the specimens that did not undergo the multi-cycle loading.

Stiffness Values

The stiffness value of each of the PMMA augmented specimens was taken as the greatest gradient in the most linear region of each of the initial load-displacement curves. The most linear region for five of the seven specimens was within the region of 2 – 5 kN. For the remaining two specimens, S15L5 and S18T10, the stiffness was taken from the 2 – 4 kN region due to the lower yield points.

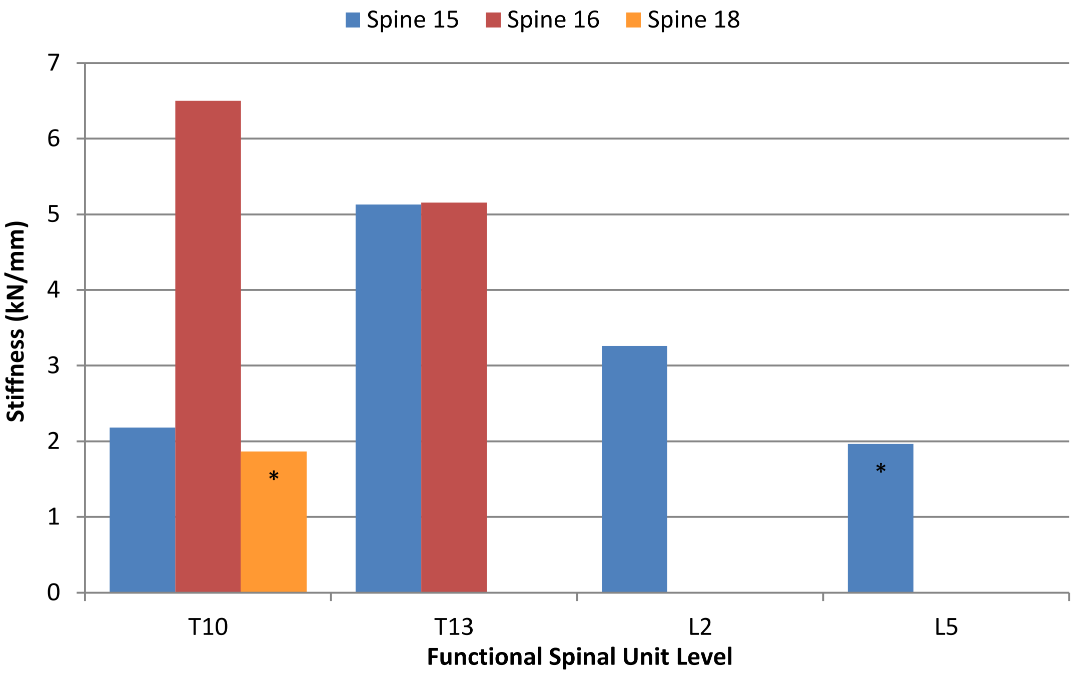

Figure 3.13 Stiffness values of the PMMA augmented multi-cycle specimens from the initial loading cycle. Note * indicates stiffness taken from 2 – 4 kN.

There was a high variation within the stiffness values of the group. The greatest stiffness value at 6.50 kN/mm (S16T10) was over three times greater than that of the minimum stiffness value of 1.87 kN/mm (S18T10).

Post-Loading Imaging

The specimen from the PMMA augmented group with the greatest fracture severity grade was S18T10. Images of S18T10 prior to, and following, the multi-cycle loading are shown in Figure 3.14.

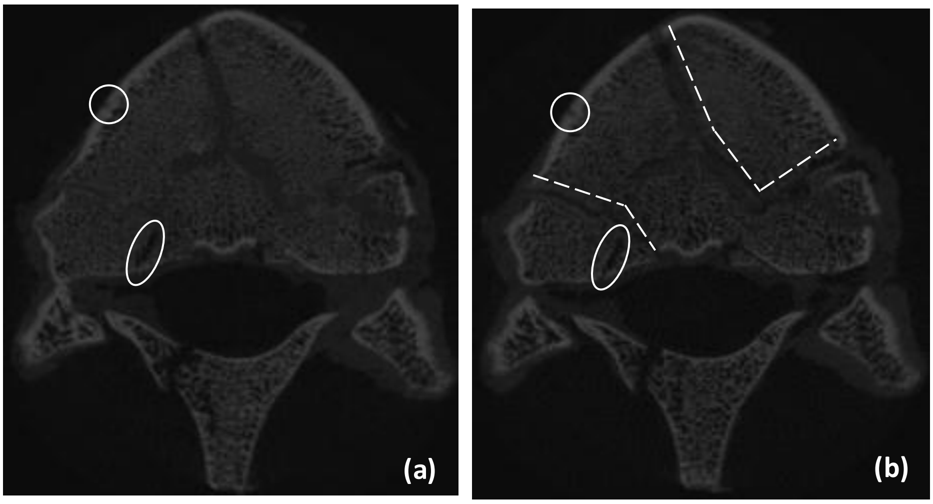

Figure 3.14 A PMMA augmented multi-cycle specimen, S18T10, (a) pre- and (b) post-loading. The circled regions represent distinguishable features and the dashed lines highlight the bone-cement interface.

The circles on the images are reference points that were used to ensure that the images were from the same transverse level. Situated below the dashed lines are regions within the vertebral body where the PMMA and bone interlock failed as a result of the multi-cycle loading.

3.3.3 Calcium Phosphate Augmented Group

The results from the CaP augmented specimens are presented in the following subsections in the same manner as the PMMA augmented specimens were presented. The fracture grade of each specimen is given, followed by the injectability, the load-displacement curves, the stiffness values and a selection of pre- and post-loading images.

Grading

The specimens were graded three times as described in Section 2.5.4 and the mean taken as an indication of the severity of the fracture. The mean fracture grades, including standard deviations, of the CaP augmented specimens are shown in Figure 3.15.

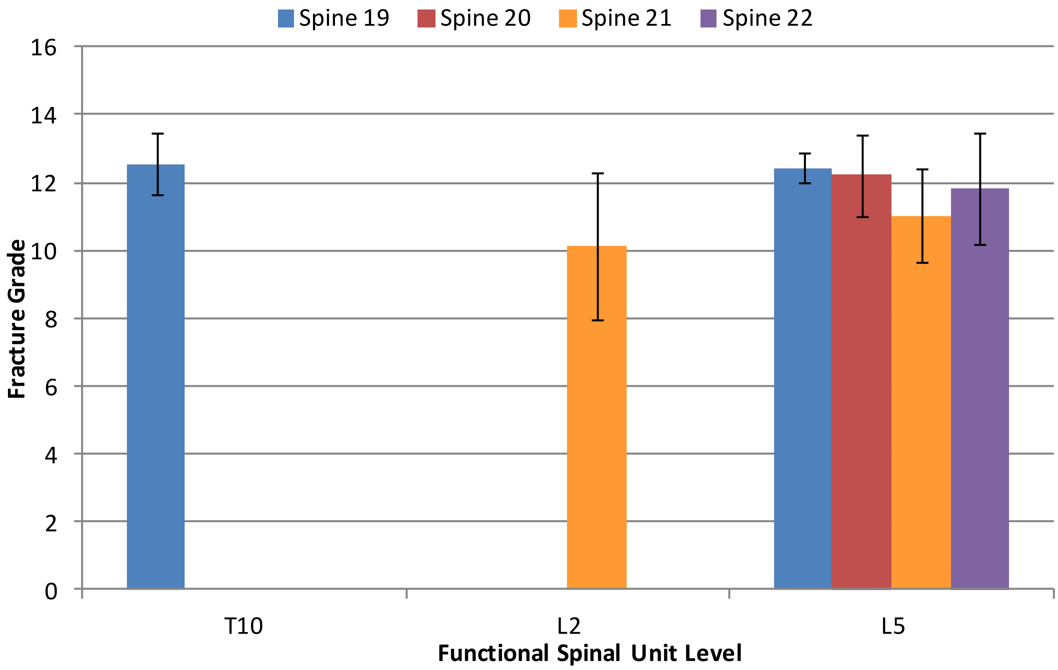

Figure 3.15 The mean fracture grade of the CaP augmented multi-cycle specimens. The error bars represent the standard deviation of the three measurements. Note there were no T13 specimens in the set.

It is likely that each of the specimens were more traumatically fractured than an ideal burst fracture because they all had a fracture severity grade greater than eight (Section 2.5.4). The grades of the CaP augmented specimens fell within a more narrow range (10.1 – 12.5) than that of the non-augmented specimens (5.6 – 14.4) and the PMMA augmented specimens (7.5 – 13.7).

The mean fracture grade of each of the anterior, middle and posterior columns is shown plotted against fracture grade for every specimen in Figure 3.16. The middle column grade was found to be the greatest of the three columns for all of the specimens.

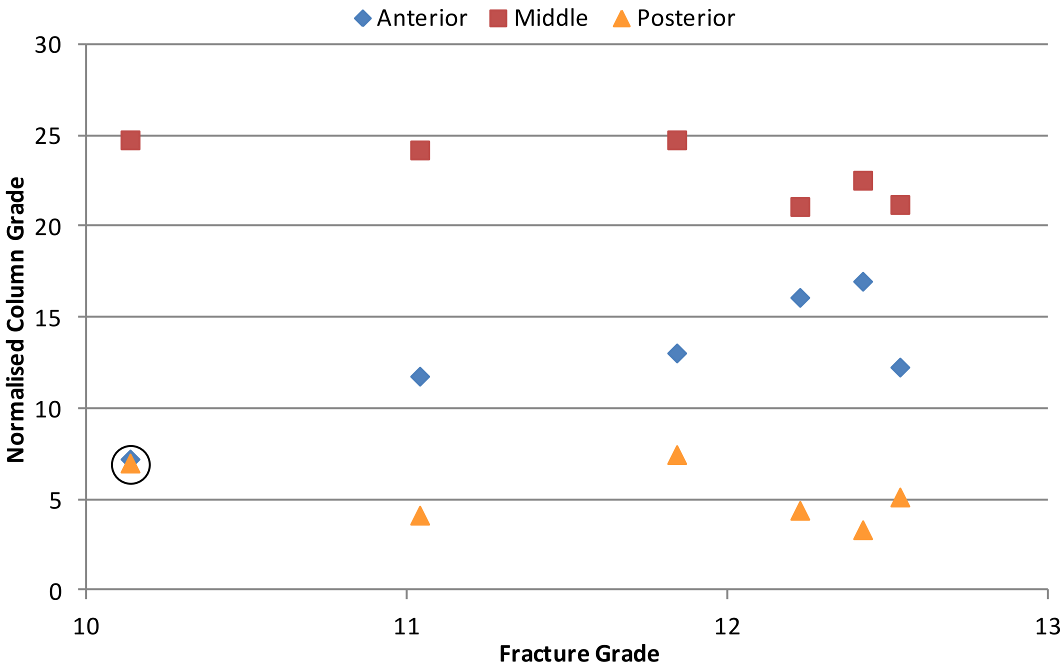

Figure 3.16 The mean fracture grade for each column of the CaP augmented multi-cycle specimens. The circled specimen, S21L2, had a similar anterior and posterior column grade.

This figure illustrated that the mean fracture grade of the anterior column was much greater than that of the posterior column grade for each specimen except for S21L2 (mean fracture grade of 10.1). For this specimen, the anterior column grade was approximately equal to the posterior column grade although the posterior area of the specimen may not have been subjected to the same level of loading that was experienced by the anterior column.

Injectability

The amount of CaP injected, as a percentage of the total fracture volume, was obtained as described in Section 2.5.5. The percentage of fracture volume filled with CaP cement is shown in Figure 3.17.

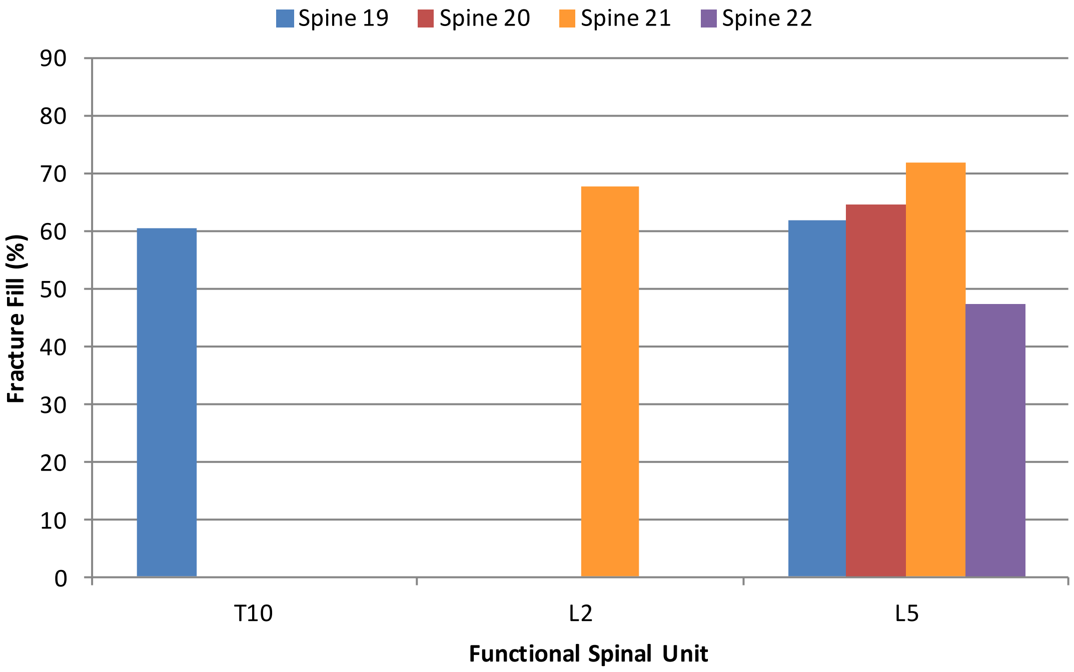

Figure 3.17 Percentage of total fracture volume successfully injected for the CaP augmented multi-cycle specimens.

The amount of fracture volume augmented ranged from 47 – 71% however, the percentage of fill cannot be taken as a direct indication of the success of an augmentation. Shown in Figure 3.18 are the inferior endplates of two specimens, S20L5 and S21L2, pre- and post-augmentation. The respective fracture fill obtained for these specimens was similar at 65% and 68%.

Pre-Augmentation **Post-Augmentation**

S20L5 (65% fracture fill)

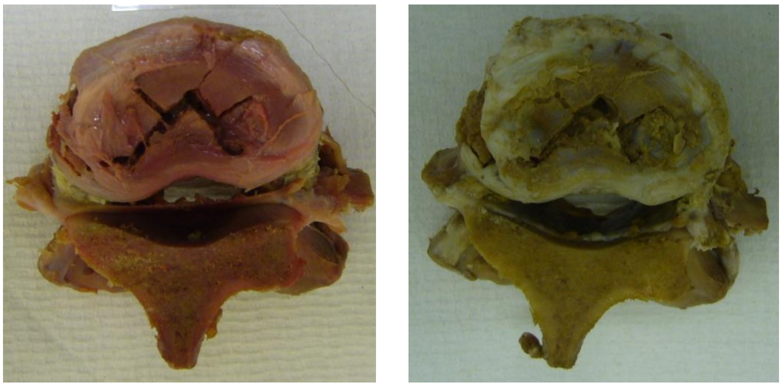

S21L2 (68% fracture fill)

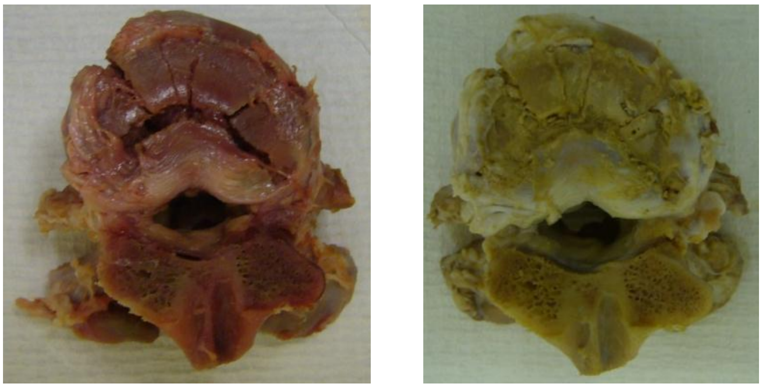

Figure 3.18 The inferior endplates of two CaP augmented multi-cycle specimens with similar levels of injectability shown pre- and post-augmentation.

The images show that although these specimens had similar values of fracture fill, the inferior endplate of S20L5 remained remarkably void of cement in contrast to S21L2 where the cement was seen to protrude from the inferior endplate.

Loading

Of the six specimens augmented with CaP, only one underwent the multi-cycle loading whilst the others were seen to yield between 2 – 5 kN. The load-displacement curves for the CaP augmented specimens are shown in Figure 3.19.

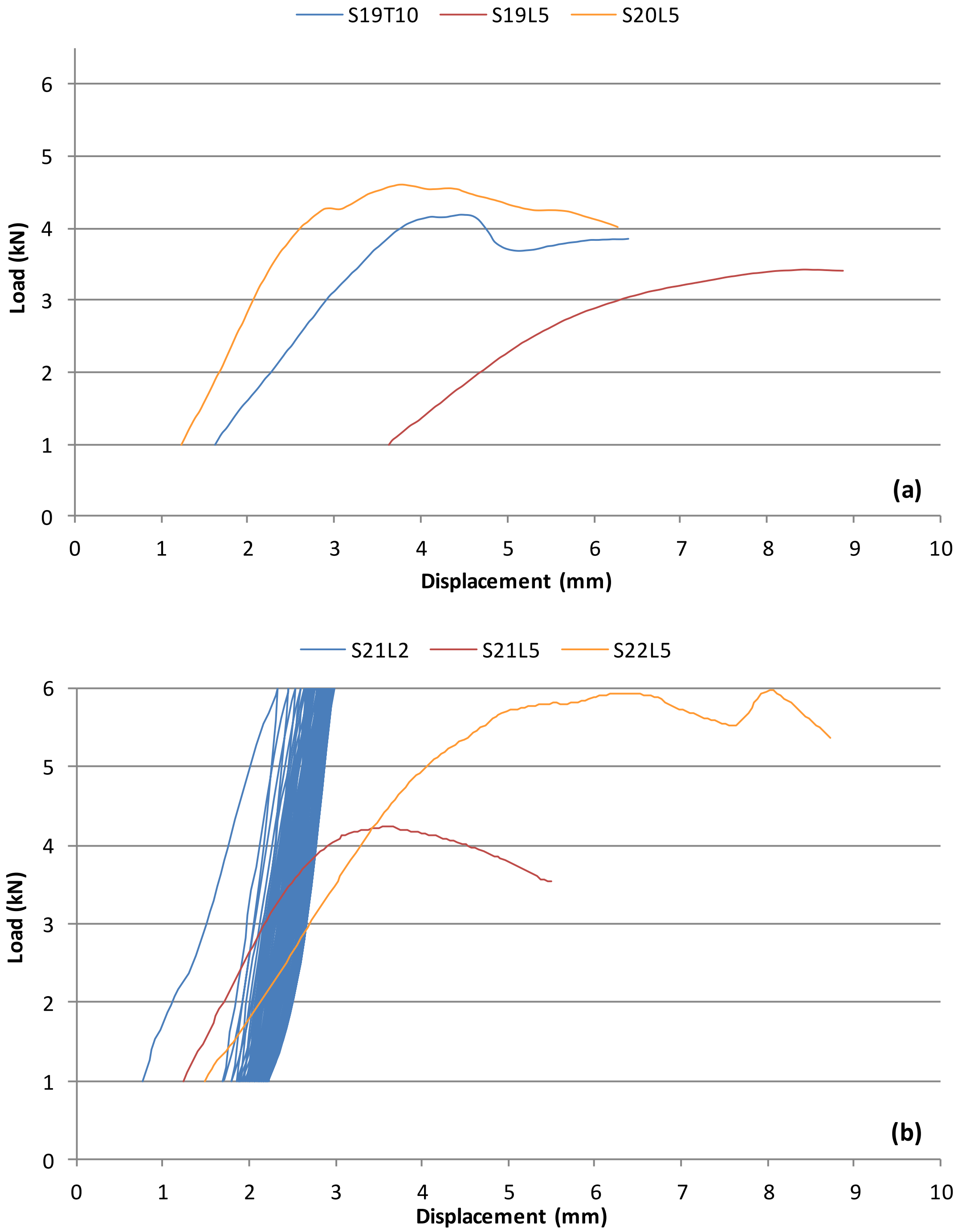

Figure 3.19 Load-displacement curves of the CaP augmented multi-cycle specimens (a) S19T10, S19L5 and S20L5 and (b) S21L2, S21L5 and S22L5.

Similar to the non- and PMMA augmented specimens, the fractured regions of five of the six CaP specimens had stabilised as the load approached 2 kN. The only specimen where the fracture had not stabilised at 2 kN was S21L2; there was a momentarily non-linear displacement at approximately 2.2 kN (Figure 3.19b). This specimen, S21L2, was the only specimen to undergo the entire multi-cycle loading regime during which a larger amount of plastic deformation was observed in the initial loading cycle. The amount of additional plastic deformation per cycle decreased gradually throughout the test.

Stiffness

The stiffness of each specimen was taken as the greatest gradient of the most linear region on the load-displacement curves. For the CaP augmented group, three different linear regions were selected from which the stiffness of each specimen was taken. For S21L2 and S22L5, this was within the region of 2 – 5 kN however, for S19L5, the most linear region was within the region of 1 – 2.5 kN due to the lower yield point. The most linear region for the remaining specimens was seen to be within the region of 2 – 4 kN.

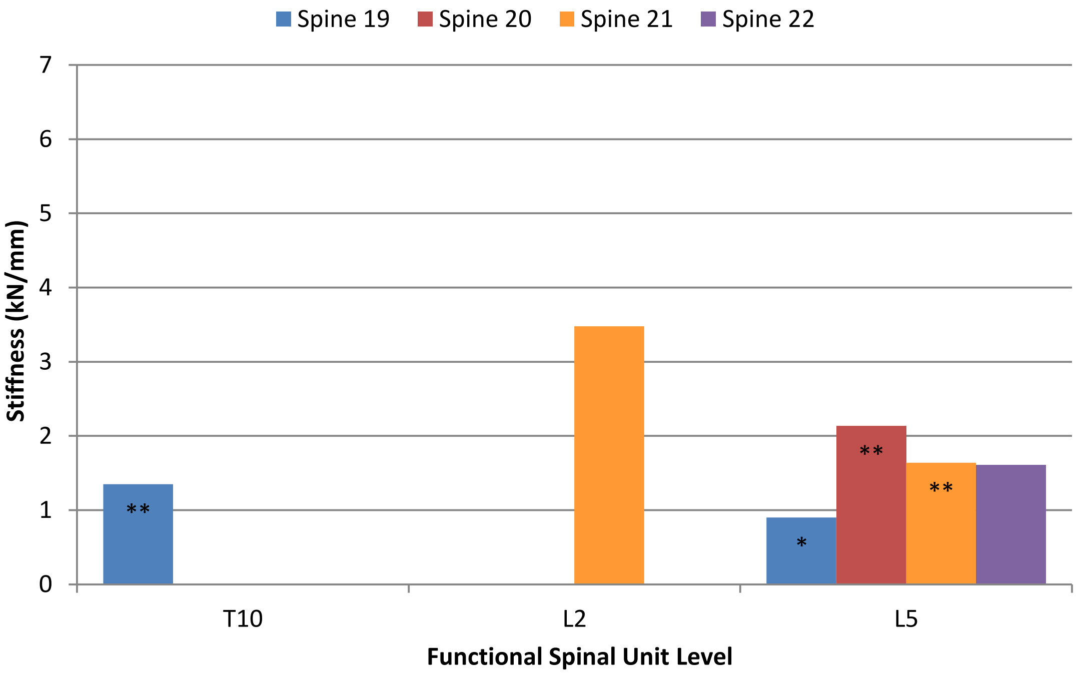

Figure 3.20 Stiffness values of the CaP augmented multi-cycle specimens from the initial loading cycle. Note * indicates stiffness taken from 1 – 2.5 kN and ** indicates stiffness taken from 2 – 4 kN.

Of the five CaP augmented specimens that did not undergo the multi-cycle loading, there was a broad range of stiffness values (0.90 – 2.14 kN/mm). Of the entire CaP set, the greatest stiffness value was that of S21L2 (3.48 kN/mm) which was the only CaP augmented specimen to withstand the multi-cycle loading.

Post-Loading Imaging

The specimens (S20L5 and S21L2) that had a similar calculated percentage of fracture volume augmentation (Figure 3.17), but different visible levels of endplate augmentation (Figure 3.18), are shown pre- and post-loading in Figure 3.21. The images were obtained as described in Section 3.3.1. Reference points were used to ensure that the pre- and post-loading images were taken from a similar transverse level.

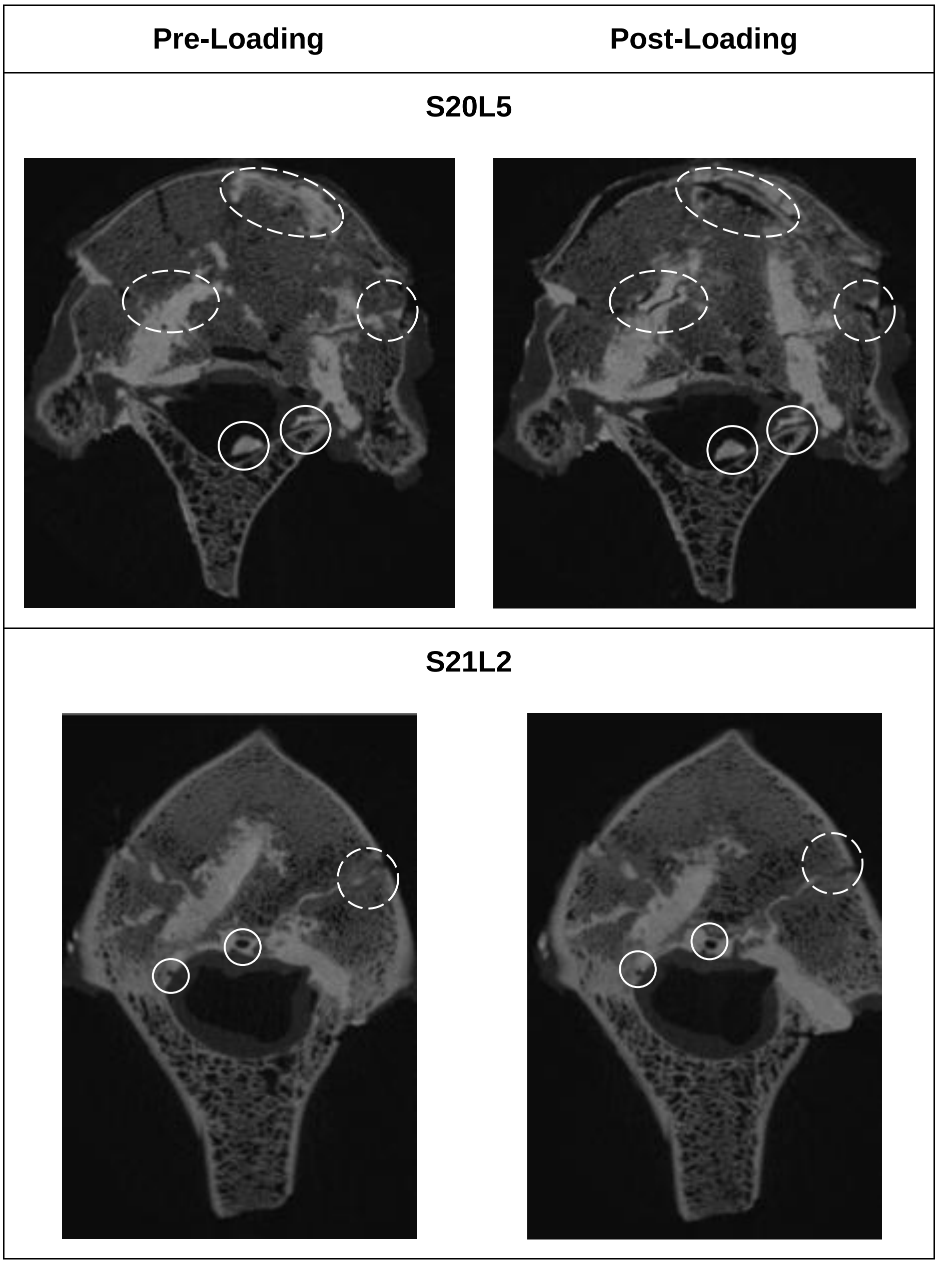

Figure 3.21 A transverse view of two CaP augmented multi-cycle specimens with similar levels of injectability shown pre- and post-loading. The solid circles are reference points whilst the dashed circles highlight areas where the CaP cement fractured during loading.

Areas where the cement had either fractured or been pushed away from the bone during loading are highlighted on the images. The post loading images showed that during loading, the cement within S20L5 developed more fractures than S21L2; S21L2 was the only CaP augmented specimen to withstand the multi-cycle loading.

3.3.4 Discussion

For the basis of this discussion, the non-augmented specimen which failed on the penultimate cycle has been assumed to have been successful because all of the failed augmented specimens did so on the initial cycle. Of the 22 specimens subjected multi-cycle loading, nine failed; four were augmented with PMMA whilst five were augmented with CaP. The failure of the augmented specimens suggested that vertebroplasty was not successful in the repair of burst fractures because the post-augmentation stiffness was not restored to the levels observed with the non-augmented specimens and the augmented specimens were generally unable to withstand 30 cycles of loading. However, there are a number of parameters which may explain why a greater prevalence of failure was observed in the augmented specimens. These parameters are discussed in this section with respect to the fracture gradings, the level of injectability, the loading and also the stiffness values.

Specimens that underwent the multi-cycle loading without failure are referred to in the following subsection as ‘successful’, whilst those that did not as ‘unsuccessful’.

Grading

Each specimen in the unsuccessful CaP group had a fracture grade that was greater, and hence more severe and less stable, than the eight of an ideal burst fracture (Figure 3.15). The mean fracture grade for the NONE, PMMA and CaP groups increased respectively from 8.6 to 10.1 and 11.7 (Figure 3.22) and this increase was relative to the increase in the incidence of unsuccessful specimens within the groups.

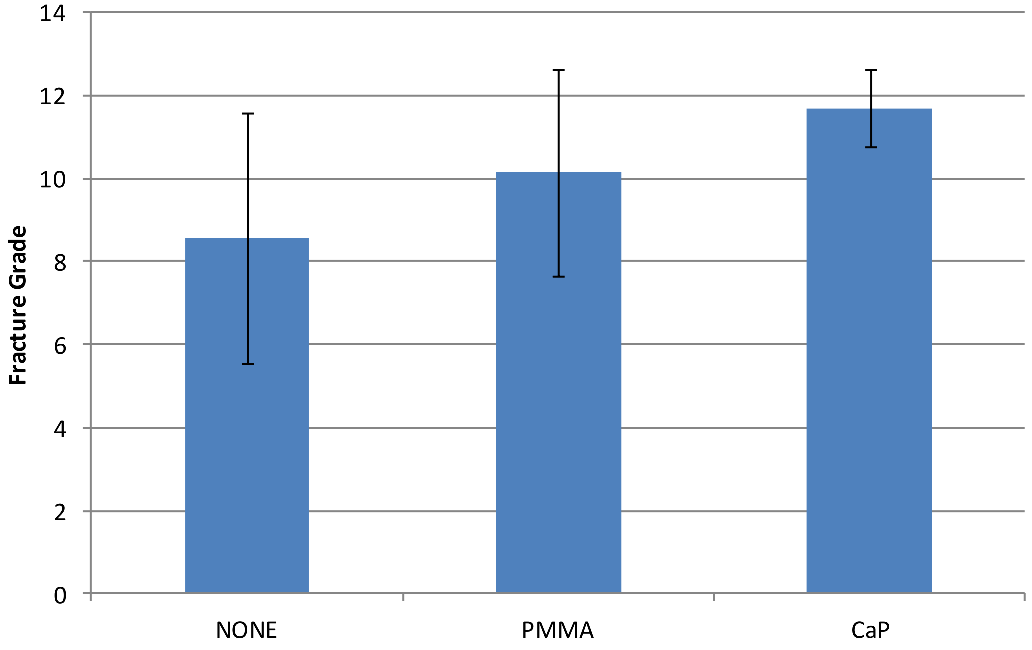

Figure 3.22 Mean fracture grade, including the standard deviation, for each group of the multi-cycle loading set.

The increase in fracture grade across the groups suggested that the augmented specimens were more severely fractured than the non-augmented specimens which may explain why a greater number of augmented specimens were unsuccessful during the multi-cycle loading. It is possible that the holes reamed into the vertebrae for the delivery of cement increased the fracture grade and decreased the stability of the augmented specimens however; this was not the case for the successful augmented specimens.

Instability has been observed to correlate to a middle column grade that was greater than the anterior and the posterior column grades (Panjabi *et al.* 1995). A plot of the mean middle column grade against the anterior column grade is shown in Figure 3.23 for all of the multi-cycle specimens.

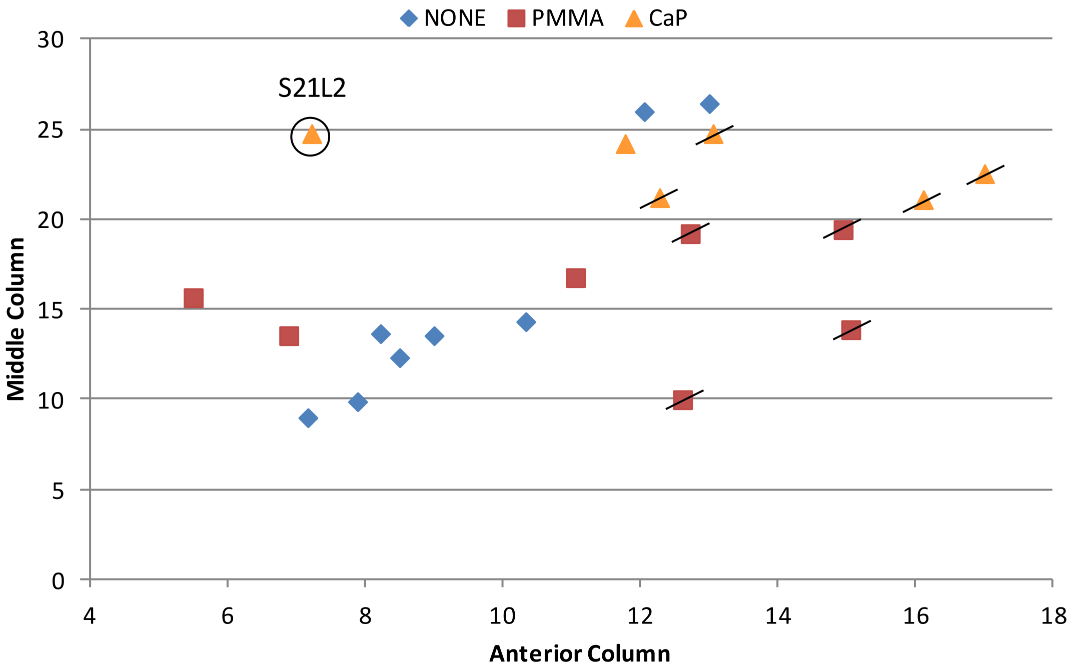

Figure 3.23 Plot of mean middle column grade against the mean anterior column for the multi-cycle loading set. The circled specimen, S21L2, was a successful outlier. The specimens with a diagonal line were unsuccessful. Note the non-zero X-axis starting position.

The general trend was that successful specimens, most of which were non-augmented, had lower anterior and middle column grades. However, the only successful CaP specimen, S21L2, did not follow the general trend. Because of the high middle column grade of this specimen, it may have been expected to fail (Panjabi *et al.* 1995). It is likely that the S21L2 specimen did not fail because the anterior and posterior grades were of a similar magnitude which may have led to a more uniform deformation, regardless of the instability of the middle column although the posterior area of the specimen may not have been subjected to the same level of loading that was experienced by the anterior column. Therefore, it is possible that the anterior grade may be a better indication of the ability of a specimen to undergo multi-cycle loading.

Injectability

A plot of the fracture grade against the amount of fracture volume filled with cement is shown in Figure 3.24.

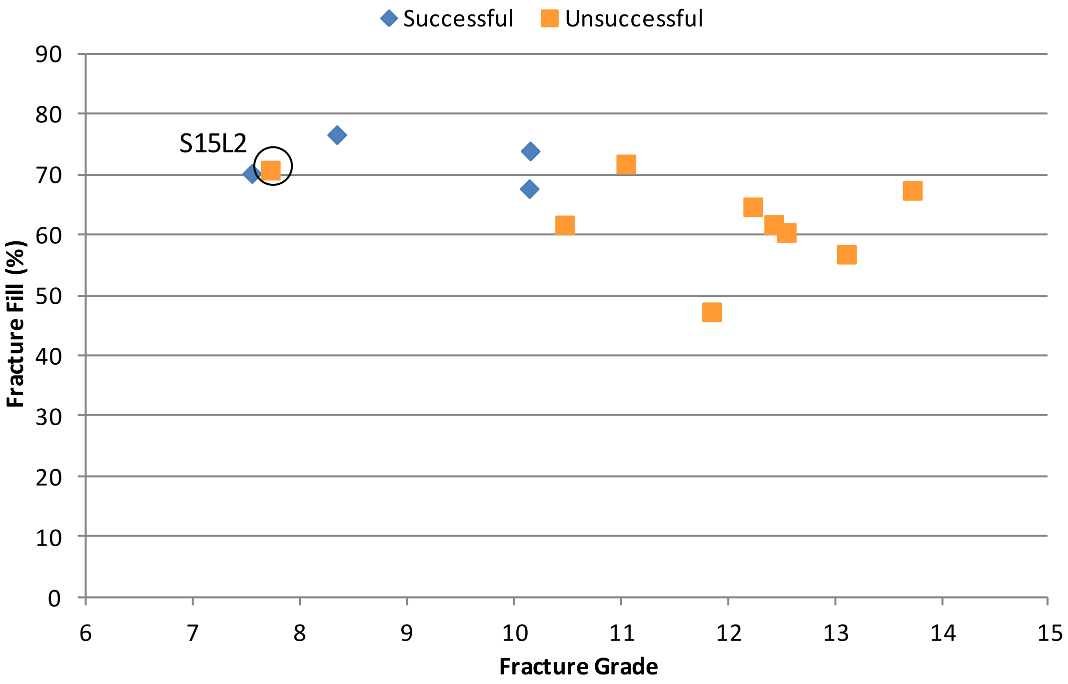

Figure 3.24 Plot of fracture grade and the amount of fracture filled with cement for the augmented multi-cycle specimens. The circled specimen, S15L2, was an outlier as it would have been expected to complete multi-cycle loading. Note the non-zero X-axis starting position.

The figure showed that the unsuccessful specimens, with a greater fracture grade, appeared to generally have a lower level of augmentation. The exception to this generalisation was the PMMA augmented specimen, S15L2, with a mean anterior column grade that was much greater than the middle column; this may have reduced the mechanical stability of a specimen that otherwise had a relatively low fracture grade and an implied stability (Figure 3.10).

It is possible that the fractures of the unsuccessful specimens were more dispersed in comparison to successful specimens and that this may have led to difficulties with cement infiltration. A visual inspection of the post-loading µCT images showed that a greater proportion of fracture remained non-augmented when the regions of fractures were disconnected. It appeared that the cement was less likely to penetrate intact trabecular bone in order to reach delocalised pockets of fracture. Therefore, the premature failure of the unsuccessful specimens may have been partly due to the non-augmentation of the dispersed, and more traumatic, fractures.

Loading

The parameters of interest from the results of the load-displacement curves, aside from the stiffness values, were the initial and final displacements of each specimen. For the unsuccessful specimens which failed on the first cycle, the initial displacements were capped at the values corresponding to the upper limit of the region where the stiffness was taken from (Section 3.3.1 - 3.3.3). Of the specimens that successfully underwent the multi-cycle loading, a trend was observed between the initial and final displacements, as shown in Figure 3.25.

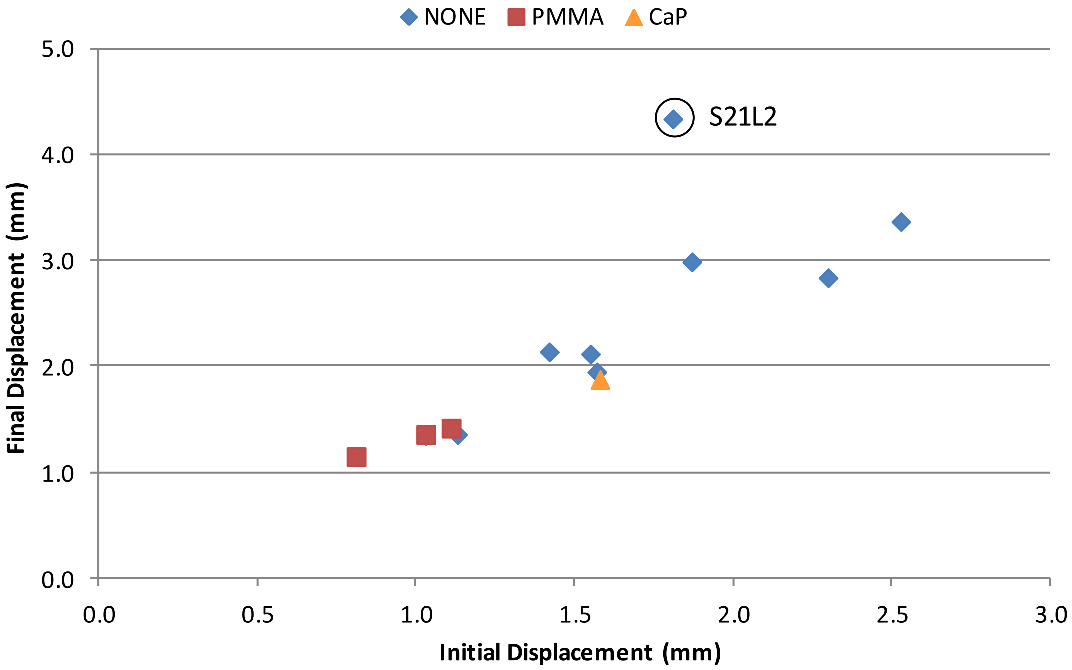

Figure 3.25 Trend between initial and final displacements of the specimens that underwent multi-cycle loading. The circled specimen, S21L2, was an outlier as it would have been expected to fail earlier than the 29th cycle.

The figure of the successful specimens illustrated that a lower initial displacement generally corresponded to a lower final displacement. The exception was the non-augmented specimen S11L2, which not only possessed the greatest fracture severity grade of the entire multi-loading set (Figure 3.4), but was also the only specimen to fail on the penultimate loading cycle (Figure 3.6). As mentioned earlier, the similarity in the grades of the anterior and posterior columns hay have increased the stability in this specimen.

A plot of the fracture grade against the initial displacements for both the successful and unsuccessful specimens is shown in Figure 3.26.

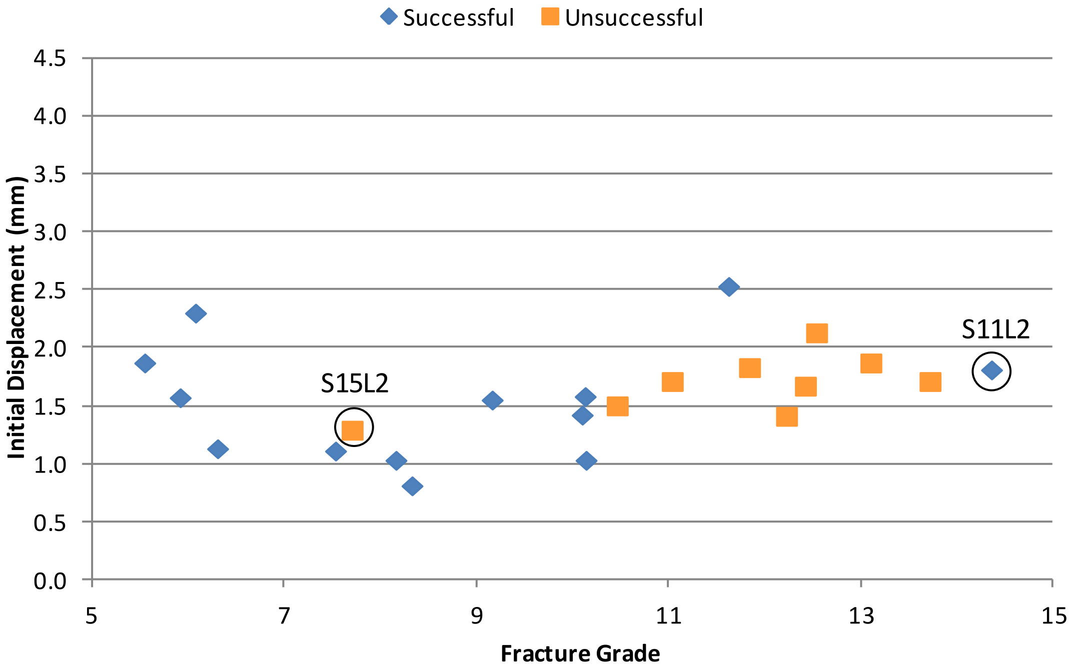

Figure 3.26 Plot of initial displacement against fracture grade for the multi-cycle loading set. The circled specimens, S15L2 and S11L2, were outliers as they would have been expected to have performed differently. Note the non-zero X-axis starting position.

There was no clear trend between the initial displacement and whether or not a specimen was successful; the range of initial displacements for the unsuccessful specimens fell within that of the successful specimens. The figure illustrated that more traumatic fractures did not undergo a greater initial displacement.

The discussion of the findings from the single cycle loading set led to the suggestion that unsuccessful specimens may have had a greater initial displacement (Section 3.2.3). However, the unsuccessful multi-cycle loading specimens highlight that this suggestion was not valid; unsuccessful specimens did not have a greater initial displacement that the successful specimens.

Stiffness Values

The respective mean stiffness values of the NONE, PMMA and CaP groups were 3.60, 3.72 and 1.81 kN/mm. The successful PMMA augmented specimens possessed stiffness values that were greater than the unsuccessful PMMA augmented specimens. Similarly, the only successful CaP specimen, S21L2, also possessed the greatest stiffness value of the CaP group. A plot of the stiffness values and the fracture grade for the successful and unsuccessful specimens is shown in Figure 3.27.

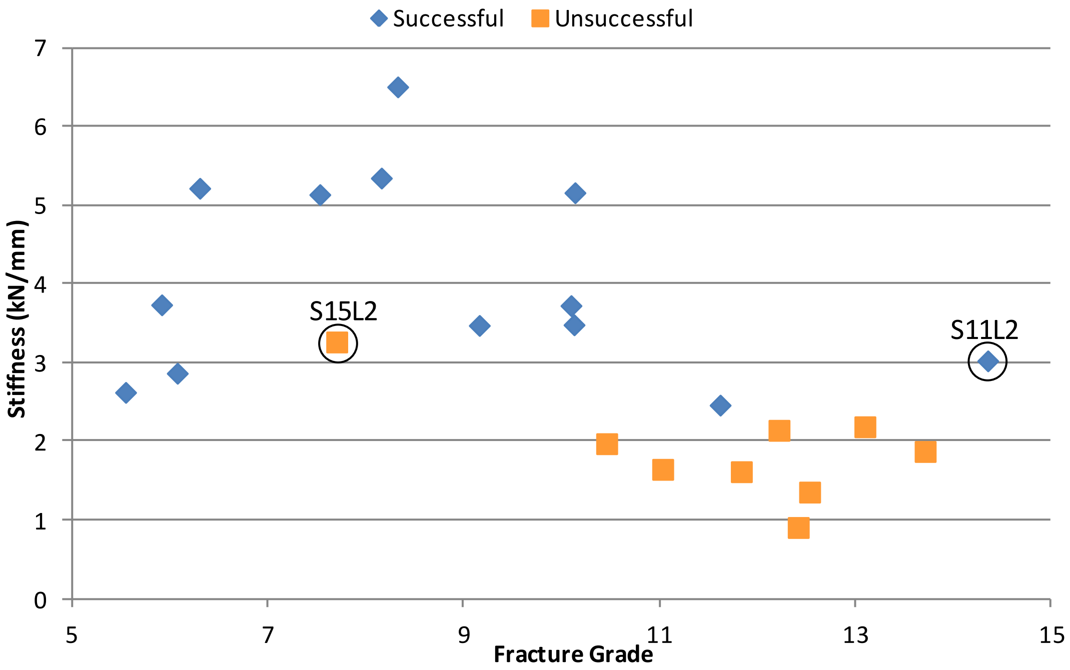

Figure 3.27 Plot of the stiffness values against the fracture grade for the multi-cycle loading set. The circled specimens, S15L2 and S11L2, were outliers as they would have been expected to have performed differently. Note the non-zero X-axis starting position.

The figure showed that the unsuccessful specimens generally possessed lower stiffness values and greater fracture grades than the successful specimens possibly due to the prevalence of more traumatic fractures within the unsuccessful specimens.

The change in the stiffness of each specimen throughout the 30 loading cycles is presented in Figure 3.28. The figure highlighted that for the majority of specimens, the stiffness generally increased throughout loading. An exception to this is the non-augmented specimen, S11L2, which failed on the penultimate loading cycle.

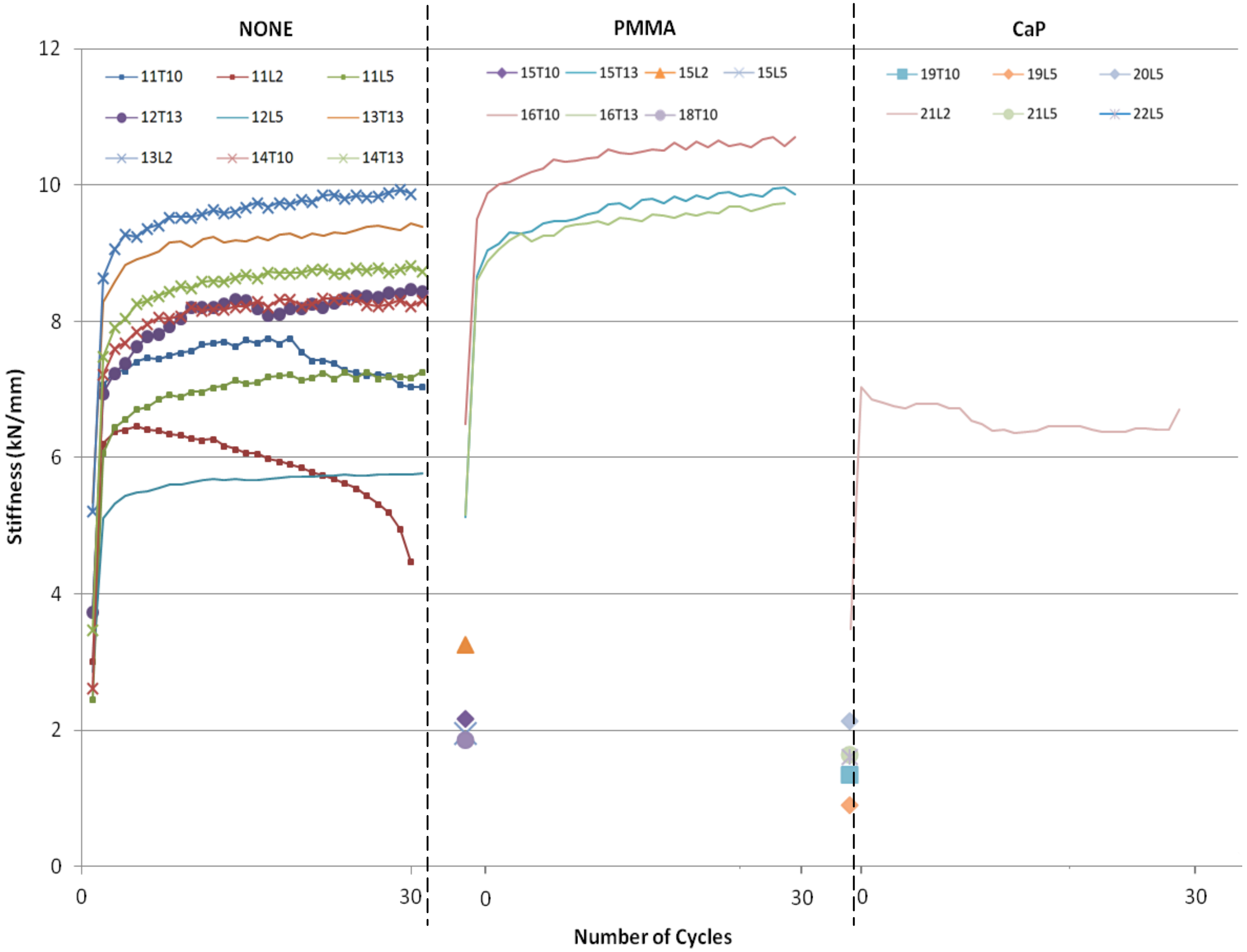

Figure 3.28 Change in stiffness across the loading cycles for each specimen of the multi-cycle loading set. Note the non-linear X-axis.

The figure showed that the unsuccessful specimens, all of which were augmented, were unable to withstand the 30 cycles of loading. The discussion has highlighted that the augmented specimens had a greater fracture grade than the non-augmented specimens, all of which were successful. The respective increase in the fracture grade across the NONE, PMMA and CaP groups suggested that the augmented specimens were more traumatically fractured than the non-augmented specimens, with the CaP augmented specimens being the most traumatically fractured of the entire set.

The hypothesis that the augmented specimen may have had a greater prevalence of failure due to an increase in the level of fracture severity can be supported by the discussion of the injectability findings. The unsuccessful augmented specimens had a lower level of injectability which may have been because the cement was unable to reach delocalised pockets of fractures which may be associated with more traumatic fractures. In conjunction to the indication that a lower level of injectability may be associated with a more traumatic fracture, the stiffness values of the unsuccessful augmented specimens were generally lower than the potentially less traumatically fractured successful specimens.

A direct comparison of the cements used during augmentation is not possible from the data available. Although the PMMA augmented specimens had a lower fracture grade than the CaP augmented specimens, it is not clear whether this is due to less traumatic fractures of a greater ability of the less viscous PMMA cement to reach delocalised pockets of fracture. Similarly, the stiffness of the PMMA specimens was greater than the CaP specimens and it was not possible to determine whether this was due a more successful augmentation or a less traumatically fractured group of specimens.

The findings of the multi-cycle loading suggested that vertebroplasty, using either PMMA or CaP, was unable to restore the stiffness levels of fractured vertebrae to the levels associated with intact vertebrae. In addition, the augmented vertebrae were generally unable to undergo 30 cycles of loading. However, all of the specimens were successfully converted into FE models and the findings presented in the current chapter were essential for model validation.

Chapter 4

Computational Methods and Preliminary Results

4.1 Introduction

This chapter presents the computational methods that were used in the study where FE models were generated from the µCT images of the experimental specimens discussed in Chapter 2. Use of the specific images of each experimental specimen allowed for direct comparison between the FE predictions and the corresponding experimental stiffness values. The manner in which specimens were converted into FE models is presented in this chapter for two sets of specimens; those that were subjected to single cycle loading and those that were subjected to multi-cycle loading. The results of the sensitivity studies that were conducted during method development are also presented.

4.2 Single Cycle Modelling

The reconstructed, pre-loading µCT images of the eight single cycle specimens (Section 2.3.2) were subjected to some preliminary preparations before being converted into FE models. The details of these preparations, the stages involved in the model development and the outcome of the sensitivity studies conducted are presented in the following section for the single cycle specimens.

4.2.1 Preliminary Preparations

Before the µCT images could be converted into specimen-specific models, they were resampled to a lower resolution, assigned material properties through the use of thresholding operations and a mesh was created. The details of these procedures are presented in the following subsection.

Resampling

The images from the µCT scanner (*.DICOM) were converted at the same resolution (74 µm) to an alternative format (*.TIFF) using a custom written algorithm (Matlab 7.9, MathWorks, USA; Jones and Wilcox 2007). Conversion of the images to TIFF format reduced the number of greyscales present in the images from 64,000 Hounsfield units to 256 greyscale colours and made the images compatible with the commercial image processing software that was available (ScanIP v4.2, Simpleware, UK). Because the image processing software converted the images into a FE mesh with the same element size as the voxel spacing, the images were downsized in ScanIP to a resolution of 1 mm using the built-in algorithm based on partial volume interpolation. A resolution of between 1 – 2 mm has been shown to be appropriate for modelling intact human and porcine vertebra on a continuum level (Wijayathunga *et al*. 2008; Jones and Wilcox 2007). Since the information on mesh density already existed for models generated using the same process, no further mesh convergence analysis was conducted. The partial volume interpolation method of resampling assigned a new greyscale value to each downsampled voxel based on the proportion of greyscale the previous voxels occupied within that space. Downsizing the images in this manner caused the definition of individual trabeculae to be averaged to a greyscale value that represented the bone and surrounding trabecular spacing, as shown in Figure 4.1.

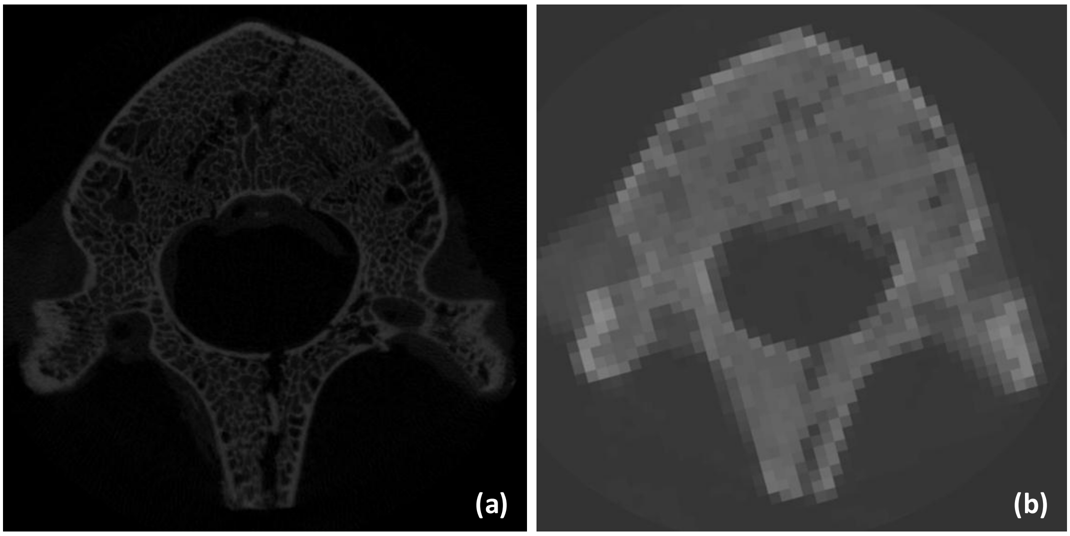

Figure 4.1 A single cycle specimen at a resolution of (a) 74 µm and (b) 1 mm.

Material Properties

Threshold operations were performed using ScanIP in order to assign masks to the regions corresponding to the bone, fracture, PMMA loading plates and radio-opaque marker. The radio-opaque marker was used experimentally as a reference point in order to apply a point load to the middle of the vertebral body (Section 2.3.1). It was necessary to apply a point load, computationally, to the same location; however, it was also necessary to remove the marker from the model in order to provide a smooth surface on the upper loading plate. Therefore, the mask of the radio-opaque marker was exported as a lone object, without material properties, to the FE software (Abaqus v6.8 – 6.9, Simulia, USA) where the coordinates of the midpoint were obtained. Following this, the mask corresponding to the marker was deleted from the image processing software. If necessary, additional voxels were added to the upper surface of the superior loading plate in order create a smooth surface for loading.

Homogenous material properties were assigned to the masks of the PMMA (Young's modulus = 2.45 GPa, Poisson's ratio = 0.3 (Wijayathunga *et al*. 2008)) and the fracture (Young's modulus = 1×10^{-9} GPa, Poisson's ratio = 0.3). A very low modulus was chosen for the fracture in order to simulate a void as previous work has shown this to be an appropriate approximation (Tarsuslugil 2011). The Young's modulus of the bone was based on the greyscale value of each individual voxel and tuned using a linear greyscale conversion value since the greyscale is related to the bone density and the density is related to the elastic modulus of bone. The optimised greyscale conversion value was obtained when the stiffness of a set of computational models was in closest agreement with the stiffness of the corresponding experimental set. For fractured porcine vertebra, the greyscale conversion value employed was 5.229 MPa/greyscale value and was obtained by another researcher using a set of 18 fractured, porcine specimens (Tarsuslugil 2011). Previous studies have shown that a linear relationship for the greyscale conversion factor provides a similar level of accuracy for intact human and porcine vertebra as a power law relationship (Tarsuslugil 2011; Jones and Wilcox 2007). It has also been shown that a Poisson's ratio of 0.3 is appropriate for modelling trabecular bone (Jones and Wilcox 2007).

Transverse and sagittal views of the thresholding used for the bone, fracture and PMMA loading plates of the specimen presented above in Figure 4.1 are shown in Figure 4.2.

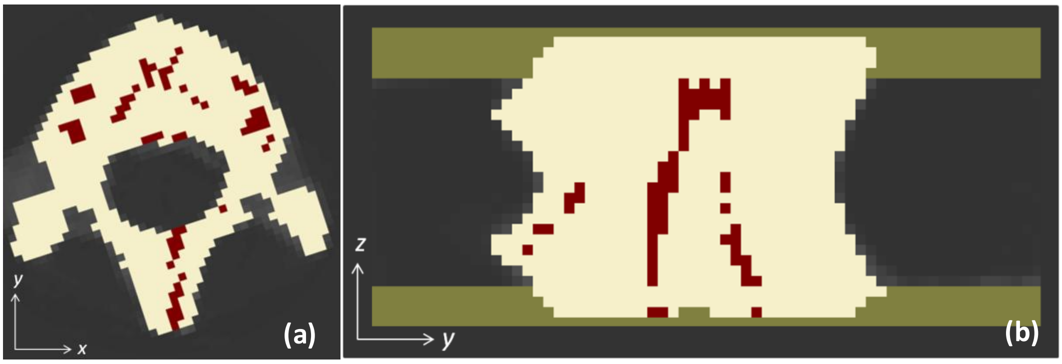

Figure 4.2 A specimen in the image processing software with masks in place for the bone (cream), fracture (red) and PMMA loading plates (green) in the (a) transverse and (b) sagittal view.

Contact pairs were created between the masks that came into contact with each other. A contact was established between each of the loading plates and both the bone and the fracture masks. A final contact set was created between the bone and fracture.

Model Exportation

Once the material properties had been assigned, the built-in topology and volume preserving algorithm was used to pre-smooth the voxels of the specimen prior to the creation of a mesh. Pre-smoothing the specimen prior to mesh generation helped to create a more accurate mesh (ScanIP v4.2, Simpleware, UK). An image of a specimen following pre-smoothing is shown in Figure 4.3.

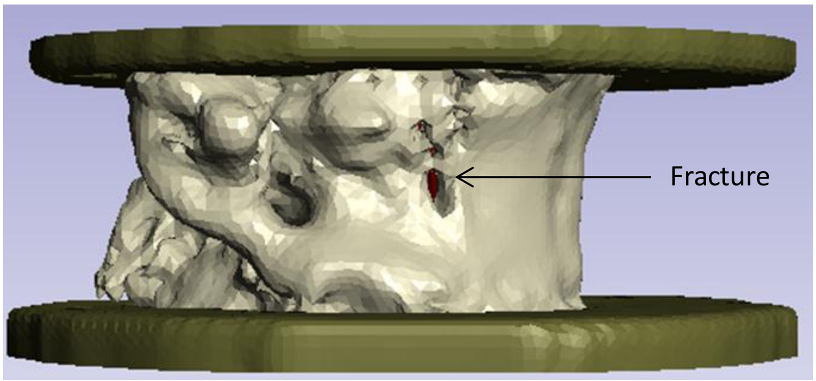

Figure 4.3 A Finite Element model of a single cycle specimen following pre-smoothing but prior to meshing and model exportation.

Once the specimen had been smoothed, a mixed mesh of hexahedral and tetrahedral elements was created based on the topology of the model using the in-built meshing algorithm, +FE Grid. With an element edge length of 1 mm, the mesh was then smoothed; this has been shown previously to improve model accuracy (Zhao 2010). The smoothed models were exported from the commercial image processing software as FE input files.

4.2.2 Model Development

All additional pre-processing and post-processing of the models was undertaken using a commercial software package (Abaqus CAE v6.8 – 6.9, Simulia, USA). An implicit solver was used for all analysis (Abaqus Standard v6.8 – 6.9, Simulia, USA). The pre- and post-processing was undertaken on a desktop PC whilst the models were solved on the University of Leeds’ central large-scale advanced research computing infrastructure.

Eight-noded brick elements were used and solved using linear interpolation. The elements were a mixture of hexahedral and tetrahedral elements and provided a more accurate surface topology than pure hexagonal elements. In addition, the use of eight-noded brick elements is less computationally expensive that using higher order non-linear elements.

Prior to the model being analysed, it was necessary to create new parts to allow for a loading scenario similar to the experimental regime to be established. Also necessary was the creation of interactions between the surfaces and the definition of the load and the boundary conditions. The details of the stages involved in the development of each model are presented in the following subsections.

New Parts

A steel loading plate (Ø140 x 7.5 mm) with a countersunk hole (Ø13 x 7.5 mm), similar to that used experimentally, was created and assigned a Young’s modulus of 210 GPa and Poisson’s ratio of 0.3. An analytical rigid plate (Ø14 mm) was also created and aligned on the surface of the steel loading plate to allow for the application of the load. The steel loading plate was meshed with a node spacing of approximately 1 mm in order to match the mesh density of the specimen.

Interactions

The fractured regions were modelled as a void with a very low modulus and, where applicable, were tied to the bone and loading plates. A previous study has shown that the results obtained from modelling the fracture with a tied constraint produced similar levels of accuracy as when employing frictionless contact (Tarsuslugil 2011).

A node set was created on the superior loading plate at the location that corresponded to the midpoint of the radio-opaque marker. The analytical rigid plate was tied to the centre point of the steel loading plate which was in turn tied, at the node set, to the smooth surface of the superior PMMA loading plate. The bone was tied to the PMMA loading plates as minimal movement was expected due to the bond between the PMMA and bone.

Boundary Conditions

The inferior surface of the lower PMMA loading plate was subjected to an encastre boundary condition in order to simulate the manner in which all degrees of freedom were constrained experimentally (Section 2.3.3). A point load of 3 kN was applied to the midpoint of the analytical rigid loading plate. The point of load application was constrained in the horizontal direction, but free to rotate in order to replicate the steel loading ball that was used experimentally (Section 2.3.3).

Final Model

An image of a typical completed single cycle model can be seen in Figure 4.4.

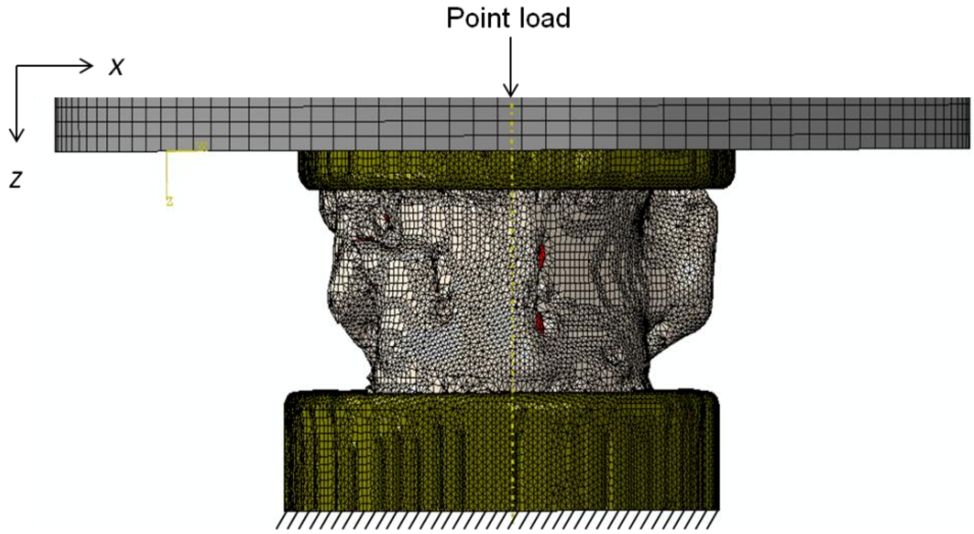

Figure 4.4 A finalised Finite Element model of a single cycle specimen showing the mesh density, boundary conditions and load.

Once Abaqus converged on a solution, the displacement at the node set was recorded and the stiffness obtained by dividing the applied load by this value. The results of the specimen-specific modelling of the single cycle specimens are presented in the following chapter.

4.2.3 Sensitivity Studies

Two sensitivity studies were performed during the thresholding procedure in the image processing software and before the final model was completed in order to investigate the most appropriate manner to select the regions corresponding to bone and fracture. The details of the sensitivity studies performed are presented in the following subsections.

Bone Threshold

When the µCT images were imported into the image processing software, it was not possible to identify the specimen as the brightness and contrast were at such low values. As the contrast was increased, it was possible to identify features ranging from the soft tissue to the trabecular bone and finally the cortical shell (Figure 4.5).

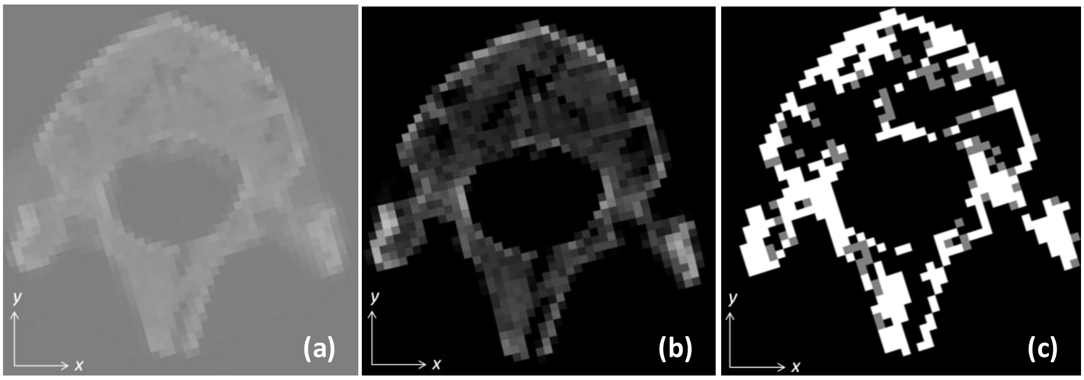

Figure 4.5 Distinguishing between bone and fracture became more difficult as the contrast increased (a – c).

However, the fracture appeared to grow in volume as the contrast was increased and when the images were at a lower contrast, it was difficult to visually distinguish between soft and hard tissue. Therefore, it was essential that the method of thresholding was as automated as possible in order to reduce variability between specimens and between future users.

Models corresponding to three variations of three specimens were made, each variation of a given specimen was assigned a bone mask that corresponded to a different threshold level. An image comparing the amount of bone captured using each of the threshold levels is shown in Figure 4.6. A threshold level of 17 – 255 captured the least number of voxels (24,800), whilst a threshold level of 16 – 255 captured slightly more (26,000) and a threshold level of 15 -255 captured the greatest number of voxels that corresponded to bone (27,200). It should be noted that the threshold values selected were dependant on the settings of the µCT scanner used and the resolution of the model in the image processing software.

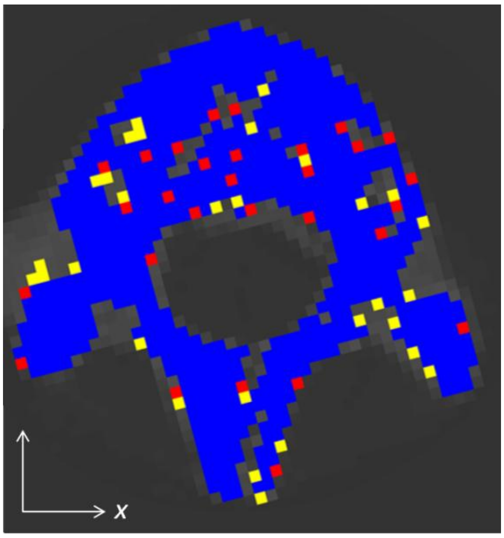

Figure 4.6 Bone threshold sensitivity with a minimum selection of bone (blue, 17 -255), median (red, 16 -255) and maximum selection of bone (yellow, 15 - 255).

For each model, additional masks were made for the PMMA loading plates and the fractured region. The models were exported from the image processing software as FE input files and solved.

The model variation that incorporated a threshold level of 17 -255, which captured the least amount of bone, underestimated the group stiffness of the specimens by 7% as there were too few voxels with a high modulus (bone) and too many voxels that had a low modulus (fracture). Likewise, the model with a threshold level of 15 – 255 with the greatest volume of bone overestimated the group stiffness by 12%. The optimum threshold level for bone, 16 -255, was the operation that captured the median amount of voxels and overestimated the group stiffness of the specimens by 3%.

Fracture Selection

It was desirable to be able to select the fractured regions in a manner that was as automated as possible because, as shown in Figure 4.5, it was difficult to positively identify the fractured regions as the contrast varied which may have led to errors between specimens and users. A series of close operations were performed in order to capture the fracture. A close operation captured any small holes in the mask by firstly dilating (increasing), and then eroding (decreasing), in all directions by a certain number of voxels, X. Images illustrating the steps involved in a close operation are shown in Figure 4.7.

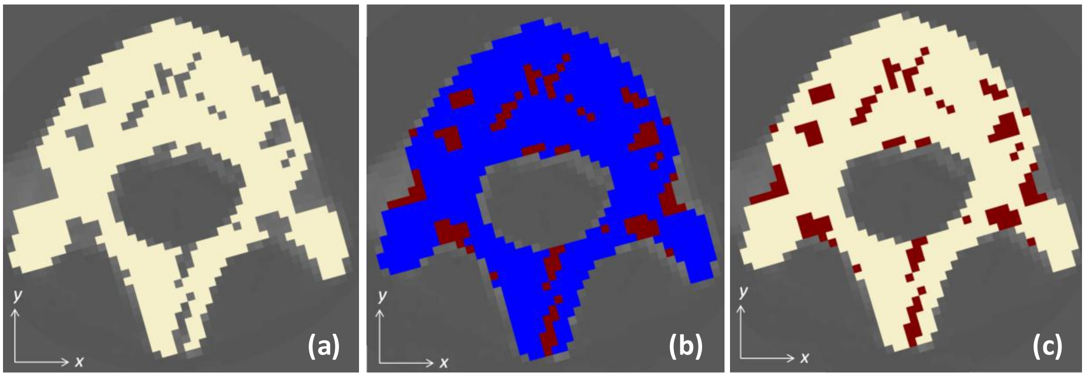

Figure 4.7 The original bone mask (a), the duplicated bone mask following the close operation (blue and red) (b) and the overlap between the masks deleted leaving fracture behind (c).

The original bone mask (Figure 4.7a) was duplicated and this new mask was subjected to the close operation. When the duplicated mask grew, it assessed all of the surrounding voxels and their greyscale values and when it decreased, the voxels that were not greater in size than X and of a similar greyscale value were added to the mask (Figure 4.7b). The overlap between the bone mask and the duplicated mask was deleted (Figure 4.7c) and the duplicated mask that remained represented the fractured region. The fracture was manually deleted from the regions where it was known there was no fracture present, such as around the facet joints and the spinal canal. An image of the specimen in Figure 4.7, following manual deletion of the excess fracture, can be seen in Figure 4.2. To reduce errors at the FE stage, it was especially important to delete the excess fracture from regions that would be in contact with the PMMA loading plates because during the simulation, the elements representing fracture deformed too much and resulted in errors. The excessive deformation of the fracture elements was due to the low modulus assigned to the fracture and the high modulus assigned to the PMMA.

Three models of one specimen were created where the close operation was performed to encompass three different region sizes, where X was varied from one to three voxels which corresponded to 1 – 3 pixels added in each direction (Figure 4.8). The blue mask captured the least number of voxels (1,600), the red captured slightly more (2,000) and the yellow captured the greatest number of voxels which corresponded to fracture (2,300).

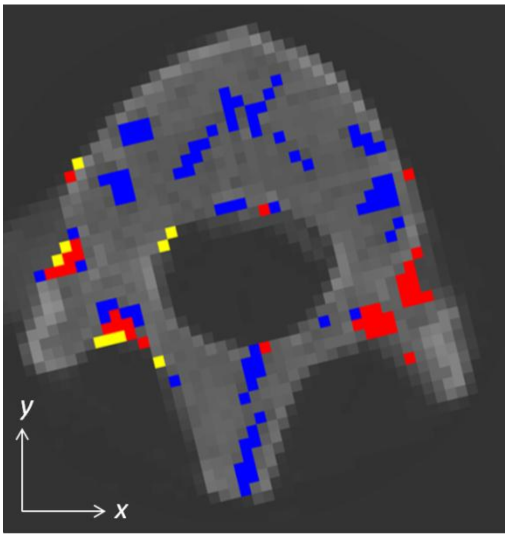

Figure 4.8 Fracture selection sensitivity with a minimum selection of fracture (blue, 1 pixel), median (red, 2 pixels) and maximum selection of fracture (yellow, 3 pixels .

As the excess fracture from around the facet joints and spinal canal were deleted, the results of the models were similar; the greatest difference observed between the stiffness values was less than 2%. However, because the entire set of specimens occasionally had regions of fracture that were greater in volume than those displayed in Figure 4.8, the optimum fracture selection technique was defined to employ a close operation that incorporated voxels in each direction up to a size of 2 mm^3.

4.3 Multi-Cycle Modelling

The method used to model the multi-cycle specimens was similar to that of the single cycle specimens except for the addition of plastic properties in order to simulate the permanent deformation that occurred during each loading cycle. With the addition of plastic material properties to the multi-cycle models, some minor adjustments needed to be made to the manner in which the specimen-specific models were generated. The method used to model the multi-cycle specimens, which differs from the method used to model single cycle specimens, is presented in the following section in conjunction with the outcome of the sensitivity studies performed. Also presented is the method that was used to model the subsequent cycles of the multi-cycle specimens.

4.3.1 Segmentation and Meshing

The images of the multi-cycle specimens were manipulated in the same manner as the single cycle (Section 4.2.1). There was an additional floodfill threshold operation involved in order to mask the PMMA and CaP augmented specimens, which possessed a different greyscale value to the bone. Images of a CaP augmented specimen prior to resampling and following resampling, with the addition of masks, can be seen in Figure 4.9.

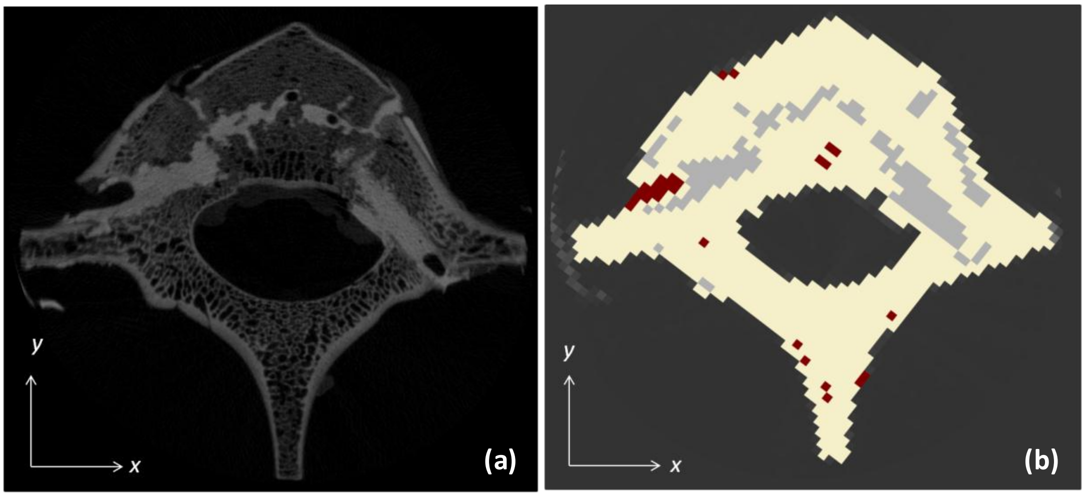

Figure 4.9 A calcium phosphate augmented specimen at (a) 74 µm and at (b) 1 mm with masks applied. The cream masks represents bone, the grey represents cement and the red represents fracture.

The best estimate of Young’s modulus assigned to the PMMA (1.035 GPa) was obtained by another researcher following compression tests upon cores of injected PMMA (Tarsuslugil 2011). The Young’s modulus assigned to the CaP (0.585 GPa) was obtained in a similar fashion (O’Hara 2010). The Poisson’s ratio of both cements was set at 0.3.

The smoothed models were exported from the image processing software as FE input files.

4.3.2 Model Development

Before the multi-cycle models could be solved, it was necessary to create an additional mesh in order to allow for a loading scenario similar to the experimental regime to be established. Also necessary was the creation of interactions between the surfaces and the definition of the load and the boundary conditions. In addition to these steps, the Von Mises criterion for plastic yield was added to the material properties of the bone in order to simulate the permanent deformation observed experimentally. The methods and outcome of the sensitivity studies performed are also presented in the following subsections. Finally, the manner in which cycles subsequent to the initial loading cycle were modelled is presented.

New Parts

It was not possible to load the multi-cycle specimens via a steel plate as with the single cycle models (Section 4.2.2) because the additional part created complications with the method that was later used to model the subsequent loading cycles. The displacement of specimens was taken from the rigid plate using a reference point however, the addition of the reference point introduced an extra node which caused errors when modelling the subsequent cycles. To avoid these complications, an additional mesh was created, or offset from the existing mesh on the superior face of the upper PMMA loading plate. The additional mesh was offset to a height of 7 mm which was approximately equal to the height of the steel loading plate used experimentally and during the modelling of the single cycle specimens. A node set was created at the node that was in closest proximity to the location corresponding to the midpoint of the radio-opaque marker and used as the point of load application. The offset mesh was assigned the material properties of steel (Young's modulus = 210 GPa, Poisson's ratio = 0.3).

Interactions

The interactions that were created between the surfaces of the non-augmented models were the same as those created for the single cycle specimens (Section 4.2.2). However, there were some additional interactions defined for the augmented specimens. Where applicable, the PMMA loading plates were tied to the augmented cement and the augmented cement was in turn tied to the surface of the bone and fracture.

Boundary Conditions

The boundary conditions created for the multi-cycle specimens were as described in Section 4.2.2. However, an additional step was created in each model to allow for both the application of the 6 kN point load (Step 1) and the removal of the point load to 1 kN (Step 2) as was performed experimentally (Section 2.3.3).

Plastic Properties

Each model was comprised of approximately 100 different materials that defined the bone. To manually add plastic properties to each of these materials through the Abaqus interface would have been very time consuming. Instead, an algorithm was written to read the input file of each FE model, to add plastic properties to the materials and to rewrite a new input file, complete with plastic properties (Wilcox 2012). Materials not subjected to plastic deformation, such as the steel and the fracture, were not assigned plastic material properties.

The new input file was imported into the FE software and a data check was performed in order to check that the model was capable of being solved. Some additional lines of text were added to the input file in order to request two output parameters which could not be requested through the Abaqus user interface. These lines instructed Abaqus to record the elements that had reached plastic yield and the final coordinates of all the nodes in the model in an output file. The nodal coordinates of the deformed elements were used in the following input file that was used to model the subsequent cycle.

Final Model

An image typical of a completed multi-cycle model is shown in Figure 4.10.

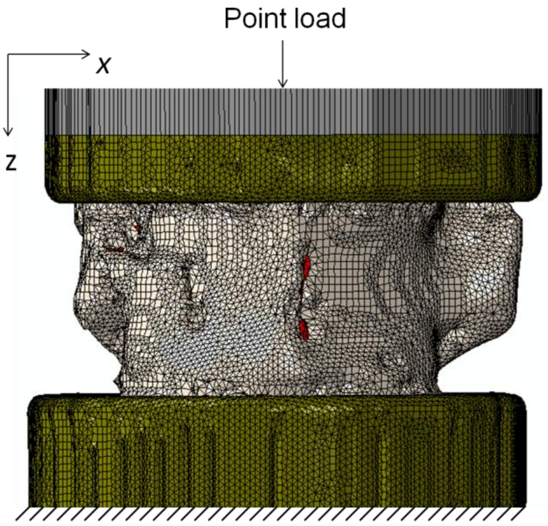

Figure 4.10 A finalised Finite Element model of a non-augmented multi-cycle specimen showing the mesh density, boundary conditions and load.

Once Abaqus converged on a solution, the displacement at the node set of each model was recorded at various stages throughout the loading and unloading steps.

The stiffness of the specimen was taken as the slope of the linear region of the computational load-displacement curve and the loaded and permanent deformations were recorded in order to compare against experimental values.

An investigation into the effectiveness of the cement/bone interface was performed to determine whether or not the interface had an effect upon the accuracies of the models. The reason for the investigation into the cement/bone interface was because a visual inspection of the post-loading images of the augmented specimens showed that the interlock between the bone and augmentation failed during loading. Therefore, experimentally, the specimens displayed greater levels of sliding at the fracture rather than the computational tie contact that was defined between the cement and fracture. The augmented specimens were modelled with the material property of the PMMA and CaP cement altered to be that of the fracture. This represented the extreme case where the cement had no effect on the behaviour of the vertebrae, for example where there is complete non-union between the bone and the cement throughout the loading cycle, or a non-augmented scenario.

The results of the specimen-specific modelling of the multi-cycle specimens are presented in the following chapter.

4.3.3 Sensitivity Studies

Three sensitivity studies were performed for the multi-cycle models, the first of which was to investigate the effect of not creating the steel loading plate as an additional part. The second sensitivity study was to determine which value of yield stress, as a percentage of the Young’s modulus, which best replicated the experimental permanent deformation of the specimens. The final sensitivity test was to investigate whether a greater level of permanent deformation could be simulated by assigning plastic material properties to the fracture region. The details of these sensitivity studies are presented in the following subsections.

Steel Loading Plate Replacement

It was not possible to use a steel loading plate in the modelling of the multi-cycle specimens because, as discussed above, the additional part created complications for the algorithm that was used to model the subsequent loading cycles. Instead, an offset mesh was created and assigned the material properties of steel. To investigate the effect of using an offset mesh rather than a steel loading plate, three single cycle specimens with experimental stiffness values that corresponded to the maximum, median and minimum values of the set were used for a sensitivity study. The models were solved with the removal of the steel loading plate and the addition of an offset mesh.

The results of using the steel offset mesh instead of a steel loading plate was that the computational stiffness of the group was 1% greater than when a steel loading plate was used. Therefore, the steel mesh was used with confidence for the multi-cycle models as it had a minimal effect upon the accuracy of the single cycle models.

Appropriate Yield Stress Value

A wide range of yield stress values were applied to the model of one specimen, S14T13, which had an experimental stiffness corresponding to the median of the non-augmented, multi-cycle specimens. The values of yield stress were specified as a percentage of the Young's modulus of each material. The range of yield stress values were taken from the literature where the yield stress of porcine bone was between 2 – 13% of the Young's modulus (Ryan, Pandit and Dimitrios 2008; Tsai, Chang and Lin 1996). The plastic strain at the yield stress was defined in Abaqus as zero therefore, once the yield stress had been reached, the models behaved in a linear elastic manner and then in a perfectly plastic manner. The experimental load-displacement curve for S14T13 and the computational load-displacement curves for a selection of yield stress values are shown in Figure 4.11.

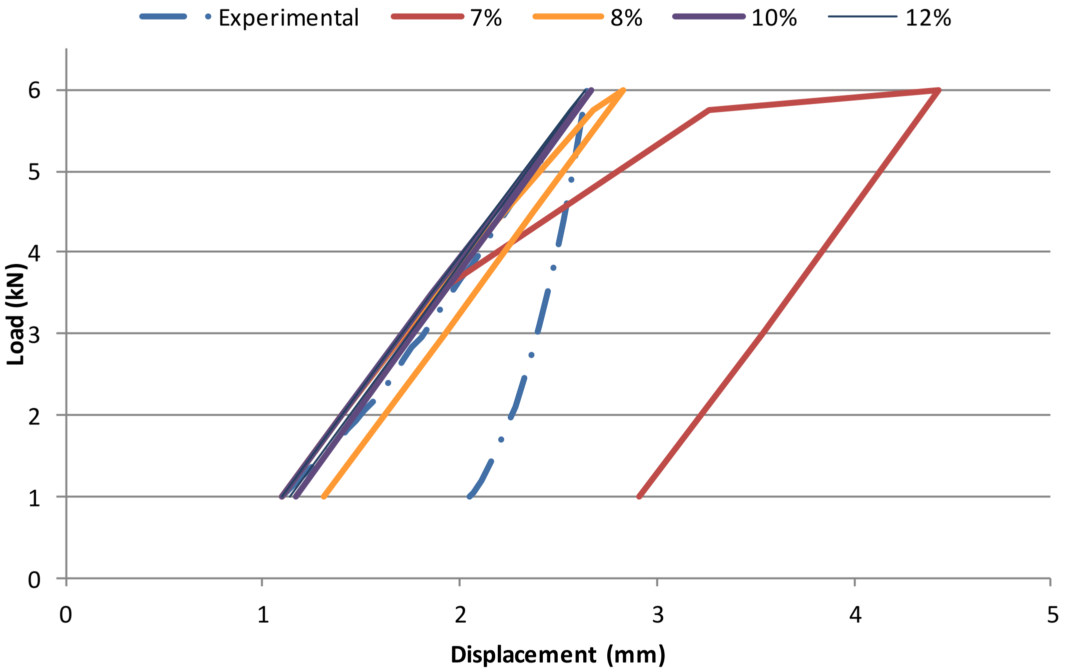

Figure 4.11 Sensitivity study on the range of yield stress values to be applied to a model, as percentage of the Young's modulus, in order to replicate the experimental permanent deformation. Note that the line for 12% yield stress cannot be seen as predicted the same displacements as the 10% yield stress and lies below the 10% yield stress line.

The models could not represent the non-linear behaviour of the experimental specimens during unloading, therefore, a match between the displacements at 6 kN, or what will be referred to as the loaded displacement, was sought as an indication of an appropriate yield stress value. The computational displacement at 6 kN for the model of S14T13, where the yield stress had been assigned as 11% of the Young's modulus, was the same as the experimental displacement to within two decimal places. Therefore, two further non-augmented specimens, S11L5 and S13T13, were solved with the yield stress value at 10, 11 and 12% of the Young's modulus of each material. The experimental and computational load-displacement curves of S11L5 and S13T13 are shown in Figure 4.12 where the computational data has been translated in order to begin at the same displacement as the experimental data.

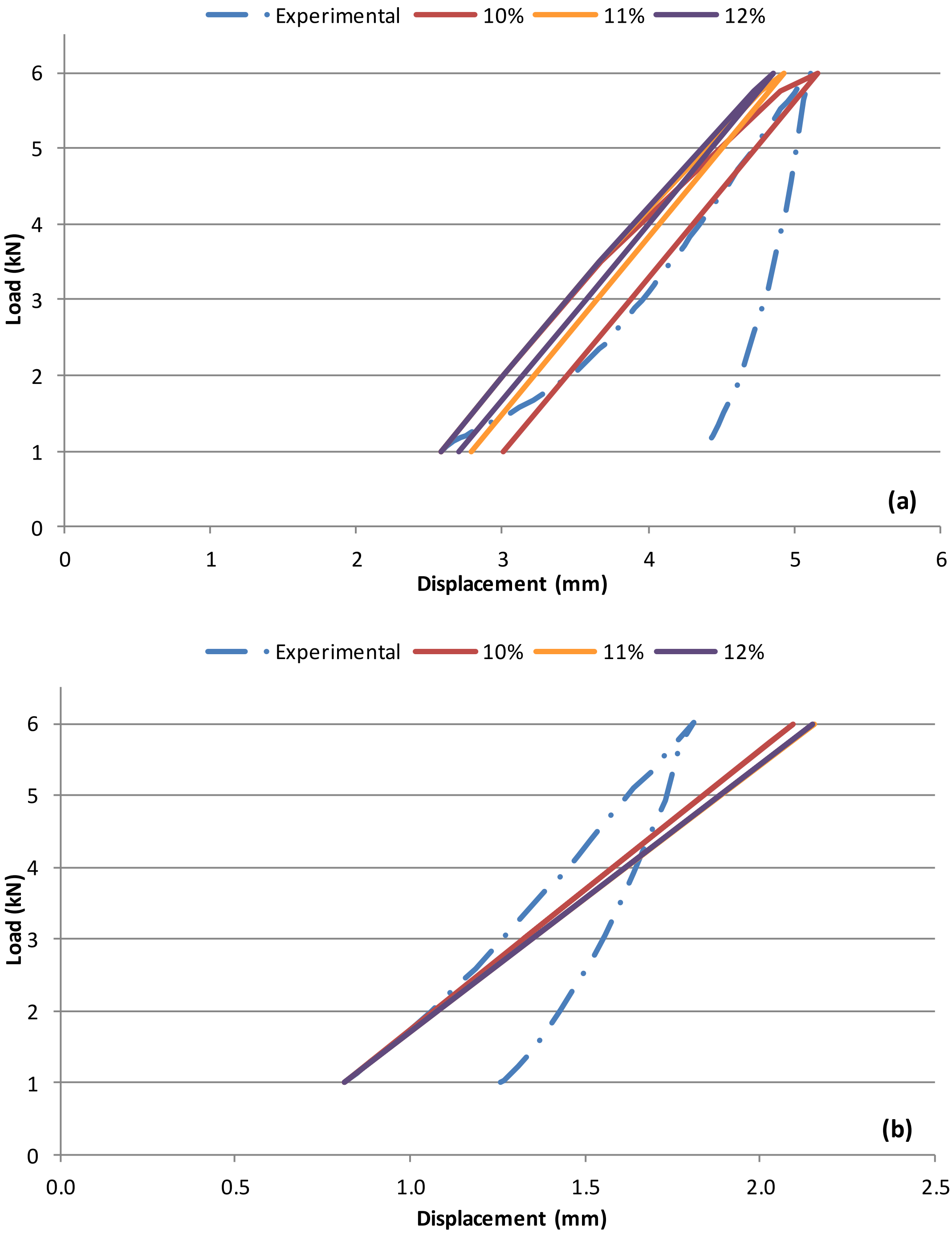

Figure 4.12 Non-augmented specimen-specific model of (a) S11L5 and (b) S13T13 with a range of yield stress values, as a percentage of Young's modulus (Note for S13T13, 11% and 12% followed the same curve).

The results of the sensitivity study indicated that the optimum yield stress value was 10% of the Young's modulus of each material because this value provided the greatest computational accuracy for the loaded displacement of the three specimens used in the sensitivity study. The yield stress value of 10% was applied to the remaining multi-cycle specimens and the results are presented in the following chapter.

Plastic Properties Applied to Fracture

In an attempt to increase the permanent deformation observed computationally, a range of plastic properties were applied to the fractured region, as a percentage of the Young's modulus assumed for that region (2 – 50%). It was envisioned that if the fracture deformed plastically, the fracture height would reduce as the surfaces of fracture came together and the overall permanent deformation of the computational model may have been more similar to what was observed experimentally.

The model was unable to converge upon a solution when plastic properties were applied to the fracture. As it may not have been possible for the model to converge at 6 kN, the point load was removed and a corresponding displacement was specified instead. However, the model still failed to converge due to the gross deformation of the mesh representing the fracture region.

4.3.4 Subsequent Cycles

To model the loading cycles subsequent to the initial cycle, two approaches were investigated. In the first, a series of steps were created in the FE software in order to load and unload the specimen a multiple of times. In the second instance, the output file of the initial loading cycle, which gave the nodal coordinates of the deformed elements, was used to create an input file for the second loading cycle where a modulus reduction technique was used that was based on the plastic strain that occurred in the previous cycle.

Five Loads

A model was made of one non-augmented specimen where ten steps were defined in order to load and unload the specimen between 6 kN and 1 kN five times. Plastic deformation was observed following the initial loading cycle but no additional plastic deformation occurred in the remaining four. The load-displacement graph of the five loading cycles can be seen in Figure 4.13.

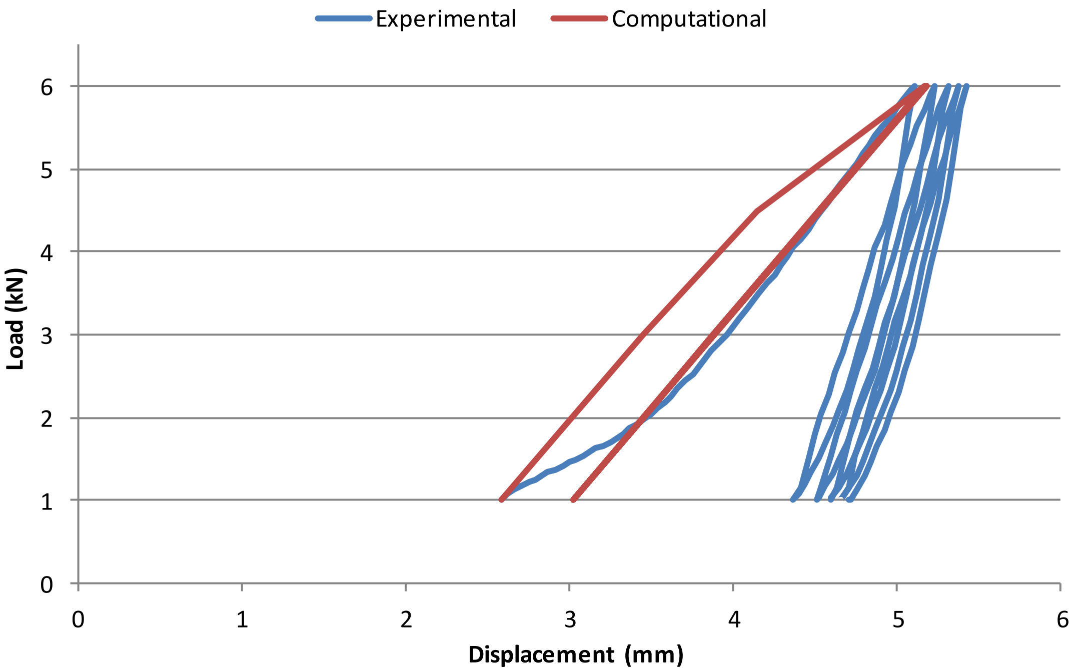

Figure 4.13 Five computational and experimental loading cycles for a non-augmented specimen (Note the final four computational cycles were linear).

As it was not possible to capture the permanent deformation of the specimen in the subsequent loading cycles, the technique of introducing multiple steps in Abaqus was no longer investigated.

Material Property Reduction

An algorithm was written in order to create an input file for the second loading cycle using the nodal coordinates of the deformed elements from the first loading cycle (Wilcox 2012b). In addition to using the deformed coordinates in the subsequent input file, the algorithm also reduced the material properties of the deformed elements. The material properties were reduced in accordance with a relationship that was observed experimentally when trabecular cores from human lumbar vertebrae were overloaded (Keaveny, Wachtel and Kopperdahl 1999). The reduction in the Young's modulus and the yield stress of an element was described in terms of the plastic strain, ε_p, as shown in Equation 4.1 and Equation 4.2.

Equation 4.1 Formula for percentage reduction of Young's modulus in terms of the plastic strain, ε_p (Keaveny, Wachtel and Kopperdahl 1999).

$$Young's\ modulus\ reduction = \frac{111\varepsilon_p}{\varepsilon_p + 0.751}$$

Equation 4.2 Formula for percentage reduction of yield stress in terms of the plastic strain, ε_p (Keaveny, Wachtel and Kopperdahl 1999).

$$Yield\ stress\ reduction = 20.8\varepsilon_p - 6.4$$

The reduction in Young's modulus was capped at 85% as this was reported in the study as the average modulus reduction observed for specimens that were subjected to greater levels of plastic strain. The average reduction in yield stress for high levels of plastic strain was not given and was therefore capped at 60% which, from the data provided, appeared to be the maximum reduction that was observed. One non-augmented multi-cycle specimen was chosen to have its subsequent loading cycles modelled in this manner.

Once the model converged on a solution, the displacement at the node set was recorded at various stages throughout each loading cycle. The stiffness of the specimen was taken from each loading curve as the slope of the most linear region of the computational load-displacement curve. The results of the specimen-specific modelling of the subsequent cycles for the multi-cycle specimen are presented in the following chapter.

4.3.5 Clinical Application

Three specimen-specific models from each of the non-augmented, PMMA augmented and CaP augmented groups were subjected to further simulations to represent a variety of clinical possibilities. The three models selected from each group possessed the minimum, median and maximum experimental stiffness values of each respective group.

For the non-augmented models, the clinical scenarios that were replicated included assigning the properties of the fracture to that of bone in order to examine the effect of bone regrowth on the stiffness of the models. The material properties of the most prevalent bone material were used (Young's modulus = 0.11 GPa, Poisson's ratio = 0.3). The three non-augmented models were also solved with the material properties of the fracture altered to both that of the PMMA and then the CaP cement to simulate "perfect" augmentation (100% of the fracture void filled with PMMA/CaP) and to investigate the effect of this on the stiffness values.

Similarly, the augmented models were also solved with both PMMA and CaP augmentations (100% PMMA/CaP). The augmented models were also solved with the non-augmented sections of the fracture void assigned material properties to represent partial bone regrowth (X% Bone). Finally, the CaP augmented specimens were solved to simulate the complete resorption of the CaP cement and full bone remodelling within the fracture void (100% Bone) which is not possible when PMMA is *in situ*.

This chapter detailed how the single cycle specimens were modelled as linear elastic whilst the bone of the multi-cycle specimens was modelled as being elastic and then perfectly plastic after the yield point. As a result of the addition of plastic material properties to the multi-cycle specimens, some adjustments had to be made to the manner in which they were modelled such as the removal of the steel loading plate and the addition of an offset mesh. To model the subsequent cycles of the multi-cycle specimens, the input file of the initial loading cycle was edited in order to request the output of the nodal coordinates of the deformed elements. Using the deformed coordinates and an algorithm to reduce the Young's modulus and yield stress based on a relationship taken from the literature, a new input file was analysed for the subsequent loading cycle. One non-augmented model was solved over a greater number of loading cycles using this methodology.

The results of the single cycle models and of both the initial and subsequent loading cycles for the multi-cycle models are given in the following chapter.

Chapter 5

Computational Results

5.1 Introduction

Presented in this chapter are the results of the specimen-specific models which were subjected to single cycle loading and multi-cycle loading. The stiffness values of the single cycle models are compared to the experimental stiffness values. Similarly, the computational stiffness values of the multi-cycle specimens from the initial loading cycle are compared to the corresponding experimental stiffness values. In conjunction, the displacements of the multi-cycle specimens during the first loading cycle when fully loaded and unloaded are also presented. The outcome of the simulation of the subsequent loading cycles and the results of the further modification of the multi-cycle models to simulate a variety of clinical outcomes are also presented.

5.2 Single Cycle Modelling

The results from computational modelling of the single cycle specimens are presented in the following section.

5.2.1 Stiffness Values

The computational stiffness values obtained for the eight single cycle specimens are shown plotted against the corresponding experimental stiffness values in Figure 5.1.

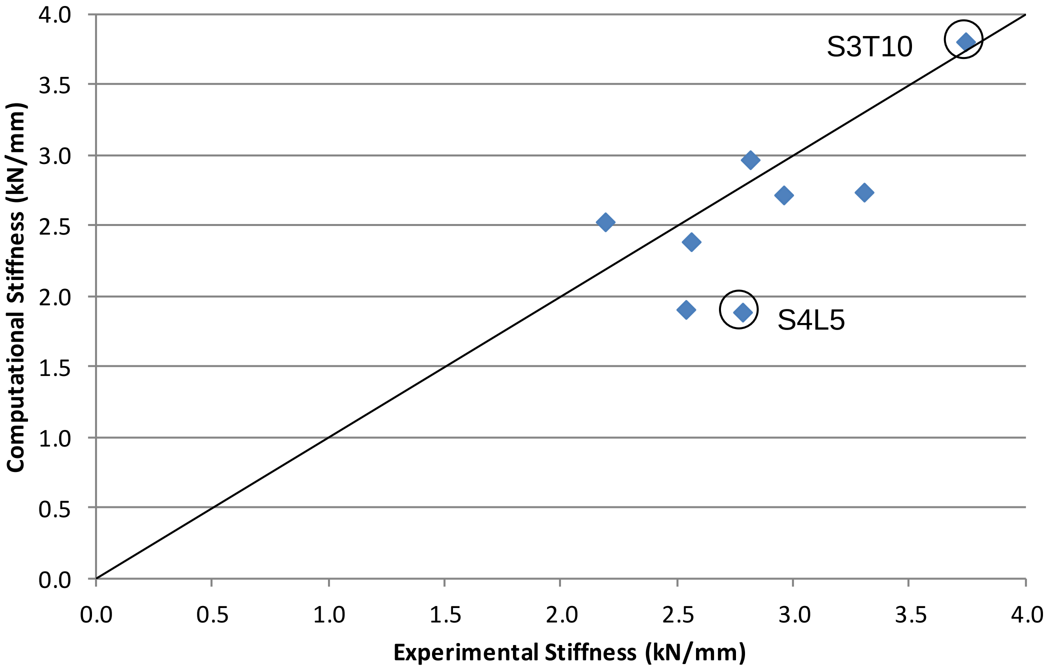

Figure 5.1 Computational and experimental stiffness values for the single cycle specimens. The circled specimens, S3T10 and S4L5, possessed the greatest and least computational accuracy, respectively.

The model predictions were generally in good agreement with the experimental results. The mean absolute error of the computational models was 14%. The greatest error observed was an underestimation of the experimental stiffness of S4L5 by 32% whilst the model of S3T10 exhibited the greatest computational accuracy with an overestimation of 2% of the experimental stiffness. Both of these specimens are shown highlighted in Figure 5.1.

The mean-difference plot of the experimental and computational stiffness values is shown in Figure 5.2. The specimens with the greatest and least computational accuracy, S3T10 and S4L5, respectively, are shown highlighted on the figure.

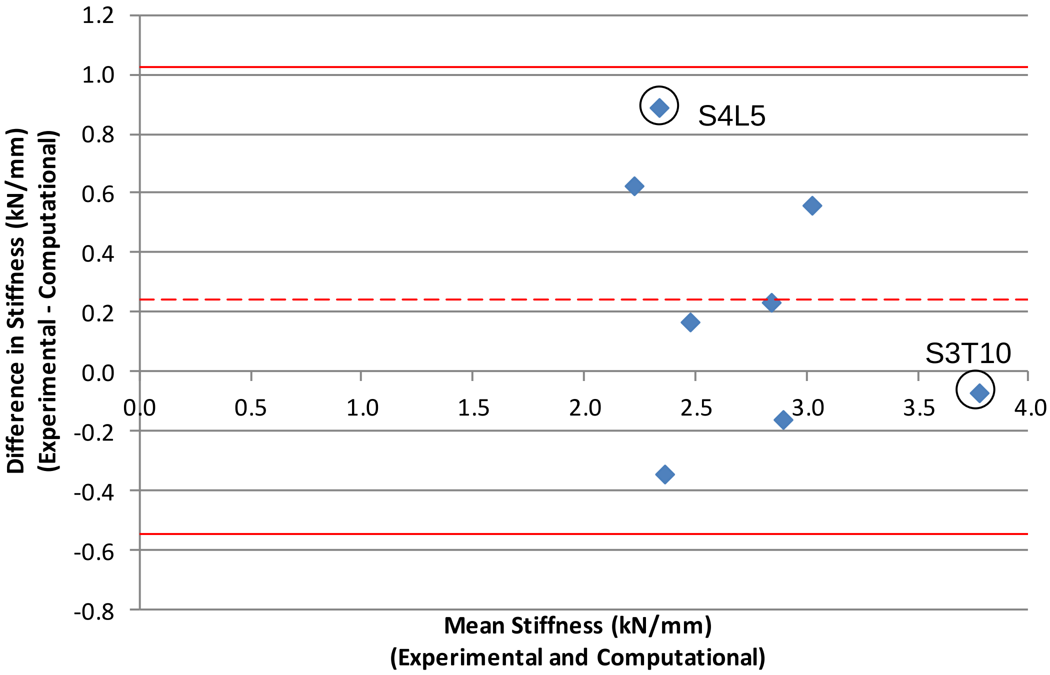

Figure 5.2 A mean-difference plot of the experimental and computational stiffness values for the single cycle specimens. The dashed and solid red lines show the mean difference value and the limits of agreement (1.96 x standard deviation). The circled specimens, S3T10 and S4L5, possessed the greatest and least computational accuracy, respectively.

The figure showed that there was a general tendency for the computational models to underestimate the experimental stiffness values although the difference between all of the experimental and computational stiffness values fell within the limits of agreement.

5.2.2 Discussion

The agreement found between the experimental and computational stiffness values indicated that it was possible to model fractured vertebrae, at a resolution of 1 mm^3 and with a tied contact between the low-modulus fracture void and the bone, to a reasonable level of accuracy.

In order to investigate the reasons for the difference in predictions between specimens, images of the models with the greatest and least computational accuracy are presented in Figure 5.3.

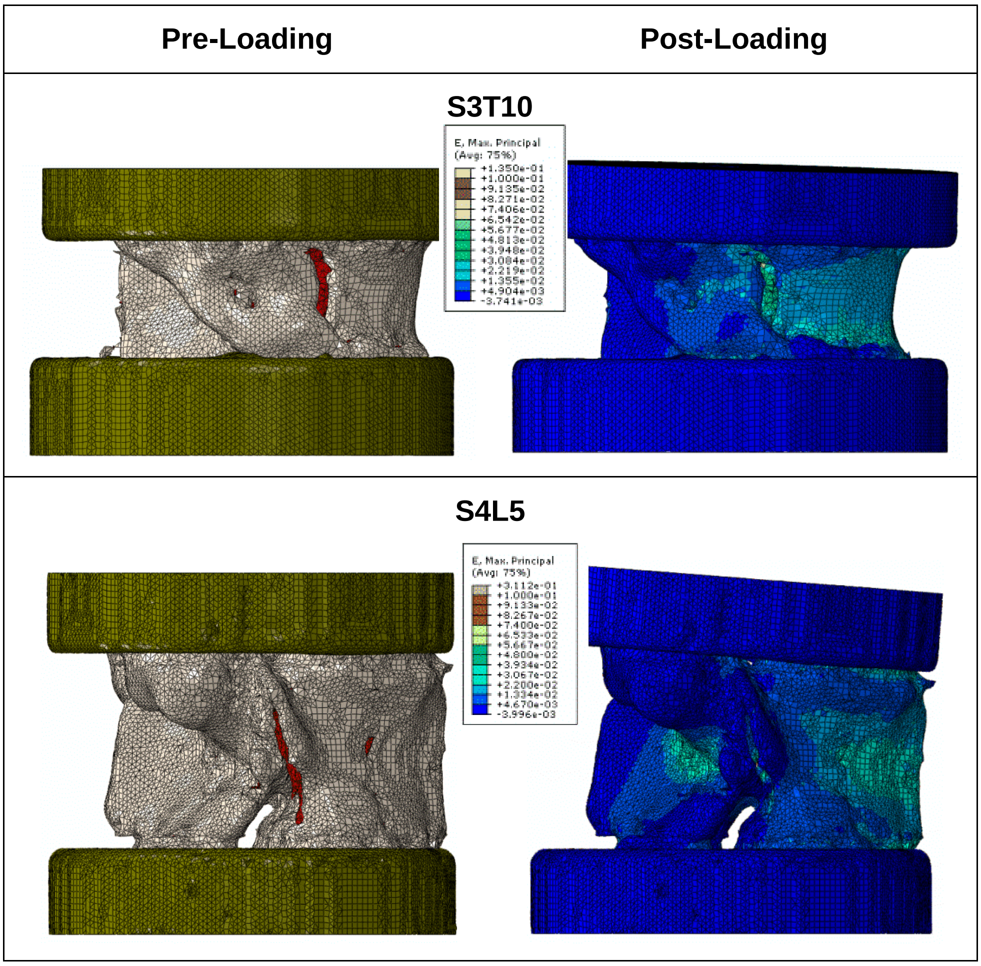

Figure 5.3 Lateral images of the models with the greatest and least computational accuracy, S3T10 (2%) and S4L5 (32%), shown pre- and post-loading. The post-loading images show the maximum principal strain which has been capped at 0.1 to allow for comparison. The fracture is shown in the red in the pre-loading images. The posterior elements are on the left hand side of all images and the vertebral body is on the right.

Both of the specimens were seen to deform mostly in the anterior direction both experimentally and computationally. The greatest prevalence of fracture within each model was located in the vertebral body which may suggest why the models deformed most in that direction. The model of S4L5 had a more concentrated strain distribution in the anterior of the vertebral body than S3T10 and also displayed greater levels of strain in the posterior elements which is why the model of S4L5 deformed to a greater extent than the model of S3T10.

Upon further evaluation of the two models, the specimen with the greatest computational accuracy, S3T10, was found to possess a marginally greater percentage of fracture. The percentage of fracture elements, in relation to bone elements, was 5% for S3T10 and 4% for S4L5. As these values were quite similar, it may be likely that the percentage of fracture does not have as great an effect on the stiffness of the specimen in comparison to the location and extent of the fracture.

The models of S3T10 and S4L5 are shown, pre-loading and without the PMMA loading plates, in lateral and posterior views in Figure 5.4. Also shown are the corresponding semi-transparent views where the distribution of the fracture is visible.

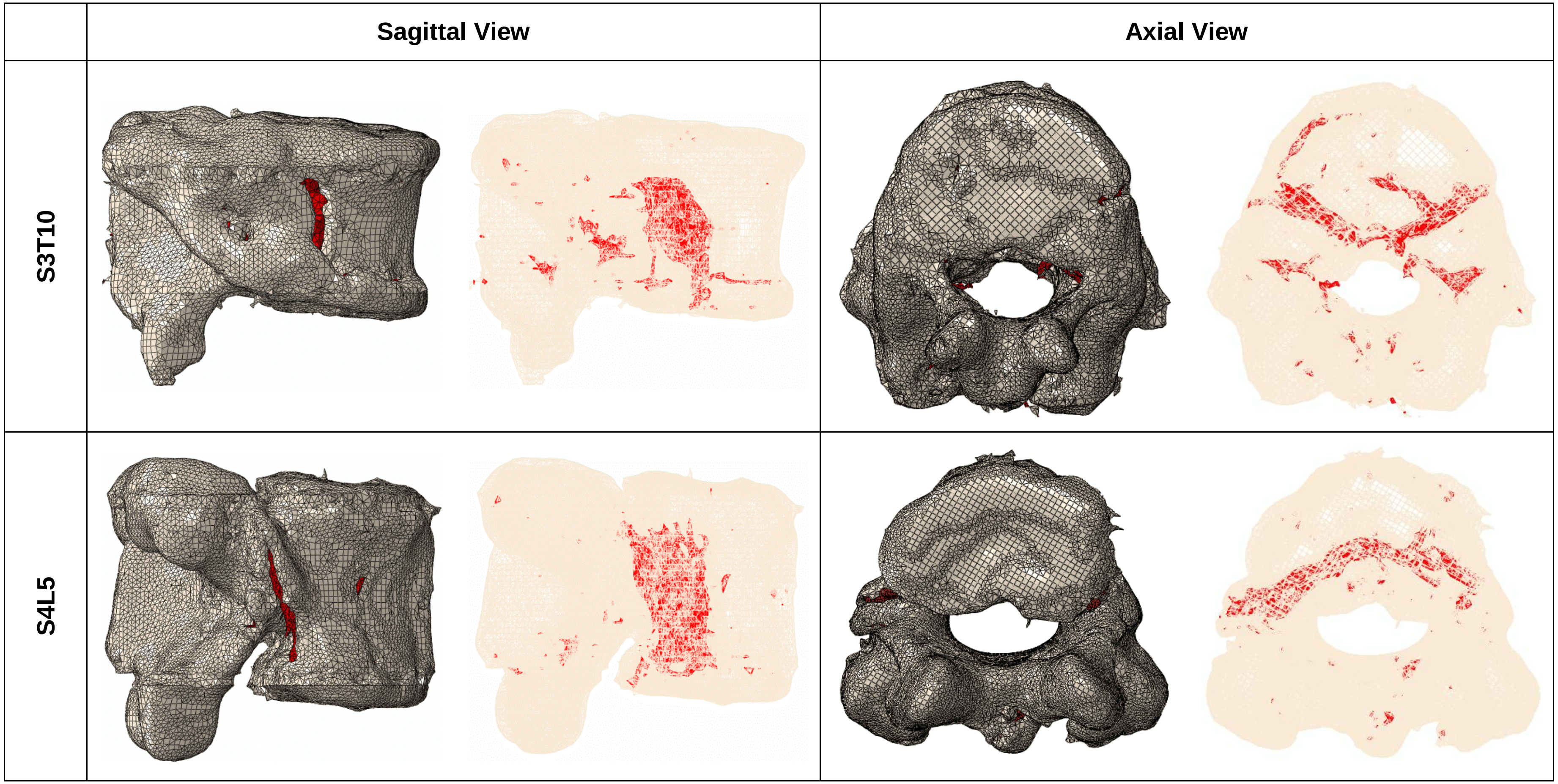

Figure 5.4 The single cycle models with the greatest and least computational accuracy, S3T10 (2%) and S4L5 (32%). For the sagittal view, the posterior elements are on the left hand side and the vertebral body is on the right hand side. The fracture is shown in red.

The lateral images show that the majority of the fracture of the least computationally accurate specimen, S4L5, appeared to be more column-like in shape than the fracture of S3T10 and that it also spanned a greater percentage of the vertebral height which may suggest why it was more prone to anterior buckling. The posterior view of S4L5 showed that the fracture was more prevalent in the vertebral body than that of S3T10. The fracture of S3T10 can be seen to have divided into two distinct regions within the vertebral body and extended to the pedicles. In general, the fracture of the specimen with the least computational accuracy, S4L5, appeared to encompass a greater extent of the vertebral body than the fracture of the most computationally accurate specimen, S3T10.

It is possible that a greater level of fracture in the vertebral body resulted in less computational accuracy. Therefore, it is feasible that the modelling technique may have been more suitable for simulating the behaviour of specimens where the fracture did not extend across the height and width of the vertebrae in such an extensive manner. However, the general agreement was good and not too dissimilar from the accuracy obtained for intact porcine vertebra (Tarsuslugil 2011) which increased confidence in the modelling technique.

5.3 Multi-Cycle Modelling

The results of the computational modelling of the multi-cycle specimens are presented in the following section. The findings from the modelling of the initial loading cycles for the non-augmented, PMMA augmented and CaP augmented specimens are presented in the three initial subsections. The results are presented in terms of the stiffness values, the loaded displacements, the permanent deformations and where applicable, an investigation into the effectiveness of the cement/bone interface. A discussion is presented at the end of the non-augmented, PMMA and CaP augmented subsections. The results from the simulation of subsequent loading cycles and the clinical applications are presented in the final subsections.

5.3.1 Non-Augmented Group

The experimental and computational load-displacement curves for the non-augmented multi-cycle specimens are shown in Figure 5.5. The computational permanent deformation was simulated using the criteria for plastic yielding as outlined in Section 4.3.3.

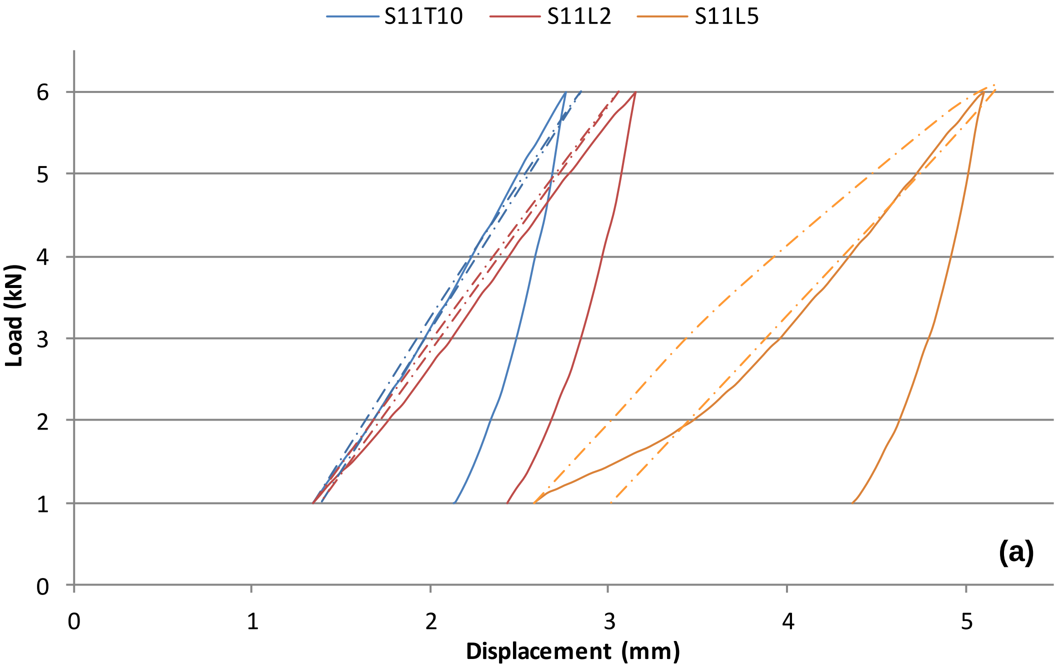
S11T10
S11L2
S11L5
Load (kN)
0
1
2
3
4
5
6
Displacement (mm)
0
1
2
3
4
5
(a)

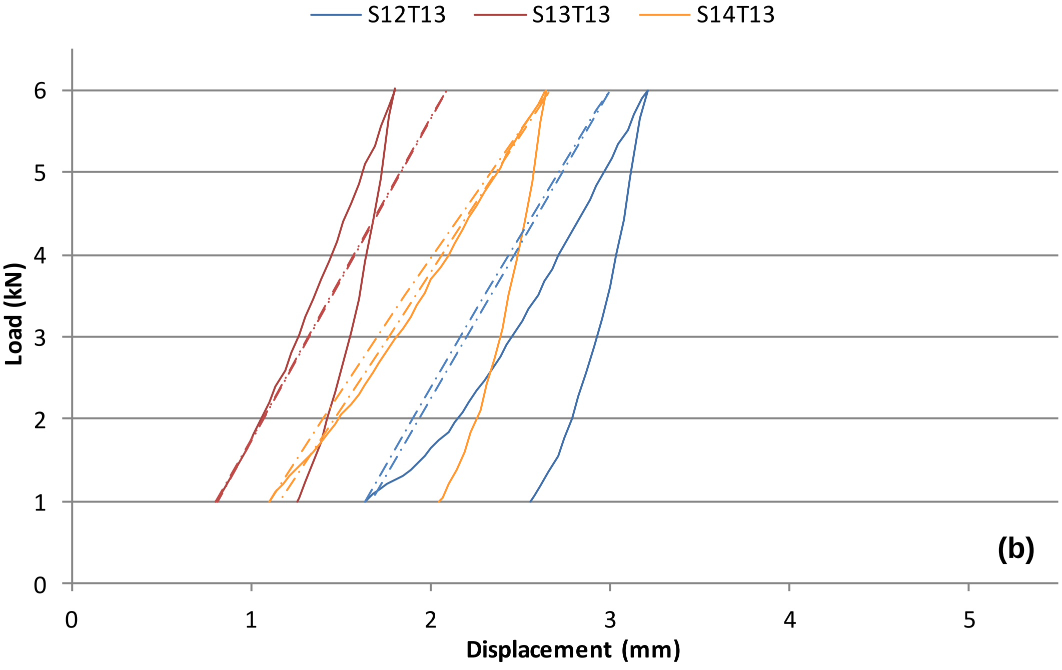
S12T13
S13T13
S14T13
Load (kN)
0
1
2
3
4
5
6
Displacement (mm)
0
1
2
3
4
5
(b)

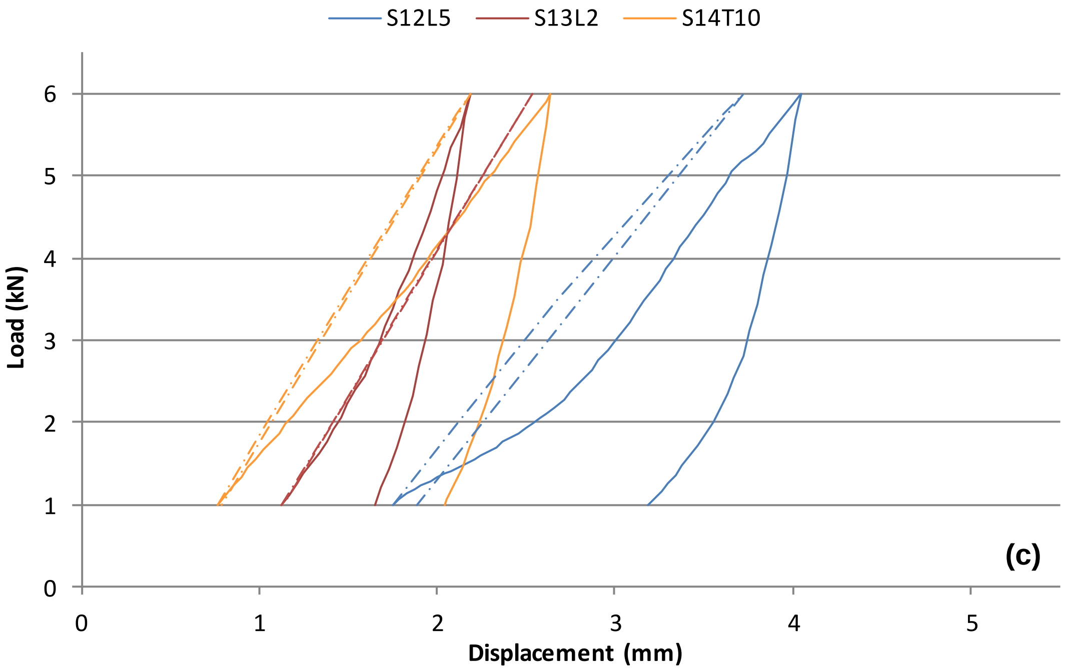

Figure 5.5 Experimental and computational (dashed lines) load-displacement curves for the non-augmented multi-cycle specimens (a) S11T10, S11L2 and S11L5, (b) S12T13, S13T13 and S14T13 and (c) S12L5, S13L2 and S14T10.

The experimental and computational load-displacement curves were used to determine the errors associated with the predicted stiffness values, the loaded displacements and the permanent deformations of the group.

Stiffness Values

A plot of the experimental and computational stiffness values of each of the non-augmented specimens is shown in Figure 5.6.

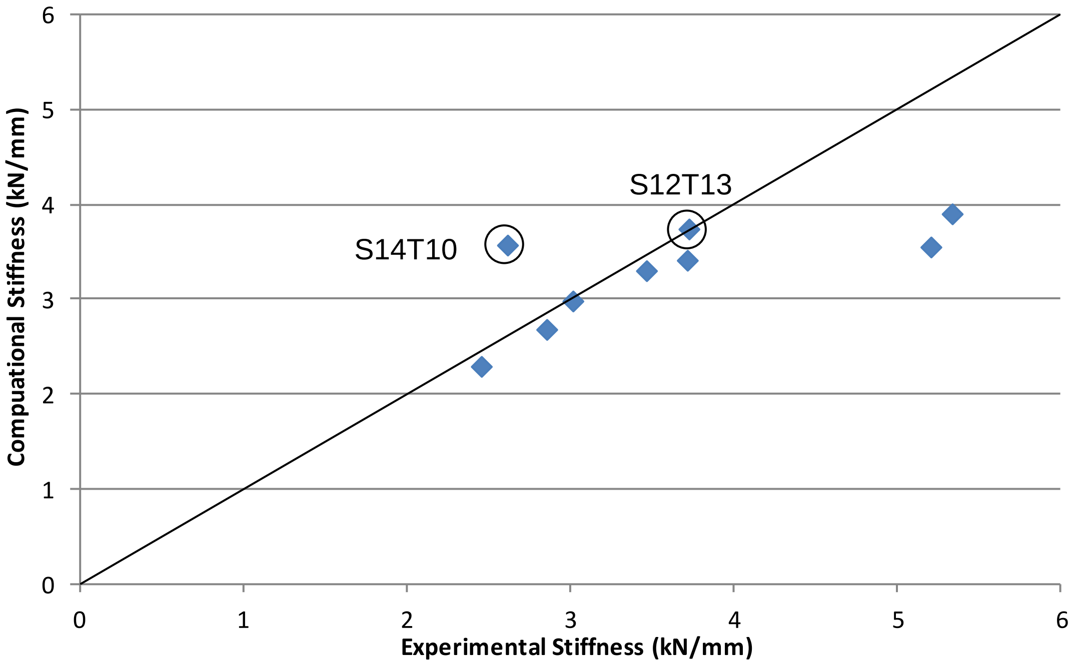

Figure 5.6 Computational and experimental stiffness values of the non-augmented multi-cycle specimens. The circled specimens, S12T13 and S14T10, possessed the greatest and least computational accuracy for stiffness, respectively.

There was generally good agreement between the FE predictions and the experimental results. As for the single cycle specimens, the mean absolute error of the predicted stiffness values for the set was 14%. The greatest computational error was associated with the model of S14T10 which overestimated the experimental stiffness by 36% whilst the greatest computational accuracy was displayed by the model of S12T13 which overestimated the experimental stiffness by less than 1%; both of these specimens can be seen highlighted on Figure 5.6.

The mean-difference plot of the experimental and computational stiffness values for the non-augmented specimens is shown in Figure 5.7. The specimens with the greatest and least computational accuracy in terms of stiffness, S12T13 and S14T10, are shown highlighted on the figure.

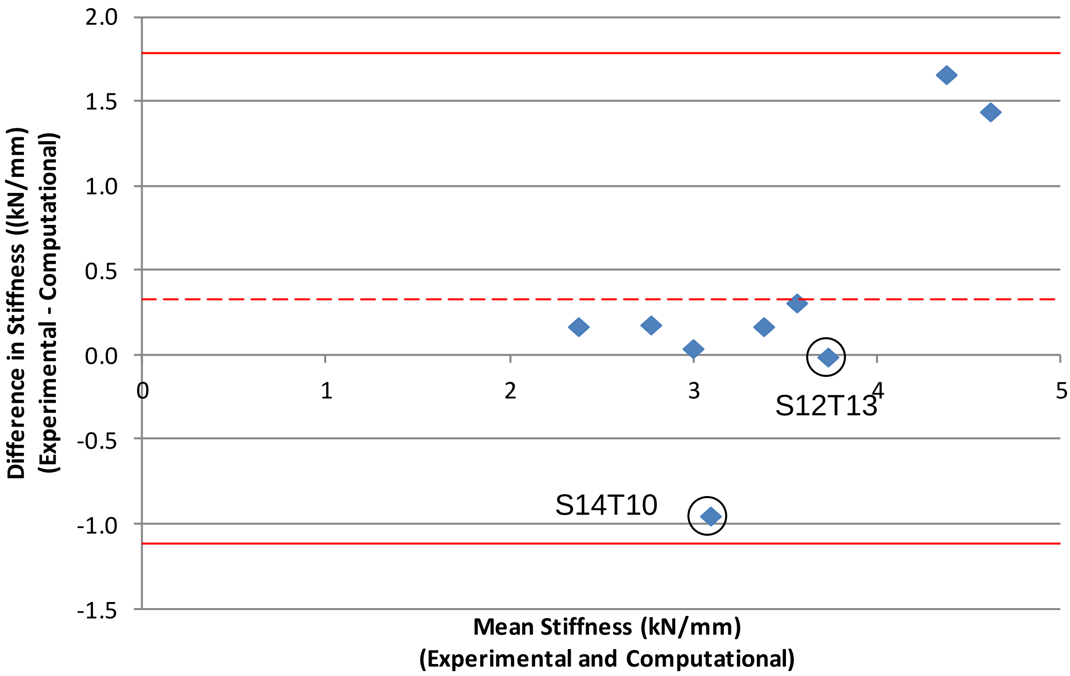

Figure 5.7 A mean-difference plot of the experimental and computational stiffness values for the non-augmented multi-cycle specimens. The dashed and solid red lines show the mean difference value and the limits of agreement (1.96 x standard deviation). The circled specimens, S12T13 and S14T10, possessed the greatest and least computational accuracy for stiffness, respectively.

There was a general trend for the computational model to slightly overestimate the experimental stiffness although the difference between all of the experimental and computational stiffness values fell within the limits of agreement.

Loaded Displacements

The experimental and computational values of displacement when the non-augmented specimens were fully loaded to 6 kN during the first loading cycle are shown in Figure 5.8.

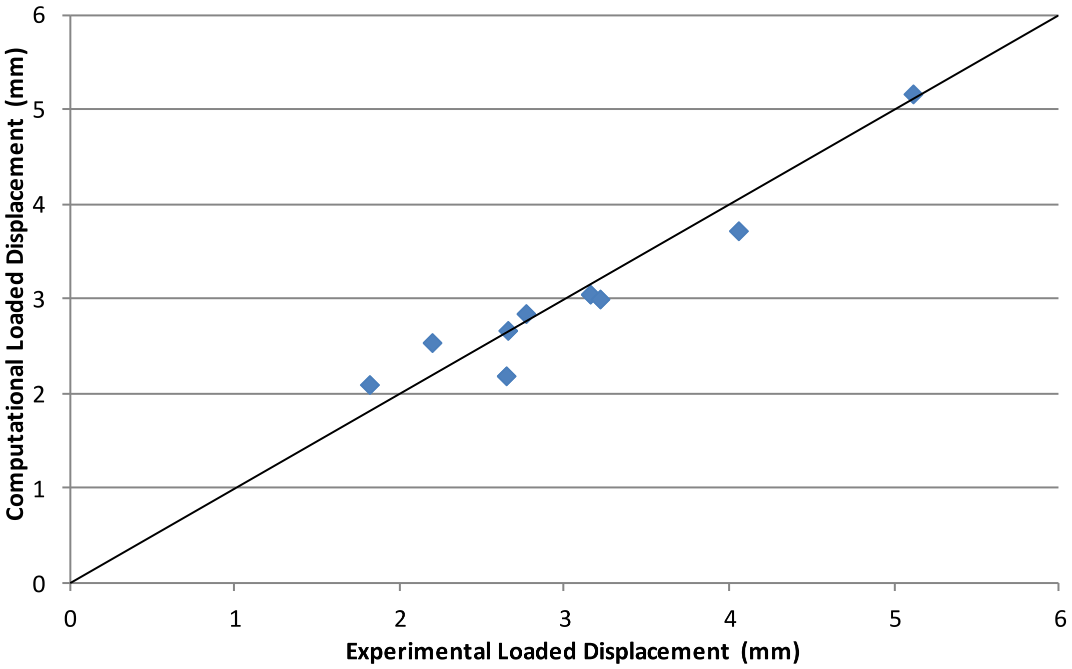

Figure 5.8 The experimental and computational values for displacement of the non-augmented multi-cycle group when the specimens were loaded to 6 kN.

There was generally good agreement for the FE predicted loaded displacement. The absolute error for the simulation of the loaded displacement was 8%. The greatest computational error was an underestimation of 17% whilst the most accurate was an overestimation of less than 1%.

The mean-difference plot for the experimental and computational values of loaded displacement is shown in Figure 5.9.

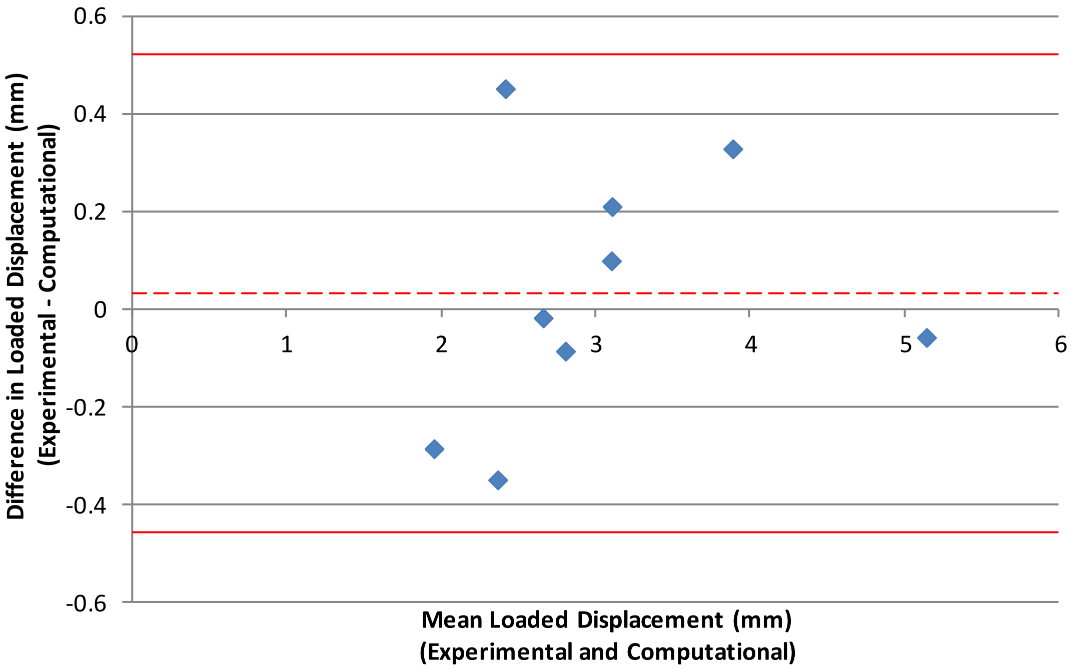

Figure 5.9 A mean-difference plot of the experimental and computational loaded displacement values for the non-augmented multi-cycle specimens. The dashed and solid red lines show the mean difference value and the limits of agreement (1.96 x standard deviation).

There was a slight bias towards the overestimation of the computational loaded displacement but the difference between all of the experimental and computational loaded displacement values fell within the limits of agreement.

Permanent Deformations

The experimental and computational values observed for the permanent deformation of the non-augmented specimens following the initial loading cycle are shown in Figure 5.10.

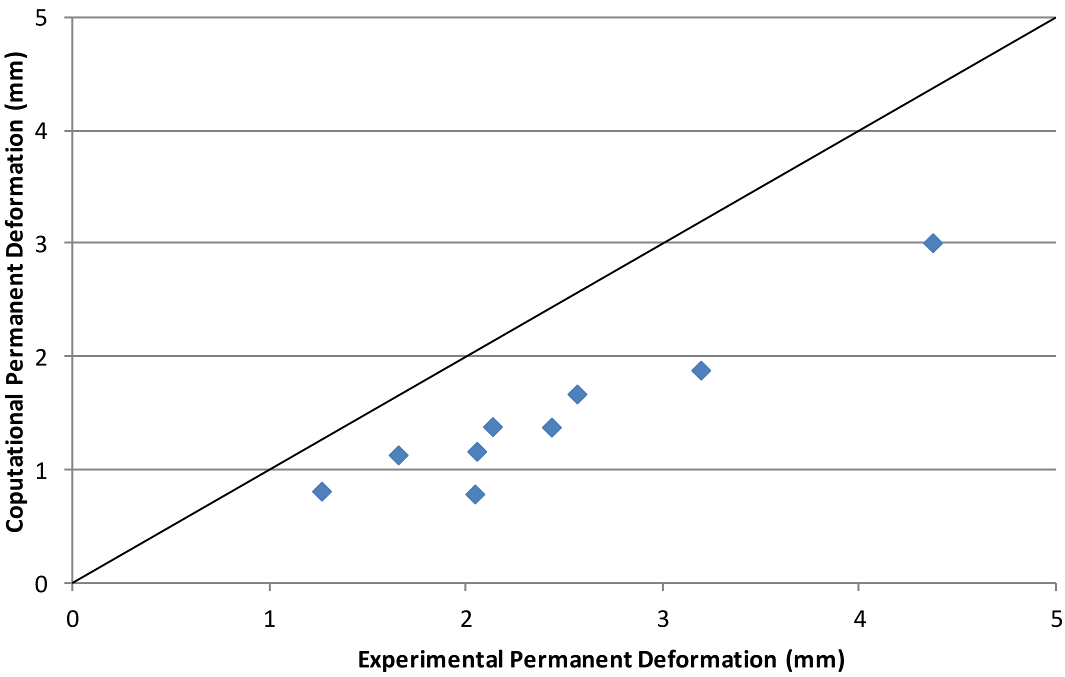

Figure 5.10 The experimental and computational values for the permanent deformation of the non-augmented multi-cycle specimens when the specimens were unloaded to 1 kN.

The level of agreement between the FE predicted permanent deformation and the experimental deformation was poor. The absolute error for the simulation of the permanent deformation was 40%. The greatest computational error was an underestimation of the permanent deformation by 61% whilst the most accurate was an underestimation of 31%. Although the results appeared to lie on a straight line, it was not the line of agreement.

The mean-difference plot for the experimental and computational values of permanent deformation is shown in Figure 5.11.

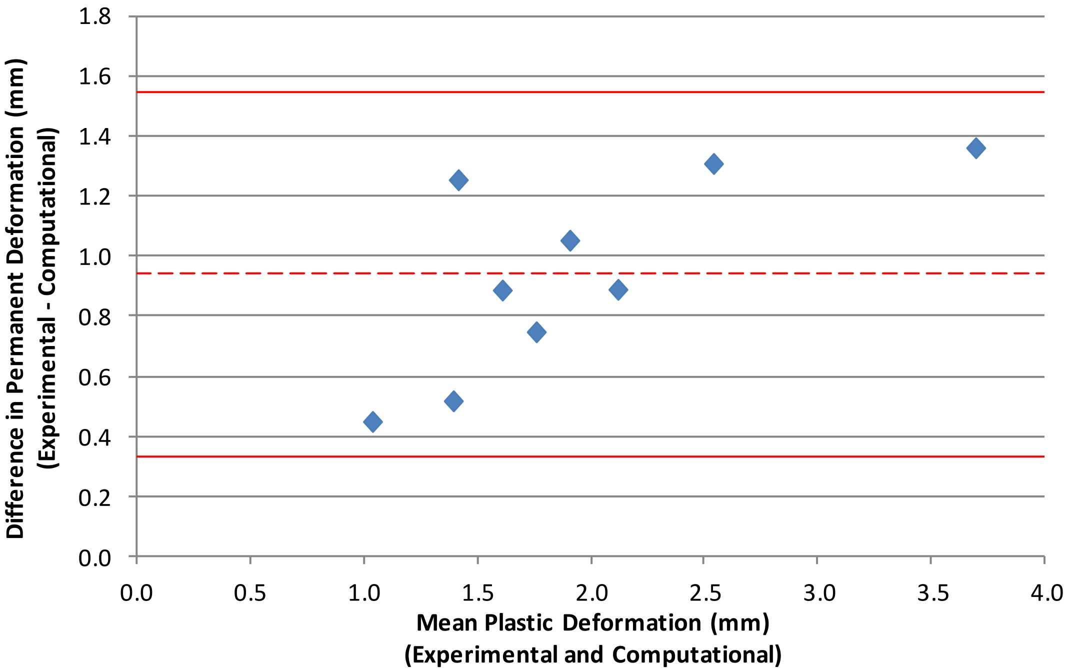

Figure 5.11 A mean-difference plot of the experimental and computational permanent deformation values for the non-augmented multi-cycle specimens. The dashed and solid red lines show the mean difference value and the limits of agreement (1.96 x standard deviation).

Each model underestimated the experimental loaded displacement however; the difference between all of the experimental and computational permanent deformation values fell within the limits of agreement.

Discussion

The percentage of fracture present in the models with the greatest and least computational accuracy, in terms of stiffness, was 4% for S12T13 and 6% for S14T10. As was observed with the single cycle specimens presented in the discussion above, the values are quite similar which again implies it is likely that the percentage of fracture did not have as great an effect on the prediction of the stiffness of the specimen in comparison to the location and extent of the fracture. The models of S12T13 and S14T10 are shown, pre-loading and without the PMMA loading plates, in lateral and posterior views in Figure 5.12. Also shown are the corresponding semi-transparent views where the fracture is visible.

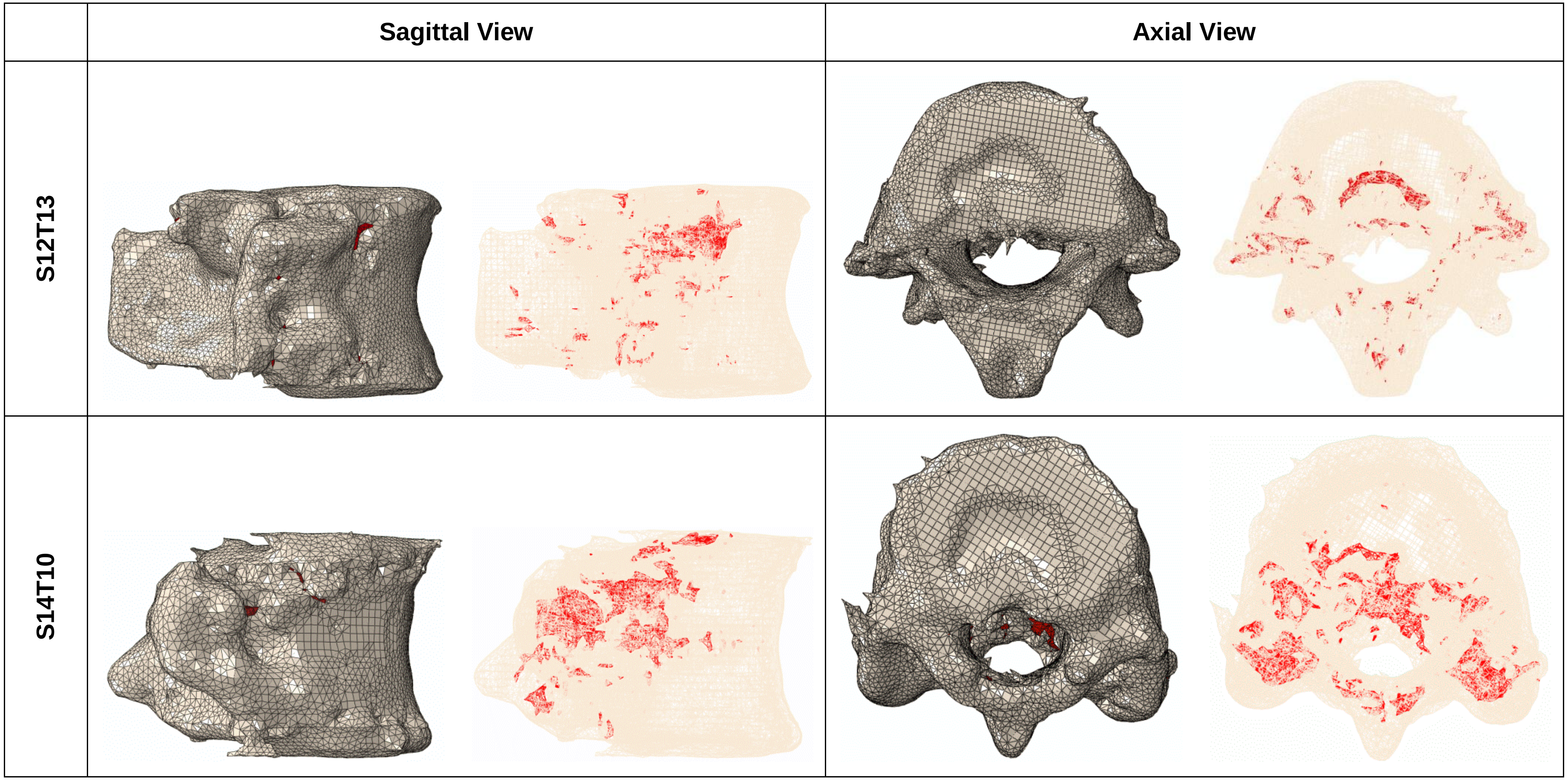

Figure 5.12 The non-augmented multi-cycle models with the greatest and least computational accuracy in terms of stiffness, S12T13 (1%) and S14T10 (36%). For the sagittal view, the posterior elements are on the left hand side and the vertebral body is on the right hand side. The fracture is shown in red.

It can be seen from the images that the fracture pattern of the least computationally accurate model, S14T10, was more dispersed than that of S12T13 and can be seen to have covered a greater extent of the vertebral body. As was hypothesised with the single cycle specimens, it is possible that the modelling technique employed may have been more suitable for simulating the behaviour of specimens with less dispersed fracture patterns. However, the level of agreement between the single and multi-cycle specimens provides additional confidence for the modelling technique.

5.3.2 Polymethylmethacrylate Augmented Group

The experimental and computational load-displacement curves for the PMMA augmented multi-cycle specimens are shown in Figure 5.13. The computational permanent deformation was simulated for the successful specimens using the criteria for plastic yielding as outlined in Section 4.3.3.

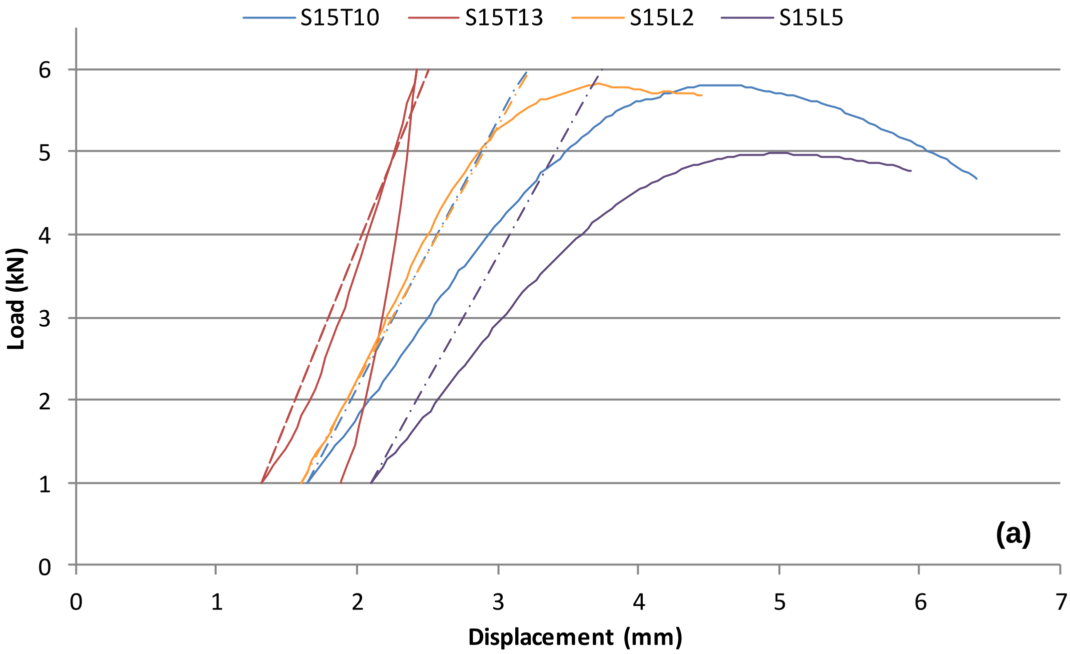

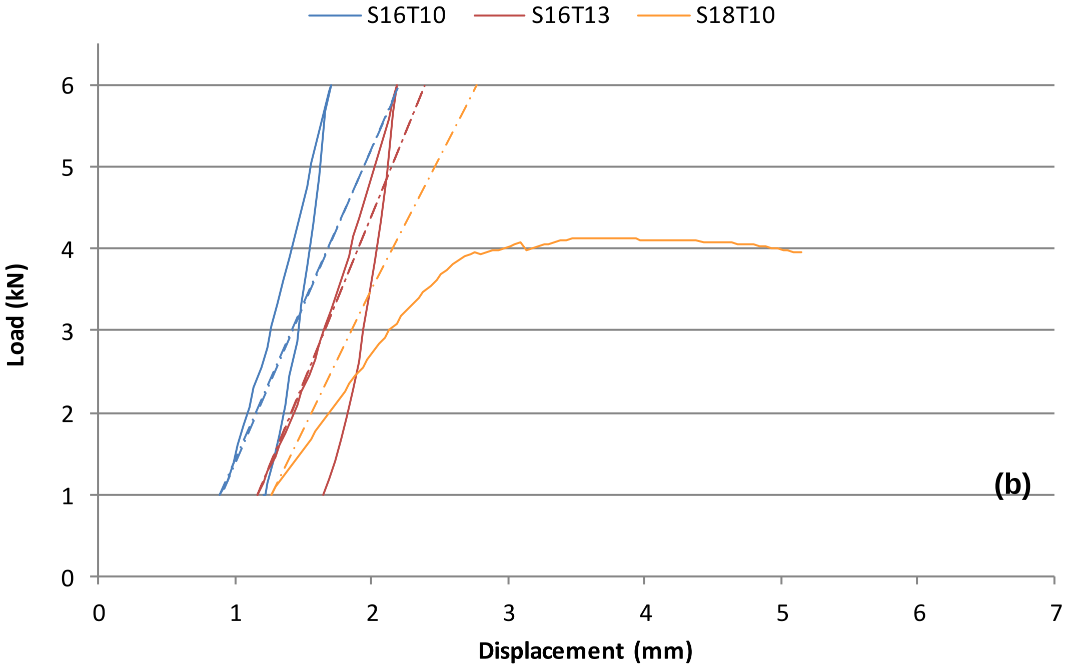

Figure 5.13 Experimental and computational (dashed lines) load-displacement curves for the PMMA augmented multi-cycle specimens (a) S15T10, S15T13, S15L2 and S15L5 and (b) S16T10, S16T13 and S18T10.

The experimental and computational load-displacement curves were used to determine the errors associated with the predicted stiffness values, the loaded displacements and the permanent deformations of the group.

Stiffness Values

A plot of the experimental and computational stiffness values of each of the PMMA augmented specimens is shown in Figure 5.14.

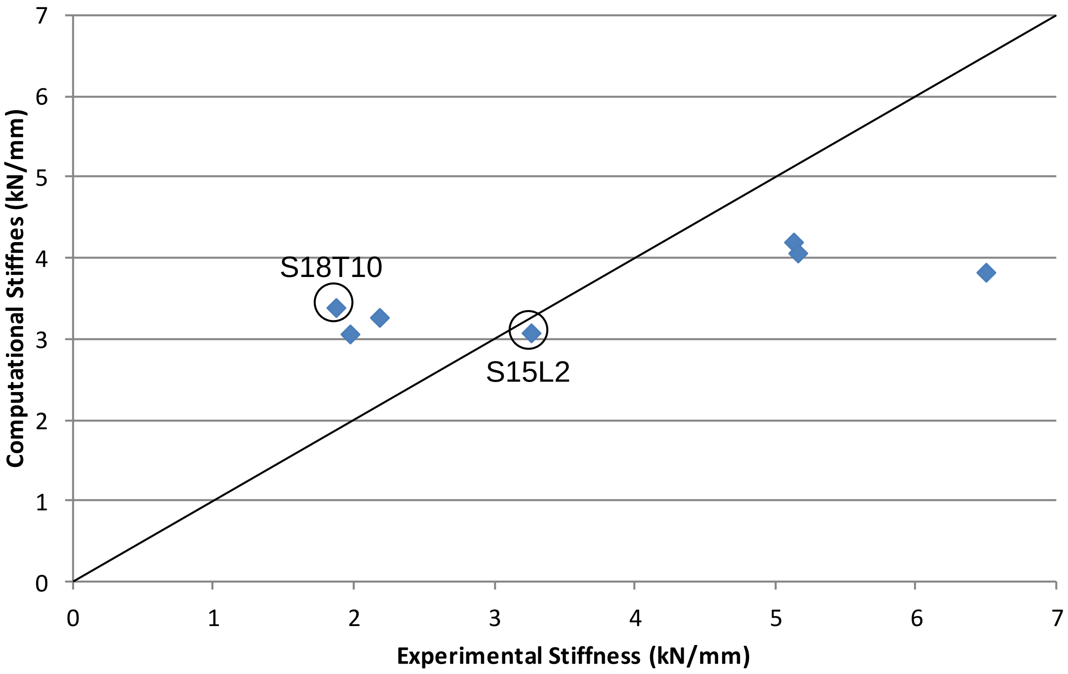

Figure 5.14 Computational and experimental stiffness values of the PMMA augmented multi-cycle specimens. The circled specimens, S15L2 and S18T10, possessed the greatest and least computational accuracy for stiffness, respectively.

There was poor agreement between the computational and experimental stiffness values and the mean absolute error of the predicted stiffness values for the set was 39%. The greatest computational error was associated with the model of S18T10 which overestimated the experimental stiffness by 82% whilst the greatest computational accuracy was displayed by the model of S15L2 which underestimated the experimental stiffness by 6%. Both of these specimens can be seen highlighted on Figure 5.14.

The mean-difference plot of the experimental and computational stiffness values for the PMMA augmented specimens is shown in Figure 5.15. The specimens with the greatest and least computational accuracy in terms of stiffness, S18T10 and S15L2, respectively, are shown highlighted on the figure.

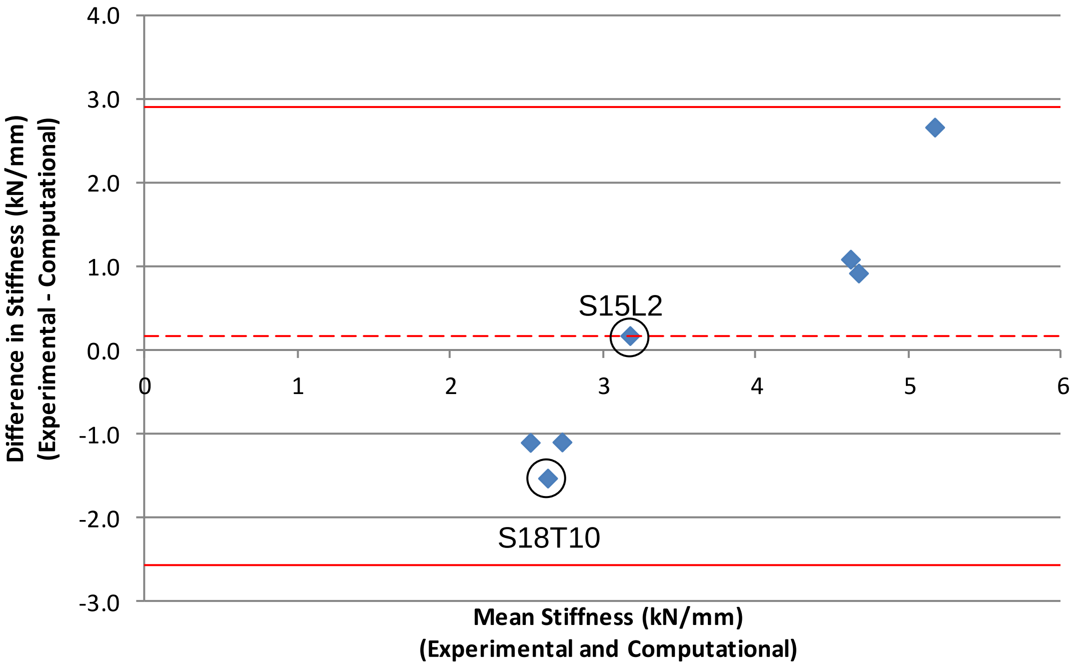

Figure 5.15 A mean-difference plot of the experimental and computational stiffness values for the PMMA augmented multi-cycle specimens. The dashed and solid red lines show the mean difference value and the limits of agreement (1.96 x standard deviation). The circled specimens, S15L2 and S18T10, possessed the greatest and least computational accuracy for stiffness, respectively.

There was no clear distinction between a general under- or overestimation of the experimental stiffness. The difference between all of the experimental and computational stiffness values fell within the limits of agreement although the model could not predict the variation in stiffness as seen in the experimental specimens (Figure 5.14), where all of the predicted values lay within in a range of approximately 1.2 kN/mm.

Loaded Displacements

The experimental and computational values of displacement when each specimen was fully loaded are shown in Figure 5.16. For the specimens that failed during the initial loading cycle, the value of displacement was capped, experimentally and computationally, at point where the maximum value of experimental stiffness was taken from, as discussed in Section 3.3.2.

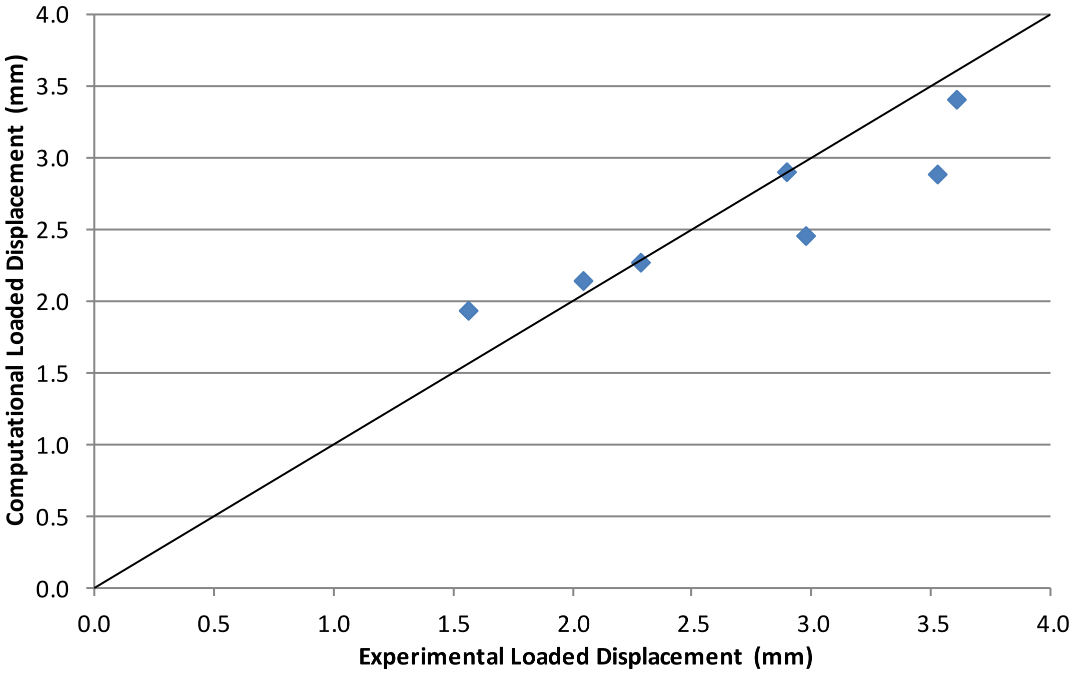

Figure 5.16 The experimental and computational values for displacement of the PMMA augmented group when the specimen was loaded to 6 kN.

There was good agreement between the predicted and experimental loaded displacement values and the mean absolute error for the simulation of the loaded displacement was 10%. The greatest computational error was an underestimation of 24% whilst the most accurate model overestimated the initial displacement by less than 1%.

The mean-difference plot for the experimental and computational values of loaded displacement is shown in Figure 5.17.

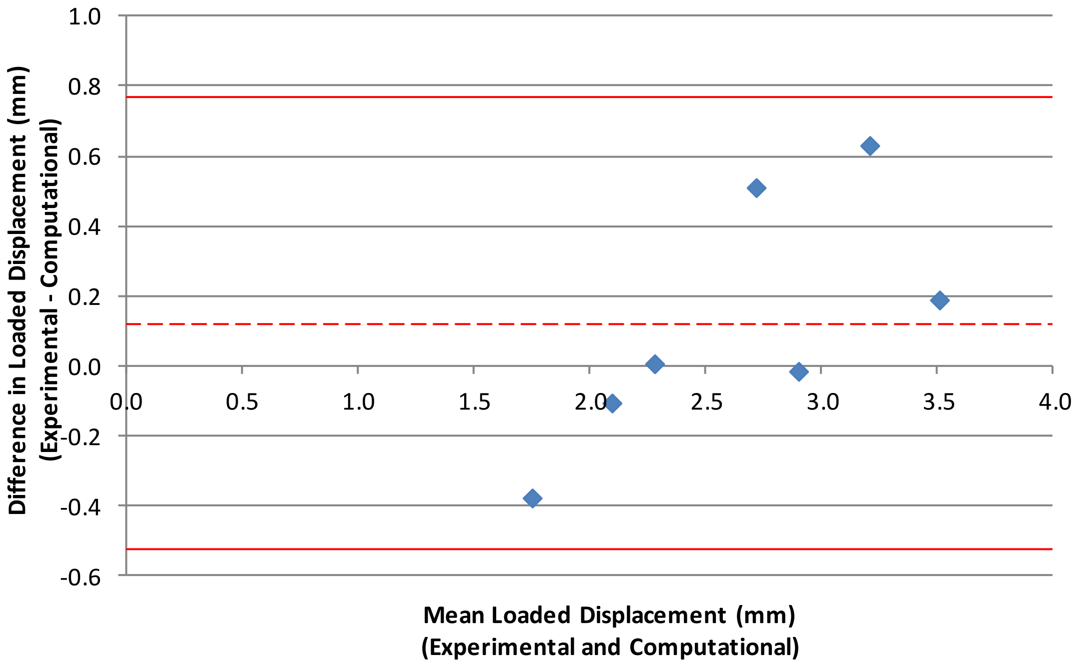

Figure 5.17 A mean-difference plot of the experimental and computational loaded displacement values for the PMMA augmented multi-cycle specimens. The dashed and solid red lines show the mean difference value and the limits of agreement (1.96 x standard deviation).

There was a general tendency for the predicted loaded displacement to underestimate the experimental value but the difference between all of the experimental and computational loaded displacement values fell within the limits of agreement.

Permanent Deformations

The computational permanent deformation of the PMMA augmented specimens that were successfully tested during the experimental loading were each approximately zero (Figure 5.13). For this reason, a plot of the experimental and computational values for permanent deformation is not presented.

Cement/Bone Interface

When the material properties of the PMMA cement in each model was altered to be that of fracture, which had a very low modulus of $1x10^{-9}$ GPa and therefore approximated frictionless contact, the computational error of the group in terms of stiffness decreased from the original value of 39% to 35%. The values for predicted stiffness for the original computational models and the models with 100% fracture can be seen for a selection of three specimens, in conjunction with the experimental stiffness values, in Figure 5.18.

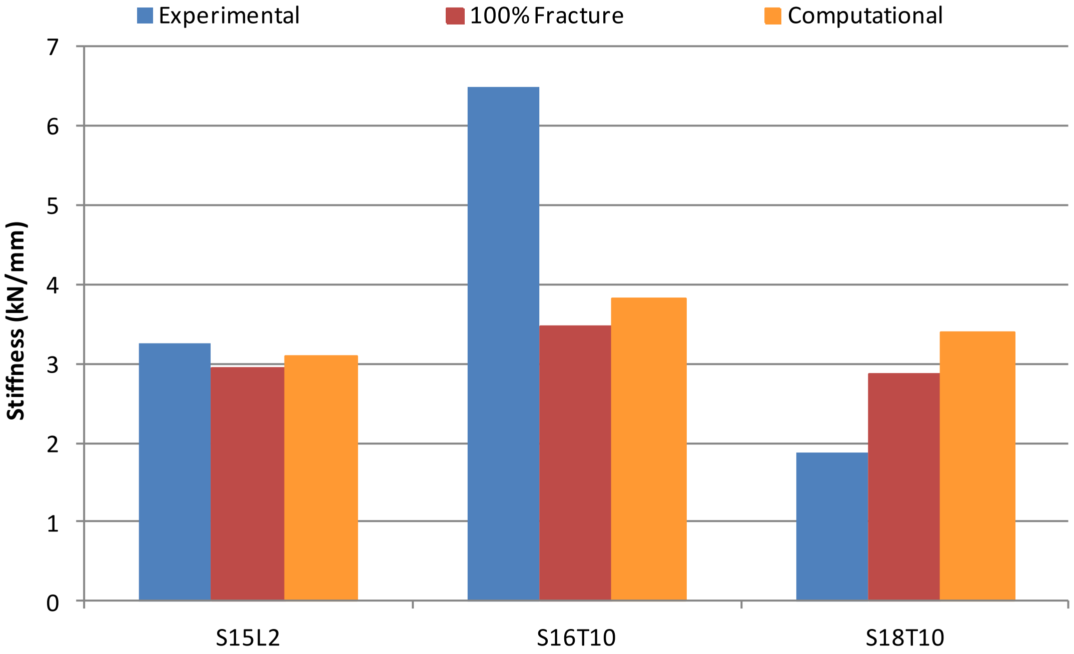

Figure 5.18 Experimental and predicted stiffness values for the original computational models and models with the material properties of PMMA altered to those of fracture (100% Fracture) for three PMMA augmented multi-cycle specimens.

For two of the specimens, S15L2 and S16T10, the original computational stiffness underestimated the experimental value and when 100% fracture was simulated, the accuracy of the predicted stiffness decreased. However, the predicted stiffness for S18T10 was closer to the experimental value when the material properties of the PMMA were altered to those of the fracture (100% Fracture). The improvement in the computational accuracy of S18T10 was a reduction in the predicted stiffness of 16%. As the overall group improvement in the stiffness error was only 4%, it is unlikely that the interface between the PMMA cement and the bone was the only, or main, reason why there was poor agreement between the experimental and computational values for the PMMA augmented set.

Discussion

The specimens with the least and greatest computational accuracy, in terms of stiffness, were S18T10 and S15L2, with respective errors of 86% and 6%. For each model, the percentage of fracture elements in relation to bone elements and the percentage of fracture filled with PMMA was 3% fracture with 71% fill for S15L2 and 17% fracture with 67% fill for S18T10. Unlike the models presented in the previous discussions, there was a variation in the percentage of fracture elements present although the level of augmentation was similar. Therefore, as hypothesised above, it is likely that the distribution of the fracture and the level of fracture present may have had an effect on the computational accuracy in terms of stiffness.

The models of S15L2 and S18T10 are shown, pre-loading and without the PMMA loading plates, in lateral and posterior views in Figure 5.19. Also shown are the corresponding semi-transparent views.

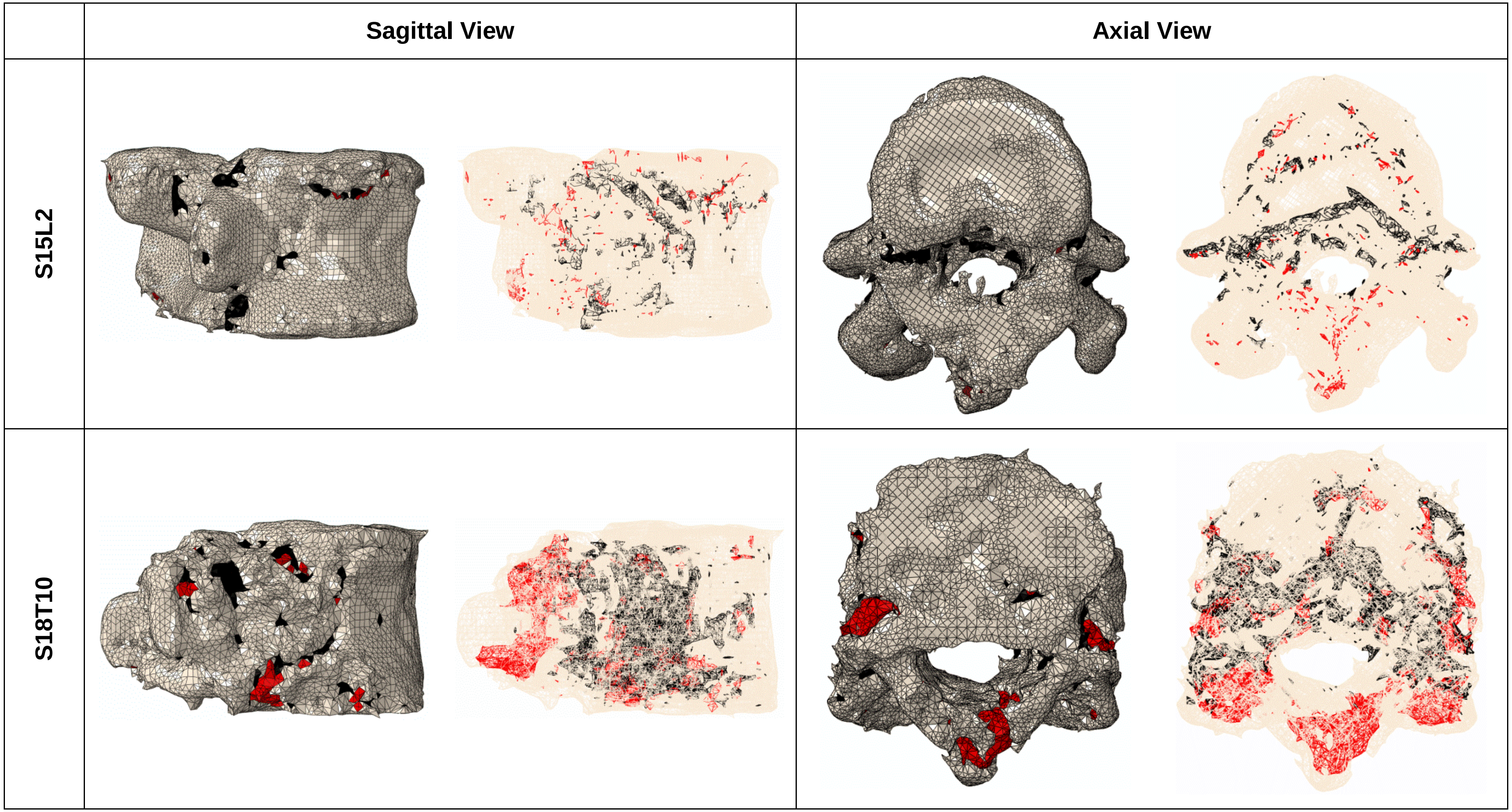

Figure 5.19 The PMMA augmented multi-cycle models with the greatest and least computational accuracy in terms of stiffness, S15L2 (6%) and S18T10 (86%). For the sagittal view, the posterior elements are on the left hand side and the vertebral body is on the right hand side. The unfilled fracture is shown in red and the cement is shown in black.

It can be seen from the images that the fracture and augmentation patterns of the least computationally accurate model, S18T10, were more dispersed than that of S15L2 and covered a greater extent of the vertebral body. As was hypothesised previously, it is likely that the modelling technique employed may have been more suitable for simulating the behaviour of specimens with less dispersed fracture and augmentation patterns. Therefore, it is possible that the group error of the PMMA augmented specimens, in terms of stiffness, was relatively large at 39% due to the dispersed fracture and the dispersed augmentation.

5.3.3 Calcium Phosphate Augmented Group

The experimental and computational load-displacement curves for the CaP augmented multi-cycle specimens are shown in Figure 5.20. The computational permanent deformation was simulated for the successful specimen using the criteria for plastic yielding as outlined in Section 4.3.3.

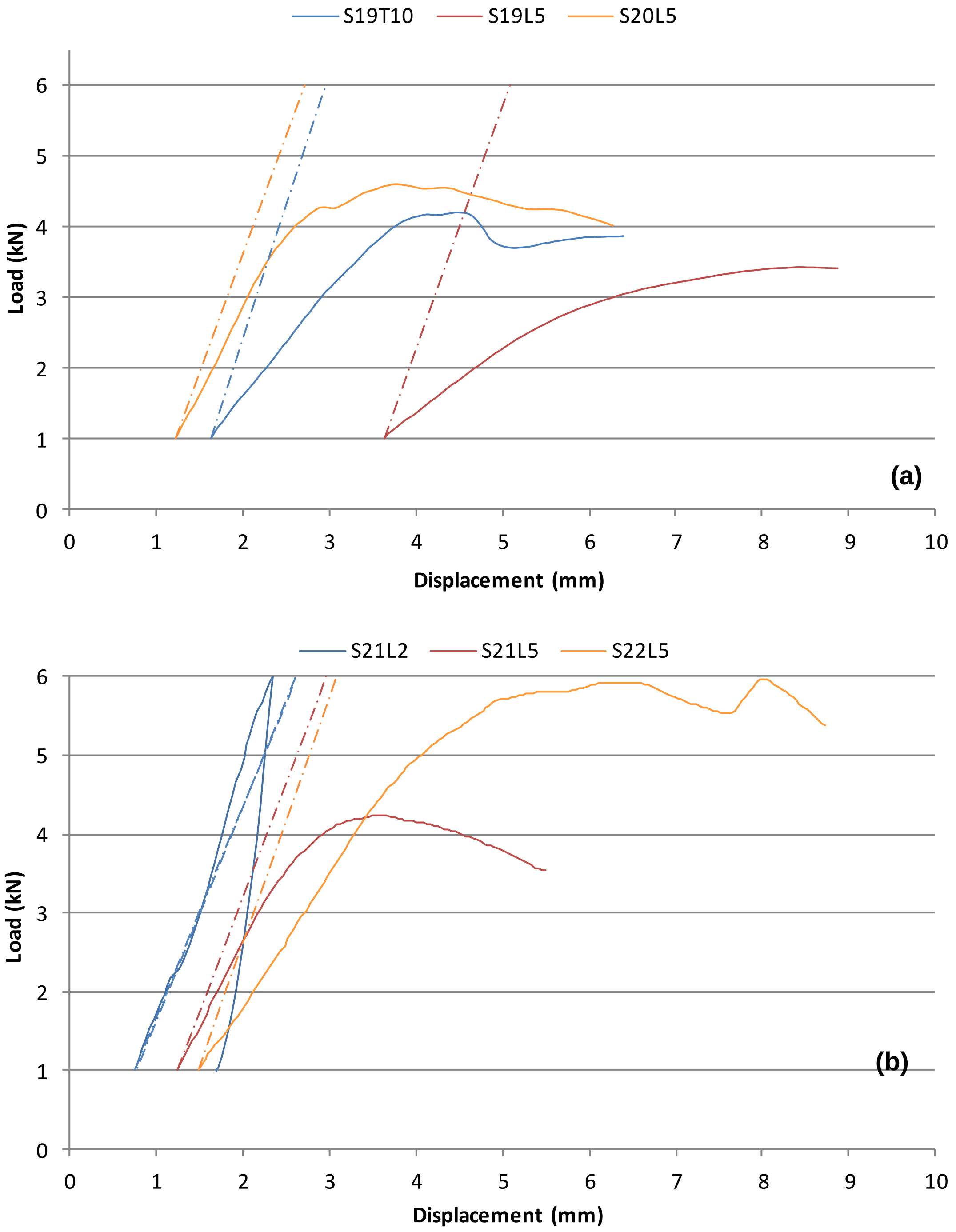

Figure 5.20 Experimental and computational (dashed lines) load-displacement curves for the CaP augmented multi-cycle specimens (a) S19T10, S19L5 and S20L5 and (b) S21L2, S21L5 and S22L5.

The experimental and computational load-displacement curves were used to determine the errors associated with the predicted stiffness values, the loaded displacements and the permanent deformations of the group.

Stiffness Values

A plot of the experimental and computational stiffness values of each of the CaP augmented specimens is shown in Figure 5.21.

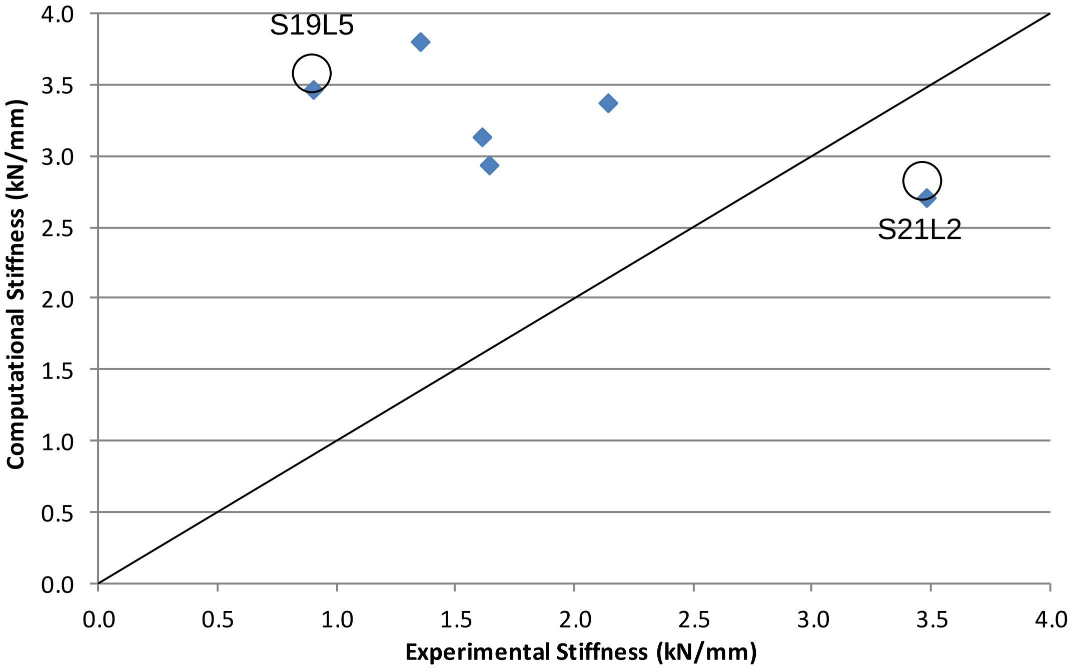

Figure 5.21 Computational and experimental stiffness values of the CaP augmented multi-cycle specimens. The circled specimens, S21L2 and S19L5, possessed the greatest and least computational accuracy for stiffness, respectively.

There was very poor agreement between the predicted and experimental stiffness values and the mean absolute error of the predicted stiffness values for the set was 120%. The greatest computational error was associated with the model of S19L5 which overestimated the experimental stiffness by 286% whilst the greatest computational accuracy was displayed by the model of S21L2 which underestimated the experimental stiffness by 22%. Both of these specimens can be seen highlighted on Figure 5.21.

The mean-difference plot of the experimental and computational stiffness values for the non-augmented specimens is shown in Figure 5.22. The specimens with the greatest and least computational accuracy, S21L2 and S19L5, respectively, are shown highlighted on the figure.

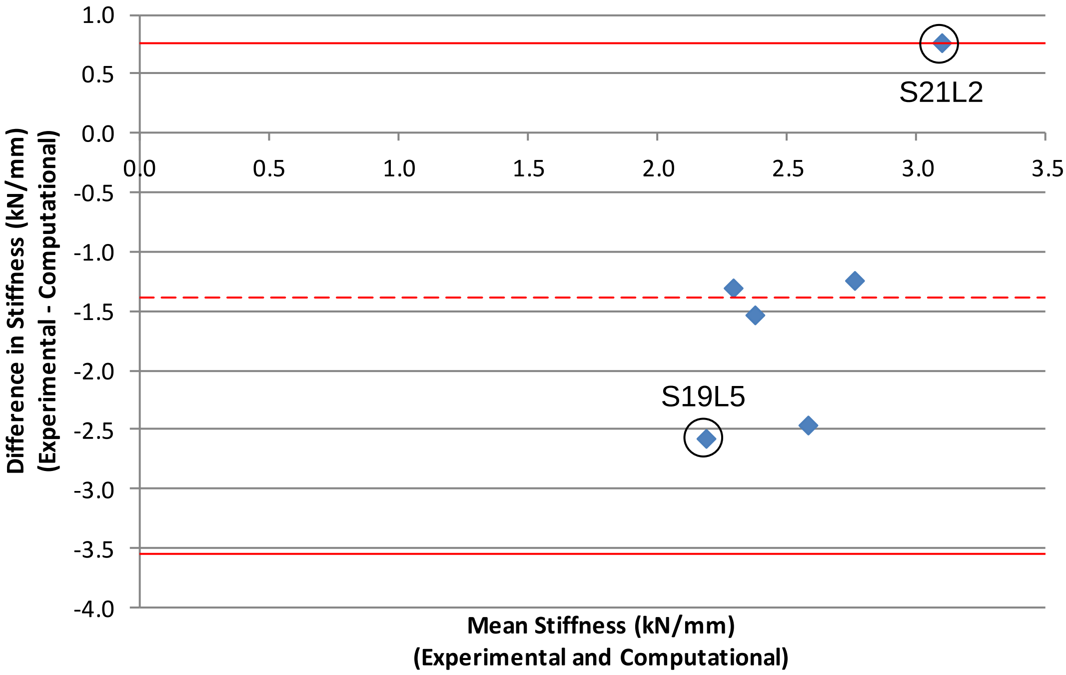

Figure 5.22 A mean-difference plot of the experimental and computational stiffness values for the CaP augmented multi-cycle specimens. The dashed and solid red lines show the mean difference value and the limits of agreement (1.96 x standard deviation). The circled specimens, S21L2 and S19L5, possessed the greatest and least computational accuracy for stiffness, respectively.

There was a general underestimation of stiffness for all specimens except S21L2. The difference between all of the experimental and computational stiffness values fell within the limits of agreement.

Loaded Displacements

The experimental and computational values of displacement for the CaP augmented group when the specimens were fully loaded is shown in Figure 5.23.

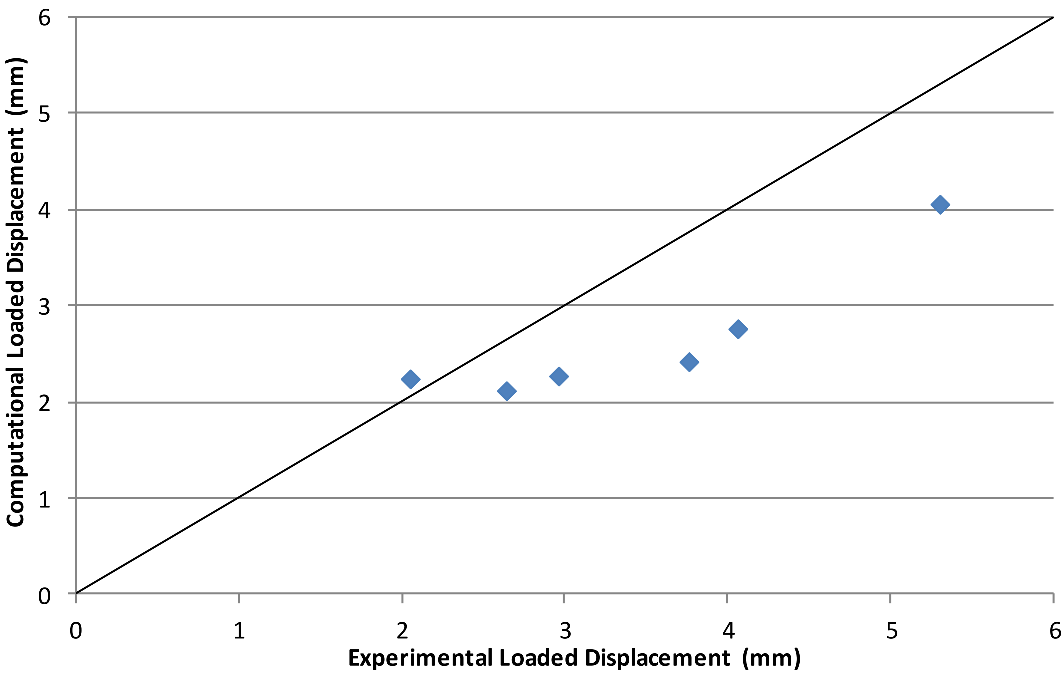

Figure 5.23 The experimental and computational values for displacement of the CaP augmented specimens when loaded to 6 kN.

There was generally good agreement between the computational and experimental loaded displacements. Although the data followed a straight line and had a similar ranking, the results did not fall on the line of agreement and the absolute error for the simulation of the loaded displacement was 24%. The greatest computational error was an underestimation of 36% whilst the most accurate model overestimated the initial displacement by 9%.

The mean-difference plot for the experimental and computational values of loaded displacement is shown in Figure 5.24.

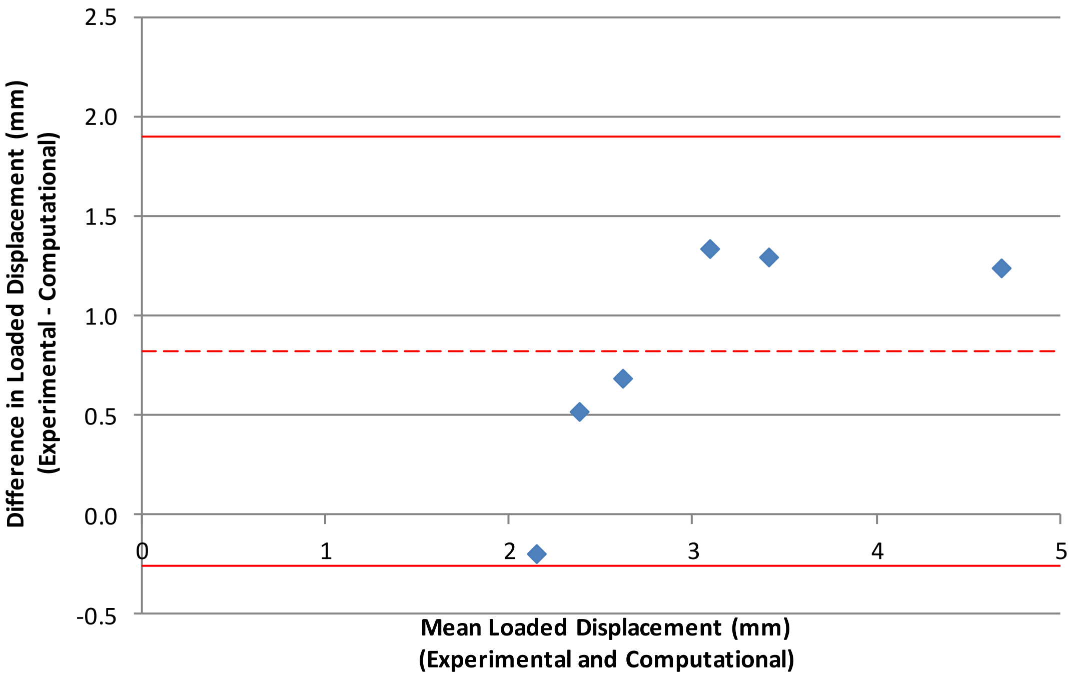

Figure 5.24 A mean-difference plot of the experimental and computational loaded displacement values for the CaP augmented multi-cycle specimens. The dashed and solid red lines show the mean difference value and the limits of agreement (1.96 x standard deviation).

There was an underestimation of the loaded displacement for all specimens except S21L2 however; the difference between all of the experimental and computational loaded displacement values fell within the limits of agreement.

Permanent Deformations

The computational permanent deformations of all the successful CaP augmented specimens was approximately zero (Figure 5.20). For this reason, a plot of the experimental and computational values for permanent deformation is not presented.

Cement/Bone Interface

When the material properties of the CaP cement in each model was altered to be that of fracture, the computational error of the group in terms of stiffness decreased from the original value of 120% to 99%. The values for predicted stiffness for the original computational models and the models with 100% fracture can be seen for a selection of three specimens, in conjunction with the experimental stiffness values, in Figure 5.25.

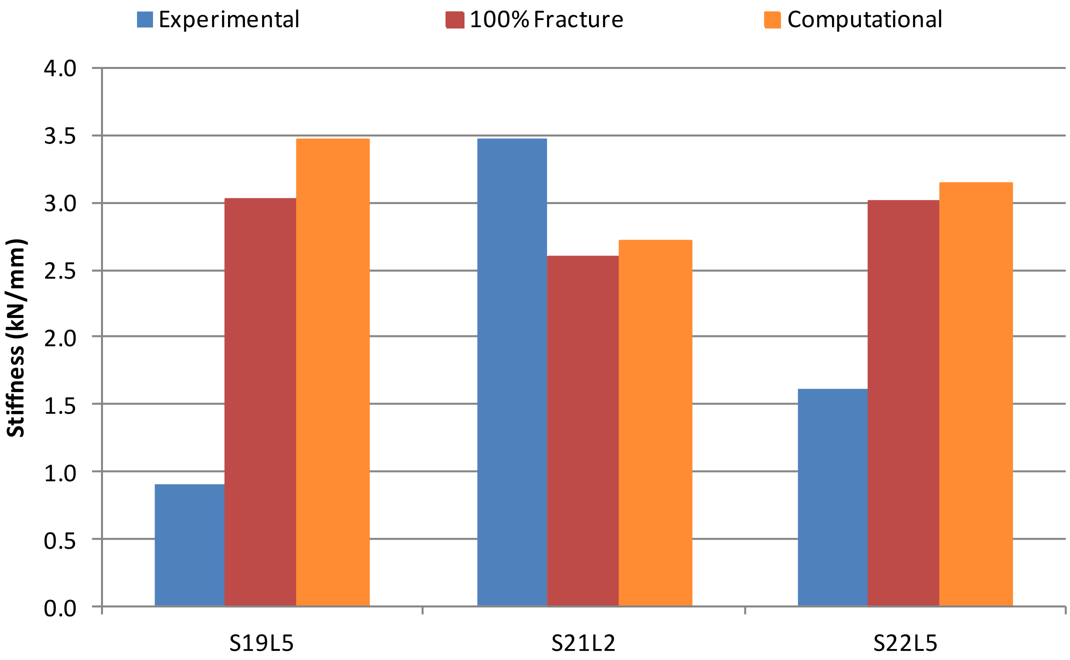

Figure 5.25 Experimental and predicted stiffness values for the original computational models and models with the material properties of CaP altered to those of fracture (100% Fracture) for three CaP augmented multi-cycle specimens.

For the specimen where the original computational stiffness underestimated the experimental value, S21L2, the simulation of 100% fracture led to a further increase in the error of the predicted stiffness. For the remaining specimens, S19L5 and S22L5, the predicted stiffness values were in greater agreement to the experimental value when the material properties of the PMMA were altered to those of the fracture (100% Fracture). However, as the magnitude of the improvement in the group stiffness error was 21%, it is unlikely that the interface between the CaP cement and the bone was the only or main reason why there was poor agreement between the experimental and computational values.

Discussion

The specimens with the least and greatest computational accuracy, in terms of stiffness, were S19L5 and S21L2 with errors of 286% and 22%, respectively. For each model, the percentage of fracture elements, in relation to bone elements, and the percentage of fracture filled with CaP was 4% fracture with 68% fill for S21L2 and 13% fracture with 62% fill for S19L5. Similar to the models presented in the PMMA augmented discussion, there was a variation in the level of fracture elements present although the percentage of augmentation was similar. Therefore, it is likely that both the level of fracture present and the distribution of the fracture may have an effect on the computational accuracy in terms of stiffness.

The models of S21L2 and S19L5 are shown, pre-loading and without the PMMA loading plates, in lateral and posterior views in Figure 5.26. Also shown are the corresponding semi-transparent views.

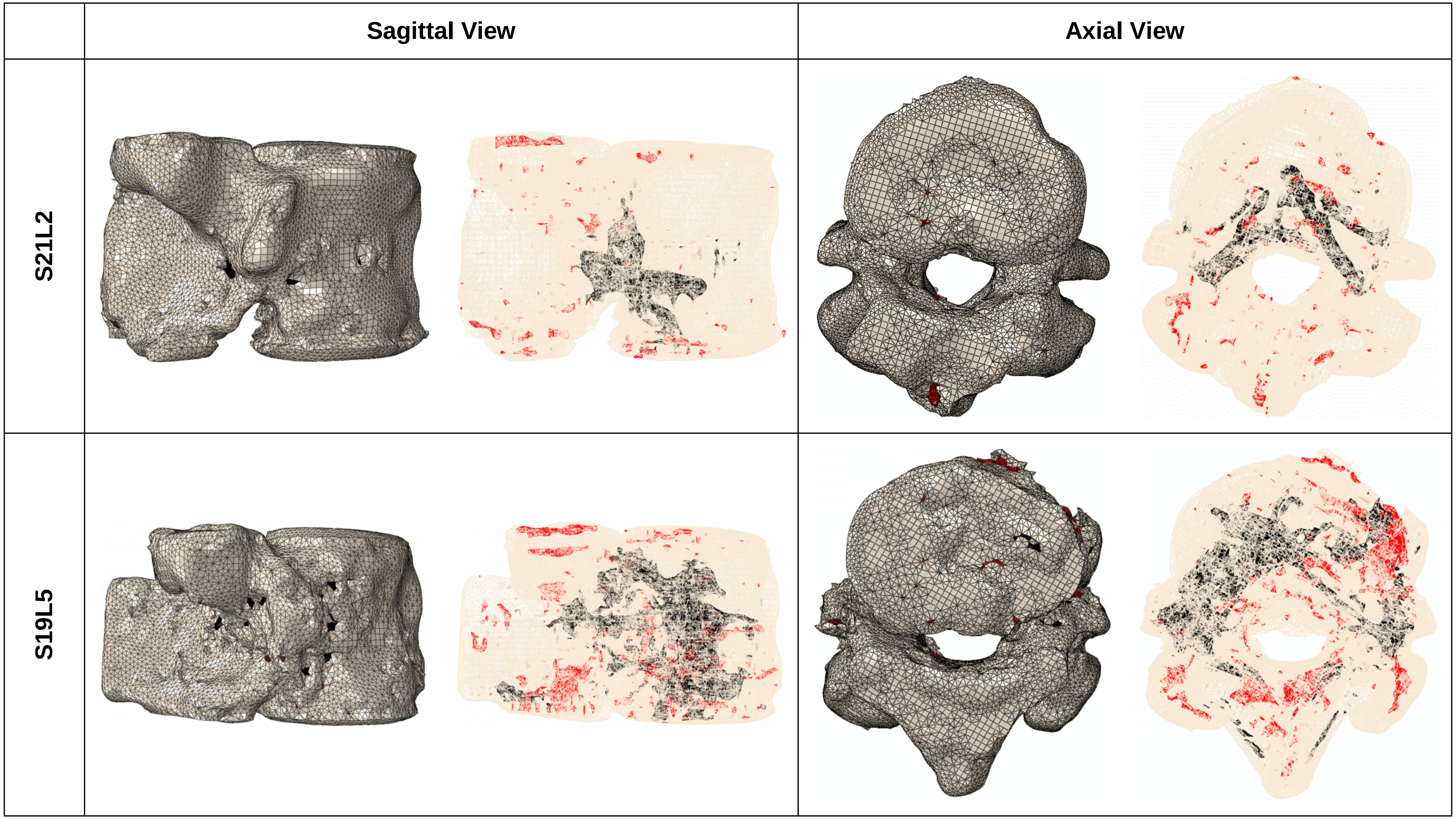

Figure 5.26 The CaP augmented multi-cycle models with the greatest and least computational accuracy in terms of stiffness, S21L2 (22%) and S19L5 (286%). For the sagittal view, the posterior elements are on the left hand side and the vertebral body is on the right hand side. The unfilled fracture is shown in red and the cement is shown in black.

It can be seen from the images that the fracture and augmentation patterns of the least computationally accurate model, S19L5, were more dispersed than that of S21L2 and covered a greater extent of the vertebral body. As was hypothesised previously, it is likely that the modelling technique employed may have been more suitable for simulating the behaviour of specimens with less dispersed fracture and augmentation patterns which were not present in the CaP augmented specimens.

5.3.4 Subsequent Loading Cycles

The subsequent loading cycles of a non-augmented specimen, S11L2, were modelled as described in Section 4.3.4. The results are presented in the following subsection with respect to the stiffness values, the loaded displacements and the permanent deformations of each cycle. The experimental and computational load-displacement curves for the initial three loading cycles of S11L2 are shown in Figure 5.27.

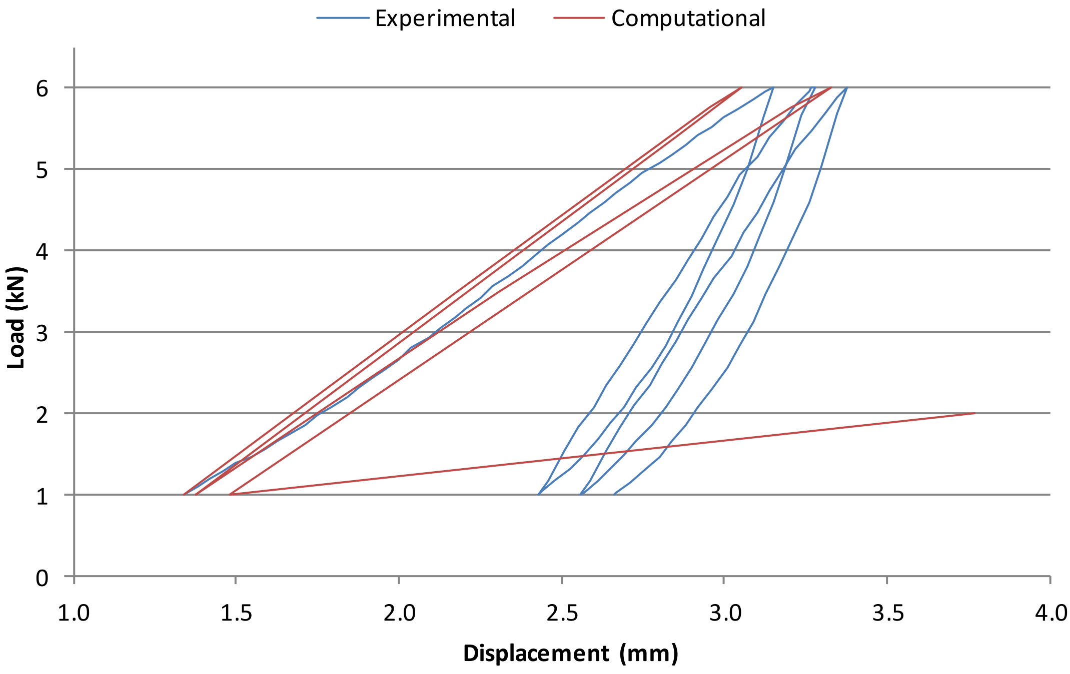

Figure 5.27 Initial three experimental and computational load-displacement curves for the non-augmented multi-cycle specimen S11L2. Note the non-zero X-axis starting position.

The figure showed that although the computational simulations correctly predicted a progressive increase in the loaded displacements, the increase per cycle was much larger than what was observed experimentally. A loaded displacement was not obtained for the third cycle as Abaqus failed to converge upon a solution. The computational stiffness incorrectly decreased across each loading cycle; the corresponding experimental stiffness increased. The simulated permanent deformation increased in an accurate manner following unloading across the initial two cycles but not to the extent that was observed experimentally.

The experimental and computational stiffness values for the three loading cycles of the non-augmented specimen S11L2 are shown in Figure 5.28.

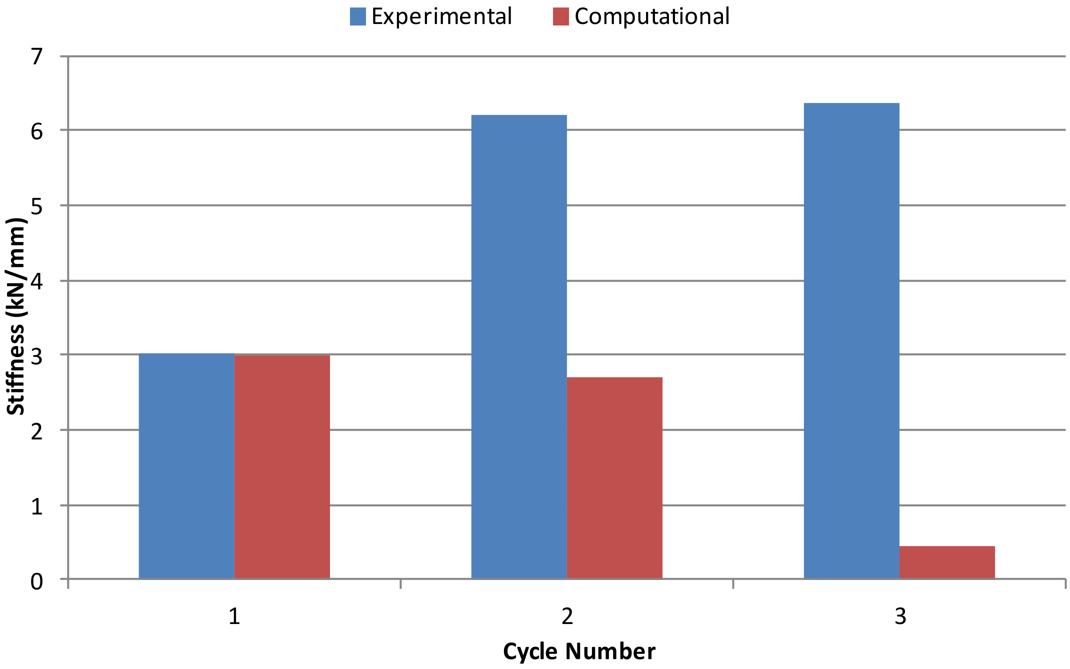

Figure 5.28 Experimental and computational stiffness values for the non-augmented specimen S11L2 across each of the three initial loading cycles.

The figure showed that model failed to replicate the experimental increase in stiffness that was observed across each cycle. The predicted stiffness of the initial loading cycle was very accurate and only 1% less than the experimental stiffness. However, for the second and third loading cycles, the predicted stiffness errors were much greater with underestimations of 57% and 93% of the experimental stiffness values.

The experimental and computational loaded displacement values of S11L2 from two of the loading cycles are shown in Figure 5.29.

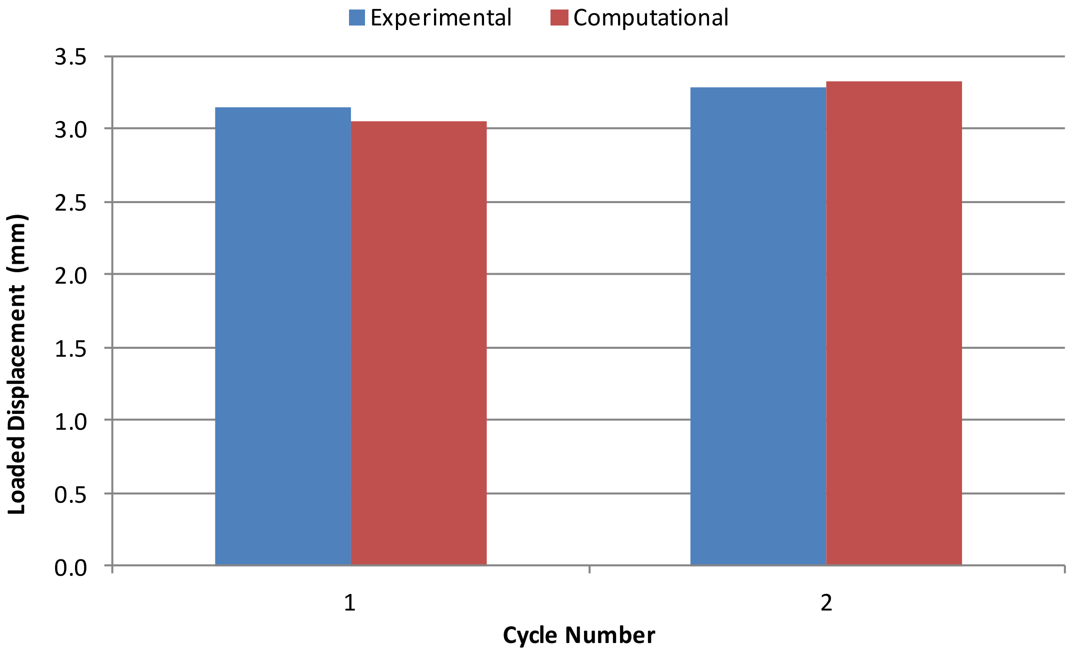

Figure 5.29 Experimental and computational loaded displacement values for the non-augmented specimen S11L2 across two of the loading cycles.

The initial loaded displacement predicted by the model was 3% lower than that observed experimentally and on the second cycle, the loaded displacement was 1.5% greater than the experimental value. However, as Abaqus was unable to converge upon a solution for the third loading cycle, it was not possible to determine the error although it is likely to have been large (Figure 5.27).

Discussion

The method that was used to model the subsequent loading cycles employed an algorithm which reduced the Young’s modulus of each element that had yielded. The elements behaved in an elastic, perfectly plastic manner. Because of the gradual reduction in the moduli of the elements in the model, it was not possible to simulate the experimental increase in stiffness that was observed across each loading cycle. However, it was envisioned that the reduction of the moduli would allow for a progressive decrease in the height of the model to be simulated which may have replicated the experimental behaviour which was not possible when using elastic models. It was possible to simulate the increase in loaded displacement (Figure 5.27 and Figure 5.29) although the unloaded displacement was not as large as what was seen experimentally. For these reasons, the method of modulus reduction was not used to simulate the subsequent loading cycles of any further specimens.

5.3.5 Clinical Application

The results of the clinical application are presented in the following subsection for the non-augmented, PMMA and CaP augmented specimens. The change in the predicted stiffness values is evaluated for different clinical scenarios.

The results of the clinical application, where several possibilities were simulated for a selection of non-augmented, PMMA and CaP specimens, are presented in Figure 5.30. The details of the simulations performed are given in Section 4.3.5. For the non-augmented specimens, the series in the figure labelled as Computational corresponds to the original models presented above where all of the elements that corresponded to the fracture void were assigned the arbitrarily defined materials properties of fracture. For the augmented models, the computational value listed in the figure corresponds to the original models where the fracture void was composed of elements that represented the areas which had been not been augmented with PMMA/CaP (X% Fracture) and the areas which had been augmented (100-X% PMMA or 100-X% CaP).

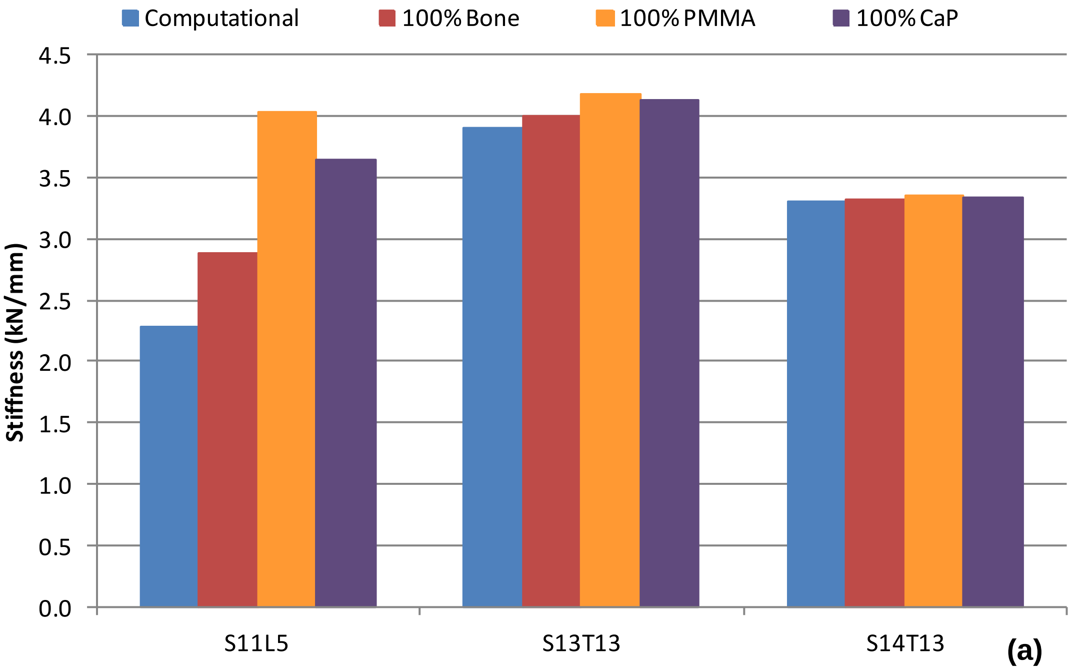

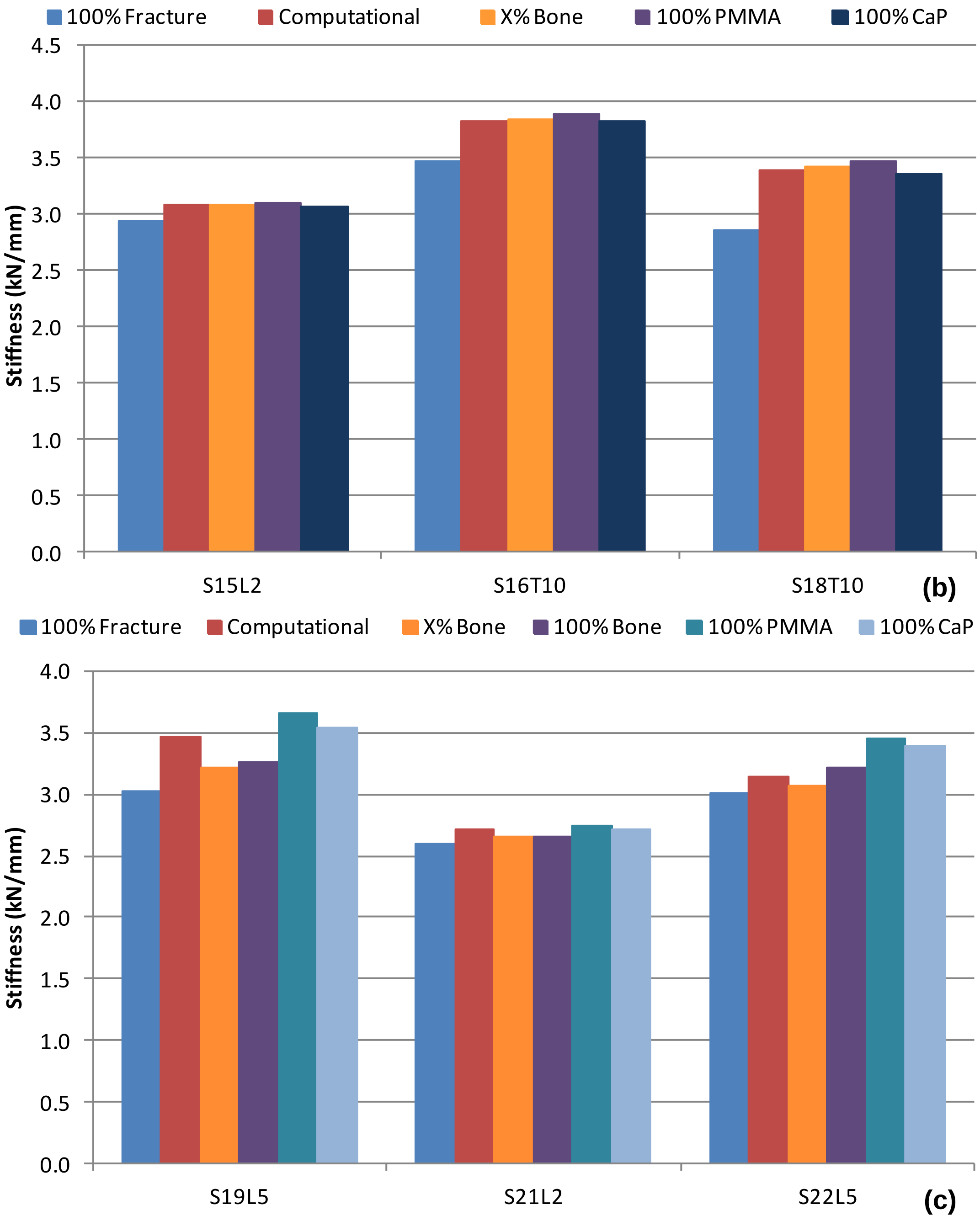

Figure 5.30 The stiffness of three (a) non-augmented, (b) PMMA augmented and (c) CaP augmented specimens when various clinical possibilities were simulated. The data for the computational series was obtained from the original models which contained 100% Fracture for the non-augmented models and X% Fracture with 100-X% PMMA/CaP for the augmented models.

For all of the specimens, the lowest predicted stiffness was seen when the elements representing the fracture void were fully assigned the arbitrary material properties of fracture (Computational for non-augmented and 100% Fracture for augmented). As expected, the perfect augmentations of all of the models with the material with the greatest Young’s modulus, PMMA, resulted in the greatest stiffness values

(100% PMMA). The predicted stiffness values for all of the CaP augmented specimens when the material properties of the fracture void were changed to simulate partial bone remodelling (X% Bone) and complete bone remodelling (100% Bone) were lower than that of the original computational models. This was in contrast to what would have been expected because the Young's modulus of the bone was greater than that of the fracture and of the CaP cement.

Some of the models were more susceptible to a change in the material properties of the fracture voids than others. Of the non-augmented specimens, the biggest variation in predicted stiffness values was observed in the model of S11L5 whilst for the PMMA augmented specimens, the biggest variation was observed in the model of S18T10. The CaP augmented specimens S19L5 and S22L5 were most susceptible to a change in the material properties of the fracture void. There was approximately 10% more fracture in the models of the specimens which were more susceptible than the ones which weren't. It is likely that the bigger the fracture void, the more pronounced the change in predicted stiffness is when the material properties of the fracture void are altered.

5.4 Discussion

The computational results are discussed in the following two subsections. The first subsection focuses on the accuracy of the single and multi-cycle specimens whilst the second subsection investigates the potential implications of the results for the clinical environment.

5.4.1 Model Accuracy

The mean absolute errors of the predicted stiffness and loaded displacement for the single and multi-cycle models are shown in Figure 5.31.

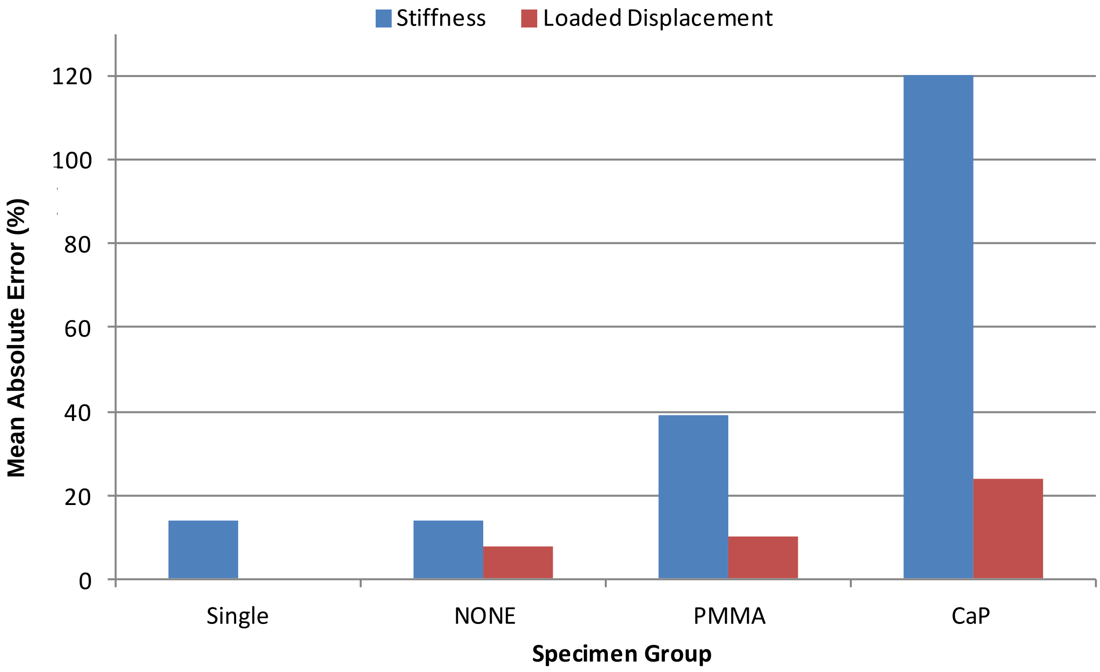

Figure 5.31 Mean absolute errors for the single cycle and multi-cycle models in terms of stiffness and loaded displacement.

The figure showed that there was a greater success in the prediction of the loaded displacement for each group than for the stiffness values. The mean absolute error for predicted stiffness values of the eight single cycle specimens (14%) was similar in magnitude to that observed by another researcher (19%) where 11 fractured porcine specimens were modelled using a similar technique (Tarsuslugil 2011). However, the mean absolute errors for the predicted stiffness values of the seven PMMA and six CaP augmented specimens were not in agreement with previous studies. The error associated with the PMMA augmented specimens was 39% whilst a previous study observed a mean absolute error of 8% across six specimens (Tarsuslugil 2011). The difference between the errors observed for the predicted stiffness of CaP augmented specimens was much greater in this study than in another study. In both investigations, six CaP augmented models were created and the mean absolute error in the present study was 120% whilst the previous study observed an error of 16%. It is possible that the CaP augmented specimens in the previous study were not as traumatically fractured and did not contain as dispersed fractures as in the current study although it is not possible to determine this as a grading system was not used in the previous study.

It is not possible to compare the results of the loaded displacement to previous findings as there are no publications in the literature of a study similar to the current investigation.

A plot of the absolute error for each specimen from the single and multi-cycle sets is shown in Figure 5.32 against the percentage of fracture void in each model. For the augmented specimens, the percentage of fracture was inclusive of the percentage of augmented fracture void.

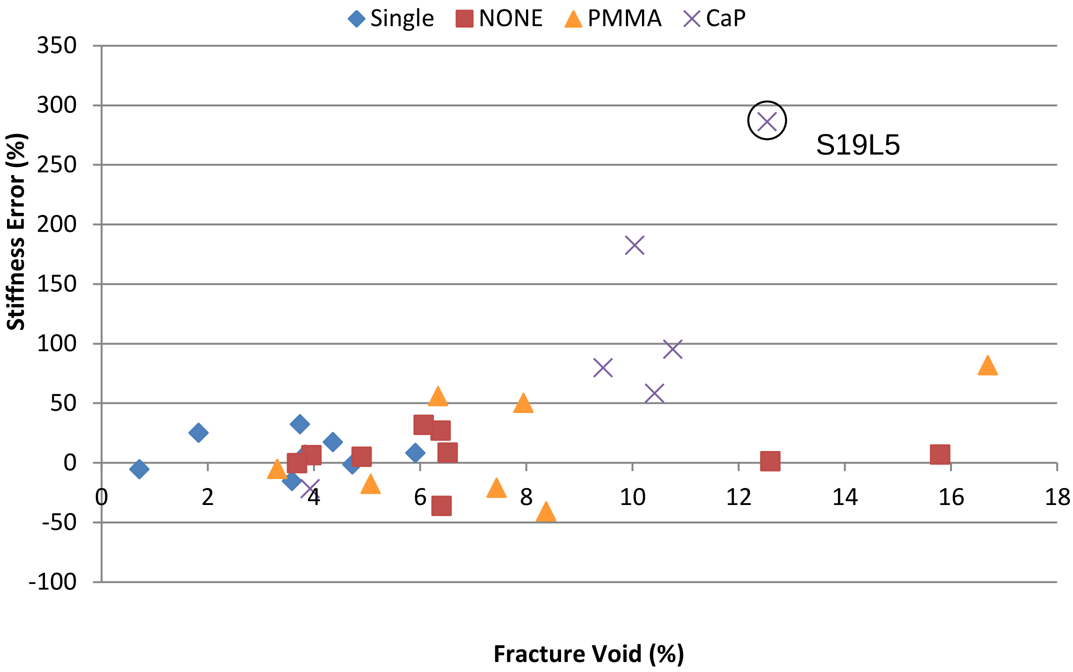

Figure 5.32 Error in predicted stiffness for the single and multi-cycle specimens. The percentage of fracture void is inclusive of the voxels representing the augmented PMMA or CaP cements and is given as a percentage of the total number of voxels of bone. The circled specimen, S19L5, was discussed previously in relation to the distributed fracture pattern.

The figure showed that generally a more accurate prediction in stiffness was accompanied by a lower percentage of fracture. However, two non-augmented specimens both possessed a high level of fracture but had absolute errors of less than 7%. It appeared that the CaP augmented specimens, which possessed errors in the predicted stiffness of over 150%, were in fact outliers due to a highly distributed fracture pattern which, as discussed above, has been witnessed to lead to higher errors in predicted stiffness values. It is possible that the greater the number of interactions created in Abaqus between the bone and fracture, the bone and cement and the cement and fracture, the greater the model error due to a greater percentage of the elements undergoing excessive deformation.

The absolute error in the predicted stiffness of each of the multi-cycle specimens is shown against the fracture grade in Figure 5.33. The single cycle specimens are not included as they were not graded.

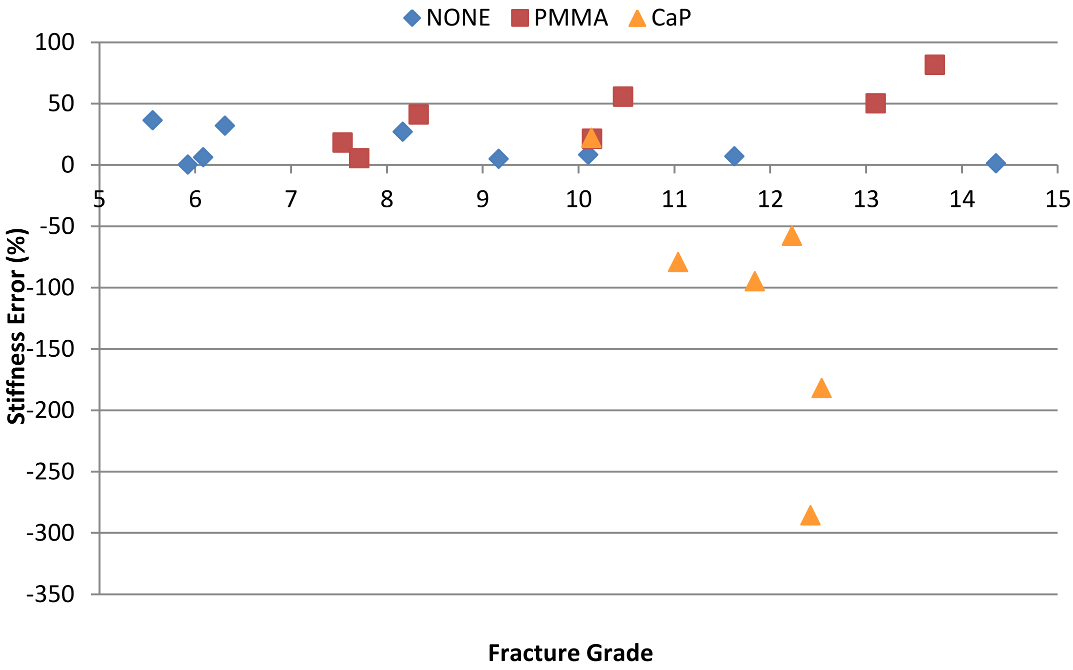

Figure 5.33 The error in the predicted stiffness values is shown for the multi-cycle specimens plotted against the fracture grade. Note the non-zero X-axis starting position.

The figure showed that there was no clear correlation between a higher fracture grade and a higher error in the predicted stiffness values which is in agreement with Figure 5.32 where the error in predicted stiffness was plotted against the percentage of fracture. Figure 5.32 and Figure 5.33 showed that generally, a greater percentage of fracture void or a higher fracture grade resulted in less accurate predicted stiffness values.

The absolute error in the predicted stiffness values is shown plotted against the level of injectability in Figure 5.34.

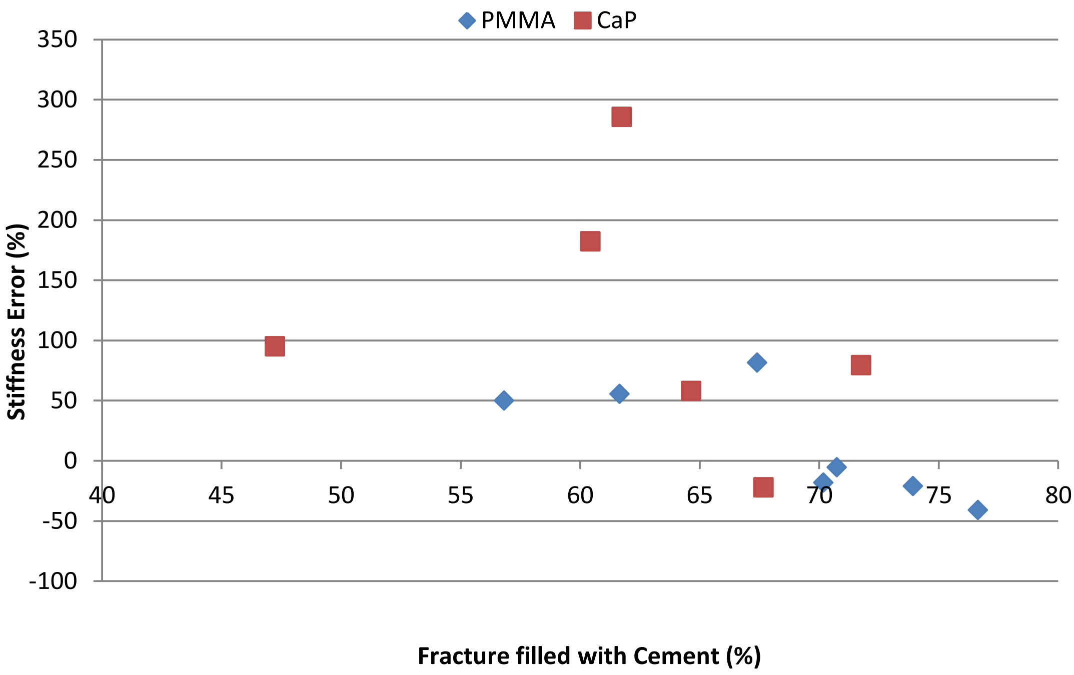

Figure 5.34 The error in predicted stiffness against the level of injectability. Note the non-zero X-axis starting position.

There was no clear trend between the percentage of fracture filled with cement and the observed errors. Therefore, the amount of cement injected did not appear to have an effect on the accuracy of the models.

Overall, there was greater agreement between the experimental and computational stiffness values for the single cycle and the non-augmented specimens. Both of the mean absolute errors associated with these groups were lower than those observed in another similar study (Tarsuslugil 2011). It is not clear why there were such disparities between the values of the non-augmented stiffness values and the augmented stiffness values which were much greater than observed during a previous study. It is possible that the fractures of the specimens in the current study were greater in volume and more dispersed than in a previous study (Tarsuslugil 2011) which, as mentioned above, appears to have increased the error in the predicted stiffness values and would have been more apparent in the current study if the fractures were larger. The potential energies of the drop-masses used to generate fractures in the current study were higher than what was employed in a previous study by approximately 15% which may have led to more traumatic and more dispersed fractures.

It may be possible that the augmentation procedure resulted in an increase in the size of the fractures when the cement was forced in. This may have resulted in an increased overall deformation of the specimens that was not replicated computationally. As the PMMA cement was much more viscous than the CaP cement, it would have been more likely to push the fractures further apart than the CaP cement. However, the greatest error in predicted stiffness was associated with the group of CaP specimens which means it is unlikely the injection alone caused the errors observed.

Alternatively, the guide holes drilled during augmentation may have altered the mechanical integrity of the specimen in a manner which was not simulated. The CaP specimens may have had a greater incidence of experimental augmentation via the pedicles in comparison to the PMMA specimens where it may have been possible for the augmentation to have taken place partly through the cortical shell which would not have compromised the mechanical integrity of the specimen as much. However, upon inspection of semi-transparent images of the models, there was no trend between the needle placement in the PMMA and CaP specimens.

The specimen-specific models of the CaP augmented specimens were constructed using images from a different µCT scanner (Section 2.5.3) which may suggest why the errors associated with this group of specimens were greater. However, there was no trend or bias in the predicted and experimental stiffness values of the CaP specimens (Figure 5.21) which suggests that the different µCT scanner did not result in the large errors associated with the CaP specimens. If the conversion of the CaP images from the alternative µCT scanner was incorrect, all of the CaP models would have either under- or overestimated the stiffness by a constant value which would have resulted in a consistent trend in the plot.

The investigation into the cement/bone interface highlighted that the large errors in the CaP specimens were not the sole result of the interactions between the CaP cement and the bone. The clinical investigation saw that a perfect augmentation with PMMA failed to increase the predicted stiffness to the levels observed experimentally which implies that the bone was not being simulated correctly. However, the single cycle and non-augmented specimens had reasonable levels of errors, therefore the micro-cracks in the bone were simulated correctly through the greyscale conversion factor.

The CaP specimens possessed the greatest mean fracture grade of the three multi-cycle groups. In conjunction to this, it is likely that the CaP specimens possessed the greatest distribution of fracture which led to the large errors observed. As discussed previously, it appears that the greater the percentage of fracture and the greater the extent of the fracture, the more difficult it is to predict the stiffness values which may explain the large errors observed with the CaP augmented models.

5.4.2 Clinical Outcomes

The results of the clinical application showed that the greater the percentage of fracture within a model, the more sensitive it was to a change in the material properties of the fracture void. Of the nine specimens selected from the non-augmented, PMMA and CaP augmented groups, the ones that were most susceptible to a change in material properties had approximately 10% more fracture present than the ones that were not as sensitive to a change in material properties (Figure 5.30).

The results showed that the greatest predicted stiffness was observed when the material properties of the fracture void were changed to represent a perfect augmentation with PMMA. These findings would be beneficial in a clinical environment when it was desirable to optimise the stiffness of fractured vertebrae. However, PMMA does not support complete bone remodelling and therefore, augmentation with CaP may be more appropriate. The predicted stiffness values associated with perfect CaP augmentation were similar to those of PMMA and complete *in vivo* bone remodelling with this cement is possible.

The findings of the computational results in terms of predicted stiffness values and loaded displacement were reasonable considering the limitations associated with the modelling procedure. It was not possible to predict the unloaded displacements because the models were unable to replicate the non-linear unloading that occurred experimentally. The over-simplified tie constraint that was used to simulate the fracture/bone/cement interface was inadequate possibly due to *in vitro* sliding at the surface however, the tie constraint gave agreeable results for the fracture/bone interface of the non-augmented models. The greyscale conversion factor used to allow for modelling on the continuum level was able to successfully capture the micro-damage in the bone and gave results which were in agreement to previous studies (Tarsuslugil 2011; Wijayathunga *et al*. 2008). Overall, the findings indicate that is it possible to model fractured specimens on a continuum level although it is more challenging for augmented models.

Chapter 6

Discussion and Conclusion

6.1 Introduction

The aim of the work presented in this thesis was to model the longer term effect of spinal burst fracture repair using vertebroplasty. Throughout the development process, traumatically fractured porcine spines were used to represent human burst fractures. Experimental and computational methodologies were devised whereby traumatic fractures were generated in porcine specimens and used to validate computational models. This chapter presents an overall discussion of the work presented in Chapter 2, Chapter 3, Chapter 4 and Chapter 5, recommendations for future works and the overall conclusions of this study.

6.2 Discussion

The main findings of the study are discussed in the following section in addition to the associated limitations.

6.2.1 Experimental Methodologies

Generation of Burst Fractures

Few other groups have produced repeatable burst fractures for the comparison of different fixation methods and obtaining repeatable burst fractures in a large number of specimens was a challenge. However, the success rate of fracture generation throughout the whole study was approximately 50% which was tolerable for use with animal tissue and comparable with a previous study (Tarsuslugil 2011).

The use of porcine spines was a limitation in the study because the spines were harvested from relatively young pigs where it was possible to identify the vertebral growth plates on µCT images. In addition, if the water content in the porcine nucleus pulposus was different from human, the load distribution during fracture creation may have been different and may not have been entirely representative of a clinical burst fracture. The alternative was the use of specimens from bovine, ovine or cadaveric spines. Bovine spines were not used due to the risks associated with the use of this tissue such as BSE and CJD whilst ovine spines were not used in the study because of the difficulty in obtaining a regular supply of specimens from similarly aged animals. In addition, the vertebrae of ovine spines are more conical than human which may have led to fractures which were not representative of the burst fractures seen in human spines. The vertebrae from cadaveric spines are generally from older, and possibly osteoporotic, individuals; these specimens would not be representative of the young and healthy spines in which burst fractures usually occur. Additionally, there are ethical issues associated with using cadaveric specimens at such an early stage of investigation; there were a number of specimens used in this study during method development that were not incorporated into the sets of validated FE models. Therefore, the use of porcine spines was justifiable in this study as an approximation of young, previously healthy, human vertebrae.

The fractures were generated using an *in vitro* approach with a drop weight, similar to the *in vivo* mechanism. However, a further limitation of the fracture generation technique was that, of the fractured porcine vertebrae obtained, not all were representative of burst fractures because they did not possess the characteristic V-shaped retropulsed bony fragment (Denis 1983). The low rate of characteristic burst fracture generation may have been due to the presence of the growth plates which seemed to direct the fracture pattern. However, to minimise wastage and expense, it was decided to use all of the traumatically fractured specimens, rather than continue with fracture generation in order to obtain the characteristic burst fracture injury. Since not all the fractures were of a burst type, they were subsequently referred to as ‘traumatically fractured’ vertebrae.

Grading Technique

The use of the grading system was highly beneficial to the study because it allowed for the post-fracture behaviour of the specimen to be quantified. The method that was developed is a significant step forward for future research because it allows for better grouping of specimens.

A limitation in this study that was highlighted by the grading was that there was a difference in the fracture severities and FSU levels present in each group. The variation in the fracture severity grades was as a result of sequentially working through each group in the laboratory. This is why the CaP augmented specimens had a higher incidence of L5 specimens present. The fracture grades of the augmented specimens may have been greater than the non-augmented specimens because the augmented specimens were graded post-augmentation. When the specimens were graded post-augmentation, the vertebroplasty guide holes were included in the overall fracture severity grade. However, because of the manner in which the study progressed and the limited access to the µCT scanner, it would not have been possible to work upon the specimens in the laboratory in any way other than sequentially. Therefore, the bias in the fracture severity grade and FSU levels present was a limitation in the study that could not have been eliminated in the timeframe that was available.

Cement Augmentation

The level of injectability was based on the µCT assessment and showed that a greater level of CaP injectability occurred than in a previous study which used the same cement (Tarsuslugil 2011). The level of injectability in the previous study was found to be 10 – 60% whilst the levels in the current study were between 47 and 77%. This may be because a push-syringe was employed following findings that a high level of filter-pressing occurred with the CaP cement when a twist-syringe was used (Tarsuslugil 2011). In that study, filter-pressing resulted in a greater extrusion of the liquid part of the CaP cement and meant that a high level of the solid component remained in the syringe. However, filter-pressing was not evident in the current study and this gave confidence in the material properties that were assigned at the computational stage.

A limitation of the augmentation procedure was that it was not performed under fluoroscopic guidance which is used *in vivo* to ensure accurate needle position and cement delivery. However, *in vitro*, it was possible to handle the specimens and visually inspect them from all sides which allowed for the angle and depth of the guideholes to be gauged against the exterior of the vertebral body. Since the progression of the injected cement could not be tracked in real time, as would have occurred using fluoroscopy, a high level of cement leakage occurred during augmentation that was also not representative of the *in vivo* procedure. Because of this, it was not possible to record the experimental level of injectability at the time of injection although a quantitative method based on the µCT images was subsequently applied.

Single Cycle Loading

The experimental technique to test single cycle specimens was not new, but it did allow for a direct comparison with the computational models. Few groups have previously modelled the post-traumatic fracture behaviour of porcine spines

(Tarsuslugil 2011). The level of agreement of the computational models was comparable with previous studies of both intact and fractured specimens (Tarsuslugil 2011; Wijayathunga *et al*. 2008; Sun and Liebschner 2004) which provided confidence that the approach was able to capture the behaviour of these specimens. The single cycle modelling provided a method that was used to model the augmented specimens.

Multi-Cycle Loading

The multi-cycle testing of fractured specimens was the major area of novelty of this study. Initially, two approaches were investigated: a low load, high cycle testing regime using a six-station spine fatigue simulator and a high load, low cycle regime using a materials testing machine. The simulators are generally designed for the testing of artificial replacements and the poor results illustrated the challenge in adapting the equipment to test natural tissue, which is more variable from specimen to specimen. Therefore, it is more difficult to achieve the necessary control using a machine of this kind. The high load, low cycle tests were more successful and a set of parameters for the test were defined using the method development specimens. The loading regime allowed for the testing of most of the specimens to be performed over 30 cycles with some propagation of damage but without complete failure.

A limitation of this part of the study was that the augmented specimens were generally unable to withstand the multi-cycle loading in comparison to the non-augmented specimens. However, the method was developed using non-augmented specimens, which did not have the reinforcement of an augmentation material and were able to withstand the loading, therefore it was envisioned that the reinforced augmented specimens would have withstood the loading regime. Ultimately, the magnitudes of the loads that were employed during multi-cycle loading were appropriate to the study.

6.2.2 Computational Methodologies

Single Cycle Loading

A limitation of the single cycle modelling was that the mesh density was not subjected to a convergence analysis. However, a resolution of greater than 1 mm would have incorporated individual trabecular detail into the model which was outside the scope of this project. Therefore, the findings from previous studies that a mesh density of 1 mm^3 was appropriate for modelling porcine vertebra was assumed to apply to fractured porcine vertebrae (Wijayathunga *et al*. 2008; Jones and Wilcox 2007).

Multi-Cycle Loading

The tests allowed for the computational models to be compared and different approaches to model the progression of damage to be investigated. The elastic-plastic approach with a 10% yield strain worked best and was able to reasonably predict the progressive displacement, but none of the methods investigated fully the experimental load-displacement behaviour over multiple cycles. The modulus-reduction method proposed by Liebschner, Rosenberg and Keaveny (2001) for human trabecular bone did not match the experimental data obtained in this study. *In vitro*, the stiffness of the specimens was seen to increase upon each loading cycle whereas computationally, due to the modulus-reduction technique, the stiffness decreased. The experimental increase in stiffness may have been due to the compression of the trabeculae upon each other which was not possible to simulate using the modulus-reduction technique.

Cement Augmentation

The models following cement augmentation did not match the experimental behaviour as well as the non-augmented specimens. This may be due to a combination of the specimens being more severely fractured and the failure of the cement to fully bond to the fracture.

The augmented models had greater fracture grades than the non-augmented models and it appeared from the visual inspection of the fracture distribution that larger errors were associated with vertebral bodies where the fracture encompassed a greater region. This may explain why the errors of a previous FE study, where the fractures were created using lower impact energies, were in better agreement with experimental data (Tarsuslugil 2011). Similarly, the results of the computational assessment of injectability indicated that the greater the volume of cement injected, the greater the errors in the model predictions. Again, the levels of injectability were greater in the current study than in the previous work (Tarsuslugil 2011). These findings suggested that the more interactions that were present in the model between the bone, fracture and cement, the less capable the model was at predicting the stiffness. A previous study has displayed a trend similar to the current study whereby a PMMA augmented osteoporotic cadaveric specimen yielded much greater errors than the non-augmented specimens (Wijayathunga *et al*. 2008).

Because the augmented specimen was osteoporotic, it is likely that the cement infiltrated within the trabeculae to a greater extent and that there was a greater level of bone, fracture and cement interactions in the computational models.

A visual inspection of the post-loading µCT images showed there was a tendency for the interlock between the bone and cement, in particular the CaP cement, to fail during multi-cycle loading. A limitation of the model was that this behaviour was not simulated because there was a tie constraint in place between the bone and cement interface. Therefore, in the models, the cement helped to reinforce the structure and transfer some of the load which in turn reduced the stress on the bone, which may account for why the augmented models did not undergo as much plastic deformation as the non-augmented models. *In vitro*, there was poor interlock between the bone and cement which resulted in the failure of the bone that was not captured computationally. The use of a tie constraint at the cement/bone interface was implemented following recommendations from previous studies (Tarsuslugil 2011; Zhao, Jin and Wilcox 2010) where it appeared to have adequately represented the interlock between the cement and bone. Further investigation of the best technique to model the cement/bone interface was outside the scope of the project, but this should be considered a limitation.

The present study did not incorporate bone regrowth into the models of CaP augmented specimens as this information was not available from the collaborators at the time of model generation. To incorporate bone regrowth into the models, the technique that was used to reduce the modulus of the yielded elements of bone could be applied to the CaP cement to alter the material properties, as a function of time, to be those of bone. However, this study has shown that the prediction of stiffness for the simulation of 100% bone regrowth did not match the experimental levels of stiffness. Therefore, if bone regrowth had been incorporated into the models, the computational errors would have been large.

6.2.3 Clinical

The major area of novelty for this study was to subject augmented burst fractures to multi-cycle loading. The results indicated that the performance of the augmentation may suffer over time, especially when CaP cements are used. Visual inspection of the post-loading images showed that there were instances where the interlock between the cement and bone failed during loading and that the CaP cement was more prone to failure than the PMMA cement.

The experimental and computational results indicated that augmentation may not be suitable for more severe burst fractures. The results of the multi-cycle loading show that specimens with a fracture grade greater than 10.5 were generally unable to withstand the loading (Figure 3.24, Figure 3.26 and Figure 3.27). Larger computational errors were associated with the specimens that had a fracture grade greater than 10.5 (Figure 5.33) which suggests that more useful predictions can be made when less severe burst fractures are modelled.

The computational results suggest that the differences between the PMMA and CaP cements are relatively minor in terms of the predicted stiffness values. Therefore, CaP cement could potentially stabilise a fractured vertebra to the same extent as the more stiff PMMA whilst providing the opportunity for bone remodelling. However, the *in vitro* analysis indicated that there are issues with the CaP cement that were not captured in the models such the weak interlock that occurred between the cement and the trabecular bone.

6.3 Future Recommendations

From the discussion presented above, several recommendations have been made that will aid future studies with a similar aim to the current study. These recommendations are given below for the experimental methodologies and model development, respectively.

Experimental Methodologies

For cadaveric specimens to be used in a similar study, it would be advisable to employ a fracture generation technique that had a greater success rate than that present in the current study. It is possible that an incremental trauma approach, such as the one used by another research group, could be used (Panjabi *et al*. 1995; Panjabi *et al*. 1995b; Kifune *et al*. 1995; Kifune *et al*. 1997). The use of an incremental trauma approach would allow for specimens to be repeatedly impacted upon until the appropriate fracture pattern was obtained. Although this is not representative of the clinical burst fracture mechanism, it would reduce the waste associated with the drop-mass technique that was employed in the current study.

Because of the developmental nature of this study and the limited access to the µCT scanner, it was only possible to work upon each group of specimens in the laboratory in a sequential manner. However, there would be several advantages if it were possible to work in a non-sequential manner and if access to the µCT scanner were increased. To eliminate the bias that was present in the fracture severity across the three groups of multi-cycle specimens, it would be advisable to scan and grade the specimens prior to group creation. That way, it would be possible to have a similar distribution of fracture grades in each group and a similar number of specimens from each FSU level. The scanning of specimens at this stage would also prove beneficial during augmentation. The images could be used to better guide needle placement and to provide an estimation of the volume of cement required for augmentation.

However, pre-augmentation grading would not take into account the effect of the guideholes on the mechanical integrity of the augmented specimens in comparison to the non-augmented specimens. The addition of guideholes to the non-augmented specimens would ensure that all of the specimens had a similar level of instability and that the fracture grades remained consistent across groups.

An alternative method of ensuring that every specimen in each group had a similar level of fracture would be to employ corpectomy, where part of the vertebral body is removed. The use of corpectomy would eliminate the waste associated with fracture creation, standardise the level of fracture within each group and provide a known volume of fracture void present for augmentation in order to compare directly between augmentation materials. However, corpectomy is not representative of the *in vivo* fracture mechanism and does not take into account changes to the surrounding areas of the fractured vertebra, but it would allow for more qualitative results to be obtained in a shorter length of time.

Model Development

The µCT scanner that was used in the current study allowed for only one fractured vertebra to be scanned at a time. In order to model the longer term effects of burst fracture repair using vertebroplasty, the effect of the augmentation on the adjacent vertebra would need to be considered. To do this, three vertebrae would need to be scanned and created into a FE model. However, to do so would require further validation of the way in which the intervertebral disc is represented on a continuum level model.

It may be possible to increase model accuracy by incorporating an additional mask into the model to represent the bone that is in contact with the fracture. In the current study, the material properties of bone were applied to this region. However, the bone in this region is not intact and does not possess the same continuum level properties as intact bone. Therefore, the material properties assigned to this region should be lower than the properties of intact bone.

The tie constraint between the bone and cement in the models did not replicate the experimental conditions. An investigation into how best to simulate the cement/bone interface on a continuum level may increase the accuracy of the models. It is possible that experimental trials could indicate the level of friction between the cement and bone once the interlock has failed and that this could be incorporated into future models.

The elastic-plastic model was unable to match the experimental behaviour of the specimens. The modulus-reduction technique did not allow for the *in vitro* increase in stiffness of the specimens per cycle to be simulated. A study similar to this would benefit from an improved material model where the behaviour of an augmented vertebra over a number of cycles could be simulated. A possible route of investigation would be to model the behaviour of cylindrical samples of intact porcine trabecular bone over multiple cycles before incorporating fracture, augmentation and ultimately whole porcine vertebrae.

6.4 Conclusion

The aims and objectives of this study were as highlighted in Section 1.8. The main experimental and computational findings are presented in this section. Also presented are the implications that this research has for the clinical environment.

The main conclusions of the study are as follows:

- The specimen-specific modelling approach was able to capture the behaviour of the specimens following fracture to a good degree of accuracy.
- The experimental multi-cycle loading method that was developed was appropriate for evaluating the performance of specimens over time using an accelerated high load, low cycle loading regime.
- Further work is necessary to develop computational material models that provide better predictions of the fractured bone behaviour over multiple cycles.
- The current method of cement modelling works best when fracture voids are smaller in volume and when there is little dispersion of the cement within the vertebral body.

- With current cements, fractures with a severity grade greater than 10.5 should not be augmented.
- Before CaP cements can be recommended, more works needs to be done on improving their flow characteristics and their ability to interlock with trabecular bone.

Access to patient-specific models by surgeons prior to augmentation could greatly increase the success of vertebroplasty. Using a patient-specific model, a surgeon may be able to determine the cement volume and distribution required to optimise treatment. It is also possible that longer term outcomes could be assessed on an individual basis taking into account medical history and lifestyle choices. However, there is no such model available to surgeons at present. The models developed in this study were at the continuum level in order to work towards providing a patient-specific analysis approach that is possible to perform using a desktop PC. From this study, it is clear that the models are not yet of a reliable level of accuracy, however the methods developed form a platform for future study and model improvement. Until the models are sufficiently developed, surgeons should use the grading technique to help identify burst fracture patients that would most benefit from vertebroplasty.

Chapter 7

Bibliography

Ahlgren, B.D., A. Vasavada, R.S. Brower, C. Lydon, H.N. Herkowitz and M.M. Panjabi. 1994. Annular Incision Technique on the Strength and Multidirectional Flexibility of the Healing Intervertebral Disc. *Spine.* **19**, pp.948–954.

Allan, D.G., G.G. Russell, M.J. Moreau, V.J. Raso and D. Budney. 1990. Vertebral End-Plate Failure in Porcine and Bovine Model of Spinal Fracture Instrumentation. *Journal of Orthopedic Research.* **8**, pp.154-156.

Amoretti, N., E. Hovorka, P.Y. Marcy, C. Lamasse, P. Brunner, C. Roux, P. Chevallier, P. Boileau, and J.N. Bruneton. 2005. Burst fracture of the spine involving vertebrae presenting no other lesions: the role of vertebroplasty. *J Clinical Imaging.* **29**, pp.379-382.

Ananthakishnan, D., S. Berven, V. Deviren, K. Cheng, J.C. Lotz, Z. Xu and C.M. Puttlitz. 2004. The effect on anterior loading due to different vertebral augmentation techniques. *C Biomechanics.* **20**, pp.25-32.

Anatomy TV. 2012 *Lumbar vertebra* [online]. [Accessed 1st September 2012]. Available from: http://www.anatomy.tv

Anderson, A.E., E.J. Benjamin and J.A Weiss. 2007. Verification, validation and sensitivity studies in computational biomechanics. *Computer Methods in Biomechanics and Biomedical Engineering*. **10**, pp.171-184.

Bai, B., L.M. Jazawi, F.J. Kummer and J.M. Spivak. 1999. The use of injectable, biodegradable calcium phosphate bone substitute for the prophylactic augmentation of osteoporotic vertebrae and the management of vertebral compression fractures. *Spine*. **24**, pp.1521-1526.

Baroud, G. and M. Bohner. 2006. Biomechanical impact of vertebroplasty - Postoperative biomechanics of vertebroplasty. *Joint Bone Spine.* **73**(2): pp.144-150.

Baroud, G., J. Nemes, P. Heini and T. Stefen. 2003. Load shift of the intervertebral disc after vertebroplasty: a finite-element study. *Eur Spine J*. **12**, pp.421-426.

Bass, C.R., K.A. Rafaels, R.S. Salzar, M. Carboni, R.W. Kent, M.D. Lloyd, S. Lucas,

K. Meyerhoff, C. Planchak, A. Damon and G.T. Bass. 2008. Thoracic and lumbar spinal impact tolerance. *Accident Analysis & Prevention*. **40**, pp.487-495.

Belkoff, S.M., J.M. Mathis, HH. Deramond and L.E. Jasper. 2001. An ex-vivo biomechanical evaluation if a hydroxyapatite cement for use with kyphoplasty. *Am J Neuroadiol.* **22**, pp.1212-1216.

Bensch, F.V., M.P. Koivikko, M.J. Kiuru and S.K. Koskinen. 2006. The incidence and distribution of burst fractures. *American Society of Emergency Radiology*. **12**, pp.124–129.

Berkman, E.F., R.N. Kruse, D.P. Mukherjee, K.K. Sadasivan and J.A. Albright. 1995. A method to characterize burst fractures. *In:* Biomedical Engineering - BioMED*, 7-9 April 1995, Shreveport, LA*. IEEE, pp.51-52.

Berlemann, U., S.J. Ferguson, L.P. Nolte and P.F. Heini. 2002. Adjacent vertebral failure after vertebroplasty: a biomechanical investigation. *Journal of Bone and Joint Surgery [British].* **84-B**(45), pp.748-752.

Boerger, T.O., D. Limb, R.A. Dickson. 2000. Does canal clearance affect neurological outcome after thoracolumbar burst fractures? *Journal of Bone and Joint Surgery.* **82B**, pp.629-635.

Bogduk, N. ed. 2005. *Clinical Anatomy of the Lumbar Spine and Sacrum.* Elsevier Churchill Livingstone.

Bohlman, H.H. 1985. Current Concepts Review: Treatment of fractures and dislocations of the thoracic and lumbar spine. *Journal of Bone and Joint Surgery: American.* **67,** pp.165-169.

Boisclair, D., J.M. Mac-Thiong, S. Parent and Y. Petit. 2011. Effect of spinal level and loading conditions on the production of vertebral burst fractures in a porcine model. J Biomech Eng. **133**(9):094503.

Brekelmann, W.A.M., H.W. Poort and T.J. Slooff. 1972. A New Method to Analyse the Mechanical Behaviour of Skeletal Parts. *Acta Orthopaedica Scandinavica*. **43**, pp.301-317.

Briem, D., A. Behechtnejad, A. Ouchmaev, M. Morfeld, K. Schermelleh-Engel, M. Amling and J.M. Rueger. 2007. Pain regulation and health-related quality of life after thoracolumbar fractures of the spine. *European Spine Journal.* **16**(11), pp.1925-1933.

Brinckmann, P., M. Biggemann and D. Hilweg. 1989. *In:* Adams, M.A. and K. Burton, ed. *The Biomechanics of Back Pain.* Elsevier Health Sciences, Volume 55, p.277.

Buchbinder, R., R.H. Osborne, P.R. Ebeling, J.D. Wark, P. Mitchell, C. Wriedt, S. Graves, M.P. Staples, B. Murphy. 2009. A randomized trial of vertebroplasty for painful osteoporotic vertebral fractures. *The New England Journal of Medicine*. **361**(6), pp.557-568.

Busscher, I., J.J.W. Ploegmakers, G.J. Verkerke and A.G. Veldhuizen. 2010. Comparative anatomical dimensions of the complete human and porcine spine*. Eur Spine J.* **19**(7), pp.1104-1114.

Callaghan, J.P. and S.M. McGill. 2001. Low back joint loading and kinematics during standing and unsupported sitting. *Ergonomics.* **44(**3), pp.280-294.

Callaghan, J.P., A.E. Patla and S.M. McGill. 1999. Low back three-dimensional joint forces, kinematics, and kinetics during walking. *Clinical Biomechanics*. **14**, pp.203-216.

Cappozzo, A. 1984. Compressive loads in the lumbar vertebral column during normal level walking. *Journal of Orthopaedic Research*. **1**(3), pp.292–301.

Chen, H.H., W.K. Wang, K.C. Li and T.H. Chen. 2004. Biomechanical efficiency of the body augmenter for reconstruction of the vertebral body. *Spine*. **29**, pp.E382-E387.

Chen, J.F. and S.T. Lee. 2004. Percutaneous vertebroplasty for treatment of thoracolumbar spine bursting fracture. *Journal of Surgical Neurology*. **62**, pp.494-500.

Chen, J.F., C.T. Wu and S.T. Lee. 2004. Percutaneous vertebroplasty for the treatment of burst fractures*. Journal of Neurosurg (Spine).* **1**(2), pp.228-231.

Chen, W.J., Y.H. Kao, S.C. Yang, S.W. Yu, Y.K. Tu and K.C. Chung. 2010. Impact of cement leakage into disks on the development of adjacent vertebral compression fractures. *J Spinal Disord Tech.* **23**(1), pp.35-39.

Cotterill, P.C, J.P. Kostuik, G. D'Angelo and G.R. Fernie. 1986. An anatomical comparison of the human and bovine thoracolumbar spine. *J Orthop Res.* **4**, pp.298-303.

Cotterill, P.C, J.P. Kostuik, J.A. Wilson, G.R. Fernie and B.E. Maki. 1987.

Production of a reproducible spinal burst fracture for use in biomechanical testing. *J Orthopaedic Research*. **5**, pp.462-465.

Crawford, R.P., C.E. Cann and T.M. Keaveny. 2003. Finite element models predict *in vitro* vertebral body compressive strength better than quantitative computed tomography. *Bone.* **33**(4), pp.744-750.

Crawford, R.P., W.S. Rosenberg and T.M. Keaveny. 2003. Quantitative computed tomography-based finite element models of the human lumbar vertebral body: effect of element size on stiffness, damage, and fracture strength predictions. *J Biomech Eng.* **125**(4), 434-438.

Currey, J.D. 2006. *Bones: Structure and Mechanics.* Princeton University Press.

Dai, L.Y. 2001. Remodeling of the spinal canal after thoracolumbar burst fractures. *Clinical Orthopaedics*. **382**, pp.119- 123.

Dath, R., A.D. Ebinesan, K.M. Porter and A.W. Miles. 2007. Anatomical measurements of porcine lumbar vertebrae. *Clinical Biomechanics.* **22**, pp.607–613.

Denis, F. 1983. The three column spine and its significance in the classification of acute thoracolumbar spinal injuries. *Spine*. **8**, pp.817-831.

Doody, O., C. Czarnecki, M.F. Given and S.M. Lyon. 2009. Vertebroplasty in the management of traumatic burst fractures: a case series. *Journal of Medical Imaging and Radiation Oncology.* **53***,* pp.489 - 492.

Eggli, S., F. Schlapfer, M. Angst, P. Witschger and M.M. Aebi. 1992. Biomechanical Testing of Three Newly Developed Transpedicular Multisegmental Fixation Systems. *European Spine Journal.* **1**, pp.109-116.

Eriksson, R.A., T. Albrektsson and B. Magnusson, B. 1984. Assessment of bone viability after heat trauma: a histological, histochemical and vital microscopic study in the rabbit. *Scandinavian Journal of Plastic and Reconstructive Surgery.* **18**, pp.261-268.

Ferguson, R.L. and B.L. Allen. 1984. A mechanistic classification of thoracolumbar spine fractures. *Clinical Orthopaedics and Related Research*. **189**, pp.77-88.

Fredrickson, B.E., W.T. Edwards, W. Rauschning, J.C. Bayley and H.A. Yuan. 1992. Vertebral burst fractures: An experimental, morphologic, and radiographic study (1992 Volvo Award in Experimental Studies). *Spine*. **17**, pp.1012–1021.

Galibert, P., H. Deramond, P. Rosat and D. Legars. 1987. Preliminary notes on the treatment of vertebral angiomas using percutaneous acrylic vertebroplasty. *Neurochirurgie*. **33**, pp.166-168.

Gardner-Morse, M., I.A.F. Stokes and J.P. Laible. 1995. Role of muscles in lumbar spine stability in maximum extension efforts. *Journal of Orthopaedic Research.* **13**(5), pp.802–808.

Garfin, S.R., H.A. Yuan and M.A. Reiley. 2001. Kyphoplasty and vertebroplasty for the treatment of painful osteoporotic compression fractures. *Spine*. **26**, pp.1511-1515.

Goel, V.K., W. Kong, J.S. Han, J.N. Weinstein and L.G. Gilbertson. 1993. A Combined Finite Element and Optimization Investigation of Lumbar Spine Mechanics With and Without Muscles. *Spine*. **18**(11), pp.1531-1541.

Goh, M.I., A. Thambyah, K. Bose. 1998. Effects of varying backpack loads on peak forces in the lumbosacral spine during walking. *Clinical Biomechanics*. 13(Supp 1), pp.S26-S31.

Guilak, F., H.P. Ting-Beall, A.E. Baer, W.R. Trickey, G.R. Erickson and L.A. Setton. 1999. Viscoelastic properties of intervertebral disc cells. Identification of two biomechanically distinct cell populations. *Spine*. **24**(23), pp.2475-2483.

Grados, F., C. Depriester, G. Cayrolle, N. Hardy, H. Deramond and P. Fardellone. 2000. Long-term observations of vertebral osteoporotic fractures treated by percutaneous vertebroplasty. *Rheumatology*. **39**, pp.1410-1414.

Gurwitz, G.S., J.M. Dawson, M.J. McNamara, C.F. Federspiel and D.M. Spengler. 1993. Biomechanical analysis of three surgical approaches for lumbar burst fracture using short-segment instrumentation. *Spine*. **18**, pp.977-982.

Heini, P.F., B. Walchli and U. Berlemann. 2000. Percutaneous transpedicular vertebroplasty with PMMA: operative technique and early results. A prospective study for the treatment of osteoporotic compression fractures. *European Spine Journal.* **9**, pp.445-450.

Holdsworth, F. 1963. Fractures, dislocations, and fracture-dislocations of the spine. *J of Bone and Joint Surgery*. **13**, pp.1534-1551.

Hongo, M., E. Abe, Y. Shimada, H. Murai, N. Ishikawa and K. Sato. 1999. Surface Strain Distribution on Thoracic and Lumbar Vertebrae Under Axial Compression: The Role in Burst Fractures. *Spine*. **24**(12), p.1197.

Huet, H., P. Cabal, R. Gadan, A. Borha and E. Emery. 2005. Burst-fractures and cementoplasty. *J Neuroradiol.* **32**(1), pp.33–41.

Jensen, M.E., A.J. Evans, J.M. Mathis, D.F. Kallmes, H.J. Cloft and J.E. Dion. 1997. Percutaneous polymethylmetacrylate vertebroplasty in the treatment of osteoporotic vertebral body compression fractures: technical aspects.*Am J Neuradiol*. **18**, pp.1897-1904.

Jones, A. 2009. *Verification, validation and sensitivity testing*, lecture notes distributed in MECH3380 Finite Element Methods of Analysis. *University of Leeds*.

Jones, A.C. and R.K. Wilcox. 2007. Assessment of factors influencing finite element vertebral model predictions. *Journal of Biomechanical Engineering.* **129**, pp.898-903.

Jones, A.C. and R.K. Wilcox. 2008. Finite element analysis of the spine: Towards a framework of verification, validation and sensitivity analysis. *Medical Engineering & Physics*. **30**, pp.1287-1304.

Kallmes, D.F. *et al*. 2009. A randomized trial of vertebroplasty for osteoporotic spinal fractures. *The New England Journal of Medicine*. **361**(6), pp.569-579.

Keaveny, T.M., E.F. Wachtel and D.L. Kopperdahl. 1999. Mechanical Behaviour of Human Trabecular Bone after Overloading. *J. Ortho. Res.* **17**, pp.346-353.

Keller T.S., V. Kosmopoulos and I.H. Lieberman. 2005. Vertebroplasty and kyphoplasty affect vertebral motion segment stiffness and stress distributions: a microstructural finite-element study. Spine*.* **30**(11), pp.1258-1265.

Keller, T.S., S.H. Holm, T.H. Hansson and D.M. Spengler. 1990. The dependence of intervertebral disc mechanical properties on physiologic conditions. *Spine*. **15**, pp.751-761.

Kifune M., M.M. Panjabi, M. Arand and W. Liu. 1995. Fracture pattern and instability of thoracolumbar injuries. European Spine Journal. **4**(2), pp.98-103.

Kifune M., M.M. Panjabi, W. Liu, M. Arand, A. Vasavada and T. Oxland. 1997. Functional morphology of the spinal canal after endplate, wedge, and burst fractures. *Journal of Spinal Disorders.* **10**(6), pp.457-466.

Klazen, C.A.H. *et al*. 2010. Vertebroplasty versus conservative treatment in acute osteoporotic vertebral compression fractures (Vertos II): an open-label randomised trial. *The Lancet.* **376**(9746), pp.1085-1092.

Kopperdahl, D.L., E.F. Morgan and T.M. Keaveny. 2002. Quantitative computed tomography estimates of the mechanical properties of human vertebral trabecular bone. *J Orthop Res.* **20**(4), pp.801-805.

Kopperdahl, D.L., J.L. Pearlman and T.M. Keaveny. 2000. Biomechanical Consequences of an Isolated Overload of the Human Vertebral Body. *J. Ortho Res.* **18**, pp.685-690.

Korovessis, P., A. Hadjipavlou and T. Repantis. 2008. Minimal Invasive Short Posterior Instrumentation Plus Balloon Kyphoplasty With Calcium Phosphate for Burst and Severe Compression Lumbar Fractures. *Spine*. **33**(6), pp.658-667.

Levine, S.A., L.A. Perin, D. Hayes and W.S. Hayes. 2000. An evidence-based evaluation of percutaneous vertebroplasty. *Managed Care*. **9**, pp.56-63.

Liebschner, M.A.K., W.S. Rosenberg and T.M. Keaveny. 2001. Effects of bone cement volume and distribution on vertebral stiffness after vertebroplasty. *Spine*. **26**, pp.1547-1554.

Lim, T.H., G.T. Brebach, S.M. Renner, W.J. Kim, J.G. Kim, R.E. Lee, G.B.J. Andersson and H.S. An. 2002. Biomechanical evaluation of an injectable calcium phosphate cement for vertebroplasty*. Spine*. **27**(12), pp.1297-1302.

Lin, R.M., K.H. Tsai and G.L. Chang. 1997. Distribution and regional strength of trabecular bone in the porcine lumbar spine. *Clinical Biomechanics.* **12**, pp.331-336.

Linde, F., I. Hvid and F. Madsen. 1992. The effect of specimen geometry on the mechanical behaviour of trabecular bone specimens. *J Biomech.* **25**(4), pp.359-368.

Lu, W.W, K.M. Cheung, Y.W. Li, D.K. Luk, A.D. Holmes, Q.A. Zhu and J.C.Y. Leong. 2001. Bioactive bone cement as a principle fixture for spinal burst fracture. *Spine*. **26**, pp.2684-2691.

McAfee, P.C., H.A. Yuan, B.E. Fredrickson and J.P. Lubricky. 1983. The value of computed tomography in thoracolumbar fractures. *J of Bone and Joint Surgery*. **65**, pp.461-473.

Menhusen, M. 2002. Comparative Human/Porcine Anatomy. [Accessed 12th March 2009], Available from: www.anesth.uiowa.edu/rasci/assets/COMPARAT.PDF

Mjoberg, B., H. Pettersson, R. Rosenqvist and A. Rydholm. 1984. Bone cement, thermal injury and the radiolucent zone. *Acta Orthop Scand*. **55**, pp.596-600.

Mosekilde, L. 1993. Vertebral Structure and Strength *In vivo* and *In vitro*. *Calcified Tissue International.* **53**, pp.S121-S126.

O'Hara, R.M. 2010. *Injectable calcium phosphate cements for spinal repair*. Ph.D. thesis, Queen's University Belfast: Belfast.

Ochia, R.S. and R.P. Ching. 2002. Internal pressure measurements during burst fracture formation in human lumbar vertebrae. *Spine.* **27**(11), pp.1160-1167.

Oner, F.C., J.J. Verlaan, A.J. Verbout and J.A. Dhert. 2006. Cement Augmentation Techniques in Traumatic Thoracolumbar Spine Fractures. *Spine*. **26**(24), pp.S89–S95.

Panjabi, M.M., H. Hoffman, Y. Kato and J. Cholewicki. 2000. Superiority of incremental trauma in experimental burst fracture studies. *C Biomechanics*. **15**, pp.73-78.

Panjabi, M.M., M. Kifune, L. Wen, M. Arand, T.R. Oxland, R.M. Lin, W.S. Yoon and A. Vasavada. 1995b. Dynamic canal encroachment during the thoracolumbar burst fractures. *J Spinal Disord.* **8**(39), p.48.

Panjabi, M.M., T.R. Oxland, M. Kifune, M. Arand, L. Wen A. and Chen. 1995. Validity of the three-column theory of thoracolumbar fractures. *Spine.* **20**, pp.1122-1127.

Poitout, D.G. 2004. *Biomechanics and Biomaterials in Orthopedics*. Springer

Polikeit, A., L.P. Nolte and S.J. Ferguson. 2003. The effect of cement augmentation on the load transfer in an osteoporotic functional spinal unit: finite-element analysis. *Spine*. **28**, pp.991-996.

Qui, T.X., K.W. Tan, V.S. Lee and E.C. Teo. 2006. Investigation of thoracolumbar T12-L1 burst fracture mechanism using finite element method. *Medical Engineering and Physics*. **28**, pp.656-664.

Rad, A.E., L.A. Gray, M. Sinaki and D.F. Kallmes. 2011. Role of physical activity in new onset fractures after percutaneous vertebroplasty. *Acta Radiol*. **52**(9), pp.1020-1023. Epub 2011 Sep 23.

Roaf, R. 1980. A study of the mechanics of spinal injuries. *Journal of Bone and Joint Surgery*. **42**(B), pp.810-823.

Ryan, G., A. Pandit and A. Dimitrios. 2008. Stress distribution in the intervertebral disc correlates with strength distribution in subdiscal trabecular bone in the porcine lumbar spine. *Clinical Biomechanics*. **23**(7), pp.859-869.

Shono, Y, P.C. McAfee and B. Cunningham. 1994. Experimental study of thoracolumbar burst fractures. *Spine*. **19**, pp.1711-1722.

Siddall, P.J. and M.J. Cousins. 1997. Spinal pain mechanisms. *Spine.* **22**, pp.98-104.

Silva, M.J., C. Wang, T.M. Keaveny and W.C. Hayes. 1994. Direct and Computed Tomography Thickness Measurements of the Human, Lumbar Vertebral Shell and Endplate. *Bone.* **15**, pp.409-414.

Silva, M.J., T.M. Keaveny and W.C. Hayes. 1997. Load sharing between the shell and centrum in the lumbar vertebral body. *Spine.* **22**, pp.140-150.

Slosar, P.J., A.G. Patwardhan, M. Lorenz, R. Havey and M. Sartori. 1995. Instability of the Lumbar Burst Fracture and Limitations of Transpedicular Instrumentation. *Spine.* **20**(13), 1452-1461.

Smit, T. H. 2002. The Use of a Quadruped as an *In vivo* Model for the Study of the Spine- Biomechanical Considerations. *European Spine Journal.* **11**, pp.137-144.

Sun, K. and M.A.K. Liebschner. 2004. Biomechanics of prophylactic vertebral reinforcement. *Spine*. **29**(13), pp.1428-1435.

Sun, K. and M.A.K. Liebschner. 2004b. Evolution of vertebroplasty: a biomechanical perspective. *Ann Biomed Eng*. **32**(1), pp.77-91.

Tarsuslugil, S. 2011. *Computational Modelling of Spinal Burst Fractures for the Development of Calcium Phosphate Cement*. Ph.D. thesis, The University of Leeds: Leeds.

Tohmeh, A.G., J.M. Mathis, D.C. Fenton, A.M. Levine and S.M. Belkoff. 1999. Biomechanical efficacy of unipedicular versus bipedicular vertebroplasty for the management of osteoporotic compressive fractures. *Spine.* **24**, pp.1772-1776.

Tran, N.T., N.A. Watson, A.F. Tencer, R.P. Ching and P.A. Anderson. 1995. Mechanism of the Burst Fracture in the Thoracolumbar Spine: The Effect of Loading Rate. *Spine.* 20(19), pp.1984-1988.

Trout, A.T. and D.F. Kallmes. 2006. Does vertebroplasty cause incident vertebral fractures? A review of available data. *Am J Neuroradiol.* **27**(7), pp.1397-1403.

Trout, A.T., D.F. Kallmes and T.J. Kaufmann. 2006. New Fractures after Vertebroplasty: Adjacent Fractures Occur Significantly Sooner. *Am J Neuroradiol.* **27**(1), pp.217-223.

Tsai, K.H, G.L. Chang and R.M. Lin. 1997. Differences in mechanical response between fractured and non-fractured spines under high-speed impact. *C Biomechanics.* **12**, pp.445-451.

Tsai, K.H., G.L. Chang and R.M. Lin. 1996. Trabecular orientation and mechanical behaviour of porcine lumbar vertebrae in static testing. *Journal of Medical and Biological Engineering*. **16**(1), pp.84-96.

Uppin, A.A., J.A. Hirsch, L.V. Centenera, B.A. Pfiefer, A.G. Pazianos and I.S. Choi. 2003. Occurances of new vertebral body fracture after percutaneous vertebroplasty in patients with osteoporosis*. Radiol.* **226**, pp.119-124.

Vaccaro, A.R., D.H. Kim, D.S. Brodke, M. Harris, J. Chapman, T. Schildhauer, C. Routt and R.C. Sasso. 2003. Diagnosis and management of thoracolumbar spine fractures. *Journal of Bone and Joint Surgery - American Volume.* **85A**(12), pp.2456-2470.

Valentini, M.C., R. Busch, M.M. Ferraris and F. Venturi. 2006. The role of imaging in the choice of correct treatment of unstable thoraco-lumbar fractures. *European Journal of Radiology.* **59**(3), pp.331–335.

van der Roer, N., E.S.M. de Lange, F.C. Bakker, H.C.W. de Vet and M.W. van Tulder. 2005. Management of traumatic thoracolumbar fractures: a systematic review of the literature. *European Spine Journal*. **14**(6), pp.527-534.

Verlaan, J.J., F.C. Oner and J.A. Dhert. 2006. Anterior spinal column augmentation with injectable bone cements*. Biomaterials*. **27**, pp.290-301.

Verlaan, J.J., J.A. Dhert, A.J. Verbout and F.C. Oner. 2005. Balloon vertebroplasty in combination with pedicle screw instrumentation. *Spine*. **30**(3), pp.E73-E79.

Wang, X.Y, L.Y. Dai, H.Z. Xu and Y.L. Chi. 2008. Biomechanical effect of the extent of vertebral body fracture on the thoracolumbar spine with pedicle screw fixation: an *in vitro* study. *J Clinical Neuroscience*. **15**, pp.286-290.

Wang, Z.L., J.C.M. Teo, C.K. Chui, S.H. Ong, C.H. Yan, S.C. Wang, H.K. Wong and S.H. Teoh. 2005. Computational biomechanical modelling of the lumbar spine using marching- cubes surface smoothened finite element voxel meshing.

Computer Methods and Programs in Biomedicine. **80**(1), pp.25-35.

Wellcome Images. 2009. *The spine* [online]. [Accessed 18th April 2009]. Available from: www.wellcomeimages.com

Wijayathunga, V.N., A.C. Jones, R.J. Oakland, N.R. Furtado, R.M. Hall and R.K. Wilcox. 2008. Development of specimen-specific finite element models of human vertebrae for the analysis of vertebroplasty. *Journal of Engineering In Medicine*. **222**, pp.221 - 228.

Wilcox, R.K, T.O. Boerger, D.J. Allen, D.C. Barton, D. Limb, R.A. Dickson and R.M. Hall. 2003. A dynamic study of thoracolumbar burst fractures. *J of Bone and Joint Surgery*. **85**, pp.2184-2189.

Wilcox, R.K. 2004. The biomechanics of vertebroplasty: a review. *J Engineering in Medicine*. **218**, pp.1-10.

Wilcox, R.K. 2006. The biomechanical effect of vertebroplasty on the adjacent vertebral body: a finite element study. *Proceedings of the Institute of Mechanical Engineers Part H - Journal of Engineering in Medicine*. pp.565-572.

Wilcox, R.K. 2007. The influence of material property and morphological parameters on specimen-specific finite element models of porcine vertebral bodies. *J of Biomechanics.* **40**, pp.669-673.

Wilcox, R.K. 2012. *Addition of plastic properties to an Abaqus input file.* Unpublished.

Wilcox, R.K. 2012b. *Creation of an input file based on the plastic deformation of a vertebral specimen*. Unpublished.

Wilcox, R.K., D.J. Allen, R.M. Hall, D. Limb, D.C. Barton and R.A. Dickson. 2004. A dynamic investigation of the burst fracture process using a combined experimental and finite element approach. *European Spine Journal.* **13**, pp.381-488.

Willen, J., S. Lindhal, L. Irstam, B. Aldman and A. Nordwall. 1984. The thoracolumbar crush fracture. *Spine.* **9**, pp.624-631.

Wood, K., A. Buttermann, G. Mehbod, T. Garvey, R. Jhanjee and V. Sechriest. 2003. Operative compared with nonoperative treatment of a thoracolumbar burst fracture without neurological deficit: A prospective, randomized study. *Journal of Bone and Joint Surgery: American Edition*. **85**, pp.773-781.

Yeni, Y.N., G.T. Christopherson, X.N. Dong, D.G. Kim and D.P. Fyhrie. 2005. Effect of microcomputed tomography voxel size on the finite element model accuracy for human cancellous bone*. Journal of Biomechanical Engineering*. **127**, pp.1-8.

Zhao, Y. 2010. *Finite Element Modelling of Cement Augmentation and Fixation for Orthopaedic Applications.* Ph.D thesis, The University of Leeds.

Zhao, Y., Z.M. Jin and R.K. Wilcox. 2010. Modelling cement augmentation: a comparative experimental and finite element study at the continuum level. Journal of Engineering in Medicine. **224**(7), pp.903-911.

Chapter 8

Appendix

A total of 15 specimens were used in the development of a multi-cycle loading regime; three were prepared for use in the spine fatigue simulator (Section 2.4.2) and the remaining 12 were used throughout multi-cycle compressive loading (Section 2.4.3). The 12 specimens were tested either using load control, displacement control or displacement control with maximum load settings as listed in Table 8.1. A summary of each trial every specimen was used in is listed in Table 8.2.

Table 8.1 Specification of the trials used in the development of a multi-cycle loading regime. Note that the any number following the specimen name indicates the number of times it was tested during that specific trial. For example, S8T13 was tested twice during LC1.

	Trial Name	**Pre-load Rate**	**Pre-load**	**Loading Rate**	**Maximum Load/ Displacement**	**Specimen/s**
Load Control	LC1	1000 N/min	500 N	2500 N/min	3000 N	S6L5
						S8T13 ***x2***
						S10T10
	LC2	1000 N/min	500 N	3000 N/min	3500 N	S6T13
Displacement Control	DC1a	10 mm/min	0.5 mm	10 mm/min	2 mm	S6L5
	DC1b	10 mm/min	0.5 mm	60 mm/min	2 mm	S6L5
	DC1c	10 mm/min	0.5 mm	180 mm/min	2 mm	S6L5
	DC2a	10 mm/min	0.5 mm	60 mm/min	3.5 mm	S5L5
	DC2b	10 mm/min	0.5 mm	100 mm/min	3.5 mm	S8L2
	DC3	10 mm/min	0.5 mm	100 mm/min	5 mm	S9L2
Displacement Control with Maximum Load	DCML1	10 mm/min	1000 N	25 mm/min	5000 N	S8L5
						S9T13
						S10T10
						S10T13
	DCML2	10 mm/min	1000 N	25 mm/min	7500 N	S6T13
	DCML3	10 mm/min	1000 N	25 mm/min	9500 N	S5T10 ***x4***
						S6T13
						S9T10
						S9T13
						S10T10

Table 8.2 Summary of specimens used throughout multi-cycle loading development and the trials they were subjected to. Note that the any number following the specimen name indicates the number of times it was tested during that specific trial. For example, S5T10 was tested four times during DCML3.

Specimen	**Trial**
S5T10	DCML3 ***x4***
S5L5	DC2a
S6T13	LC2 DCML2 DCML3
S6L5	LC1 DC1a DC1b DC1c
S8T13	LC1 ***x2***
S8L2	DC2b
S8L5	DCML1
S9T10	DCML3
S9T13	DCML1 DCML3
S9L2	DC3
S10T10	LC1 DCML1 DCML3
S10T13	DCML1